AD-A079 329 INSTITUTE FOR DEFENSE ANALYSES ARLINGTON VA SCIENCE A--ETC F/G 9/2
PRELIMINARY EVALUATION OF AN ALGORITHM FOR ANALYSIS OF STATIONA--ETC(U)
JUL 79 H HIDALGO, W WASYLKIWSKYJ MDA903-79-C-0202
UNCLASSIFIED IDA-P-1388 IDA/HQ-79-21079 NL

1 OF 2
AD
A079329

LEVEL III (12)
AD-E500 114
Copy 19 of 85 copies

IDA PAPER P-1388

ADA 079329

PRELIMINARY EVALUATION OF AN ALGORITHM FOR ANALYSIS OF STATIONARY RANDOM DATA FROM A MULTIPLE-INPUT LINEAR SYSTEM

Henry Hidalgo
Wasyl Wasylkiwskyj

July 1979

DDC
JAN 11 1980
A

DISTRIBUTION STATEMENT A
Approved for public release;
Distribution Unlimited

Prepared for
Defense Advanced Research Projects Agency

INSTITUTE FOR DEFENSE ANALYSES
SCIENCE AND TECHNOLOGY DIVISION

80- 8 1 050
IDA Log No. HQ 79-21079

The work reported in this document was conducted under contract MDA 903 79 C 0202 for the Department of Defense. The publication of this IDA Paper does not indicate endorsement by the Department of Defense, nor should the contents be construed as reflecting the official position of that agency.

Approved for public release; distribution unlimited.

UNCLASSIFIED

SECURITY CLASSIFICATION OF THIS PAGE (When Data Entered)

REPORT DOCUMENTATION PAGE

READ INSTRUCTIONS BEFORE COMPLETING FORM

1. REPORT NUMBER

2. GOVT ACCESSION NO.

3. RECIPIENT'S CATALOG NUMBER

4. TITLE (and Subtitle)
Preliminary Evaluation of an Algorithm for Analysis of Stationary Random Data from a Multiple-Input Linear System

5. TYPE OF REPORT & PERIOD COVERED
FINAL
Jan— Dec—1978

6. PERFORMING ORG. REPORT NUMBER
IDA Paper P-1388

7. AUTHOR(s)
Henry Hidalgo
Wasyl Wasylkiwskyj

8. CONTRACT OR GRANT NUMBER(s)
MDA903-79-C-0202

9. PERFORMING ORGANIZATION NAME AND ADDRESS
Institute for Defense Analyses
400 Army-Navy Drive
Arlington, Virginia 22202

10. PROGRAM ELEMENT, PROJECT, TASK AREA & WORK UNIT NUMBERS
DARPA Assignment A-49

11. CONTROLLING OFFICE NAME AND ADDRESS
Defense Advanced Research Projects Agency
Director, Tactical Technology
1400 Wilson Blvd., Arlington, Virginia 22209

12. REPORT DATE
July—1979

13. NUMBER OF PAGES
167

14. MONITORING AGENCY NAME & ADDRESS (if different from Controlling Office)

15. SECURITY CLASS. (of this report)
UNCLASSIFIED

15a. DECLASSIFICATION/DOWNGRADING SCHEDULE

16. DISTRIBUTION STATEMENT (of this Report)
Approved for public release; distribution unlimited.

79 21079
AD A500114

17. DISTRIBUTION STATEMENT (of the abstract entered in Block 20, if different from Report)
None

18. SUPPLEMENTARY NOTES
N/A

19. KEY WORDS (Continue on reverse side if necessary and identify by block number)
least-mean-squared estimation; spectral analysis; simulation of stationary random processes; bias errors in spectral analysis; signal extraction from noise; detection of spectra of magnetic field gradients.

20. ABSTRACT (Continue on reverse side if necessary and identify by block number)
This paper deals with a preliminary evaluation of a mean-squared estimated algorithm for the extraction of a signal that is embedded in superposed stationary noise processes. The motivation for this study is the processing and interpretation of data obtained in recent experiments to measure gradients of magnetic fields induced by internal waves in a shallow ocean.

DD FORM 1 JAN 73 1473 EDITION OF 1 NOV 65 IS OBSOLETE

UNCLASSIFIED

SECURITY CLASSIFICATION OF THIS PAGE (When Data Entered)

20.

The approach used is simulation of the signal and noise processes through construction of random time series for the signal and interfering noise processes whose spectra can readily be adjusted to study parametrically a wide range of situations.

The principal conclusions are: (1) the algorithm, in the form commonly applied to the reconstruction of the output of the main data channel, is valid only if a very special form of linear relationship is assumed between each of the superposed time series in the main channel and the time series in each of the subsidiary channels; an assumption that can lead to grossly erroneous estimates of the signal spectrum and (2) severe cumulative bias errors can be introduced in the reconstructed signal, partial coherences and transfer functions through the algebraic operations necessary in the application of the algorithm. This procedure can lead to large uncertainties in the functional form of the reconstructed signal spectra and, even more important, to false indications of the state of partial coherence.

IDA PAPER P-1388

PRELIMINARY EVALUATION OF AN ALGORITHM FOR ANALYSIS OF STATIONARY RANDOM DATA FROM A MULTIPLE-INPUT LINEAR SYSTEM

Henry Hidalgo
Wasyl Wasylkiwskyj

July 1979

INSTITUTE FOR DEFENSE ANALYSES
SCIENCE AND TECHNOLOGY DIVISION
400 Army-Navy Drive, Arlington, Virginia 22202

Contract MDA 903 79 C 0202
DARPA Assignment A-49

ACKNOWLEDGMENTS

The authors would like to express their gratitude to Mr. John Diggs for his dedicated computer programming efforts and to Mr. Craig Jackson for giving generously of his time and talents during the construction of the simulation algorithm.

The authors are also indebted to the reviewers of a draft of this paper for many valuable comments and suggestions. They were Dr. Philip A. Selwyn of DARPA, Dr. George Balanis from Areté Associates and their IDA colleagues, Drs. Joseph M. Aein, Gabriel Frenkel, Irvin W. Kay, Arthur Krinitz as well as Ms. Patricia Draper.

Accession For
NTIS GRA&I ☑
DDC TAB ☐
Unannounced ☐
Justification
By
Distribution/
Availability Codes
Dist | Avail and/or special
A

ABSTRACT

This paper deals with a preliminary evaluation of a mean-squared estimated algorithm for the extraction of a signal that is embedded in superposed stationary noise processes. The motivation for this study is the processing and interpretation of data obtained in recent experiments to measure gradients of magnetic fields induced by internal waves in a shallow ocean.

The approach used is simulation of the signal and noise processes through construction of random time series for the signal and interfering noise processes whose spectra can readily be adjusted to study parametrically a wide range of situations.

The principal conclusions are: (1) the algorithm, in the form commonly applied to the reconstruction of the output of the main data channel, is valid only if a very special form of linear relationship is assumed between each of the superposed time series in the main channel and the time series in each of the subsidiary channels; an assumption that can lead to grossly erroneous estimates of the signal spectrum and (2) severe cumulative bias errors can be introduced in the reconstructed signal, partial coherences and transfer functions through the algebraic operations necessary in the application of the algorithm. This procedure can lead to large uncertainties in the functional form of the reconstructed signal spectra and, even more important, to false indications of the state of partial coherence.

SUMMARY AND CONCLUSIONS

This paper deals with a preliminary evaluation of a mean-squared error estimation algorithm for the extraction of a signal that is embedded in superposed stationary noise processes. The signal, together with several additive noise processes, comprises the main sensor channel. Statistical estimates of one or more of the individual noise processes as well as of the signal are also available from several independent sensors (termed subsidiary channels), which data is employed to estimate the relative spectral content of the signal and noise constituents in the main channel. The principal application of the algorithm has been in the validation of theoretical response characteristics of linear sensors. The sensor to be evaluated is usually taken as the main channel. Subsidiary channel sensors are assumed to possess generally known response characteristics and to provide intrinsic signal-to-instrument noise ratios of sufficient magnitude to yield statistically significant information on the principal noise constituents in the main channel.

The direct motivation for this study is the processing and interpretation of data obtained in recent experiments to measure gradients of magnetic fields induced by internal wave activity in a shallow ocean. The experiment has been carried out off the coast of San Diego by Physical Dynamics, Inc. under ARPA sponsorship. The purpose of the experiment was to validate the theoretical relationships between magnetic field gradients induced by internal wave motion of sea water relative to the geomagnetic field and the hydrodynamic parameters of internal waves. The findings are expected to provide data for the design

of future at-sea experiments, the objective of which will be the verification of theoretically predicted ocean wave induced noise constituents in superconducting gradiometers when employed in magnetic anomaly detection.

Physical Dynamics has used the aforementioned algorithm to reconstruct the measured gradiometer output with the aid of data obtained from nine subsidiary sensors (channels). These included current flowmeters and thermistor chains yielding data on the signal (internal waves) as well as sensors monitoring the major main-channel noise constituents (e.g., those induced by random motion of the measurement platform). Despite the fact that the algorithm (in essentially the same form as employed by Physical Dynamics) has found extensive application in the interpretation of measurement data, a detailed evaluation of its capabilities under controlled conditions does not appear to have been undertaken.

Because the interpretation of the measurement data in the Physical Dynamics experiment as well as in other current and future ARPA nonacoustic ASW programs appears to be critically dependent on the efficacy of this algorithm, IDA was directed to undertake a limited effort to investigate the algorithm's performance characteristics under controlled conditions, using simulated data. In this preliminary study, no attempt has been made at a duplication of the functional forms of the spectra observed in the Physical Dynamics experiment. Rather, the approach has been to construct random time series for the signal and interfering noise processes whose spectra can readily be adjusted to encompass a sufficiently wide range of situations so as to increase the likelihood of uncovering the major intrinsic limitations of the data processing procedure per se. Thus, the term "gradiometer" as employed in the sequel is to be taken merely as a descriptive designation of the main data channel, and is not to be construed as implying any relation between the simulated spectra and those that might be observed with real

gradiometers. Also, instead of employing the complete set of nine channels, the numerical simulation was carried out only in the special case of one main data channel and two subsidiary channels. Nevertheless, the inherent deficiencies of the algorithm as enumerated in the following are expected to apply *a fortiori* in case more than three channels are employed. The principal conclusions are as follows:

- The form of the algorithm commonly applied to reconstruct the output of a sensor is valid only if a very special type of linear relationship subsists between each of the hypothesized time series in the main channel and the time series in each of the subsidiary channels (Eq. 15). We term this relation functional decoupling. The existence of functional decoupling would in general have to be inferred on the basis of *a priori* knowledge since its direct experimental verification is not always possible. Moreover, the consequences of incorrectly assuming functional decoupling can lead to grossly erroneous estimates of the signal spectrum [Eq. (65)] versus Eq. (67)].

- Because algebraic operations currently incorporated in the algorithm to determine the signal, partial coherences, and transfer functions are based on mathematical results derived for ideal spectra (i.e., exact Fourier transforms of the respective correlation functions), cumulative bias errors can result when the same operations are carried out with biased estimators of these spectra. Although the latter procedure conforms to standard practice, numerical simulations indicate that it can lead to significant uncertainties in the reconstructed signal spectra and, what is even more important, to false indications of the state of partial coherence between the main and a subsidiary channel. While these problems may be partially alleviated by a judicious choice of data windows, any attempt at an optimum solution would of necessity involve a reformulation of the algorithm directly in terms of spectral estimators.

- Additional observations based on the specific parameters employed in the simulation study may be found under "Concluding Remarks" on page 159.

CONTENTS

Acknowledgments iii
Summary and Conclusions vii

1. INTRODUCTION 1

1.1 Experimental Background 1
1.2 Theoretical Background 2
1.3 Scope of Parametric Numerical Simulations 8

2. MEAN-SQUARED ESTIMATION ALGORITHM 9

2.1 Basic Concepts 9
2.2 Reconstruction of Spectrum for Main Data Channel 14
2.3 Fidelity of the Reconstructed Spectrum of the Imbedded Signal 19
2.4 Constraints from Usual Linearity Form 25
2.5 Formulation of Nine-Channel Linear System 27

3. SIMULATION OF A THREE-CHANNEL LINEAR SYSTEM 31

3.1 Filter Simulation of Gradiometer and Subsidiary Channels 35
3.2 Algorithm for a Simulated Channel Linear System 42

3.2.1 Estimated Gradiometer Signal Spectrum 43
3.2.2 Estimated Gradiometer Transfer Functions 44
3.2.3 Estimator for the Gradiometer Output Spectra 46
3.2.4 Estimated Partial Coherence 47

3.3 Scope of Numerical Simulations 49
3.4 Interpretation of Numerical Simulations 53

4. RESULTS OF NUMERICAL SIMULATIONS 55

4.1 Low-Frequency Gradiometer with $L_{g_2}/L_{g_1} > 1$ 56

4.1.1 Estimated Gradiometer Signal Spectrum 56
4.1.2 Estimated Gain Factors 61
4.1.3 Estimators for Gradiometer Output Spectra 73
4.1.4 Estimated Partial Coherences 74

4.1.5 Overall Results for Low-Frequency Gradiometer with $Lg_2/Lg_1 > 1$ 81

4.2 Low-Frequency Gradiometer with $Lg_2/Lg_1 \approx 1$ 87

4.2.1 Estimated Gradiometer Signal Spectrum 87
4.2.2 Estimated Gain Factors 91
4.2.3 Estimator for Gradiometer Output Spectra 103
4.2.4 Estimated Partial Coherences 103
4.2.5 Overall Results for Low-Frequency Gradiometer with $Lg_2/Lg_1 \approx 1.0$ 104

4.3 Broad Bandwidth Gradiometer with $Lg_2/Lg_1 = 1$ 114

4.3.1 Estimated Gradiometer Signal Spectrum 114
4.3.2 Estimated Gain Factors 114
4.3.3 Estimators for Gradiometer Output Spectra 114
4.3.4 Estimated Partial Coherences 115
4.3.5 Overall Results for Broad Frequency Gradiometer with $Lg_2/Lg_1 = 1$ 115

4.4 Broad Bandwidth Gradiometer with $Lg_2/Lg_1 \neq 1$ 134

4.4.1 Gradiometer Signal-to-Noise of Unity 134
4.4.2 Effects of Gradiometer Signal-to-Noise Ratio 135

4.5 Recovery of Partial Coherence from S/N_i Ratio 136

5. CONCLUDING REMARKS 159

References 163

1. INTRODUCTION

1.1 EXPERIMENTAL BACKGROUND

Seawater, by virtue of its electrical conductivity, generates electrical currents through its motion relative to the earth's magnetic field. These electric currents generate, in turn, magnetic fields, which may be used to detect internal wave motions below the surface. Recent measurements of magnetic field gradients by Physical Dynamics (Ref. 1), 7m above the surface of 18m deep seawater, appear to show correlations between magnetic field gradients and wave motions having characteristic frequencies for swell (~100 mHz), surfbeat (~30 mHz) and internal waves (~3 mHz). The measurements were performed at an oceanographic research tower located about one mile offshore near San Diego, California. The basic instrumentation incorporated nine channels to (a) measure magnetic gradients from ocean waves with emphasis on those from internal waves and (b) monitor magnetic gradient noise from conduction and magnetization currents in nearby objects as well as instrument motions. The instrumentation consisted of a two-input gradiometer and triaxial fluxgate magnetometer above the sea surface as well as four electromagnetic-type biaxial current meters at several depths below the sea surface. Other supporting instrumentation involved two biaxial tilt meters, pressure transducers, thermistors and other sensors giving air pressure, temperature and wind speeds. The complete data records included fluctuations of the ambient magnetic field above the sea surface, seawater displacements and currents below the sea surface, motions of the gradiometer, as well as the ambient pressure, temperature and wind speeds.

The above measurements provided records of voltage fluctuations during time intervals from six to eight hours at the rate of once every second. To preclude aliasing, the data were first filtered to eliminate frequencies above 300 mHz. The data records were then averaged every 12 seconds to obtain each point of corresponding time series of 2048 discrete points. Fast Fourier transform (FFTs) operations on these time series gave corresponding auto- and cross-spectral density functions having 1024 frequencies spaced uniformly over a frequency range from 0.41 to 41.7 mHz. Each spectral density function was arithmetically averaged over 32 neighboring frequencies so as to reduce their fluctuations about their mean values. An algorithm for a multiple-input linear system was then utilized to obtain estimates of (a) the transfer functions of each subsidiary channel, (b) the spectrum of the magnetic field gradients or desired signal from the gradiometer ($\hat{S}_{g_1 g_1}$), (c) the spectra of other relevant parameters including those of the air pressure, temperature and wind speeds, and (d) the relevant partial coherences. A sample estimate of the mean values of the spectrum for the magnetic gradient, $\hat{S}_{g_1 g_1}$, indicated a frequency dependency given by $\hat{S}_{g_1 g_1} \simeq 200 f^{-2}$ within the frequency range $0.4 < f < 10$ mHz, where the units of $\hat{S}_{g_1 g_1}$ are given in $(\mathrm{pT/m})^2/\mathrm{Hz}$.

1.2 THEORETICAL BACKGROUND

The central problem in the analysis of experimentally-obtained data records (i.e., time series) is the extraction of one or more desirable signals (e.g., magnetic gradients generated by internal waves) from the invariably present "noise" background given by the superposition of other time series (e.g., conduction and magnetization currents other than those from internal waves and instrument motions). In many instances, the background "noise" is decomposable, at least in part, into a set of distinct time functions engendered by processes with known causative mechanisms susceptible to independent subsidiary

measurements. It then becomes possible, at least in principle, to employ the data from these subsidiary measurements in conjunction with a suitable estimation algorithm to effect, essentially, an enhancement of the desired signal-to-background noise ratio through a partial subtraction of the "noise" time series. If, in addition, one of the subsidiary measurements yields data linearly related to the signal itself, an algorithm based on a suitable linear combination of all the subsidiary data channels can then be used to provide a partial reconstruction of the main channel data record. In this latter case, instead of noise subtraction, one considers the modeling of the physical processes that give rise to the superposition of the time series in the main channel. In contrast with the signal-to-noise enhancement of the main channel through noise subtraction, the reconstruction of the main-channel data record constitutes mostly a verification procedure of the main-channel data. However, such verifications are usually only partial, because not all the processes contributing to the time series in the main channel are susceptible to independent observations. (For example, no independent observations of intrinsic instrument noise are possible.)

A common measure of the fidelity of reconstruction of the several time series in the main channel is the mean-squared error between the difference of the main channel output and a linear superposition of all the outputs of the subsidiary channels. If the signal and "noise" time series can reasonably be modeled as stationary stochastic processes, the algorithm incorporating the analytical solution for the minimization of the mean-squared error is given by a multi-channel Wiener Filter. The actual implementation of the filter can be of either the open loop or adaptive type. Although the latter has several advantages, only the former is of interest herein. Even though this type of algorithm has been in existence for over thirty years, it is somewhat surprising that its formulation has remained

limited to predicting the fidelity of reconstruction under only statistical ensemble averaging or, equivalently, averaging over very large (infinite) time records. The algorithm yields, for example, the transfer function of each channel based on ideal auto- and cross-spectral density functions, which are assumed to be determinable from ensemble averaging of the corresponding time series.

In actual practice, the algebraic operations dictated by the analytical solution under assumptions of perfect ensemble averaging are applied to *statistical estimates* of the self and cross spectra obtained via FFT operations and frequency averaging. Since these statistical estimates exhibit fluctuations as well as bias errors, the final quantities of interest (e.g., reconstructed signal, partial coherence) can deviate substantially from the "true" statistical averages.

As usual, the ideal auto-spectral density function, $S_{11}(f)$, of the time series $x_1(t)$ is defined by

$$S_{11}(f) = \int_{-\infty}^{\infty} R_{11}(\tau) e^{-i2\pi f\tau} d\tau \quad , \tag{1}$$

where f is the frequency and $R_{11}(\tau)$ denotes the auto-correlation function

$$R_{11}(\tau) = \langle x_1(t+\tau)\ x_1(t)\rangle \quad , \tag{2}$$

wherein the notation < > denotes the ensemble or statistical average of the stationary time series $x_1(t)$. Similarly, the ideal cross-spectral density function for two given time series is given by

$$S_{1y}(f) = \int_{-\infty}^{\infty} R_{1y}(\tau) e^{-i2\pi f\tau} d\tau \tag{3}$$

where R_{1y} denotes the cross-correlation function

$$R_{1y}(\tau) = \langle x_1(t+\tau)\ y(t)\rangle \quad . \tag{4}$$

The application of the mean-squared estimation algorithm utilizing the above ideal spectral density functions would yield the corresponding ideal transfer function for each channel as well as the ideal mean values of the spectra for the desired signal. Since under the usual experimental constraints direct use of ensemble averaging is impractical, it becomes necessary to employ statistical estimates of the correlation function based on time averaging. Since the advent of the FFT technique, it has become common practice to estimate the spectrum directly in the frequency domain instead of first computing the corresponding time-averaged correlation functions. Using the available single and finite length time series from a given channel, the estimated auto-spectral density function, for example, is obtained by computing first the unaveraged periodogram of the data record in the time domain $0 \leq t \leq T$ from

$$\hat{\hat{S}}_{11}(f,T) = \frac{1}{T} \left| \int_0^T x_1(t) e^{-i2\pi ft} dt \right|^2 \tag{5}$$

or

$$\hat{\hat{S}}_{11}(f,T) = \frac{1}{T} X_1^*(f,T) \; X_1(f,T) = \frac{1}{T} \left| X_1(f,T) \right|^2 , \tag{6}$$

where $X_1(f,T)$ is the finite Fourier transform of $x_1(t)$, i.e.,

$$X_1(f,T) = \int_0^T x_1(t) e^{-i2\pi ft} dt \tag{7}$$

and $X_1^*(f,T)$ is the complex conjugate of $X_1(f,t)$. Similarly, the cross-spectral density function for a pair of associated sample records $x_1(t)$ and $y(t)$ in the time domain $0 < t < T$ is given by

$$\hat{\hat{S}}_{1y}(f,T) = \frac{1}{T} X_1^*(f,T) \; Y(f,T) \tag{8}$$

where

$$Y(f,T) = \int_0^T y(t) e^{-i2\pi ft} dt . \tag{9}$$

The unaveraged periodogram $\hat{\hat{S}}_{11}(f,T)$ and $\hat{\hat{S}}_{1y}(f,T)$ are determined via FFTs of $x_1(t)$ and $y(t)$ to obtain $X_1(f,T)$ and $Y(f,T)$. They are usually characterized by a significant variance, i.e., fluctuations about their mean values. If the observation period T were sufficiently large, the statistical (ensemble) mean of $\hat{\hat{S}}_{11}(f, T)$ would tend to $S_{11}(f)$ as given by Eqs. (1) and (2), i.e., to the spectrum of the data record $x_1(t)$. However, $\hat{\hat{S}}_{11}(f, T)$ is not a useful estimator because its variance does not diminish regardless of how large T is chosen. In statistical terminology, the estimator $\hat{\hat{S}}_{11}(f,T)$ as given by Eq. (5) is said to be inconsistent. In practice, this problem is circumvented by introducing a second step to smooth out the fluctuations of $\hat{\hat{S}}_{11}(f,T)$ by using average values at each frequency over several adjacent frequencies. For example, if 2δ denotes the frequency interval over which $\hat{\hat{S}}_{11}(f,T)$ is averaged at each frequency, the averaging operation may be represented by*

$$\hat{S}_{11}(f,\delta,T) = \frac{1}{2\delta}\int_{f-\delta}^{f+\delta} \hat{\hat{S}}_{11}(\eta,T)d\eta \quad . \tag{10}$$

In its discrete form, Eq. (10) involves an arithmetical averaging over M frequencies *at either side* of a particular frequency, i.e.,

$$\hat{S}_{11}(f,M,T)= \frac{1}{2M+1}\sum_{\eta=f-\delta}^{f+\delta} \hat{\hat{S}}_{11}(f,T,\eta) \tag{11}$$

and $\delta = 2\pi M/T$.

The estimator of the spectrum, $\hat{S}_{11}(f,M,T)$ is usually referred to as a smoothed periodogram. A desirable consequence of frequency averaging is that the variance of $\hat{S}_{11}(f,M,T)$ can,

*The data smoothing and the Fourier transforms are, of course, performed only at discrete values of the record. This aspect is not important to the present discussion. For convenience, we assume a continuous data record $x_1(t)$.

in principle, be made as small as desired by choosing δT sufficiently large. In statistical terminology, the estimator $\hat{S}_{11}(f,M,T)$ is said to be consistent. Since the data record is usually of fixed length, the reduction in variance is effected by increasing the frequency averaging interval 2δ. Unfortunately, as δT is increased, the statistical mean of $\hat{S}_{11}(f,M,T)$ does not tend to the true spectrum of $x_1(t)$ but to some distorted version of the spectrum. The estimator $\hat{S}_{11}(f,M,T)$ is then said to be biased. The net result of increasing δ is to produce estimators that are consistent but biased, i.e., estimators with reduced fluctuations about mean values that are different from the ideal or true spectrum, the difference being made progressively greater as δ increases. It is this tradeoff between variance and bias with increasing δ that represents an unresolved thorny problem in the interpretation of periodogram averaged spectra.

The problem of the proper interpretation of the spectral features is magnified substantially when use is made of smoothed periodograms in the several algebraic operations (e.g., matrix inversions) required by the algorithm to derive the quantities of interest such as transfer functions and partial coherences. Since the analytical solution for the bias error and variance estimates for even one channel is extremely difficult, the most appropriate methodology for studying these effects in a multichannel situation is numerical simulation. For example, a particular stationary process with a known spectrum (signal) together with a number of "noise" spectra can readily be created by appropriate digital filtering of random number sequences. The spectral reconstruction algorithm can then be applied directly to these artificial time series to obtain estimates of their spectra as well as the transfer functions for each channel and desired signals. Since all the ideal spectra are known, the effects of bias errors and statistical fluctuations about the mean introduced by the algorithm can be explicitly displayed and studied parametrically not only in terms of the magnitude

of M but also as a function of specified signal-to-noise ratios. Such a numerical simulation is the subject of this paper.

1.3 SCOPE OF PARAMETRIC NUMERICAL SIMULATIONS

The scope of these parametric investigations is limited to preliminary tests of the algorithm itself under arbitrary but known conditions, and it deliberately excludes any attempt to evaluate the results based on actual data gathered by the Physical Dynamics experiments.

The subsequent sections of this paper deal with the following: (1) a brief outline of the mean-squared estimation algorithm for a multiple-input linear system, (2) detailed description of the numerical simulation scheme for a three-channel linear system, (3) presentation of the numerical results and finally, (4) the concluding remarks.

2. MEAN-SQUARED ESTIMATION ALGORITHM

The formulation of the mean-squared estimation algorithm used in the Physical Dynamics experiments, as described in the previous section, is now considered in order to bring out its basic limitations. This section, therefore, considers: (a) basic concepts in the formulation of the algorithm, (b) reconstruction of the spectrum for the main data channel, (c) fidelity of the reconstructed spectrum of the imbedded signal in the main channel, (d) constraints from the usual assumptions concerning the functional linearity among the superposed time series in the main data channel and those from the subsidiary measurements, (e) constraints from the frequency averaging of auto- and cross-spectral densities as used in common practice, and (f) formulation of the algorithm for a subsidiary nine-channel system as used in the Physical Dynamics experiments.

2.1 BASIC CONCEPTS

The basic concepts underlying the reconstruction algorithm are illustrated in Figs. 1a, b; where Fig. 1a (left) shows both the main data channel (top) as well as the subsidiary channels (bottom) for the reconstruction of the main data channel. The time series y(t) represents the main data channel, which is connected to the primary sensor or gradiometer output in these particular considerations. The main data y(t) is given by

$$y(t) = \xi_1(t) + \sum_{i=2}^{q} \xi_i(t) + z(t) \quad , \qquad (12)$$

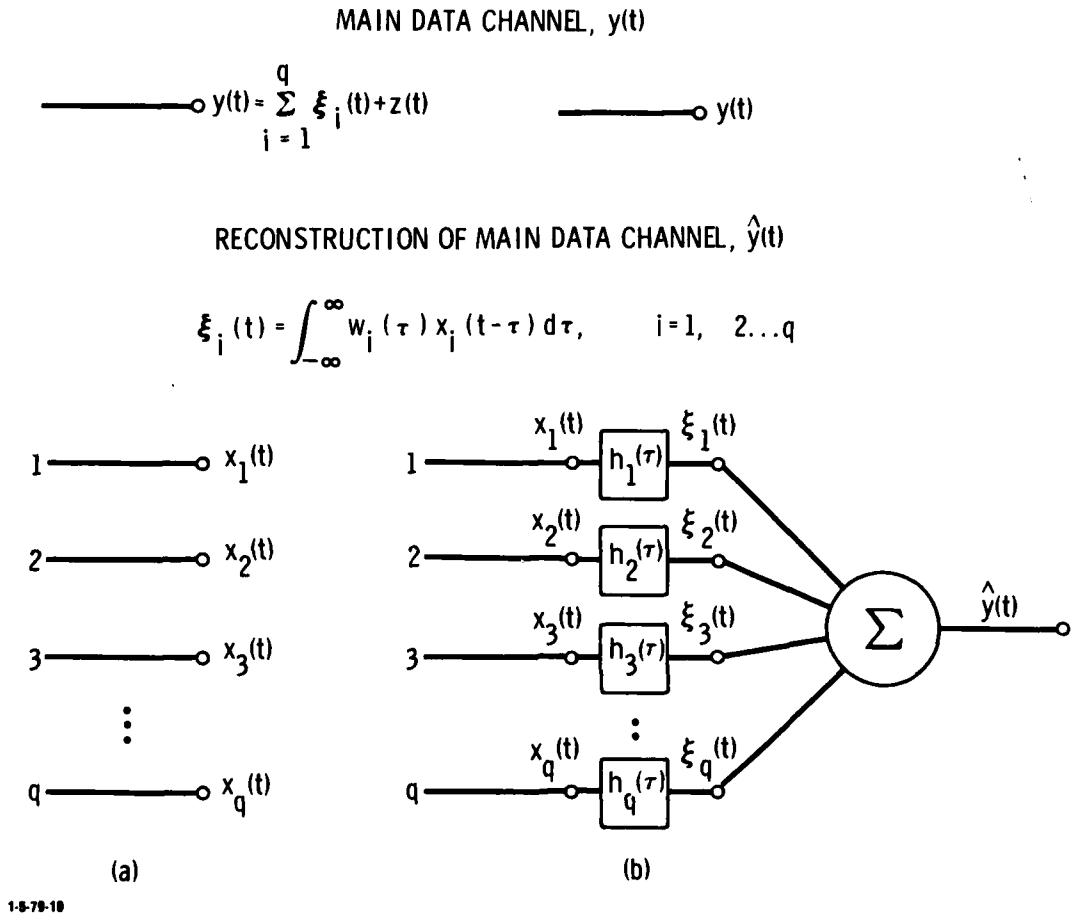

FIGURE 1. Schematic representation of linear system utilized in the algorithm to reduce the Physical Dynamics measurements in a gradiometer output. (a) Representation of superposed time series in main data channel, y(t), and time series in output of subsidiary channels. (b) Reconstruction of main data channel for simplified functional linear relationship (Eq. 15) among superposed time series in main data channel and time series in subsidiary channels.

i.e., by the desired signal denoted by the time series $\xi_1(t)$ and a superposition of time series arising from several but not necessarily independent physical sources $\xi_2(t)\ldots\xi_q(t)$, as well as a composite noise process $z(t)$, whose constituent time series are unknown. Physically, the signal $\xi_1(t)$ represents that part of the voltage fluctuations generated in the main data channel $y(t)$ due to the interaction of ocean currents with the earth's magnetic field. Hence, the remaining voltage fluctuations of $y(t)$ from the other time series in the right-hand side of Eq. (12) constitute sources of "noise" with respect to the signal $\xi_1(t)$. The objective of the reconstruction algorithm is to isolate the signal time series through utilization of the subsidiary data channels given by

$$\vec{x}(t) = [x_1(t),\ x_2(t)\ldots x_i(t)\ldots.x_q(t)] \ , \qquad (13)$$

which is a q-dimensional input vector describing the subsidiary data channels indicated in Fig. 1a. Each of the subsidiary time series in Eq. (13) is a result of a measurement of a physical process which is known to be linearly related to the superposed time series $\xi_1(t)$, $\xi_2(t)\ldots.\xi_i(t)\ldots.\xi_q(t)$ in the main data channel $y(t)$. The subsidiary time series are modeled as stationary stochastic processes with statistical properties that need not go beyond the second moments due to the interest in measurements of the spectra of the desired signal. If the linear relationship among the subsidiary and superposed time series in the main data channel is time invariant, they are, in general related by

$$\xi_i(t) = \sum_{n=1}^{q} \int_{-\infty}^{\infty} w_{in}(\tau)\ x_n(t-\tau)d\tau, \qquad i=1,\ 2\ldots q \qquad (14)$$

where $w_{in}(\tau)$ represents the impulse response function in the presence of the noise $z(t)$ and Eq. (14) is the linear superposition of the convolution integrals. Physically, Eq. (14) indicates that each of the superposed time series (ξ_i) in the

main data channel is the results of a linear superposition of the contributions to it from each of the q subsidiary data channels ($\sum_{n=1}^{q}$) given by future and past inputs ($-\infty < \tau < \infty$) from each subsidiary time series. Hence, the outputs of the subsidiary and main channels can be used to estimate $\xi_1(t)$..... $\xi_q(t)$, provided the q x q matrix of impulse reponse functions $w_{in}(\tau)$ can be determined from the experimental data. However, following common practice (e.g., Ref. 2), the algorithm used in the Physical Dynamics interpretation of the data utilizes a special form of Eq. (14), viz.,

$$\xi_i(t) = \int_{-\infty}^{\infty} w_i(\tau)\, x_i(t-\tau)d\tau, \qquad i=1,\ 2...q \qquad (15)$$

wherein only q impulse response functions $w_i(\tau)$ must be determined from the experimental data. Unlike the more general linear relationship, Eq. (14), the special form given by Eq. (15) implies a one-to-one correspondence between each $x_i(t)$ subsidiary channel and its corresponding $\xi_i(t)$ time series in the main channel. Physically, the specialized linear assumption given by Eq. (15) implies two conditions (Ref. 2): (a) that the output of several simultaneous inputs to the main channel is equal to the sum of outputs produced by each input alone and (b) that the output of the product of a constant times an input is equal to the constant times the output of the input alone. Hence, Eq. (15) assumes a complete *functional* decoupling between $\xi_i(t)$ and $x_n(t)$ whenever $n \neq i$, as shown in Fig. 1b. Equivalently, the impulse response functions in Eq. (14) become related to those in Eq. (15) by

$$w_{in}(\tau) = \begin{cases} w_i(\tau) & ;\ i = n \\ 0 & ;\ i \neq n \end{cases}, \qquad (16)$$

i.e., when only the terms along the principal diagonal of the q x q matrix of $w_{in}(\tau)$ are non-zero. Note that this functional

decoupling does not imply statistical independence among the various time series; i.e., x_n and ξ_1 are not necessarily statistically independent even though Eq. (15) holds. Whether the subsidiary channels are related to the constituent components in the main channel by Eq. (15) or by the more general form of Eq. (14) depends on *a priori* knowledge of the physical processes modeled by each $x_n(t)$, and is not readily resolvable on the basis of the experimental data alone. Some consequences of assuming incorrectly that Eq. (15) holds always will be discussed later. The fidelity of reconstruction of the main channel output y(t) in terms of the subsidiary data records $x_n(t)$ does not depend on the choice between Eqs. (14) and (15), a choice that becomes important only in the subsequent identification of $\xi_1(t)$ as the desired reconstructed signal. While Eq. (15) would isolate the signal $\xi_1(t)$, a reconstruction based on Eq. (14) would yield an unknown linear superposition of the signal and "noise" outputs $\xi_2(t).....\xi_q(t)$ in Eq. (12).

Finally, it must be emphasized that an alternative theoretical procedure to obtain the desired signal ξ_1 (Fig. 1) would be to (a) utilize only the subsidiary data channels [e.g., $x_1(t)$] simulating internal wave phenomena and (b) use the Maxwell equations to calculate directly the transfer functions $H_1(f)$, i.e., to calculate the magnetic gradients induced by internal waves. However, this more complicated approach would utilize only the available multi-channel hydrodynamic data in the Physical Dynamics experiments and would not represent an experimental verification of the gradiometer measurements. The latter consideration is important because the calculation of this transfer function must also utilize auxiliary assumptions concerning the distribution of internal wave energy among wave modes as well as the directional properties (isotropic versus nonisotropic) of the relevant processes in a shallow ocean.

2.2 RECONSTRUCTION OF SPECTRUM FOR MAIN DATA CHANNEL

Based on Eq. (15), Fig. 1b illustrates the reconstruction or estimation, $\hat{y}(t)$, of the time series $y(t)$ in the main data channel for $z(t) = 0$. If $w_i(\tau) = h_i(\tau)$ for this latter condition, the estimator $\hat{y}(t)$ is given by Eqs. (12) and (15) as

$$\hat{y}(t) = \sum_{i=1}^{q} \int_{-\infty}^{\infty} h_i(\tau)\ x_i(t-\tau)d\tau \tag{17}$$

i.e., each subsidiary channel $x_i(t)$ is passed through a time invariant linear filter with impulse response function $h_i(\tau)$ and the results summed to yield the estimate $\hat{y}(t)$. The criterion for good reconstruction of $y(t)$ is taken to be the statistical average of the mean-squared error or difference between the measured time series $y(t)$ and the estimator $\hat{y}(t)$, i.e.,

$$\langle \varepsilon^2 \rangle = \langle |y(t) - \hat{y}(t)|^2 \rangle . \tag{18}$$

The correct impulse response functions $h_i(\tau)$ in Eq. (17) are chosen such that $\langle \varepsilon^2 \rangle$ is minimized. If the stochastic processes are stationary, it is found that the $h_i(\tau)$ functions that yield such a minimum must satisfy the system of integral equations

$$\sum_{j=1}^{q} \int_{-\infty}^{\infty} h_j(\tau')R_{ji}(\tau-\tau')d\tau' = R_{yi}(\tau), \quad i=1,2.....q \tag{19}$$

where R_{ji} and R_{yi} are auto- and cross-correlation functions defined by Eqs. (2) and (4), i.e.,

$$R_{ii}(\tau) = \langle x_i(t+\tau)\ x_i(t) \rangle$$

$$R_{ji}(\tau) = \langle x_j(t+\tau)\ x_i(t) \rangle$$

$$R_{yi}(\tau) = \langle y(t+\tau)\ x_i(t) \rangle \quad .$$

The q impulse response functions satisfying Eqs. (19) define a q-dimensional Wiener filter. Since all physically realizable impulse response functions must vanish for the negative values of their argument τ, the limits of integration must be truncated to run from 0 to ∞. As a result, the matrix integral equation is then of the Wiener-Hopf type; the solution of which, in general, presents difficult problems. However, if one is willing to accept impulse response functions which are noncausal,* i.e., $h_j(\tau) \neq 0$, $\tau < 0$, the solution of Eq. (19) is found by a straightforward application of Fourier transforms. Thus, in the frequency domain, Eq. (19) factors into

$$\sum_{j=1}^{q} H_j(f)\, S_{ji}(f) = S_{yi}(f) \qquad i = 1, 2 \ldots q \tag{20}$$

where $H_j(f)$, $S_{ji}(f)$ and $S_{yi}(f)$ are Fourier transforms of $h_j(\tau)$, $R_{ji}(\tau)$ and $R_{yi}(\tau)$, respectively. Fortunately, the possible noncausal nature of $h_j(\tau)$ as obtained from Eq. (20) does not appear to be too important in the digital realization of the filter functions, so that there is no need to deal with the substantially more complicated Wiener-Hopf solution.

In order to expand Eq. (20) in matrix form, it becomes convenient to introduce the following notation:**

$$\vec{H}(f) = [H_1(f),\ H_2(f) \ldots\ldots\ldots H_q(f)] \tag{21}$$

$$\vec{S}_{xy}(f) = [S_{1y}(f),\ S_{2y}(f) \ldots\ldots S_{qy}(f)] \tag{22}$$

---

*A filter is said to be noncausal if it can produce an output *before* an input is applied.

**Since the algorithm is described in some detail in Ref. 2, the same notation is used here as far as possible to facilitate the interpretation of comparable results.

and

$$\vec{S}_{xx}(f) = \begin{bmatrix} S_{11}(f) & S_{12}(f) \cdots\cdots & S_{1q}(f) \\ S_{21}(f) & S_{22}(f) \cdots\cdots & S_{2q}(f) \\ \vdots & & \\ S_{q1}(f) & S_{q2}(f) \cdots\cdots & S_{qq}(f) \end{bmatrix} \tag{23}$$

where $\vec{H}(f)$ is the q-dimensional frequency response or transfer function vector corresponding to that in Eq. (13) under the assumption of Eq. (15), $\vec{S}_{xy}$ the q-dimensional cross-spectrum vector of the subsidiary inputs $x_i(t)$ with the main channel time series $y(t)$, and $\vec{S}_{xx}(f)$ the q x q spectral matrix of the subsidiary time series. The notation in the right-hand side of Eq. (22) has been simplified by replacing $\vec{S}_{x_i y_j}$ with $\vec{S}_{iy}$, where i = 1, 2 ...q. Similarly, in Eq. (23) $\vec{S}_{x_i x_j}$ is replaced with S_{ij}, where i, j = 1, 2 ....q. It should be noted from Eqs. (6) and (8)* that equation (23) is a Hermitian matrix $[S_{ij}]$ characterized by real-valued elements along the principal diagonal (i=j) and by complex conjugates for any two elements (S_{ij}, S_{ji}) situated symmetrically with respect to the principal diagonal. A prime superscript will be used to denote the transpose of a given vector; i.e. $\vec{H}'$ to indicate, for example, the vertical column corresponding to the row given by Eq. (21). Finally, a † superscript will indicate the complex conjugate transpose matrix (adjoint) to denote from Eq. (22), for example, by $\vec{S}^{+}_{xy}$ the vertical column with elements $S^*_{1y} \ldots S^*_{qy}$; whereas an asterisk superscript will denote, as before, the conjugate of a complex variable.** In terms of the preceding notation, Eq. (20) reads

$$\vec{H}\,\vec{S}_{xx} = \vec{S}^*_{xy} \tag{24}$$

---

*These equations can, of course, be generalized to include any X_i in Eq. (6) and any combination of $X^*_i X_j$ for $i \neq j$ in Eq. (8).

**To simplify the already cumbersome notation, the explicit dependence on frequency (f) will be omitted.

from which the solution for the transfer function column matrix is

$$\vec{H}^{\dagger} = (\vec{S}_{xx})^{-1} \vec{S}'_{xy} \tag{25}$$

where the symmetries $S_{ij} = S^*_{ji}$ and $S_{yn} = S^*_{ny}$ have been used. The filter transfer functions given by Eq. (25) yield the smallest mean-squared errors in Eq. (19). This mean-squared error is given by

$$\langle \varepsilon^2 \rangle_{min} = \int_{-\infty}^{\infty} [S_{yy} - \sum_{j=1}^{q} S_{jy} H_j] df \ . \tag{26}$$

The integrand in this expression is just the spectrum of the residual process (uncancelled noise) $y(t) - \hat{y}(t)$ in the main data channel. Upon substituting the solution from Eq. (25) for $\vec{H}'$ into Eq. (26), one can rewrite the latter entirely in terms of the auto- and cross-spectral density functions, i.e.,

$$\langle \varepsilon^2 \rangle_{min} = \int_{-\infty}^{\infty} S_{yy} \left[1 - \frac{\vec{S}^*_{xy} (\vec{S}_{xx})^{-1} \vec{S}'_{xy}}{S_{yy}} \right] df$$

or

$$\langle \varepsilon^2 \rangle_{min} = \int_{-\infty}^{\infty} S_{yy} \ [1 - \gamma^2] \ df \tag{27}$$

where the quantity γ^2 is known as the multiple coherence function as given by

$$\gamma^2 = \frac{\vec{S}^*_{xy} (\vec{S}_{xx})^{-1} \vec{S}'_{xy}}{S_{yy}} \leq 1 \tag{28}$$

and is equal to the normalized cross spectral density between the main channel time series $y(t)$ and the estimator $\hat{y}(t)$:

$$\gamma^2 = \frac{|S_{\hat{y}y}|^2}{S_{yy}\, S_{\hat{y}\hat{y}}} \quad . \tag{29}$$

If the main data channel time series y(t) were completely decomposable into a sum such as Eq. (17), then one would necessarily have $\gamma^2 = 1$ and the mean squared error would be zero. Conversely, the condition $\langle\varepsilon^2\rangle_{min} = 0$ yields from Eq. (27) $\gamma^2 = 1$, because (excluding the trivial case of $S_{yy} = 0$) S_{yy} and $1 - \gamma^2$ are always positive. From Eq. (28), it would follow that

$$S_{yy} = \vec{S}^{*}_{xy}\, (\vec{S}_{xx})^{-1} \vec{S}'_{xy} \tag{30}$$

which, with Eqs. (24) and (25) yield

$$S_{yy} = \vec{H}\, \vec{S}_{xx}\, \vec{H}^{\dagger} \tag{31}$$

or

$$S_{yy} = [H_1 \ldots H_q] \begin{bmatrix} S_{11} & S_{12} & \cdots\cdots & S_{1q} \\ S_{21} & S_{22} & \cdots\cdots & S_{2q} \\ \vdots & & & \\ S_{q1} & S_{q2} & \cdots\cdots & S_{qq} \end{bmatrix} \begin{bmatrix} H_1^* \\ H_2^* \\ \vdots \\ H_q^* \end{bmatrix} \quad . \tag{31a}$$

By direct calculation, it can be shown that the right-hand side of Eq. (31) is just the spectrum of the estimator $\hat{y}(t)$, i.e., $S_{\hat{y}\hat{y}}$. Hence $\gamma^2 = 1$ implies that $S_{yy} = S_{\hat{y}\hat{y}}$, i.e., the spectra of the time series y(t) and the estimator $\hat{y}(t)$ are identical. Thus, the departure of γ^2 from unity may be taken as a measure of the degree to which the spectrum of the estimator fails to approximate the spectrum of the time series y(t) in the main channel.

2.3 FIDELITY OF THE RECONSTRUCTED SPECTRUM OF THE IMBEDDED SIGNAL

Returning to Eq. (12), the main problem of interest is the decomposition of the series y(t) into its constituents so as to estimate the spectrum of the signal $\xi_1(t)$. Clearly, unless one can associate particular subsidiary channels with the correct set of superposed series $\xi_i(t)$ in the main data channel, no such decomposition is possible. Suppose the assumption is made that each $\xi_i(t)$ is uniquely related to x_i, as in Eq. (15). Obviously, if in addition z(t) = 0 in Eq. (12), then $w_i(t) = h_i(t)$, which are just the estimated impulse response functions and whose Fourier transforms are given by Eq. (25). Hence,

$$\xi_i = \int_{-\infty}^{\infty} h_i(t-\tau)\ x_i(\tau)d\tau\ . \tag{32}$$

In particular, the reconstructed signal spectrum is

$$S_{\xi_1\xi_1} = |\ H_1\ |^2\ S_{11}\ . \tag{33}$$

When y(t) comprises a noise output z(t) not accounted for by the $x_i(t)$ subsidiary series, the use of Eq. (33) will involve errors since perfect reconstruction of y(t) would no longer be possible. While the closeness of the multiple coherence function to unity may be regarded as a figure of merit of the fidelity of reconstruction of the overall output y(t), it is not necessarily a good measure of the fidelity of reconstruction of a particular constituent of y(t), e.g., $\xi_1(t)$ in Eq. (12). The quantity that plays a role analogous to the multiple coherence for S_{yy} and gives a quantitative measure of the fidelity of reconstruction of ξ_i is the so-called partial (or conditional) coherence function. This function is defined as the normalized cross-spectral density between a pair of conditioned random variables via the following procedure.

Instead of estimating y(t) on the basis of the q-dimensional vector given by Eq. (13), the procedure consists in doing so only on the basis of q - 1 subsidiary channels. Specifically, if the excluded channel output is $x_1(t)$, the estimator $\hat{y}^{(1)}(t)$ based on the remaining channels is given by

$$\hat{y}^{(1)}(t) = \sum_{i=2}^{q} \int_{-\infty}^{\infty} h_{yi}^{(1)}(\tau)\, x_i\,(t - \tau)\, d\tau \,. \tag{34}$$

The impulse response functions $h_{yi}^{(1)}(\tau)$ are now determined subject to the minimization of

$$\langle \varepsilon^{(1)2} \rangle = \langle\, |y(t) - \hat{y}^{(1)}(t)|^2 \,\rangle \,. \tag{35}$$

If the Fourier transform of $h_{yi}^{(1)}(\tau)$ is denoted by $H_{yi}^{(1)}$ and the corresponding column matrix by $\vec{H}_y^{\prime(1)}$ the solution to the minimization problem is again given by a matrix equation similar to Eq. (25), viz.

$$\vec{H}_y^{\dagger(1)} = \left(\vec{S}_{xx}^{(1)}\right)^{-1} \vec{S}_{xy}^{\prime(1)} \,, \tag{36}$$

where $\vec{S}_{xx}^{(1)}$ is the reduced (q - 1) x (q - 1) covariance matrix obtained from $\vec{S}_{xx}$ by deleting the first row and first column. Similarly, $\vec{S}_{xy}^{\prime(1)}$ is the reduced column matrix with q - 1 elements corresponding to the horizontal vector:

$$\vec{S}_{xy}^{(1)} = [S_{2y}\ S_{3y}\ \ldots\ldots\ S_{qy}] \,. \tag{37}$$

Having determined $\hat{y}^{(1)}(t)$, the reduced (conditioned) random process $\Delta_1 y(t)$ may be considered by subtracting from y(t) its best linear estimate based on the knowledge of $x_2(t)$, $x_3(t)$ ..... $x_q(t)$, i.e.,

$$\Delta_1 y(t) = y(t) - \hat{y}^{(1)}(t) \,. \tag{38}$$

Clearly, with the best linear estimate obtained from $x_2(t)$ ..... $x_q(t)$ subtracted out, $\Delta_1 y(t)$ should be a better representation of $\xi_1(t)$ than $y(t)$ itself provided, of course, that $y(t)$ indeed does contain a linear functional dependence on $x_1(t)$, i.e., that the assumption given by Eq. (15) holds. In the same manner as $\Delta_1 y(t)$, one can also estimate $x_1(t)$ on the basis of $x_2(t)$ ..... $x_q(t)$ and subtract this estimate from $x_1(t)$, thereby forming the reduced process $\Delta_1 x(t)$, i.e.,

$$\Delta_1 x(t) = x_1(t) - \hat{x}_1(t) \tag{39}$$

where

$$\hat{x}_1(t) = \sum_{i=2}^{q} \int_{-\infty}^{\infty} h_{x_1 i}^{(1)}(\tau) \quad x_i(t-\tau)d\tau \ . \tag{40}$$

If Fourier transforms of the impulse response function $h_{x_1 i}^{(1)}(\tau)$ are denoted by $H_{x_1 i}^{(1)}$ with the corresponding column matrix $\vec{H}_x'^{(1)}$, one has

$$\vec{H}_x'^{(1)} = \left(\vec{S}_{xx}^{(1)}\right)^{-1} \quad \vec{S}_{x1}'^{(1)} \tag{41}$$

where $\vec{S}_{x1}'^{(1)}$ is the reduced column matrix with q - 1 elements corresponding to the horizontal vector:

$$S_{x1}^{(1)} = [S_{21} \ S_{31} \ \ldots\ldots \ S_{q1}] \ . \tag{42}$$

Since $\Delta x_1(t)$ is formed by subtracting from $x_1(t)$ the best linear estimate $\hat{x}_1(t)$ from $x_2(t)$ ..... $x_q(t)$, it is reasonable to (a) associate a high degree of correlation between the reduced (conditioned) time series $\Delta_1 y(t)$ and $\Delta_1 x(t)$, and (b) expect a faithful reproduction of the signal spectrum as given, for example, by Eq. (33). The correlation between the residual $\Delta_1 y(t)$ and $\Delta_1 x(t)$ series can be expressed in the frequency domain as a partial coherence function. The auto- and

cross-spectral densities of the residual processes $\Delta_1 x(t)$ and $\Delta_1 y(t)$ are defined by

$$S_{yy;\ 2,\ 3,\ \ldots\ldots\ q} = \int_{-\infty}^{\infty} [\langle \Delta_1 y(t+\tau)\Delta_1 y(t)\rangle] e^{-2\pi i f\tau} d\tau \quad (43)$$

$$S_{11;\ 2,\ 3,\ \ldots\ldots\ q} = \int_{-\infty}^{\infty} [\langle \Delta_1 x(t+\tau)\Delta_1 x(t)\rangle] e^{-2\pi i f\tau} d\tau \quad (44)$$

$$S_{1y;\ 2,\ 3,\ \ldots\ldots\ q} = \int_{-\infty} [\langle \Delta_1 x(t+\tau)\Delta_1 y(t)\rangle] e^{-2\pi i f\tau} d\tau \quad (45)$$

The partial coherence function is then defined by

$$\gamma^2_{1y;\ 2,3,\ \ldots\ldots\ q} = \frac{\left|S_{1y;2,3,\ldots\ldots q}\right|^2}{S_{yy;\ 2,3,\ldots\ldots q}\ S_{11;\ 2,3,\ldots\ldots q}} \quad (46)$$

Successive substitution for Eqs. (38), (39), (34), (40), and (36) for $\Delta_1 y(t)$, $\Delta_1 x(t)$, $\hat{y}^{(1)}(t)$, $\hat{x}_1(t)$ and $\vec{H}_y^{+(1)}$, respectively, into the definitions (43) - (45) yield for the latter the following:

$$S_{yy;\ 2,3,\ \ldots\ldots\ q} = S_{yy} - \vec{S}^{*(1)}_{xy} \left[\vec{S}^{(1)}_{xx}\right]^{-1} \vec{S}^{\prime(1)}_{xy} \quad (47)$$

$$S_{11;\ 2,3,\ \ldots\ldots\ q} = S_{11} - \vec{S}^{*(1)}_{x1} \left[\vec{S}^{(1)}_{xx}\right]^{-1} \vec{S}^{\prime(1)}_{x1} \quad (48)$$

$$S_{1y;\ 2,3,\ \ldots\ldots\ q} = S_{1y} - \vec{S}^{*(1)}_{x1} \left[\vec{S}^{(1)}_{xx}\right]^{-1} \vec{S}^{\prime(1)}_{xy} \quad (49)$$

In the forms given by Eqs. (47) - (49), the conditional spectral densities and hence the partial coherences may be computed directly from the unconditional spectral densities of the $\vec{x}(t)$ and $y(t)$ time series.

The conditional spectral densities and partial coherences may, of course, be defined with respect to any one of the subsidiary q-channels in Eq. (13). A convenient way of keeping track of the indexes in the corresponding Eqs. (47) - (49) is

to associate the first row and column of the subsidiary matrix $\vec{S}_{xx}$ with the channel of interest and perform a cyclical permutation of the remaining indexes. For example, $\gamma^2_{2y;\,3,\,4,\ldots\ldots q,1}$ refers to the partial coherence relative to $x_2(t)$. The corresponding conditional spectral densities are then $S_{yy;\,3,4,\ldots\ldots q,1}$, etc. Since in this manner all the formulas involving conditional spectral densities pertaining to the channel $x_1(t)$ can readily be modified for any one of the $x_2(t)$ ..... $x_q(t)$ channels, one can continue for convenience to refer specifically only to the channel $x_1(t)$.

Although the channel transfer functions may be computed directly from Eq. (25), it is also possible to compute them from the conditional spectral densities. The required formulas can be obtained by combining Eq. (25) with Eqs. (48) and (49). For this purpose, the matrix relation given by Eq. (24) is first written in the following partitioned form

$$\left[\begin{array}{c|c} S_{11} & \vec{S}^{(1)}_{1x} \\ \hline \vec{S}'^{(1)}_{1x} & \vec{S}^{(1)}_{xx} \end{array}\right] \left[\begin{array}{c} H_1^* \\ \hline \vec{H}^{\dagger}_{q-1} \end{array}\right] = \left[\begin{array}{c} S_{1y} \\ \hline \vec{S}'^{(1)}_{xy} \end{array}\right] \tag{50}$$

where $\vec{H}^{\dagger}_{q-1}$ is the q-1 dimensional column matrix containing the transfer functions $[H_2^*, H_3^* \ldots\ldots H_q^*]$. From the matrix Eq. (50), it is obtained

$$S_{11}\, H_1^* + \vec{S}^{(1)}_{1x}\, \vec{H}^{\dagger}_{q-1} = S_{1y} \tag{51a}$$

$$\vec{S}'^{(1)}_{1x}\, H_1^* + \vec{S}^{(1)}_{xx}\, \vec{H}^{\dagger}_{q-1} = S'^{(1)}_{xy}\ . \tag{51b}$$

Eliminating $\vec{H}^{\dagger}_{q-1}$ yields

$$S_{1y} - \vec{S}^{*(1)}_{x1} \left(\vec{S}^{(1)}_{xx}\right)^{-1} \vec{S}'^{(1)}_{xy} = \left[S_{11} - \vec{S}^{*(1)}_{x1} \left(\vec{S}^{(1)}_{xx}\right)^{-1} \vec{S}'^{(1)}_{x1}\right] H_1^{*}. \tag{52}$$

In view of Eqs. (48) and (49) one has

$$H_1^{*} = \frac{S_{1y;\ 2,\ 3 \ldots\ldots q}}{S_{11;\ 2,\ 3 \ldots\ldots q}} \tag{53}$$

or generalizing to an arbitrary channel $X_i(t)$

$$H_i^{*} = \frac{S_{iy;\ i+1, i+2,\ \ldots\ldots q, 1, 2, \ldots\ldots i-1}}{S_{ii;\ i+1, i+2,\ \ldots\ldots q, 1, 2, \ldots\ldots i-1}} . \tag{54}$$

For a "perfect" reconstruction of y(t), the partial coherences must be unity, a result that is shown by assuming first that the mean squared error in Eq. (26) is zero. Since the integrand is positive, it follows that

$$S_{yy} = \sum_{i=1}^{q} S_{iy} H_i \tag{55}$$

or

$$S_{yy} = H_1 S_{1y} + \sum_{i=2}^{q} S_{iy} H_i = H_1 S_{1y} + \vec{H}_{q-1} \vec{S}'^{(1)}_{xy} . \tag{56}$$

On the other hand, from Eq. (51b) it is found that

$$\vec{H}_{q-1} = \vec{S}'^{(1)}_{xy} + \left(\vec{S}^{(1)}_{xx}\right)^{-1} - \vec{S}^{*(1)}_{x1} \left(\vec{S}^{(1)}_{xx}\right)^{-1} H_1 . \tag{57}$$

The combination of Eqs. (56) and (57) yields

$$S_{yy} = H_1 \left[S_{1y} - \vec{S}^{*(1)}_{x1} \left(\vec{S}^{(1)}_{xx}\right)^{-1} \vec{S}'^{(1)}_{xy}\right] + \vec{S}^{*(1)}_{xy} \left(\vec{S}^{(1)}_{xx}\right)^{-1} \vec{S}'^{(1)}_{xy} . \tag{58}$$

Substitution from Eqs. (47) and (48) gives the relationship

$$S_{yy;\ 2,\ 3,\ \ldots\ldots\ q} = H_1\ S_{1y;\ 2,\ 3,\ \ldots\ldots\ q}\ . \tag{59}$$

In view of Eq. (53) there also follows

$$S_{yy;\ 2,\ 3,\ \ldots\ldots\ q} = |H_1|^2\ S_{11;\ 2,\ 3,\ \ldots\ldots\ q} \tag{60}$$

$$|S_{1y;\ 2,\ 3,\ \ldots\ldots\ q}|^2 = |H_1|^2\ S^2_{11;\ 2,\ 3,\ \ldots\ldots\ q} \tag{61}$$

so that the partial coherence as given by Eq. (46) is identically unity. Since this is also true for each of the remaining q-1 subsidiary channels, it is seen that perfect reconstruction of y(t) as given by Eq. (12) implies that for $z(t) \to 0$ all the partial coherences must be unity. It is therefore common practice to associate a high value of the partial coherence for a particular channel with high fidelity of spectral reconstruction of the corresponding signal as given, for example, by Eq. (33).

2.4 CONSTRAINTS FROM USUAL LINEARITY FORM

It should be noted that the foregoing association between fidelity of reconstruction of $\Delta^{(1)}y(t)$ and high values of the partial coherences is justified only if the linear relationship (15) is known to hold between the superposed and subsidiary time series $\xi_i(t)$ and $x_i(t)$, respectively. To illustrate this point, consider the ideal case when $z(t) = 0$ in Eq. (12) and assume that the general linear relationship given by Eq. (14) holds instead of Eq. (15). The reconstruction of y(t) is then given by

$$y(t) = \sum_{n=1}^{q} \sum_{i=1}^{q} \int_{-\infty}^{\infty} w_{in}(\tau)\ x_n(t-\tau)\ d\tau$$

or putting this result in the form of (17)

$$y(t) = \sum_{i=1}^{q} \int_{-\infty}^{\infty} \left[\sum_{n=1}^{q} w_{ni}(\tau)\right] x_i(t-\tau)\, d\tau \,. \tag{62}$$

The algorithm, based on Eq. (15), will then estimate the Fourier transform of the impulse response functions

$$h_i(\tau) = \sum_{n=1}^{q} w_{ni}(\tau) \,. \tag{63}$$

Denoting the Fourier transform of $w_{ni}(t)$ by $H_{ni}(f)$, then the estimated transfer function would be

$$H_i = \sum_{n=1}^{q} H_{ni} \,. \tag{64}$$

Thus, if the signal were associated with the first subsidiary channel, Eq. (33) would yield the following estimated spectrum of the signal

$$S_{\xi_1\xi_1} = \left|\sum_{n=1}^{q} H_{n1}\right|^2 S_{11} \,. \tag{65}$$

However, the actual signal imbedded in y(t) is, from (14),

$$[\xi_1(t)]_{actual} = \sum_{i=1}^{q} \int_{-\infty}^{\infty} w_{1i}(\tau)\, x_i(t-\tau) d\tau \tag{66}$$

with the corresponding spectrum

$$[S_{\xi_1\xi_1}(f)]_{actual} = \sum_{i=1}^{q} \sum_{n=1}^{q} H_{1i}\, H_{1n}^{*}\, S_{in} \,. \tag{67}$$

Clearly, Eq. (67) can be substantially different from Eq. (65). It should be noted that under the stipulated conditions, the multiple coherences and each of the partial coherences are

necessarily equal to unity. Hence, in absence of *a priori* information on the interchannel functional linear relationships, the conclusion would be made with "great confidence" that Eq. (65) is indeed the signal. With the algorithm in its present form, no general remedy is apparent to remove this difficulty. In essence, the degree of confidence assigned to the correctness of the reconstructed signal can then be no greater than the degree of confidence in the *a priori* knowledge that a subsidiary channel i responds only to one physical mechanism. These considerations lead then to a need for a linear superposition into one channel of all the subsidiary time series that are functionally related to the signal, and that may be suspected to be present in more than one subsidiary channel. This linear superposition would then yield a smaller set of subsidiary channels that are indeed functionally decoupled. One way to test the functional relationship among the subsidiary channels would obviously be to test the assumption implied by Eq. (15) with the outputs of the subsidiary channels by themselves.

2.5 FORMULATION OF NINE-CHANNEL LINEAR SYSTEM

The formulation of the reconstruction algorithm for the nine subsidiary channels of the Physical Dynamics experiments is based on Eq. (15), instead of Eq. (14), for the functional linear relation among the superposed time series in the main data channel [e.g., Eq. (12)] and the subsidiary channels [Eq. (13)]. In view of the typical result given by Eq. (33), which relates the spectrum of a given superposed time series in the main channel to the transfer function of the corresponding subsidiary channel, the main interest in this formulation is focused on the transfer functions of the subsidiary channels. Because the fidelity of reconstruction of the superposed time series in the main data channel is given by the corresponding partial coherences [e.g., Eq. (46)], the considerations on the transfer

functions for the subsidiary channels must include the corresponding partial coherences. Hence, the formulation of the nine-channel linear system is based on the specialization of Eq. (54) for the transfer function for q = 9 as well as the corresponding generalized Eq. (46) for the corresponding partial coherence.

The formulation of the nine-channel linear system, based on the results of Ref. 3, utilizes Eqs. (13), (21), (22) and (23) for the vectors $\vec{x}(t)$, $\vec{H}(f)$, $\vec{S}_{xy}$ and $\vec{S}_{xx}$, respectively. The q-dimensional vector $\vec{S}_{xy}$ consists of cross-spectra densities involving each of the subsidiary channels with the main data channel, whereas the $\vec{S}_{xx}$ is a q x q Hermitian matrix involving only the *subsidiary* channels. As indicated in Refs. 2 and 3, the use of Eq. (54) for the transfer function as well as of Eq. (46) for the partial coherences may be put in a partitioned form similar to that of the matrix Eq. (50). This procedure requires the partitioning of an *augmented* matrix $\vec{S}_{yxx}(f)$ given by

$$\vec{S}_{yxx} = \left[\begin{array}{cc|cc} S_{yy} & S_{y1} & S_{y2} & S_{y3}\cdots\cdots S_{y9} \\ S_{1y} & S_{11} & S_{12} & S_{13}\cdots\cdots S_{19} \\ \hline S_{2y} & S_{21} & S_{22} & S_{23}\cdots\cdots S_{29} \\ S_{3y} & S_{31} & S_{32} & S_{33}\cdots\cdots S_{39} \\ \vdots & & & \\ S_{9y} & S_{91} & S_{92} & S_{93}\cdots\cdots S_{99} \end{array}\right] \tag{68}$$

The partitioned matrix (68) can be represented as

$$\vec{S}_{yxx} = \left[\begin{array}{c|c} A(2,\ 2) & B(2,\ 8) \\ \hline C(8,\ 2) & D(8,\ 8) \end{array}\right] \tag{69}$$

where matrices A, B, C and D with their specified ranks correspond to each respective matrix in the partition of (68). It is to be noted that matrix D corresponds to $\vec{S}^{(i)}_{xx}$, matrices C and B are augmented matrices involving $\vec{S}'^{(i)}_{xy}$, and matrix A is S_{11} augmented by S_{yy}, S_{y1} and S_{1y}. The partitioning of Eq. (69) permits the definition of a *residual* matrix $\vec{S}_{xy;\,2,3\ldots9}$ given by (Refs. 3, 4):

$$\vec{S}_{xy;2,3\ldots9} = A - BD^{-1}C \tag{70}$$

where D^{-1} is the inverse matrix of D. The residual matrix $\vec{S}_{xy;2,3\ldots9}$ is of the same rank as matrix A (2 x 2), with elements given by

$$\vec{S}_{xy;2,3\ldots9} = \begin{bmatrix} S_{yy;2,3\ldots9} & S_{y1;2,3\ldots9} \\ S_{1y;2,3\ldots9} & S_{11;2,3\ldots9} \end{bmatrix} \tag{71}$$

i.e., by the elements given by Eqs. (47) to (49). Therefore, it should be noted that the second row of (71) contains the numerator and denominator for the transfer function as given by Eq. (53), whereas the two diagonals contain the denominator (principal diagonal) and numerator of the partial coherence as given by Eq. (46). Hence,

$$H_1 = \frac{S_{1y;2,3\ldots9}}{S_{11;2,3\ldots9}} \tag{72}$$

and

$$\gamma^2{}_{1y;2,3\ldots9} = \frac{|S_{1y;2,3\ldots9}|^2}{(S_{11;2,3\ldots9})(S_{yy;2,3\ldots9})} \quad . \tag{73}$$

The subsequent transfer functions $H_2 \ldots H_9$ and partial coherences $\gamma^2_{2y;3,4\ldots9,1}$ ..... $\gamma^2_{9y;1,2\ldots8}$ are calculated by successive permutations of the subindexes in the augmented matrix (68).

The augmented matrix (68) contains all the spectral density functions required for the calculation of the transfer functions and, hence, the corresponding spectra of the superposed series in the main data channel (e.g., Eq. 33). These spectral density functions are in turn determined from the corresponding estimators as given by Eqs. (5) to (11), a procedure that requires use of the output time series from the respective subsidiary [Eq. (13)] and main data channels.

3. SIMULATION OF A THREE-CHANNEL LINEAR SYSTEM

A test of the algorithm utilized for the reconstruction of the main data channel in the Physical Dynamics experiments (Fig. 1) can be performed by simulating the data records for the main data channel and only two, instead of the nine, subsidiary channels used in such experiments. By expanding such approach to include a successively increasing number of subsidiary channels, it would become possible to identify any systematic growth in the bias of the spectrum of the imbedded signal as a result of (a) the increased number of estimators in the augmented matrix in Eq. (68) and (b) the algebraic operations [Eqs. (72), (73)] with such biased estimators during the application of the algorithm to a larger number of channels.

The test of the algorithm based on the use of the main data channel [y(t)] and two subsidiary channels [$x_1(t)$), $x_2(t)$] involves the construction of two 3 x 3 augmented matrices [Eq. (68)] as follows: (a) one characterized by ideal spectra and zero cross-spectra densities ($S_{12} = S_{21} = 0$) for the uncorrelated subsidiary series $x_1(t)$ and $x_2(t)$. This matrix yields then the ideal transfer function [Eq. (72)] and other parameters such as the ideal coherence based on the use of ideal spectra [e.g. Eq. (73)], and (2) another one characterized by estimators [Eq. (11)] with non-zero cross-spectra for the subsidiary channels, depending upon the degree of frequency averaging. This augmented matrix, based on estimators, yields the estimated transfer functions (Fig. 1) and the reconstructed signal spectrum $\hat{S}_{\xi_1\xi_1} = |\hat{H}_1|^2 \hat{S}_{11}$ [Eq. (33)]. The ultimate test of the algorithm is then given by comparing the fidelity of the reconstructed signal spectrum as

well as the partial coherence, i.e., the criterium for the fidelity of the reconstructed time series [$\hat{y}(t)$] in the main data channel (Fig. 1). A more detailed description of the construction of these augmented matrices as well as the specification of the ideal signal spectrum in the gradiometer output is given in the sequel.

The construction of the augmented matrices require determination of the corresponding spectral density functions from time series for the gradiometer output and subsidiary channels [Eqs. (5) - (11)]. The simulation of data records for the gradiometer [$y(t)$] and two subsidiary channels [$x_1(t)$, $x_2(t)$] is illustrated schematically in Fig. 2, which also shows four filters denoted as $G_1(f)$, $G_2(f)$, $K_1(f)$ and $K_2(f)$. Each filter is characterized by its bandwidth and the center frequency for peak amplitude of the spectral density. The first two filters are for a two-input gradiometer and the latter two for the subsidiary single-input channels such as a current meter and the fluxgate magnetometer (Section 1.1). The main purpose of these filters is to (1) specify the ideal spectra densities in the corresponding Eq. (68), which are obtained from unit impulse function inputs to the filters and the use of Eq. (6) with $T = 1$; and (2) determine the estimators in Eq. (68) by using random stationary series inputs to the filters to generate the data record $x_{g_1}(t)$, $x_{g_2}(t)$ and, therefore, $y(t)$ for the gradiometer as well as $x_1(t)$ and $x_2(t)$ for the subsidiary data channels. The series $y(t)$ simulates then the superposed time series in the main data channel, i.e., $x_{g_1}(t)$ or the desired gradiometer signal and $x_{g_2}(t)$ or the gradiometer "noise"; whereas the subsidiary time series $x_1(t)$ and $x_2(t)$ denote, respectively, the internal wave measurements below the sea surface and fluxgate magnetometer data above the sea surface. Hence, $x_1(t)$ and $x_2(t)$ simulate, respectively, the internal wave contribution to the magnetic gradients and the background "noise" from conduction as well as magnetization currents in nearby objects.

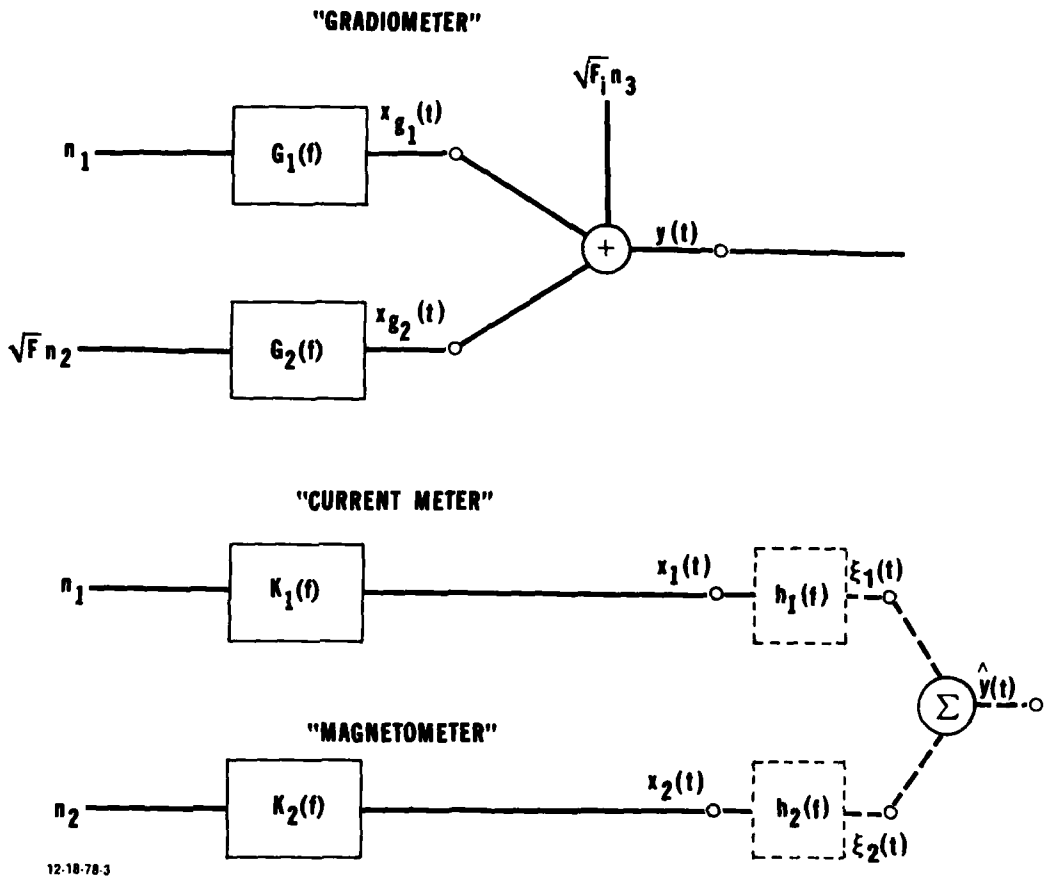

FIGURE 2. Schematic presentation of a two-input "gradiometer" and two subsidiary channels for an arbitrary simulation of the Physical Dynamics experiments.

The input series $n_1(t)$ and $\sqrt{F}\, n_2(t)$ in Fig. 2 are random stationary series that simulate uncorrelated inputs to the $G_1(f)$ and $G_2(f)$ gradiometer filters, where the $\sqrt{F}$ parameter denotes noise in the bandwidth of the $G_2(f)$ channel. The times series $\sqrt{F_1}\, n_3(t)$ in the main data channel is used to simulate intrinsic noise, where the $\sqrt{F_1}$ parameter denotes instrument white noise across the whole frequency spectrum. The output time series $y(t)$ of the main data channel simulates then a superposition of the signal $x_{g_1}(t)$ with the time series $x_{g_2}(t)$ and $\sqrt{F_1}\, n_3(t)$, both of which represent noise background including intrinsic instrument noise. The effects of the noise background in the main data channel can therefore be simulated by varying the $\sqrt{F}$ and $\sqrt{F_1}$ parameters to yield specified signal to noise ratios. The simulated time series for the filter inputs are taken as stationary series of random numbers with lengths of 2048 discrete points, just as was the case of the Physical Dynamics experiments.

As noted before, the above time series $[y(t), x_1(t), x_2(t)]$ fix the estimators for the spectral densities of the augmented matrix and, therefore, the estimated transfer functions and estimated partial coherences. Hence, by choosing the characteristics of the foregoing filters (or specified ideal spectra) and the magnitude of the $\sqrt{F}$ and $\sqrt{F_1}$ noise parameters (or signal to noise ratios), it becomes possible to test the algorithm for the reconstruction of the gradiometer signal $(\hat{S}_{\xi_1\xi_1})$ over a rather wide range of ideal spectra characteristics and signal-to-noise ratios.

Figure 2 includes the reconstruction of the superposed time series, $\hat{y}(t)$, which is as described in Fig. 1b. The reconstruction process utilizes the filter output data simulating the gradiometer and subsidiary channels outputs $[y(t), x_1(t), x_2(t)]$ to obtain, as indicated above, the estimators of the spectral densities, the estimated transfer functions and the estimated gradiometer signal. A more detailed description of the filter simulation of data channel outputs and the reconstruction process is given in the next subsections.

3.1 FILTER SIMULATION OF GRADIOMETER AND SUBSIDIARY CHANNELS

The determination of the time series for the filter outputs indicated in Fig. 2 [i.e., $x_{g_1}(t)$, $x_{g_2}(t)$, $y(t)$, $x_1(t)$, and $x_2(t)$] requires specifications of the corresponding transfer functions for each filter. The gradiometer and subsidiary channels are idealized by assuming that they have time independent properties. Furthermore, for the gradiometer output $y(t)$ it is assumed that the channels $G_1(f)$ and $G_2(f)$ are characterized by linear outputs as given in Eq. (15). This linear assumption implies two conditions (Ref. 2): (a) that the output of several simultaneous inputs is equal to the sum of outputs produced by each input alone and (b) that the output of the product of a constant times an input is equal to the constant times the output of the input alone. The dynamic characteristics of a constant parameter linear filter can be described by a weighting function, $h(\tau)$, which is defined as the output of the system at any time from a unit impulse applied to it a time τ before. The definition of the weighting function $h_{g_1}(\tau)$ for the $G_1(f)$ filter, for example, establishes both the output $x_{g_1}(t)$ and transfer function $H_{g_1}(f)$ as

$$x_{g_1}(t) = \int_{-\infty}^{\infty} h_{g_1}(\tau)\, n_1(t-\tau)d\tau \tag{74}$$

and

$$H_{g_1}(f) = \int_{-\infty}^{\infty} h_{g_1}(\tau)e^{-i2\pi f\tau}d\tau \tag{75}$$

where Eq. (74) is the convolution integral and Eq. (75) the Fourier transform of $h_{g_1}(\tau)$. The lower limit of integration in Eq. (75) reflects the assumption that $H_{g_1}(\tau) = 0$ for $\tau < 0$ (Ref. 2). The transfer function $H_{g_1}(f)$ is a complex quantity that can be expressed as $H_{g_1}(f) = |H_{g_1}(f)|\, e^{-i\phi(f)}$, where $|H_{g_1}(f)|$ is the gain factor and $\phi(f)$ the phase angle. The transfer function H_{g_1} for the $G_1(t)$ channel is given by the Fourier transform of Eq. (74), which yields

$$X_{g_1}(f) = H_{g_1}(f)\, N_1(f) \tag{76}$$

where $N_1(f) = 1$ for a normalized random input $n_1(t)$. A simulation of the frequency characteristics of the gradiometer and subsidiary channels can therefore be made by specifying the transfer function for each filter, which operates on the filter input to modify it according to its frequency characteristics. The transfer function for the $G_1(f)$ filter of the gradiometer would ideally simulate the desired spectrum of magnetic field gradients from internal waves, whereas the transfer function for the $K_1(f)$ filter would likewise simulate the spectrum of internal waves. However, for a preliminary test of the algorithm itself, the filter parameters can be varied arbitrarily to include several combinations of filter characteristics. The problem of interest is then to determine the transfer functions for each filter, which will yield *specified* ideal spectra S_{yy}, $S_{g_1g_1}$, $S_{g_2g_2}$, S_{11}, and S_{22} for the gradiometer and subsidiary channels; i.e., with $S_{12} = S_{21} = 0$ in the augmented matrix Eq. (68) for the two subsidiary channel system because of the use of uncorrelated inputs. These ideal spectra can be chosen by assuming their normalized shapes, bandwidths B, and frequencies corresponding to their peak amplitudes, which, in turn, determine the ideal transfer functions H_1 and H_2 [Eq. (72)] through the ideal augmented matrix (68).

The filter characteristics necessary to yield the specified ideal spectra can be determined by using a simple, standard type, digital recursive filter of the form (Ref. 2)

$$[x_{g1}(t)]_u = c_1[n_1(t)]_u + \sum_{\ell=1}^{L} h_\ell [x_{g_1}(t)]_{u-\ell} , \qquad (77)$$

which uses one input $[n_1(t)]_u$ and L previous outputs $[x_{g_1}(t)]u-\ell$. The summation term in Eq. (77) represents a discrete, finite sum equivalent to Eq. (74) for $t = \ell\Delta t$, $\ell = 1,2 \ldots L$. The coefficient h_ℓ represents L filter weights with $h_\ell = h_{-\ell}$ and the subscript $u - \ell$ denotes future values of the input.

Equation (77) is illustrated in Fig. 3 for a second-order (L = 2) recursive filter, where the triangles represent multiplication by the values within the triangles; the rectangles represent a delay of Δt from one point to another, and the circles represent summing operations. The Fourier transform of Eq. (77) yields

$$X_{g_1} = c_1 + X_{g_1} \sum_{\ell=1}^{L} h_\ell e^{-i2\pi f\ell\Delta t} \qquad (78)$$

where the summation involves a polynominal in powers of exp $[-i2\pi f\Delta t]$. From Eqs. (76) and (78), the transfer function for the filter is given by

$$H_{g_1}(f) = X_{g_1} = \frac{c_1}{1 - \sum_{\ell=1}^{L} h_\ell e^{-i2\pi f\ell\Delta t}} . \qquad (79)$$

The determination of the properties of the transfer function $H_{g_1}(f)$ is reduced to studying the location and nature of the poles in the denominator of Eq. (79), since a filter is defined to be stable if all of the roots of the denominator have positive real parts.

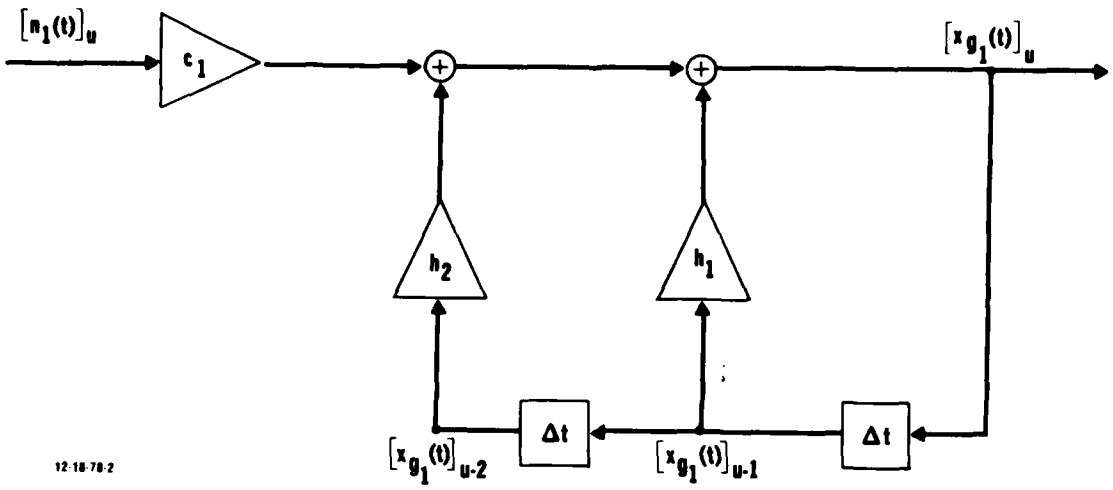

FIGURE 3. Schematic representation of a second-order recursive filter for gradiometer and subsidiary current meter channels.

The application of Eq. (77) to each of the four filters in Fig. 2 yields the simulation of the gradiometer and subsidiary channel outputs as follows:

$$\left[x_{g_1}(t)\right]_u = A_{g_1}\left[n_1(t)\right]_u + B_{g_1}\left[x_{g_1}(t)\right]_{u-1} + C_{g_1}\left[x_{g_1}(t)\right]_{u-2} \quad (80)$$

$$\left[x_{g_2}(t)\right]_u = A_{g_2}\left[n_2(t)\right]_u + B_{g_2}\left[x_{g_2}(t)\right]_{u-1} + C_{g_2}\left[x_{g_2}(t)\right]_{u-2} \quad (81)$$

$$\left[x_1(t)\right]_u = A_{k_1}\left[n_1(t)\right]_u + B_{k_1}\left[x_1(t)\right]_{u-1} + C_{k_1}\left[x_1(t)\right]_{u-2} \quad (82)$$

$$\left[x_2(t)\right]_u = A_{k_2}\left[n_2(t)\right]_u + B_{k_2}\left[x_2(t)\right]_{u-1} + C_{k_2}\left[x_2(t)\right]_{u-2} \quad (83)$$

where the above coefficients may be generalized as A_i, B_i and C_i with $i = g_1, g_2, k_1, k_2$. These coefficients, corresponding to

the c_{1i}, h_{1i} and h_{2i} coefficients in a generalized Eq. (77), can be expressed in terms of parameters of the specified ideal autospectral densities. Using Eq. (76), the corresponding ideal autospectral density functions S_{ii}, were arbitrarily chosen as

$$S_{ii}(f) = X_i X^*_i = |H_i|^2 = \frac{1}{1 + \left[\frac{\cos(\pi f/B_i) - r_i}{s_i}\right]^2} \tag{84}$$

where

$$r_i = \cos(2\pi L_i/N) \cos(\pi B_i/N) \tag{85}$$

$$s_i = \sin(2\pi L_i/N) \sin(\pi B_i/N) \tag{86}$$

$$\frac{2L_i}{N} = \frac{f_{ci}}{B_i}. \tag{87}$$

The parameter f_{ci} is the center frequency for peak amplitude of the ith spectrum, B_i the bandwidth of the ith filter and L_i the corresponding center frequency parameter as given by Eq. (87). The characteristics of each of the four filters may then be designated by the choice of the B_i and L_i parameters. The coefficients A_i, B_i and C_i were then obtained by equating the assumed form for $|H_i|^2$ in Eq. (84) to the corresponding expression obtained from a generalized Eq. (79) for $|H_i|^2$ with $L = 2$ and $\Delta t = 1/2B$. This procedure requires (1) the calculation of $X_i X_i^*$ in Eq. (79), (2) equating the corresponding trigonometric terms in the denominators of Eqs. (79) and (84) after putting Eq. (79) in a form equivalent to that of Eq. (84) by (a) retaining in Eq. (79) only the real parts and (b) dividing its resulting numerator and denominator by c^2_{1i}, (3) combining the resulting

three equations so as to solve c_{1i}, h_{1i} and h_{2i} in Eq. (79) in terms of the s_i and r_i variables in Eq. (84) as given by Eqs. (85), (86); and (4) solving the resulting quartic equation in terms of the variable defining c_{1i}, i.e., $Z_i = c_{1i}^2/2s_i^2$. These three equations yield the A_i, B_i and C_i coefficients in Eqs. (80 to (83) as follows:

$$
\begin{aligned}
A_i &\equiv c_{1i} = s_i \sqrt{2Z} \\
B_i &\equiv h_{1i} = \frac{4r_i Z_i}{Z_i+2} \\
C_i &\equiv h_{2i} = -\frac{1}{2} Z_i
\end{aligned}
\tag{88}
$$

where Z_i is a root of the quartic equation

$$
Z_i^4 - \alpha Z_i^3 - \beta Z_i^2 - \Theta Z_i + 16 = 0 \tag{89}
$$

where

$$
\begin{aligned}
\alpha &= 8(s_i^2 + r_i^2) \\
\beta &= 8[4(s_i^2 - r_i^2) + 1] \\
\Theta &= 32\,(s_i^2 + r_i^2),
\end{aligned}
$$

a root that must also satisfy the condition of filter stability given by

$$
\left| \frac{-h_{1i} \pm \sqrt{h_{1i}^2 + 4\,h_{2i}}}{2\,h_{2i}} \right| > 1,
$$

a condition that requires that the root Z_i in Eq. (88) must be real, positive and satisfy

$$
Z_i < 2 \left[\sqrt{1 + 4\,r_i^2} - 2\,r_i\right].
$$

Assuming for simplicity that every filter in Fig. 2 has the same bandwidth ($B_i = B$) as well as $L_{k_1} = L_{g_1} + B$ and $L_{k_2} = L_{g_2} - B$, the ideal spectra of the gradiometer and subsidiary filters can be specified as illustrated in Fig. 4; i.e., from the choice of the filter parameters L_{g_1}, L_{g_2} and B/2. These parameters specify also the transfer functions for each filter (Eq. 79), and the ideal transfer functions, H_1, H_2 (Fig. 2) which can be obtained either from Eq. (25) or (72) with $S_{12} = S_{21} = 0$, as

$$H_1 = \frac{S_{1y}}{S_{11}} \tag{90}$$

$$H_2 = \frac{S_{2y}}{S_{22}} \quad . \tag{91}$$

Hence, for a given selection of filter parameters, the procedure used to determine the ideal auto-spectra ($S_{g_1g_1}$, $S_{g_2g_2}$, S_{yy}, S_{11} and S_{22}) as well as the ideal transfer functions (H_1, H_2) is to (a) use the filter outputs to a unit-impulse input to each filter so as to generate the corresponding ideal time series without variance, and (b) perform FFT operations (e.g., Eqs. 5-9) with T (or N) = 1. For the spectral estimators as well as estimated transfer functions and coherences, the procedure consists in (1) using the random series inputs to the filters (Fig. 2) so as to obtain the output time series (Eqs. 80-83) as well as the gradiometer output y(t) from $x_{g_1}(t)$ and $x_{g_2}(t)$ as a function of both the filter parameters and signal-to-noise ratios, (2) performing FFT operations (Eqs. 5-9) on the filter outputs for y(t), $x_1(t)$ and $x_2(t)$, (3) doing the frequency averaging of each periodogram (Eq. 11), and (4) using the algorithm with the smoothed periodograms as spectral estimators instead of ideal spectra.

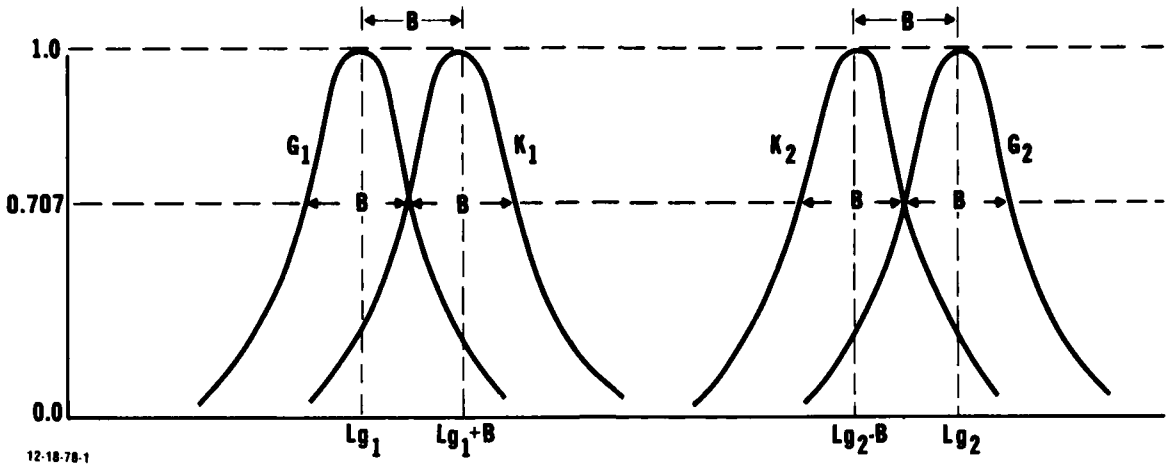

FIGURE 4. Specified ideal spectra characteristics for filter implementation of gradiometer and subsidiary current meter channels. The spectra G_1, K_1 are for the signal channels, whereas the spectra G_2, K_2 correspond to the noise channels.

3.2 ALGORITHM FOR A SIMULATED CHANNEL LINEAR SYSTEM

The basic results to be obtained from the algorithm for the reconstruction of a simulated two-input and one-output gradiometer linear system (Fig. 2) are as follows: (1) the estimated* signal spectrum $\hat{S}_{\xi_1\xi_1}$, as given by Eq. (33), corresponding to the output $x_{g_1}(t)$ from the channel $G_1(f)$, (2) estimated gain factors $|\hat{H}_1|$ and $|\hat{H}_2|$ of the transfer functions for the reconstructed time series that are superposed in the main data channel (Fig. 1), (3) the estimator for the output of the gradiometer, $\hat{S}_{yy}$, and (4) the estimated partial coherence, $\hat{\gamma}_{1y;2}$, for the subsidiary signal channel $K_1(f)$ after subtracting in

*The estimated transfer function and partial coherences are not estimators, because they are based only on the use of the estimators for their spectral densities and not on the averaging of themselves. For example, $\langle\hat{H}_1\rangle \neq \langle\hat{S}_{1y}\rangle/\langle\hat{S}_{11}\rangle$, but $|\hat{H}_1| = \langle|H_1|\rangle$.

the main reconstructed gradiometer channel the predictions from the $K_2(f)$ channel. Each of the foregoing results is given by the algorithm in terms of the estimators for the appropriate auto- and cross-spectral density functions in the augmented matrix given in Eq. (68). However, in order to facilitate the interpretation of results from subsequent numerical simulations, it is of interest to bring out the relationships among the estimators and estimated parameters directly from the subsequent brief considerations.

3.2.1. Estimated Gradiometer Signal Spectrum

As indicated in Fig. 2, the estimated gradiometer signal spectrum is conceptually obtained from the time series $\xi_1(t)$; which is an output reconstructed by the transfer function H_1 describing the contribution of the time series $x_1(t)$ or internal waves to the magnetic gradients. Hence, Eqs. (74) and (75) become applicable to the transfer function between $\xi_1(t)$ and $x_1(t)$; i.e., by replacing $x_{g_1}(t)$, $h_{g_1}(\tau)$ and $n_1(t)$ by $\xi_1(t)$, $h_1(\tau)$ and $x_1(t)$, respectively. For a pair of times t and t + τ, the product $\xi_1(t)\ \xi_1(t+\tau)$ is given from Eq. (74) by

$$\xi_1(t)\ \xi_1(t+\tau) = \iint_0^\infty h(\zeta)h(\eta)\ x_1(t-\zeta)\ x_1(t+\tau-\eta)d\zeta d\eta\ . \qquad (92)$$

Since the auto-correlation function for a stationary series is given by

$$R_{\xi_1\xi_1}(\tau) = \lim_{T\to\infty} \frac{1}{T}\int_0^T \xi_1(t)\ \xi_1(t+\tau)\ dt \qquad (93)$$

the combination of Eqs. (92) and (93), together with Eq. (1), yields the important result

$$S_{\xi_1\xi_1}(f) = |H_1(f)|^2\ S_{x_1x_1}(f) \equiv |H_1(f)|^2\ S_{11}(f)\ . \qquad (94)$$

Equation (94) indicates that the estimated spectrum of the signal, $\hat{S}_{\xi_1\xi_1}$, is given by the product of the square of the estimated gain factor of the transfer function H_1 and the estimator of the spectrum S_{11}; i.e., the estimated signal spectrum, $\hat{S}_{\xi_1\xi_1}$ is determined from the corresponding values of $|\hat{H}_1|$ and $\hat{S}_{11}$. The gain factor $|\hat{H}_1|$, for example, is based on the estimators for the auto- and cross-spectral densities of y(t), $x_1(t)$ and $x_2(t)$ as a function of frequency averaging and signal-to-noise ratios, since y(t) is specified by the $\sqrt{F}$ and $\sqrt{F_i}$ parameters in the inputs to the gradiometer filters (Fig. 2). Hence, $|H_1|$ is based on the full augmented matrix (68) i.e., where S_{12} and S_{21}, for example, are nonzero due to the bias in the estimators from the averaging of the periodograms. Hence, Eq. (94) will be an important criterion to test the bias of the estimator $\hat{S}_{\xi_1\xi_1}$ from its comparison with the corresponding value, $S_{g_1g_1}$, which is obtained from the $G_1(f)$ filter output in the time domain to a unit impulse input and the subsequent application of Eq. (6) with T = 1.

3.2.2 Estimated Gradiometer Transfer Functions

Since the linear assumption given by Eq. (15) indicates that the output $\hat{y}(t)$ for the gradiometer (Fig. 2) can be expressed by the sum of the individual outputs $\xi_i(t)$, then

$$\hat{y}(t) = \sum_{i=1}^{2} \xi_i(t) \tag{95}$$

where $\xi_i(t)$ is defined as that part of the output which is produced by the ith input when all the other inputs are zero. Expressing each output $\xi_i(t)$ in terms of its respective input $x_i(t)$ through the convolution integral [Eq. (74)],

$$\hat{y}(t) = \sum_{i=1}^{2} \int_0^{\infty} h_i(\tau)\, x_i(t-\tau)d\tau . \tag{96}$$

Calculation of the cross-correlation function, $R_{xy}(t)$, in terms of the output ξ_1, as given by Eq. (95), in a manner similar to that leading to the results given by Eqs. (92) and (94) for a single channel yields

$$S_{iy} = \sum_{j=1}^{2} H_j S_{ij} \tag{97}$$

which yields

$$S_{1y} = H_1 S_{11} + H_2 S_{12} \tag{98}$$

$$S_{2y} = H_1 S_{21} + H_2 S_{22} \ . \tag{99}$$

The input auto- and cross-spectral density functions in Eqs. (98) and (99) can be used to define the input coherence

$$\gamma^2_{12} = \frac{|S_{12}|^2}{S_{11}\ S_{22}} \tag{100}$$

where the numerator is the absolute value of the complex cross-spectral density function for the two inputs $x_1(t)$ and $x_2(t)$ and the denominator the corresponding real-valued auto-correlation density functions. The input coherence in the frequency domain is thus equivalent to the normalized cross-correlation coefficient in the time domain, i.e., both are real-valued functions with magnitudes between zero and unity. Just as the cross-correlation coefficient establishes the degree of correlation between two given time series in the time domain, the input coherences do likewise in the frequency domain. Hence, for the two uncorrelated times series $x_1(t)$ and $x_2(t)$ representing internal waves and background noise from conduction and magnetization currents, both the cross-correlation function and

input coherence must be zero. Eqs. (98) to (100) yield the transfer functions for the reconstructed gradiometer channels as

$$H_1 = \frac{S_{1y} - S_{12}S_{2y}/S_{22}}{S_{11} - S_{12}S_{21}/S_{22}} = \frac{S_{1y} - S_{12}S_{2y}/S_{22}}{S_{11}\ (1 - \gamma_{12}^2)} \tag{101}$$

and

$$H_2 = \frac{S_{2y} - S_{21}S_{1y}/S_{11}}{S_{22} - S_{21}S_{12}/S_{11}} = \frac{S_{2y} - S_{21}S_{1y}/S_{11}}{S_{22}\ (1 - \gamma_{12}^2)} \ . \tag{102}$$

Eqs. (101) and (102) will be used to obtain the estimated transfer functions and gain factors in terms of the estimators for the relevant auto- and cross-spectral densities functions. These equations also yield the corresponding ideal reference values [Eqs. (90, 91)] for which $S_{12} = S_{21} = \gamma_{12}^2 = 0$.

3.2.3 Estimator for the Gradiometer Output Spectra

The estimator for the gradiometer output spectrum, $\hat{S}_{yy}$, is obtained by a procedure similar to that leading to Eq. (97), except that instead of Eqs. (92) and (93) for the auto-correlation function of the output $\xi_1(t)$, it becomes necessary to use the auto-correlation for the output y(t). The result is then given by

$$S_{yy} = \sum_{i=1}^{2} \sum_{j=1}^{2} H_i^* H_j S_{ij} \tag{103}$$

where S_{ij} represents the cross-spectral density function between the inputs $x_i(t)$ and $x_j(t)$. Eq. (103) then yields

$$S_{yy} = |H_1|^2 S_{11} + H_1^* H_2 S_{12} + H_2^* H_1 S_{21} + |H_2|^2 S_{22} \ . \tag{104}$$

Eq. (104) shows the relationship among the estimators for $\hat{S}_{yy}$ and those involving the gain factors, transfer function and spectral density functions derived from the two current meters

in Fig. 2. Although for the ideal case $S_{12} = S_{21} = 0$, the ideal value of S_{yy} was determined by computing the two remaining terms in Eq. (104) from an addition of the ideal values of $S_{g_1g_1}$ and $S_{g_2g_2}$.

3.2.4 Estimated Partial Coherence

The partial coherence is given by a ratio similar to that for the input coherence [Eq. (100)], except that the power spectral density functions involve the residual $\Delta x_1(t)$ and $\Delta y(t)$ time series obtained by subtraction from $x_1(t)$ and $y(t)$ their respective linear least-square predictions $(\hat{x}_1, \hat{y})$ from $x_2(t)$, i.e.,

$$\Delta x_1 = x_1(t) - \hat{x}_1(t) = x_1(t) - (R_{x_2x_1}/R_{x_2x_2})\, x_2(t) \qquad (105)$$

and

$$\Delta y = y(t) - \hat{y}(t) = y(t) - (R_{x_2y}/R_{x_2x_2})\, x_2(t) \qquad (106)$$

where $R_{x_2x_1}$, $R_{x_2x_1}$ and R_{x_2y} denote the respective cross-correlation functions for the indicated inputs x_1 and output y. The partial coherence for the residuals Δx_1 and Δy time series is then given by

$$\gamma^2_{\Delta x_1 \Delta y}(f) \equiv \gamma^2_{1y.2} = \frac{|S_{1y.2}|^2}{S_{11.2}\, S_{yy.2}} \qquad (107)$$

where the subindex notation has again been simplified by dropping the respective x's and the symbol .2 denotes subtractions of the respective predictions from $x_2(t)$ as indicated by Eqs. (105) and (106). The importance of the partial coherence comes about from the fact that its value must be unity at every frequency [Eqs. (46), (60), and (61)], a result that is also obtained from expressions for the numerator and each term in the denominator of Eq. (107), as given in the sequel.

The spectral density functions necessary for the denominator of Eq. (107) are obtained by a procedure similar to that leading to Eq. (97), except that consideration must instead be given to the residual time series given by Eqs. (105) and (106). If instead of Eq. (74), the least square prediction $\hat{y}(t)$ from $x_2(t)$ is given by

$$\hat{y}(t) = \int_0^\infty h_o(\tau)x_2(t-\tau)d\tau \tag{108}$$

where $h_o(\tau)$ is a weighting function determined so that the mean square error ε^2 for the expected value of the auto-correlation of Δy is a minimum, the result is then a relationship between the cross- and auto-correlation, whose Fourier transform yields $H_o = S_{2y}/S_{22}$. Subsequent calculation of the auto-correlation function $R_{\Delta y \Delta y}(\tau)$ and its Fourier transform leads to the result

$$S_{\Delta y \Delta y} \equiv S_{yy.2} = S_{yy} - \frac{S_{2y}S_{y2}}{S_{22}} \tag{109}$$

where the subscript 2 denotes the series $x_2(t)$ from which the prediction $\hat{y}$ is made. Equation (109) applies also to the other spectral density functions in the denominator of Eq. (107), i.e.

$$S_{11.2} \equiv S_{\Delta x_1 \Delta x_1} = S_{11} - \frac{|S_{12}|^2}{S_{22}} = S_{11}(1 - \gamma_{12}^2) \ . \tag{110}$$

The numerator of Eq. (107) is likewise obtained by a procedure similar to that leading to Eq. (109), except that the cross-correlation function $R_{\Delta x_1 \Delta y}(\tau)$ must be utilized instead of $R_{\Delta y \Delta y}(\tau)$. The result is then

$$S_{1y.2} \equiv S_{\Delta x_1 \Delta y} = S_{1y} - \frac{S_{12}S_{2y}}{S_{22}} \ . \tag{111}$$

Substituting Eqs. (98) and (99) for S_{1y} and S_{2y} in Eq. (99) there follows

$$S_{1y.2} = H_1 \, S_{11} \, (1-\gamma_{12}^2) \tag{112}$$

for the numerator of Eq. (107). Similarly, substituting Eqs. (99) for S_{2y} and (104) for S_{yy} into Eq. (109) it is obtained

$$S_{yy.2} = |H_1|^2 S_{11}(1-\gamma_{12}^2) \ . \tag{113}$$

Hence, substitution of Eqs. (110), (112) and (113) into (107) yields

$$\gamma_{1y.2}^2 = 1 \tag{114}$$

at any frequency, a result that holds for $z(t) = 0$ in Eq. (12) whether or not the two inputs $x_1(t)$ and $x_2(t)$ are correlated. Hence, an important question in the test of the algorithm is the number of frequencies (M) required in the averaging of the periodograms [e.g., Eqs. (6), (8)] so as to reproduce the given signal, i.e., to obtain $\hat{S}_{\xi_1\xi_1} \approx S_{g_1g_1}$ as well as the behavior of the input ($\gamma_{12}^2 \to 0$) and partial ($\gamma_{1y,2}^2 = 1$) coherences at every frequency.

3.3 SCOPE OF NUMERICAL SIMULATIONS

Figure 5 shows the specified, normalized ideal spectra ($S_{g_1g_1}$, $S_{g_2g_2}$, S_{11}, S_{22}) for four cases of a two-input gradiometer and two subsidiary single-input channels as illustrated in Fig. 2. For a given case, each channel is identifiable by the frequency parameter for peak amplitude of the ideal spectra as follows (Fig. 4): (a) $S_{g_1g_1}$ at L_{g_1}, with a bandwidth B at the half-power level, (b) $S_{g_2g_2}$ at L_{g_2}, (c) S_{11} at L_{g_1} + B and (d) S_{22} at L_{g_2} - B. The ideal spectra for the gradiometer output, S_{yy}, is given by the sum of the corresponding spectra for each channel ($S_{g_1g_1}$, $S_{g_2g_2}$) of the gradiometer. The frequency range corresponds to one-half the length of the discrete stationary series input consisting of 2048 points in the time domain. The four cases shown in Fig. 5 are characterized by both the center

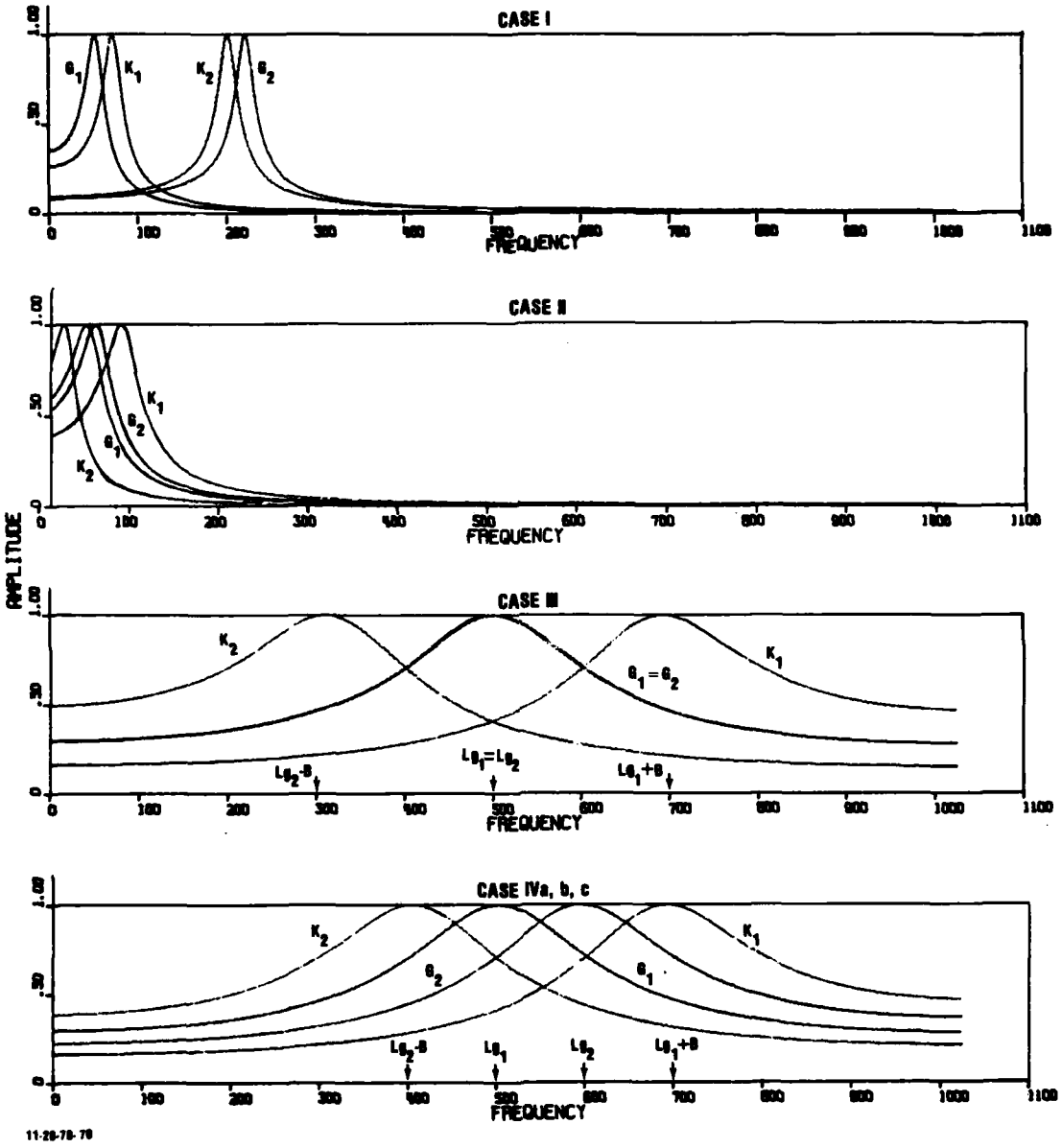

FIGURE 5. Normalized amplitudes of specified ideal spectra for gradiometer and subsidiary channels as a function of frequency.

frequency parameter for peak amplitude and the bandwidth of the spectra (Fig. 4). The first two cases are for low center frequency parameters and narrow bandwidths, whereas the last two consider broad bandwidths. Furthermore, the first low-frequency case is characterized by a ratio $L_{g_2}/L_{g_1} > 1$, whereas the second one has $L_{g_2}/L_{g_1} \cong 1$. The two cases for high frequency have $L_{g_2}/L_{g_1} \cong 1$ but somewhat different S_{yy} spectra.

Table 1 gives the values of the center frequency parameters for peak amplitude of the spectra (L_{g_1}, L_{g_2}) and half the bandwidth (B/2) for each of the four cases in Fig. 5. It should be noted that half the bandwidth is the reference for the number M of frequencies to be used at *either side* of a given frequency in the smoothing out of the periodograms for each spectral density. As indicated in Eq. (11), the degree of frequency averaging in a given periodogram is given by 2M + 1 or, approximately, by M/(B/2) relative to the bandwidth of the filters; i.e., a value of M/(B/2)≈1 indicates frequency averaging over a window equal to the bandwidth of the specified spectra. Table 1 includes the range of the gradiometer signal-to-noise ratio (S/N_F) and the corresponding values of the $\sqrt{F}$ parameter shown in Fig. 2. The gradiometer signal-to-noise ratio is inversely proportional to F and it was varied in the range 1/10 to 10, which yielded the corresponding $\sqrt{F}$ values shown in Table 1. The table includes also the range of the signal-to-instrument noise ratio (S/N_i) and the corresponding values of the $\sqrt{F_i}$ parameters indicated in Fig. 2. The white noise power within the bandwidth of the filter is given by the corresponding fraction of the white noise across the whole frequency spectrum. Therefore, the signal-to-instrument noise ratio is inversely proportional to the product of F_i and the fraction of the area within the bandwidth signal, i.e.,

$$\frac{S}{N_i} = \frac{1}{F_i \, (A_{g_1 g_1}/1024)} \tag{115}$$

where $A_{g_1 g_1}$ denotes the area under the ideal spectrum $S_{g_1 g_1}$ and 1024 is the frequency range (T/2) for the input time series of 2048 points. The signal-to-instrument noise ratio values were taken as ∞, 10 and 1; which yielded the corresponding $\sqrt{F_i}$ values in Table 1. These values of the signal-to-noise instrument ratio represent, respectively, (a) ideal conditions given by z(t) = 0 in Eq. (12), (b) signals with a moderate instrument noise background, and (c) signals that are expected to be within the threshold of detectability.

TABLE 1. FILTER PARAMETERS AND SIGNAL-TO-NOISE RATIOS

Case	L_{g_1}	L_{g_2}	B/2	S/N_F	$\sqrt{F}$	S/N_i	$\sqrt{F_i}$
I	50	220	10	1	1	∞, 10, 1	0, 1.84, 5.82
II	50	60	20	1	1	∞, 10, 1	0, 1.43, 4.51
III	500	500	100	1	1	∞, 10, 1	0, 0.59, 1.87
IV-a	500	600	100	1	1	∞, 10, 1	0, 0.58, 1.85
IV-b	500	600	100	10	0.316	∞, --, --	0, -- , --
IV-c	500	600	100	1/10	3.162	∞, --, --	0, -- , --

The filter parameters in Table 1 define the ideal transfer functions of the simulated gradiometer and subsidiary channels in Fig. 2. The use of uncorrelated input time series [$n_1(t)$, $n_2(t)$] generate the output time series given by Eqs.(80)-(83) as well as the output time series y(t), which includes $\sqrt{F_i}n_3$ (Fig. 2). The subsequent use of equations such as Eqs. (5)-(9) gives the corresponding periodograms, which are then averaged with respect to frequency as illustrated by Eq. (11). The estimators for the spectral density functions (i.e., smoothed periodograms) yield then the estimated transfer functions [Eqs. (101), (102)], the reconstructed spectra for the gradiometer output [Eq. (104)], the imbedded signal in the gradiometer [Eq. (94)], and the corresponding partial coherence [Eq. (107), (109-(111)].

3.4 INTERPRETATION OF NUMERICAL SIMULATIONS

Figure 2 indicates that the two subsidiary channels do not process stationary time series with instrument noise. Hence, the estimators for the spectra $\hat{S}_{11}$ and $\hat{S}_{22}$ as well as the estimated input coherence $\hat{\gamma}^2_{1,2}$ will be shown along with other data only for one signal-to-instrument noise ratio.

Figure 2 also shows that the simulated gradiometer output time series $x_{g_1}(t)$ and $x_{g_2}(t)$ are unaffected by the instrument noise in the main data channel. Hence, only auto- and cross-spectra densities involving the main data channel output, y(t), will be modified by the $\sqrt{F_i}$ white noise parameter. Likewise, the output time series $x_{g_1}(t)$ is unaffected by the gradiometer noise parameter $\sqrt{F}$. Hence, only the auto-spectral density $\hat{S}_{\xi_2\xi_2}$ as well as the auto- and cross-spectral densities involving the main data channel output y(t) with or without instrument noise will be modified by the $\sqrt{F}$ parameter. It is important to emphasize that the *same* set of random stationary series was always utilized for $n_1(t)$, $n_2(t)$ and $n_3(t)$, which were characterized by cross-correlation coefficients that were very small. Furthermore, each time series was assumed to be given by a sequence of random numbers of 2048 points, and their frequencies to be represented by the order of each term in such series in the frequency domain, i.e., by 1, 2, ...1024.

Before presenting the data for each case, it is important to indicate some typical trends in the periodograms. For relatively unaveraged conditions (say M = 1), the input coherence $\hat{\gamma}^2$ is highly noisy, i.e., it varies as white noise between zero and unity. These large fluctuations are smoothed out as the number of frequencies, M, in the frequency averaging (2M + 1) increases toward the bandwidth value, B, of the specified spectra in Fig. 5; i.e., as $M/(B/2) \rightarrow 1$. Similar trends take place for the gain factors, $|H_i|$, and some spectral densities when the signal-to-instrument noise is low, i.e., their magnitudes can become extremely high for relatively unaveraged (M = 1) periodograms.

4. RESULTS OF NUMERICAL SIMULATIONS

The numerical simulation of a two-input gradiometer and two subsidiary single-input channels (Fig. 2) considered the ideal spectra shown in Fig. 5, i.e., (a) two cases with *low* values of the center frequency parameters L_{g_1} and L_{g_2} (Eq. 87) and (b) two cases with *high* values of the center frequency parameters together with broader bandwidths. The low frequency cases are furthermore characterized by two values of the L_{g_2}/L_{g_1} ratio, i.e., when the gradiometer "noise" channel has a center frequency for peak amplitude of the spectrum that is significantly higher than that for the gradiometer signal channel and when these center frequencies are nearly equal.

As indicated in the preceding section, the results of the numerical simulations for each case put emphasis on (a) the estimated gradiometer signal spectrum $\hat{S}_{\xi_1\xi_1}$ (Eq. 94), (b) the estimated gain factors $|\hat{H}_1|$ and $|\hat{H}_2|$ of the simulated gradiometer transfer functions; the former appears in the expression for $\hat{S}_{\xi_1\xi_1}$ while both do so in that for the estimator of the gradiometer output spectrum $\hat{S}_{yy}$ (Eq. 104), (c) the estimators for each spectrum of the subsidiary channels, $\hat{S}_{11}$ and $\hat{S}_{22}$; again, the former appears in the expression for $\hat{S}_{\xi_1\xi_1}$, whereas both do so in that for $\hat{S}_{yy}$, (d) the estimator $\hat{S}_{yy}$, (e) the estimated partial coherences for the gradiometer signal channel (Eq. 107), and (f) the estimated input coherence (Eq. 100). These results are, in general, given for each case as a function of both the number of frequencies (M) used in the averaging of the periodograms (Eq. 11) and each of three characteristic signal-to-instrument noise ratios (Table 1). As noted previously, the ratio M/(B/2) indicates the length of the averaging window

relative to the bandwidth of the specified ideal spectra. The three characteristic signal-to-instrument noise ratios correspond to an ideal case of no instrument noise ($S/N_i = \infty$), detectable signal-to-noise ratios ($S/N_i = 10$) and signals that are within the threshold of detectability ($S/N_i = 1$).

The results for each foregoing case and parameter include comparisons of the ideal and estimated or estimators parameters, so as to exhibit the bias in the estimated or estimator parameters as a function of the frequency averaging, M/(B/2), for the three typical signal-to-noise ratios. The ideal values correspond to the filter outputs (Fig. 2) to unit impulse inputs, whereas the estimated and estimators parameters, respectively, are for the reconstructed outputs of the gradiometer and actual outputs of the subsidiary channels (Figs. 1b and 2). The results are then plotted as a function of simulated frequency, i.e., by the order of the random stationary terms in the input time series to the filters (Fig. 2).

4.1 LOW-FREQUENCY GRADIOMETER WITH $L_{g_2}/L_{g_1} > 1$

Figures 6-27, in the subsequent subsection, describe the results for the foregoing parameters for Case I in Fig. 5, which is characterized by $L_{g_1} = 50$, $L_{g_2} = 220$, $L_{g_2}/L_{g_1} = 4.4$, and $B/2 = 10$.

4.1.1 Estimated Gradiometer Signal Spectrum

Figures 6-8 show comparisons of ideal and estimated spectra for the gradiometer signal channel as a function of frequency averaging and signal-to-instrument noise ratio for $S/N_i = \infty$, 10, and 1, respectively. These figures indicate the following:

- Figure 6 compares the ideal ($S_{g_1 g_1}$) and estimated ($\hat{S}_{\xi_1 \xi_1}$) signal spectra for ideal conditions of no instrument noise and M/(B/2) that are as high as twice the bandwidth of the specified spectrum. Although not shown in these figures, the relatively unaveraged (M=1) noisy values for $\hat{S}_{\xi_1 \xi_1}$ show a peak amplitude that is larger than the

ideal peak value at $L_{g_1} = 50$ by a factor of about 1.45, This figure then indicates that frequency averaging smooths out the fluctuations about the mean signal, but it underestimates significantly the actual spectrum even when $M = 5$ or $M/(B/2) = 0.5$, i.e., when the length of the averaging window equals about half the bandwidth of the specified signal.

- Figure 7 compares the ideal ($S_{g_1g_1}$) and estimated ($\hat{S}_{\xi_1\xi_1}$) signal spectra when the signal-to-instrument noise ratio $S/N_i = 10$. Because of the increased noise relative to the previous figure, the estimated spectrum tends toward the ideal value when $1 < M/(B/2) < 2$. Although not shown in these figures, the values of $\hat{S}_{\xi_1\xi_1}$ for $M = 1$ are highly noisy at every frequency, and the magnitude of $\hat{S}_{\xi_1\xi_1}$ in the neighborhood of $L_{g_1} = 50$ is as high as 10 times that of the ideal $S_{g_1g_1}$ values. Figure 7 for detectable signal-to-instrument noise ratios indicates that an unbiased estimate of the peak amplitude of the signal $S_{g_1g_1}$ would require an averaging window given by $1 < M/(B/2) < 2$. However, the frequency characteristics of the estimated signal would not be clearly detectable due to the distortions of the shape of the estimated signal by the smoothing out of the periodogram.

- Figure 8 compares the ideal ($S_{g_1g_1}$) and estimated ($\hat{S}_{\xi_1\xi_1}$) signal spectra for $S/N_i = 1$, i.e., when the signal-to-instrument noise ratio is within the threshold of detectability. This figure indicates even greater overestimates in the peak amplitude of $\hat{S}_{\xi_1\xi_1}$ at $L_{g_1} = 50$ for $M/(B/2) = 0.5$ than those in the previous figures for $S/N_i = \infty$ and 10. Although not shown in this figure, the magnitude of $\hat{S}_{\xi_1\xi_1}$ for $M = 1$ in the neighborhood of $L_{g_1} = 50$ is as high as 100 times that of the ideal $S_{g_1g_1}$ value. The results in Fig. 8 for $S/N_i = 1$ indicate that an unbiased estimate of the peak amplitude of the signal

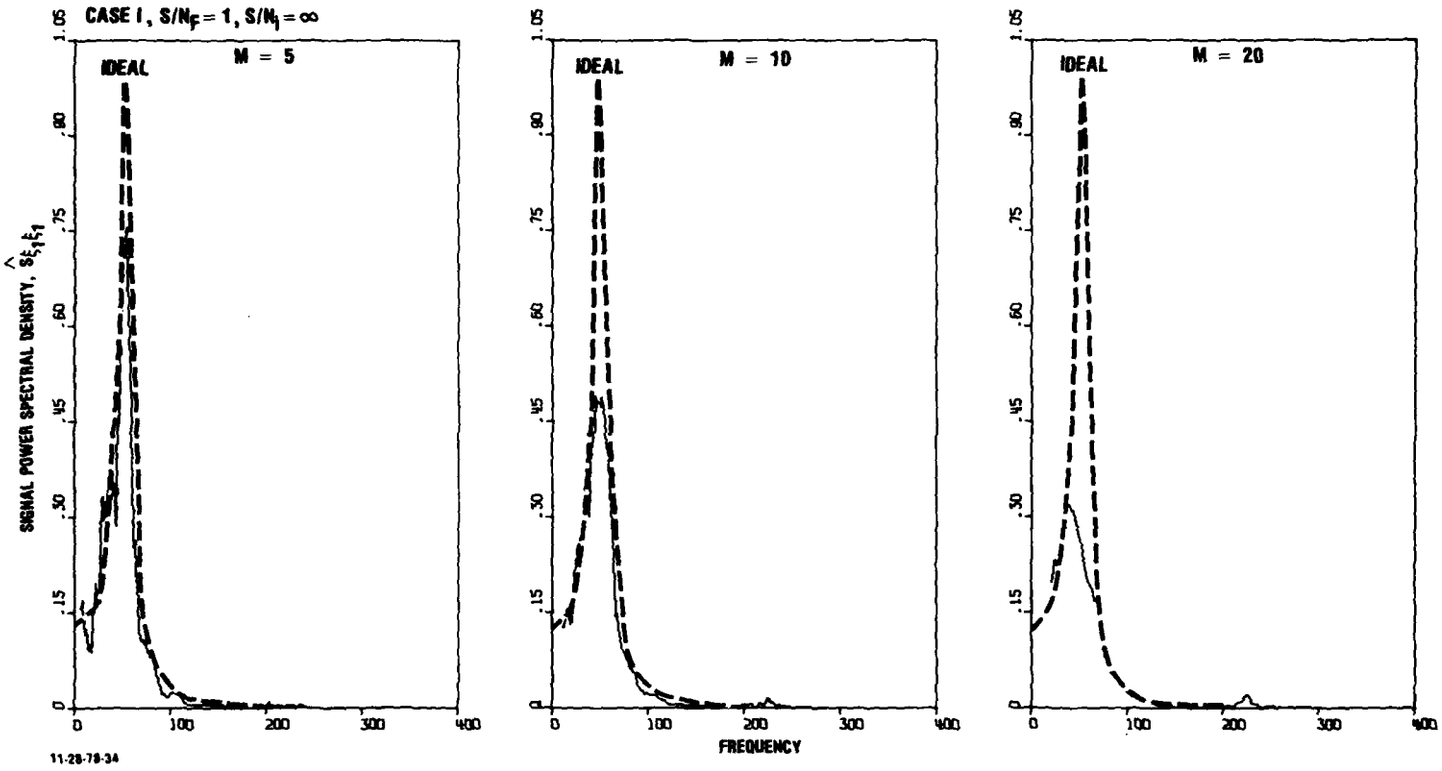

FIGURE 6. Comparison of ideal and reconstructed signal spectra for low-frequency filter with $Lg_2/Lg_1 = 4.4$ for $S/N_i = \infty$.

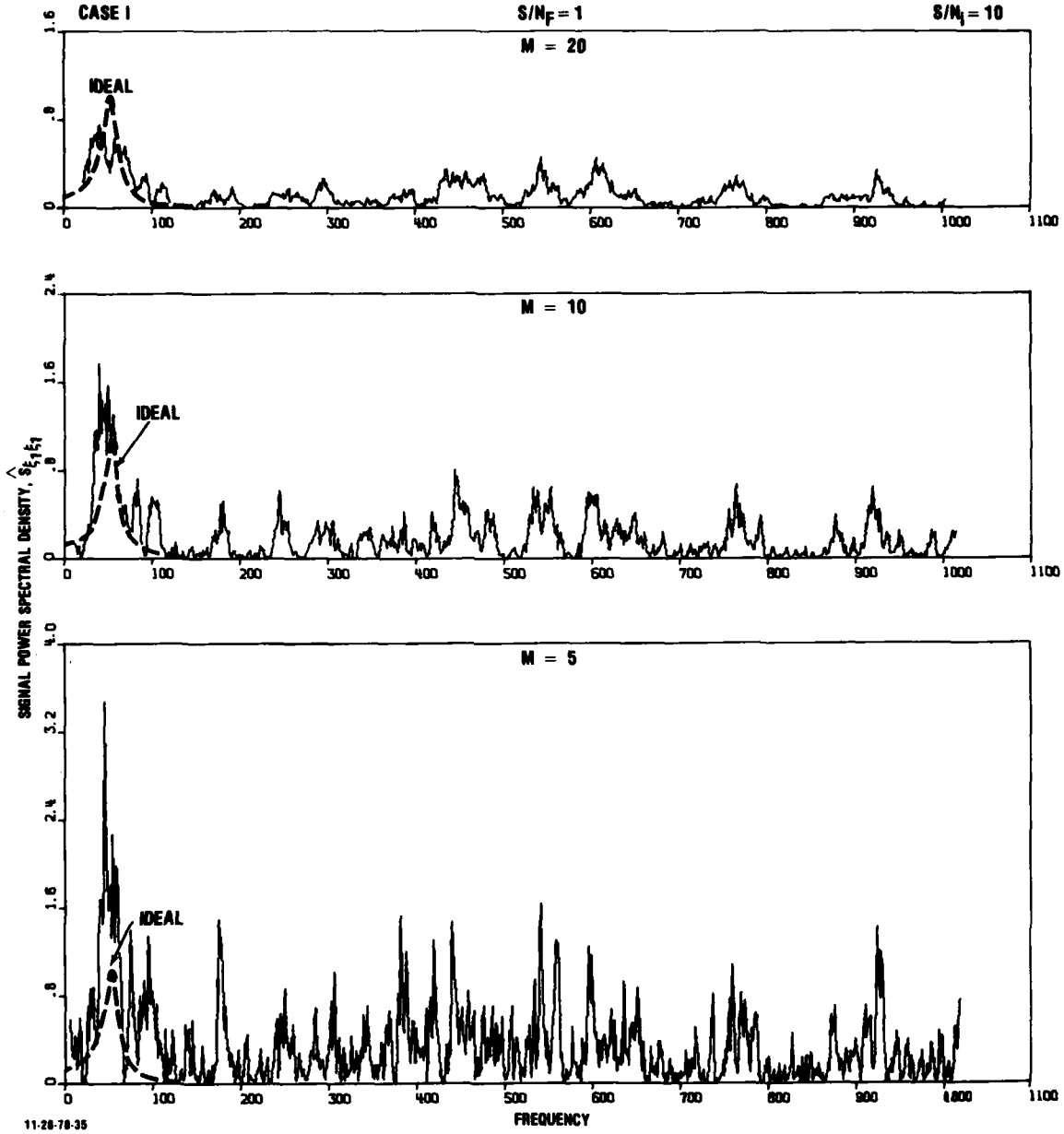

FIGURE 7. Comparison of ideal and reconstructed signal spectra for low-frequency filters with Lg_2/Lg_1 = 4.4 for S/N_i = 10.

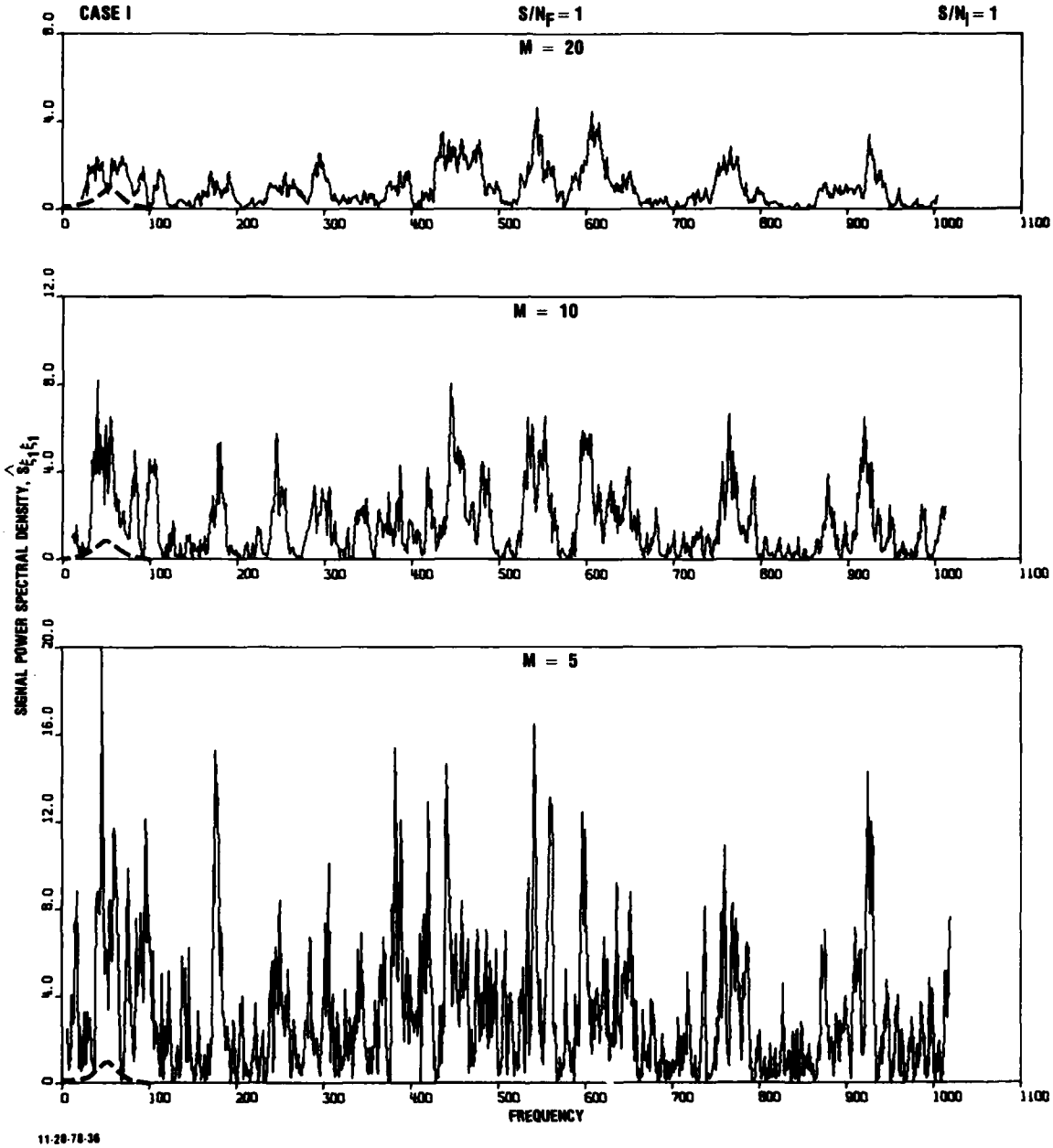

FIGURE 8. Comparison of ideal and reconstructed signal spectra for low-frequency filters with $Lg_2/Lg_1 = 4.4$ for $S/N_1 = 1$.

$S_{g_1g_1}$ would require frequency averaging given by $M/(B/2) \gtrsim 2$. Furthermore, the detectability of even the peak amplitude of an unknown $S_{g_1g_1}$ spectrum would be difficult due to the comparable white noise at other frequencies.

4.1.2 Estimated Gain Factors

Figures 9-13 and 14-18 show the estimated gain factors for the gradiometer signal and "noise" channels, respectively, as a function of frequency averaging and the signal-to-instrument noise ratio $S/N_i = \infty$, 10, and 1. These figures indicate the following:

- Figure 9 for the estimated gain factor $|\hat{H}_1|$ for the gradiometer signal channel and $S/N_i = \infty$ indicates that the transfer function itself would be detectable even without averaging, i.e., for average values as low as $M/(B/2) = 1/10$ or 0.1. However, due to numerical noise from the algorithm, a spurious signal appears in the neighborhood of L_{g_2}. It is to be noted that increasing $M/(B/2)$ as required to detect $S_{g_1g_1}$ not only introduces a corresponding bias in the amplitude of the gain factor but also magnifies the spurious signal at L_{g_2}. The reason for this spurious signal is the fact that in the neighborhood of this frequency, the denominator in Eq. (101) decreases faster than the numerator.
- Figure 10 for $|\hat{H}_1|$ and $S/N_i = 10$ indicates drastic increases in the amplitude of the gain factor at frequencies higher than L_{g_2}. Although not shown in this figure, the amplitude of $|\hat{H}_1|$ for $M = 1$ is extremely noisy at frequencies $f > 400$, as indicated by values $|\hat{H}_1| > 1000$. The significance of the high values of the gain factor at the high frequencies is that they contribute to the white noise of $\hat{S}_{\xi_1\xi_1}$ (Fig. 7) and $\hat{S}_{yy}$, as will be evident later. Figure 11 compares the ideal

and estimated gain factors as a function of M, which indicates that $M/(B/2) \approx 2$ in order to obtain unbiased estimated gain factors at L_{g_1}. However, the numerical noise at frequencies higher than L_{g_1} would make the gain factor for the signal gradiometer channel undetectable.

- Figure 12 for $|\hat{H}_1|$ and $S/N_i = 1$ indicates larger amplitudes for the gain factor by a factor of about three than those for $S/N_i = 10$ in Fig. 10. Figure 13 compares the ideal and estimated gain factors as a function of M, which shows trends somewhat similar to those in Fig. 11 for $S/N_i = 10$.
- Figure 14 for the estimated gain factor $|\hat{H}_2|$ for the gradiometer "noise" channel and $S/N_i = \infty$ shows trends similar to those for $|\hat{H}_1|$ in Fig. 9 for the same signal-to-instrument noise ratio, except that the numerical noise takes place now at the L_{g_1} frequency.
- Figure 15 for $|\hat{H}_2|$ and $S/N_i = 10$ shows trends similar to those for $|\hat{H}_1|$ in Fig. 10 for the same signal-to-instrument noise ratio, except that the amplitude of the $|\hat{H}_2|$ are lower by a factor of about 2.7 for M = 5, a factor that becomes somewhat larger as M increases. Figure 16 compares the ideal and estimated gain factors as a function of M, and shows trends similar to those in Fig. 11 for $|\hat{H}_2|$ at the same signal-to-instrument noise ratio.
- Figure 17 for $|\hat{H}_2|$ and $S/N_i = 1$ indicates a trend similar to those in Fig. 12 for $|\hat{H}_1|$ and same signal-to-instrument noise ratio, except that the amplitudes of $|H_2|$ are lower than those for $|\hat{H}_1|$ by a factor of about 1/2. Figure 18 shows comparisons of ideal and estimated $|\hat{H}_2|$ gain factors for $S/N_i = 1$, and shows trends similar to those in Fig. 13 for $|\hat{H}_1|$ and same signal-to-instrument noise ratio.

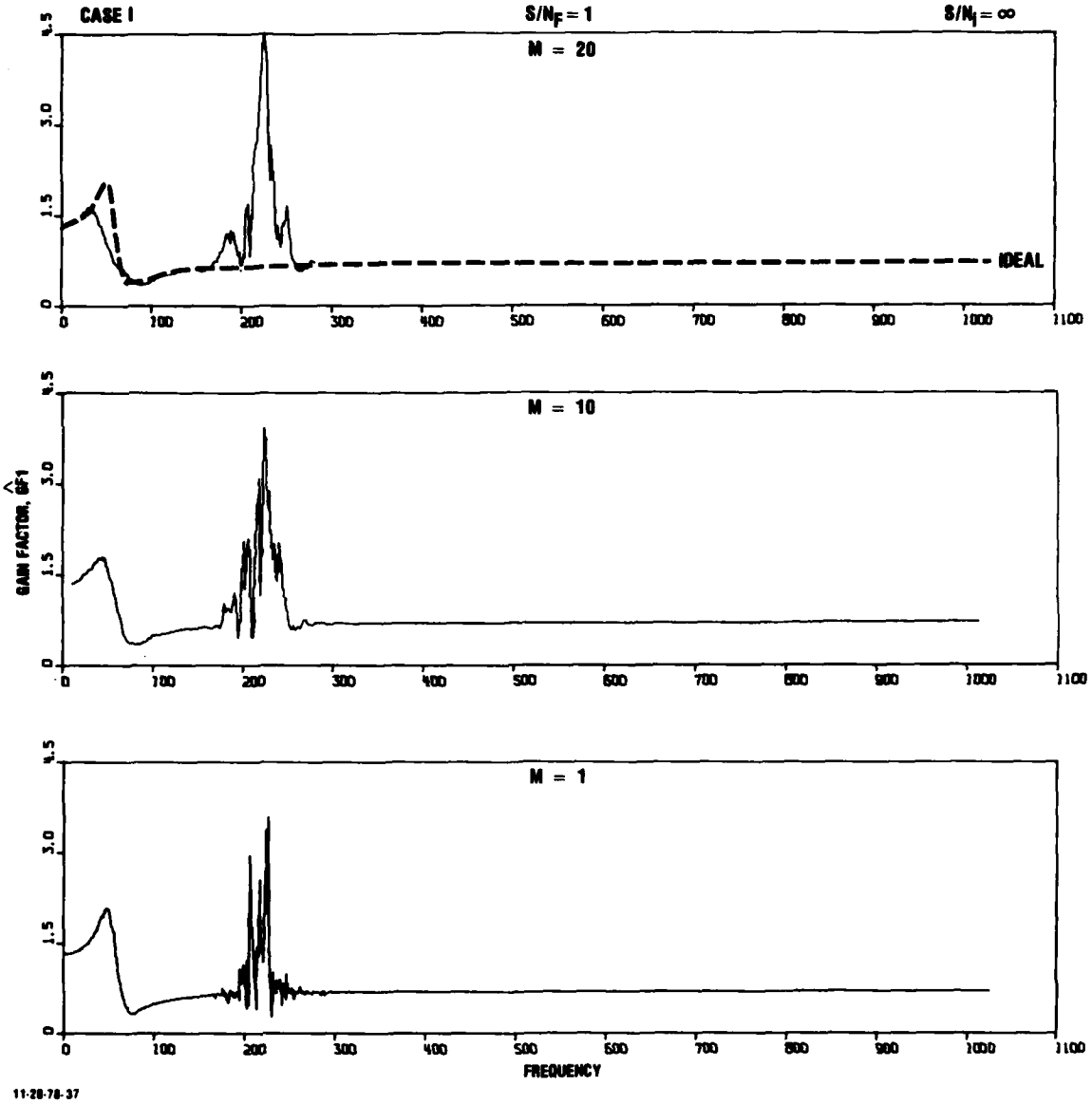

FIGURE 9. Comparison of ideal and estimated gain factors for gradiometer signal channel for low-frequency filters with $Lg_2/Lg_1 = 4.4$ for $S/N_i = \infty$.

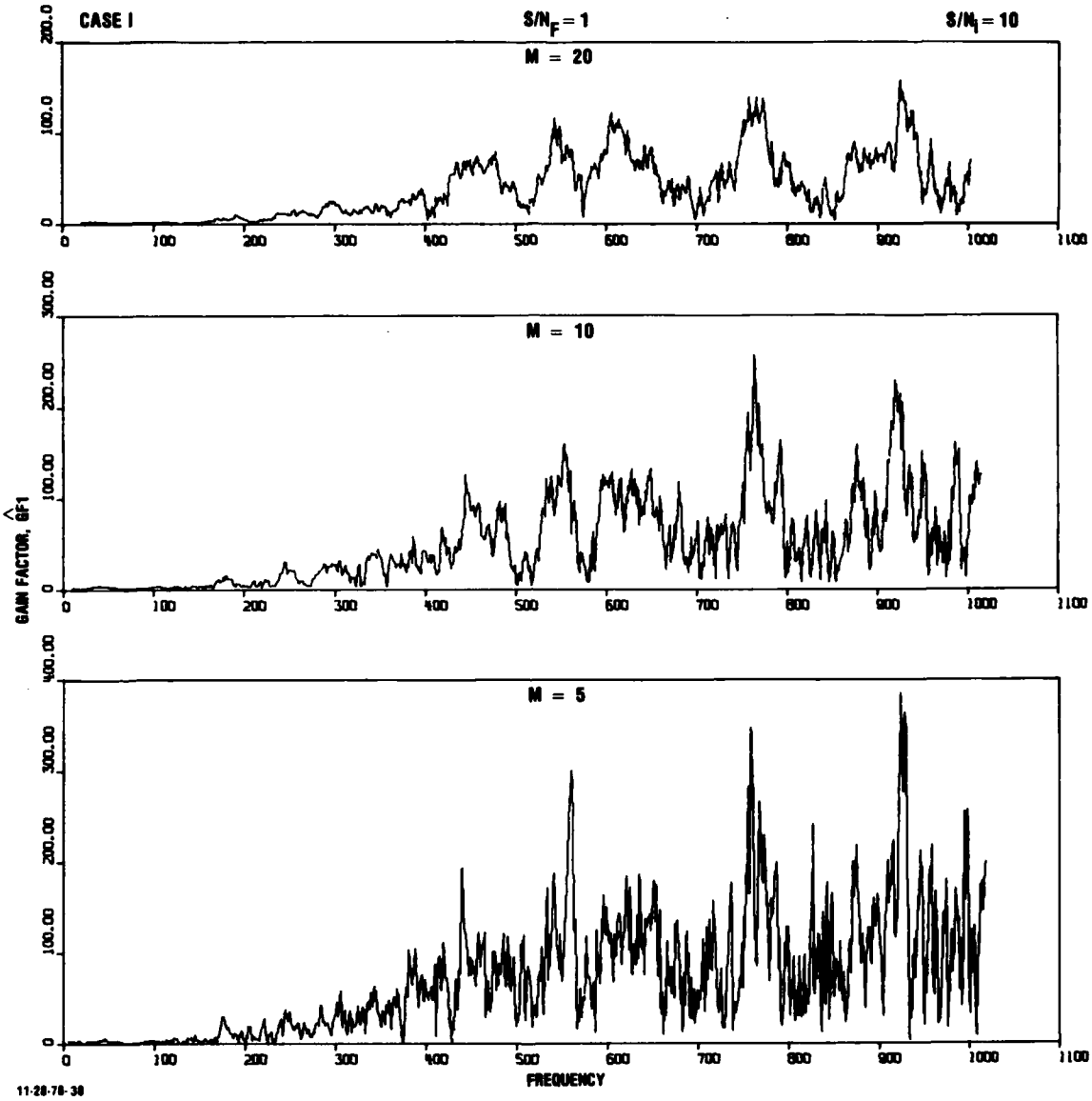

FIGURE 10. Estimated gain factor for gradiometer signal channel for low-frequency filters with Lg_2/Lg_1 = 4.4 for S/N_1 = 10.

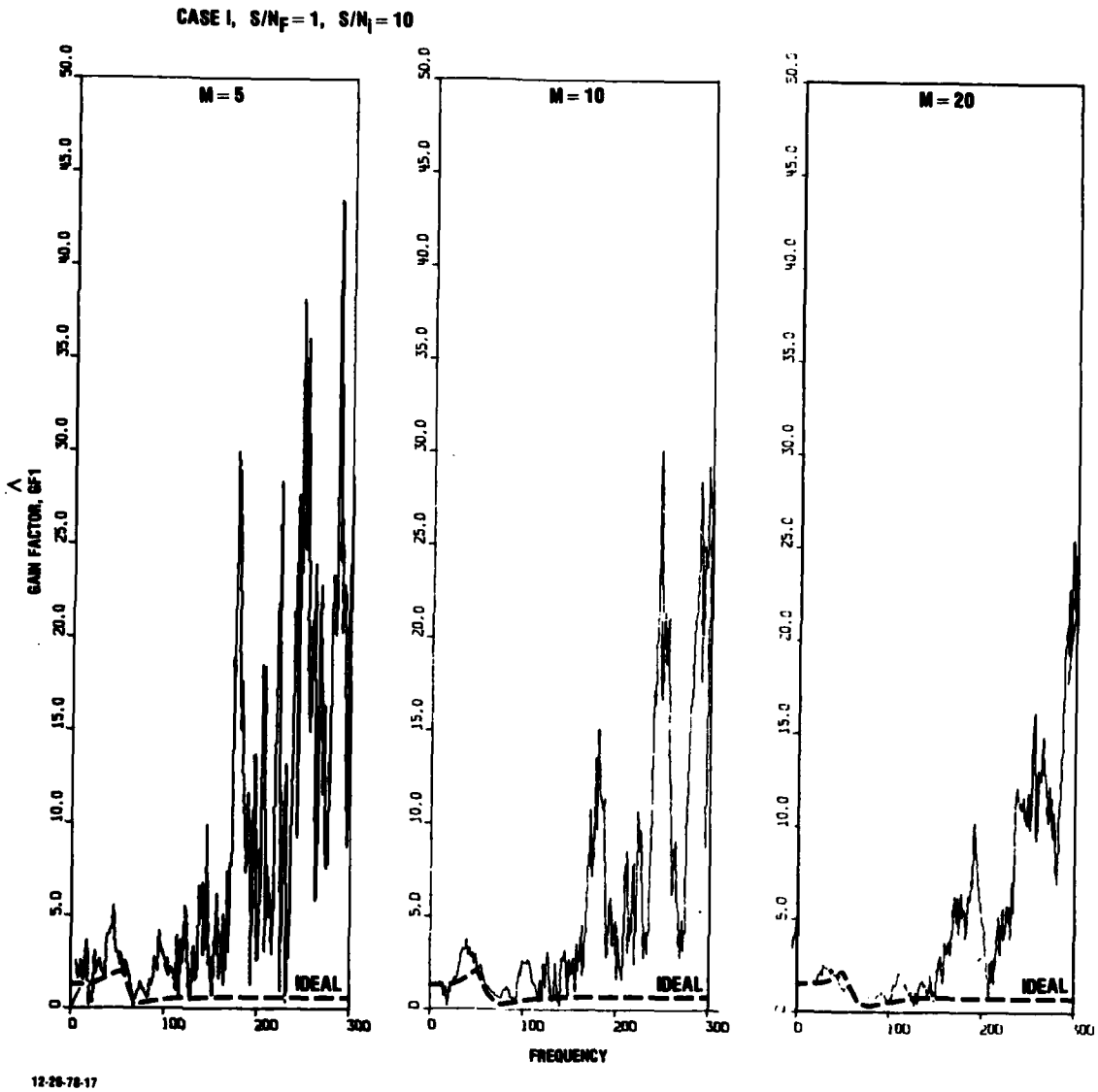

FIGURE 11. Comparison of ideal and estimated gain factors for gradiometer signal channel for low-frequency filters with Lg_2/Lg_1 = 4.4 for S/N_I = 10.

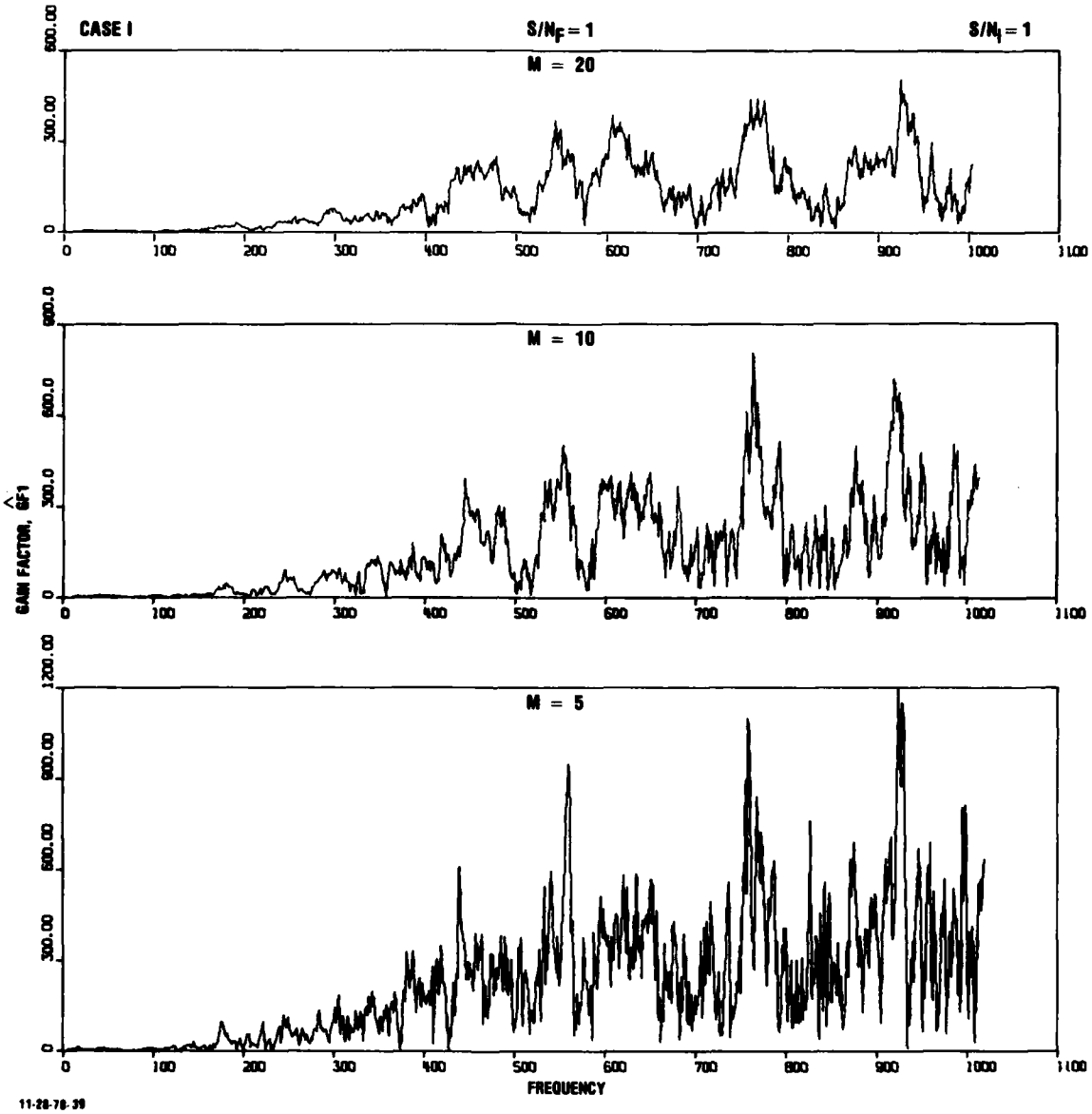

FIGURE 12. Estimated gain factor for gradiometer signal channel for low-frequency filters with $Lg_2/Lg_1 = 4.4$ for $S/N_i = 1$.

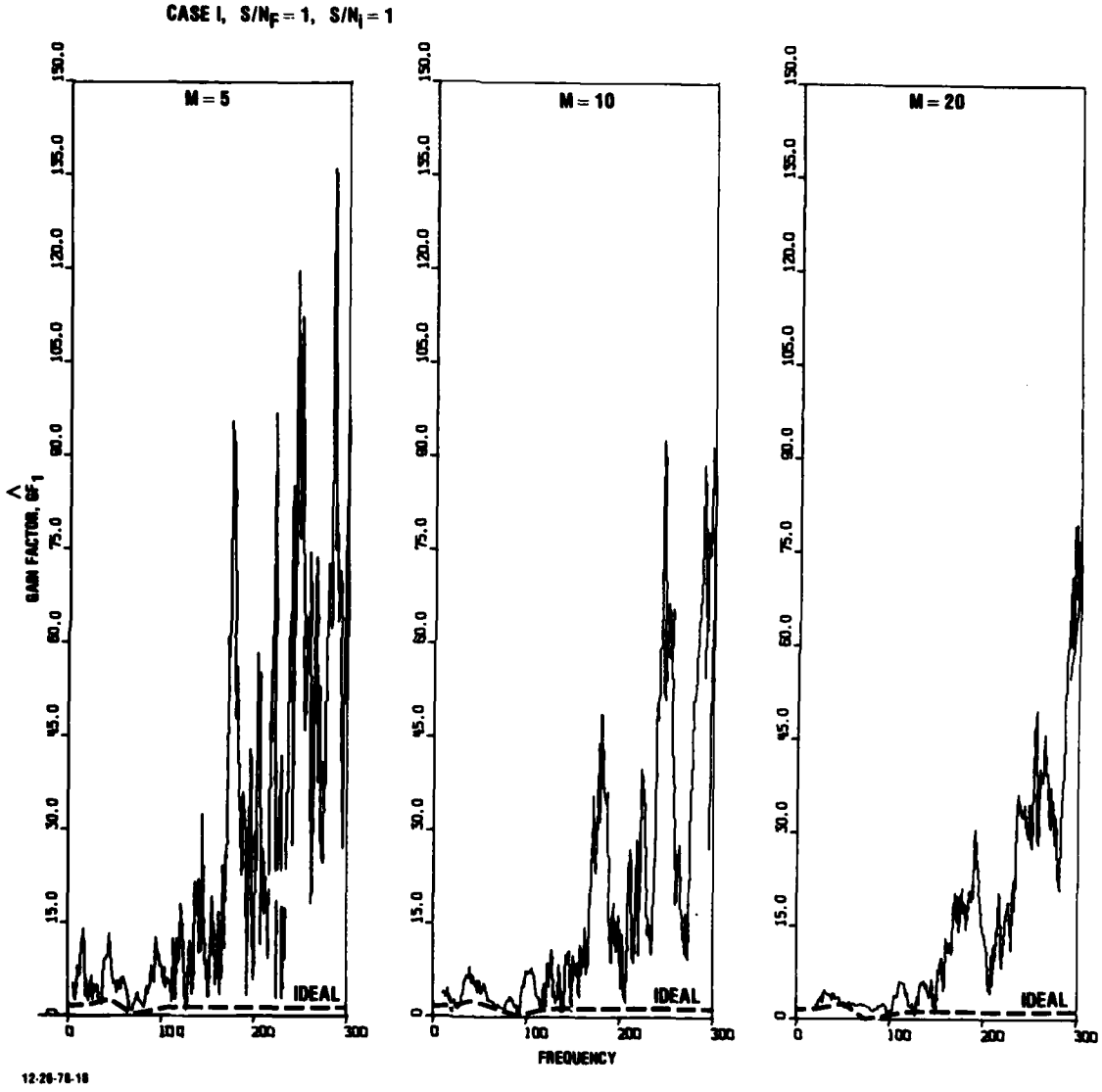

FIGURE 13. Comparison of ideal and estimated gain factors for gradiometer noise channel for low-frequency filters with Lg_2/Lg_1 = 4.4 for S/N_1 = 1.

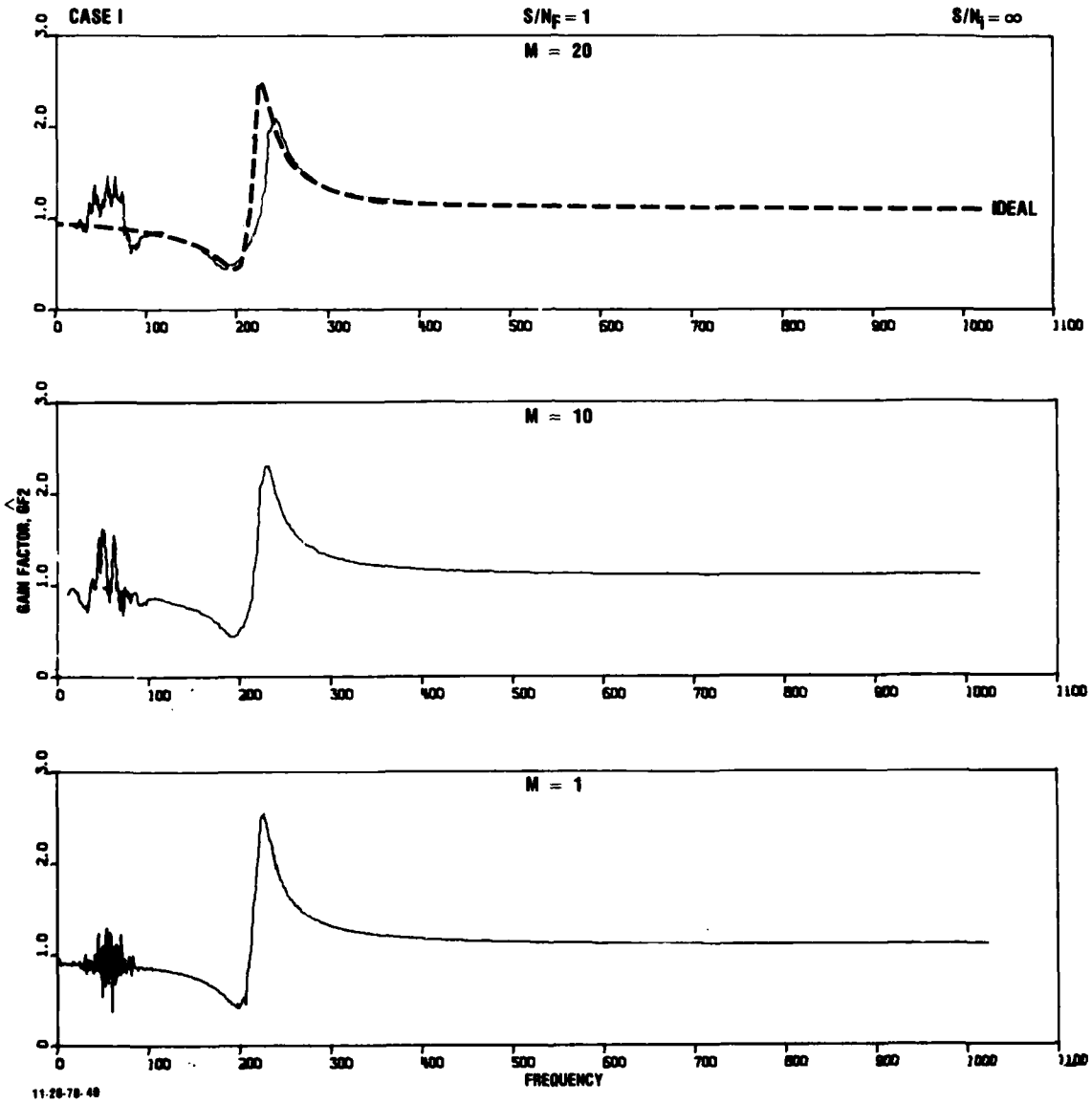

FIGURE 14. Comparison of ideal and estimated gain factors for gradiometer noise channel for low-frequency filters with $L_{g_2}/L_{g_1} = 4.4$ for $S/N_i = \infty$.

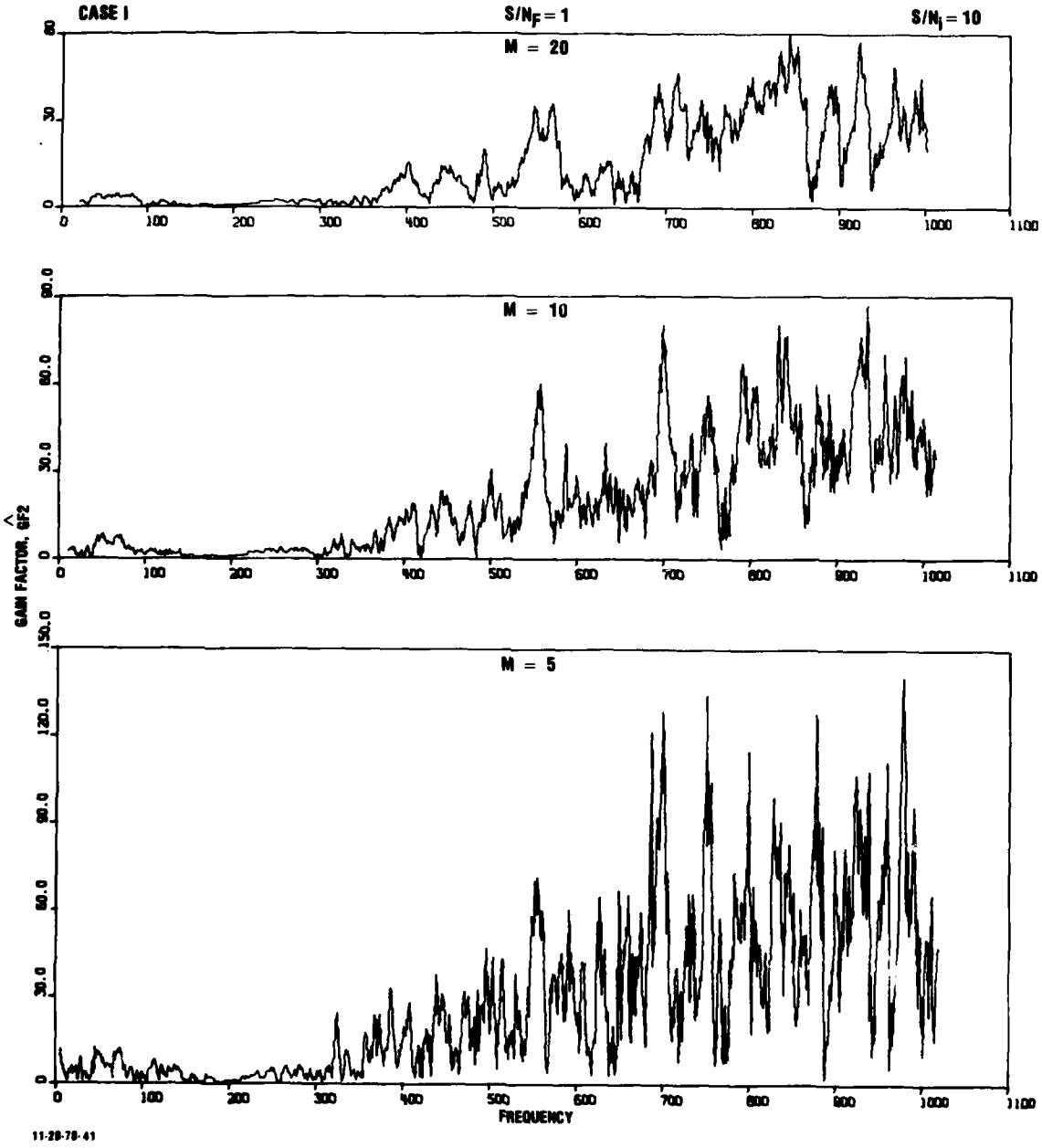

FIGURE 15. Estimated gain factor for gradiometer noise channel for low-frequency filters with $Lg_2/Lg_1 = 4.4$ for $S/N_I = 10$.

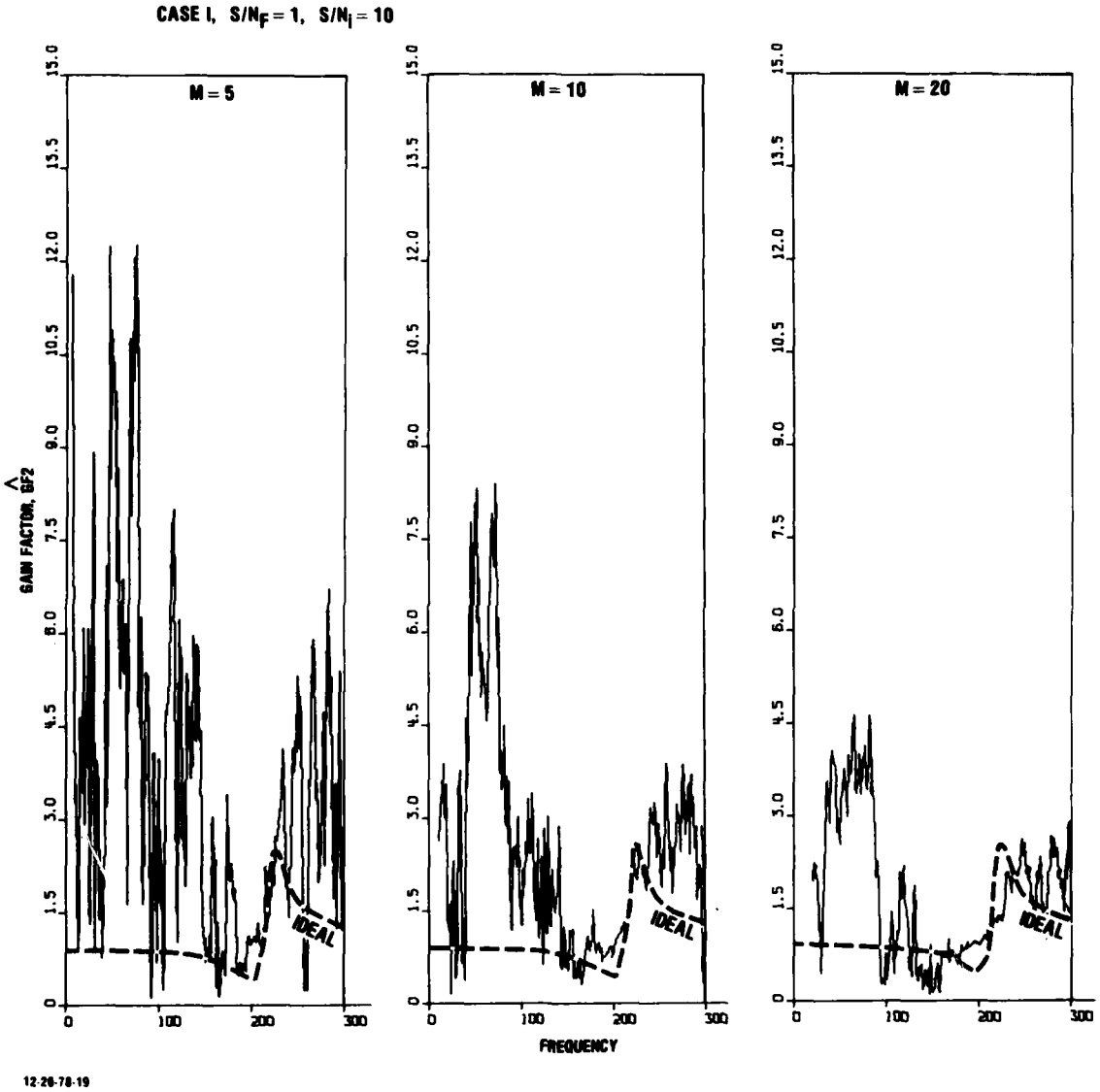

FIGURE 16. Comparison of ideal and estimated gain factors for gradiometer noise channel for low-frequency filters with Lg_2/Lg_1 = 4.4 for S/N_i = 10.

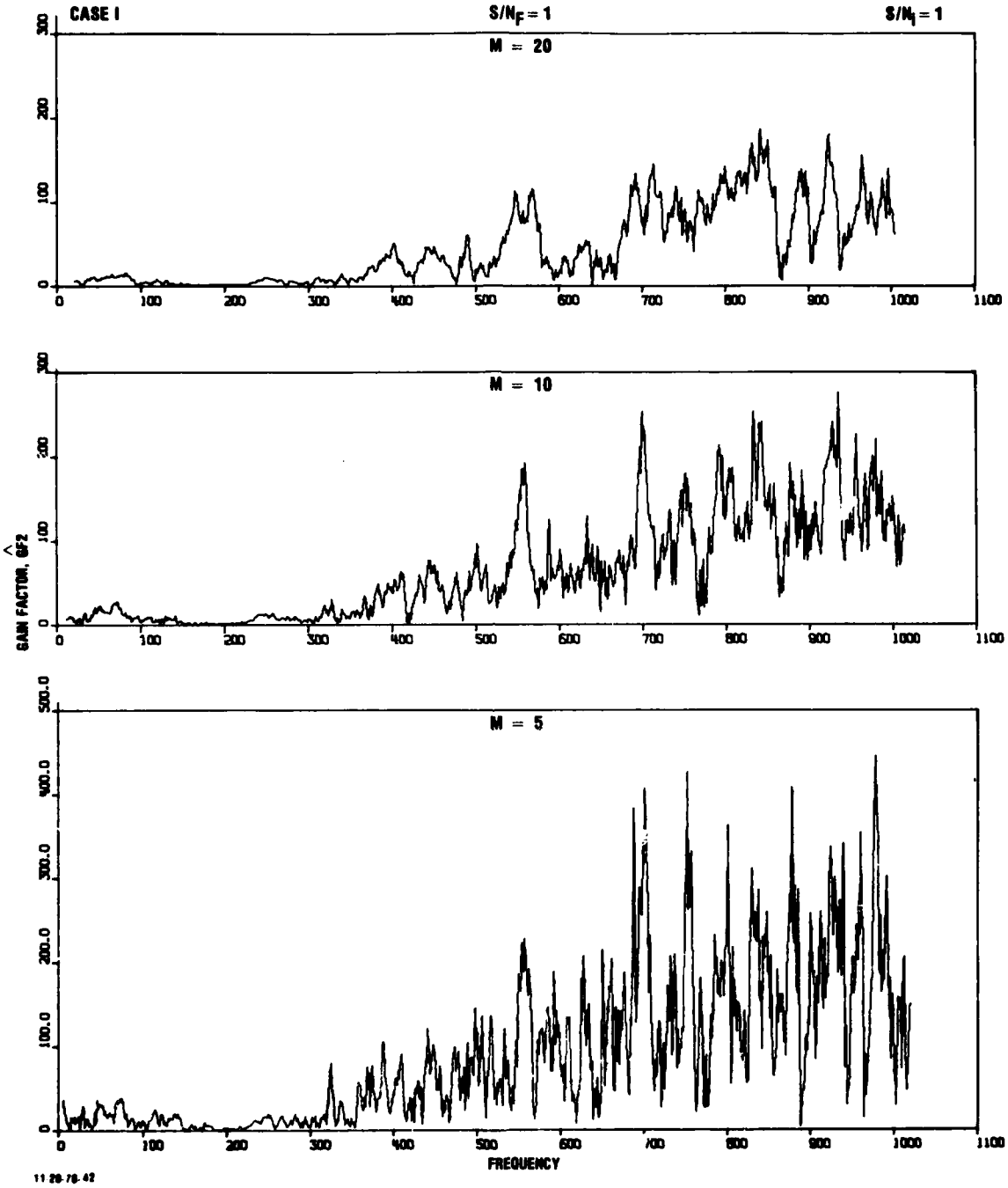

FIGURE 17. Estimated gain factors for gradiometer noise channel for low-frequency filters with $Lg_2/Lg_1 = 4.4$ for $S/N_I = 1$.

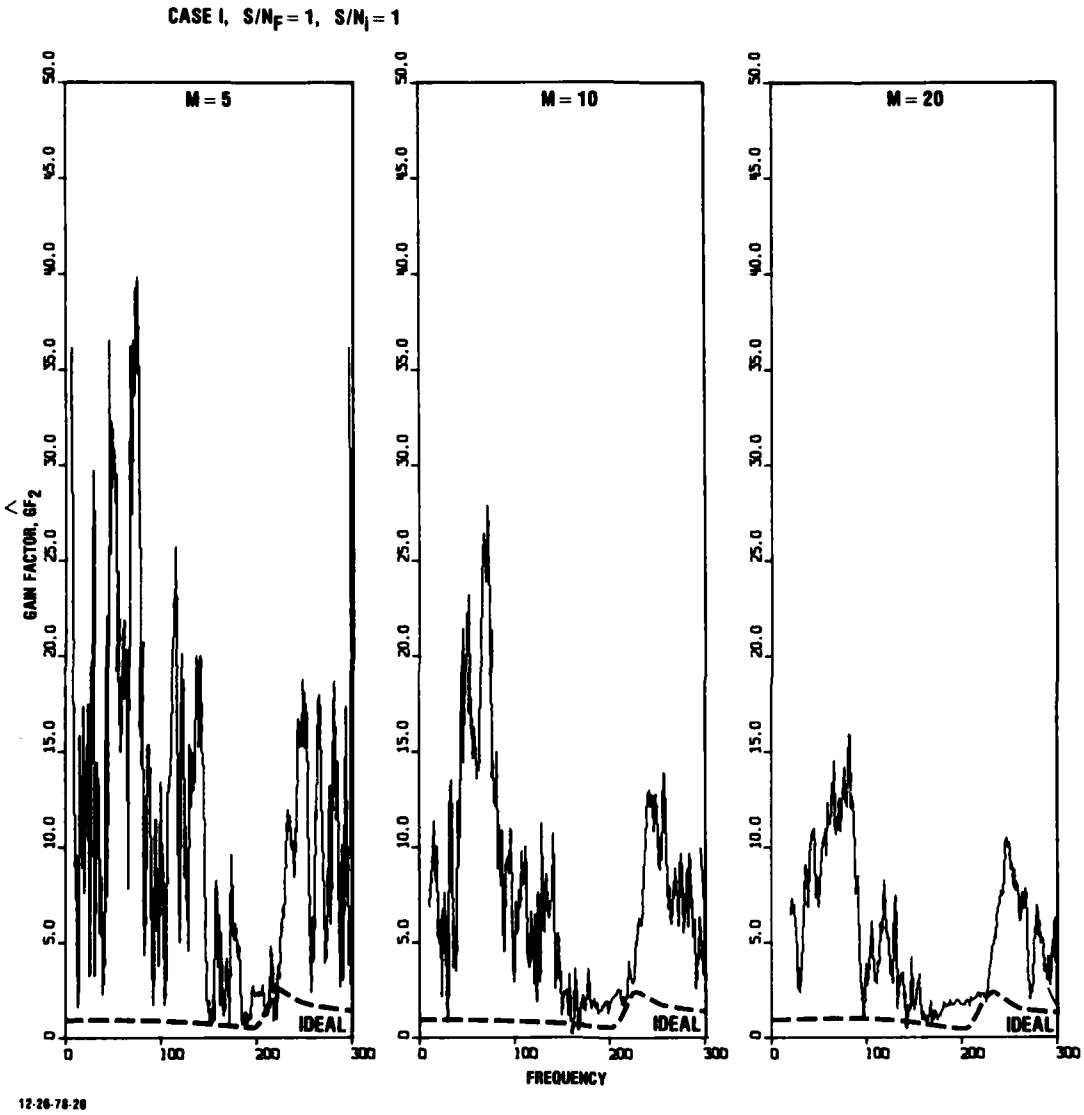

FIGURE 18. Comparison of ideal and estimated gain factors for gradiometer signal channel for low-frequency filters with L_{g_2}/L_{g_1} = 4.4 for S/N_i = 1.

4.1.3 Estimators for Gradiometer Output Spectra

Figures 19-23 show comparisons of the ideal and estimated spectra for the subsidiary channels and gradiometer output (Fig. 2) as a function of frequency averaging and signal-to-instrument noise ratio for the gradiometer output. These figures indicate the following:

- Figure 19 for $\hat{S}_{11}$ and any S/N_i value shows that significant bias is introduced for averaging values using a number of frequencies as low as $M/(B/2) \approx 5/10$ or 0.5, i.e., a result that is consistent with those for $\hat{S}_{\xi_1\xi_1}$ for $S/N_i = \infty$ in Fig. 6. Although not shown in these figures, the relatively unaveraged (M=1) values for $\hat{S}_{11}$ show a peak amplitude of about 1.24 at the frequency for the peak ideal value. It should be noted that even though the values of $\hat{S}_{11}$ at frequencies higher than L_{g_1} are very small, their combination with extremely high values of the gain factors at these higher frequencies yield the white noise background to $\hat{S}_{\xi_1\xi_1}$ in Figs. 7 and 8 at the high frequencies; i.e., in the product given by Eq. (94).

- Figure 20 for $\hat{S}_{22}$ and any S/N_i value shows results somewhat similar to those for $\hat{S}_{11}$ in the previous figure. Significant bias is introduced for averaging values as low as $M/(B/2) \approx 5/10$ or 0.5. The peak value for $\hat{S}_{22}$ at M=1 is about 1.22 at the frequency for the peak ideal value.

- Figure 21 for $\hat{S}_{yy}$ and $S/N_i = \infty$ indicates results similar to those for $\hat{S}_{\xi_1\xi_1}$, i.e., significant bias is introduced for averaging values as low as $M/(B/2) \approx 5/10$ or 0.5. Although not shown in the figure, the relatively unaveraged (M=1) values for $\hat{S}_{yy}$ have peak values of about 1.6 at the L_{g_1} and L_{g_2} frequencies for the peak ideal values.

- Figure 22 for $\hat{S}_{yy}$ and $S/N_i = 10$ indicates a significant increase in the amplitude of $\hat{S}_{yy}$ relative to those for $S/N_i = \infty$ for frequency averaging in the range $0.5 < M/(B/2) < 2$. Although not shown in this figure, the relatively unaveraged (M=1) values for $\hat{S}_{yy}$ can be an order of magnitude higher than the ideal values, which are furthermore characterized by a white noise structure across the whole frequency spectrum. These latter characteristics are reflected in this figure for averaging as high as $M/(B/2) = 2$. The results of this figure indicate that the ideal $\hat{S}_{yy}$ would not be detectable at any amount of frequency averaging for low frequency signals with signal-to-instrument noise ratios as high as 10.
- Figure 23 for $\hat{S}_{yy}$ and $S/N_i = 1$ indicates increases in the amplitude of the output auto-spectral density function that are larger by nearly an order of magnitude than those for $S/N_i = 10$ in the previous figure. Although not shown in Fig. 23, the relatively unaveraged (M=1) values for $\hat{S}_{yy}$ can now be about two orders of magnitude higher than the ideal values, which are again characterized by a white noise structure. As in the previous figure, the results in Fig. 23 indicate that $\hat{S}_{yy}$ would not be detectable at any frequency averaging for low frequency signals with signal-to-instrument noise ratios within the threshold of detectability.

4.1.4 Estimated Partial Coherences

Figures 24-26 show the estimated partial coherences for the gradiometer signal channel (Fig. 2) after subtracting out the predictions from the gradiometer noise channel (Eq. 106). The estimated partial coherences are shown as a function of frequency averaging and the signal-to-instrument noise ratio. The ideal value of the partial coherence for negligible instrument noise is unity (Eq. 114). This set of figures also includes

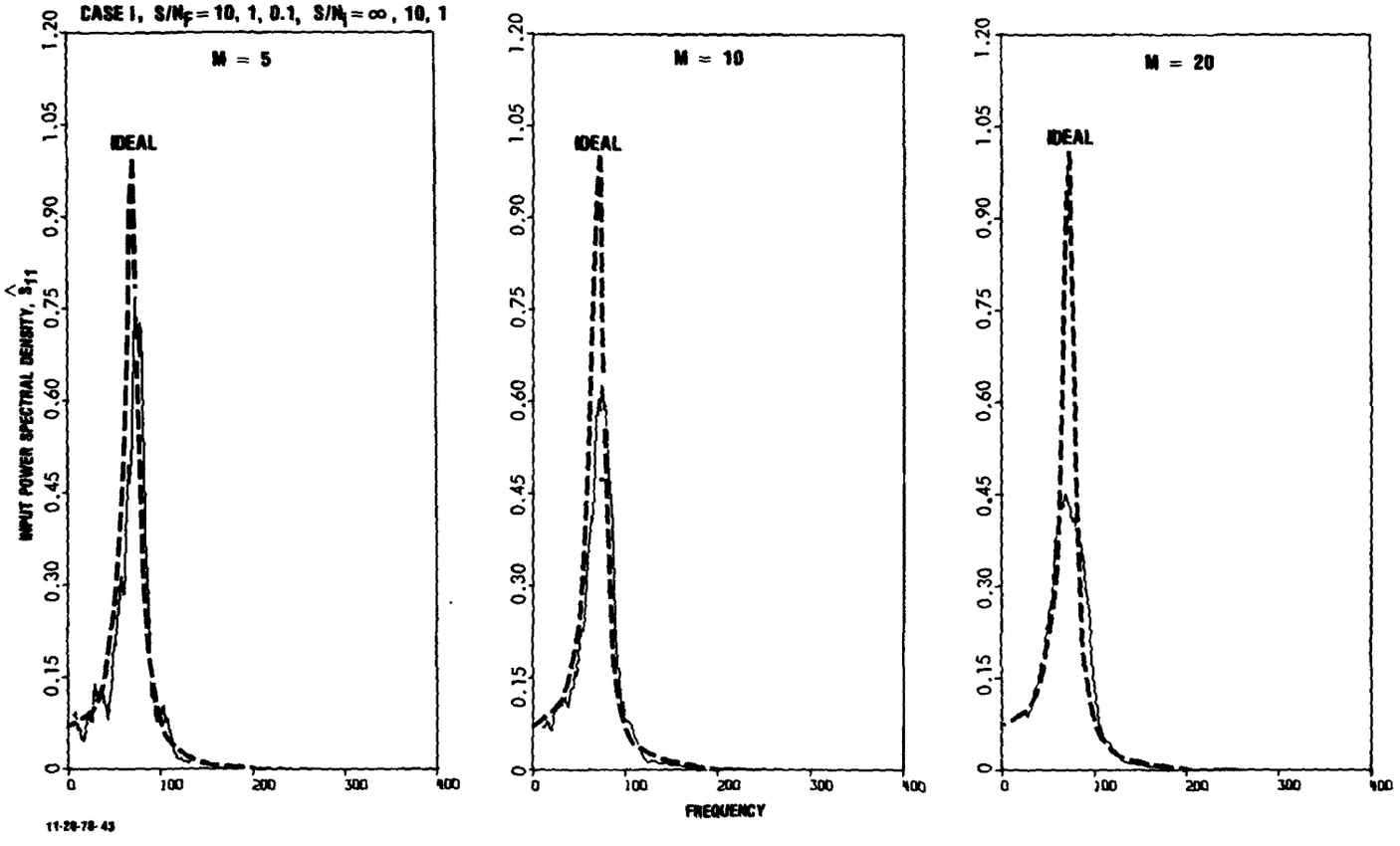

FIGURE 19. Comparison of ideal and estimator spectra for subsidiary "signal" channel for low-frequency filters with $L_{g_2}/L_{g_1} = 4.4$.

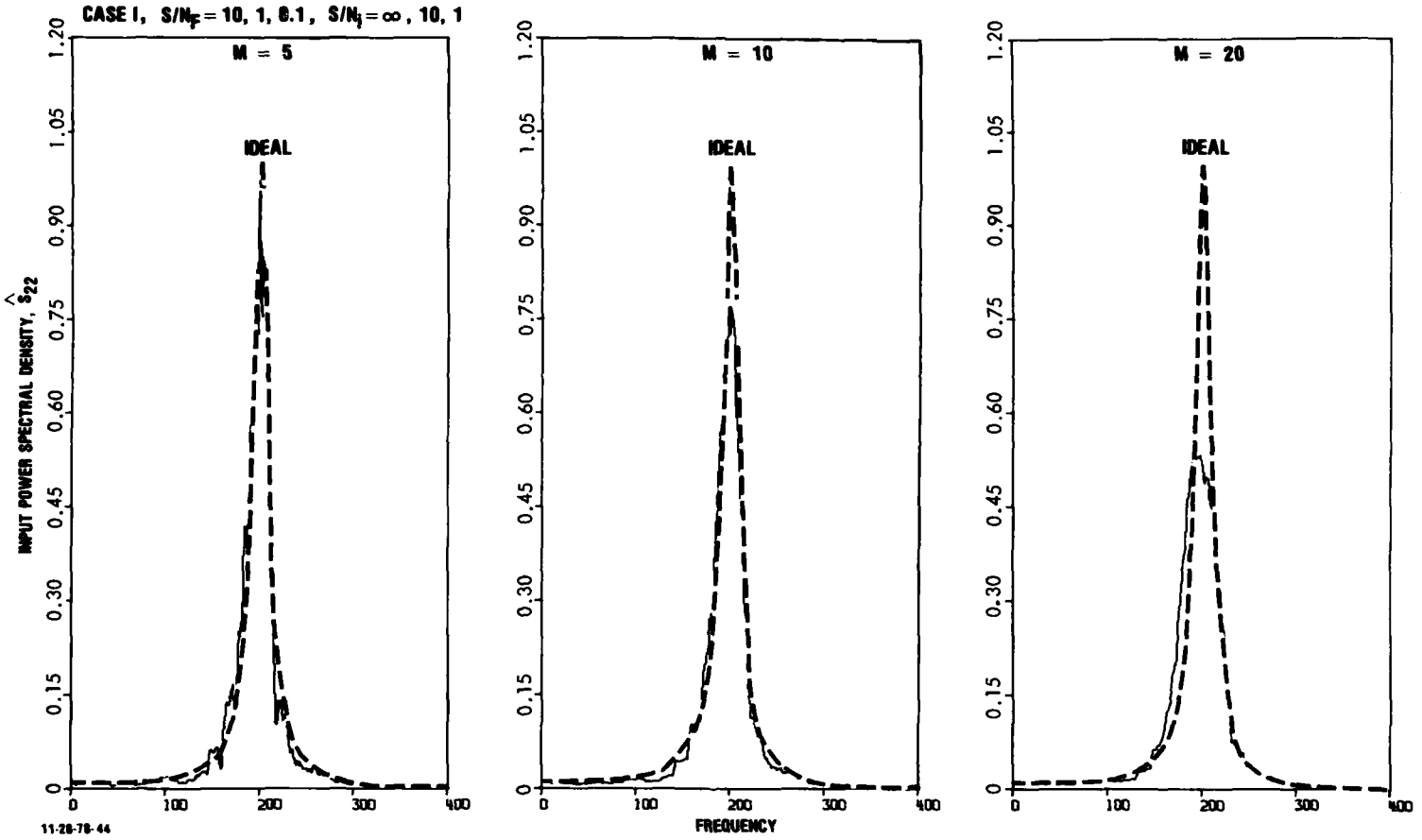

FIGURE 20. Comparison of ideal and estimator spectra for subsidiary "noise" channel for low-frequency filters with $Lg_2/Lg_1 = 4.4$.

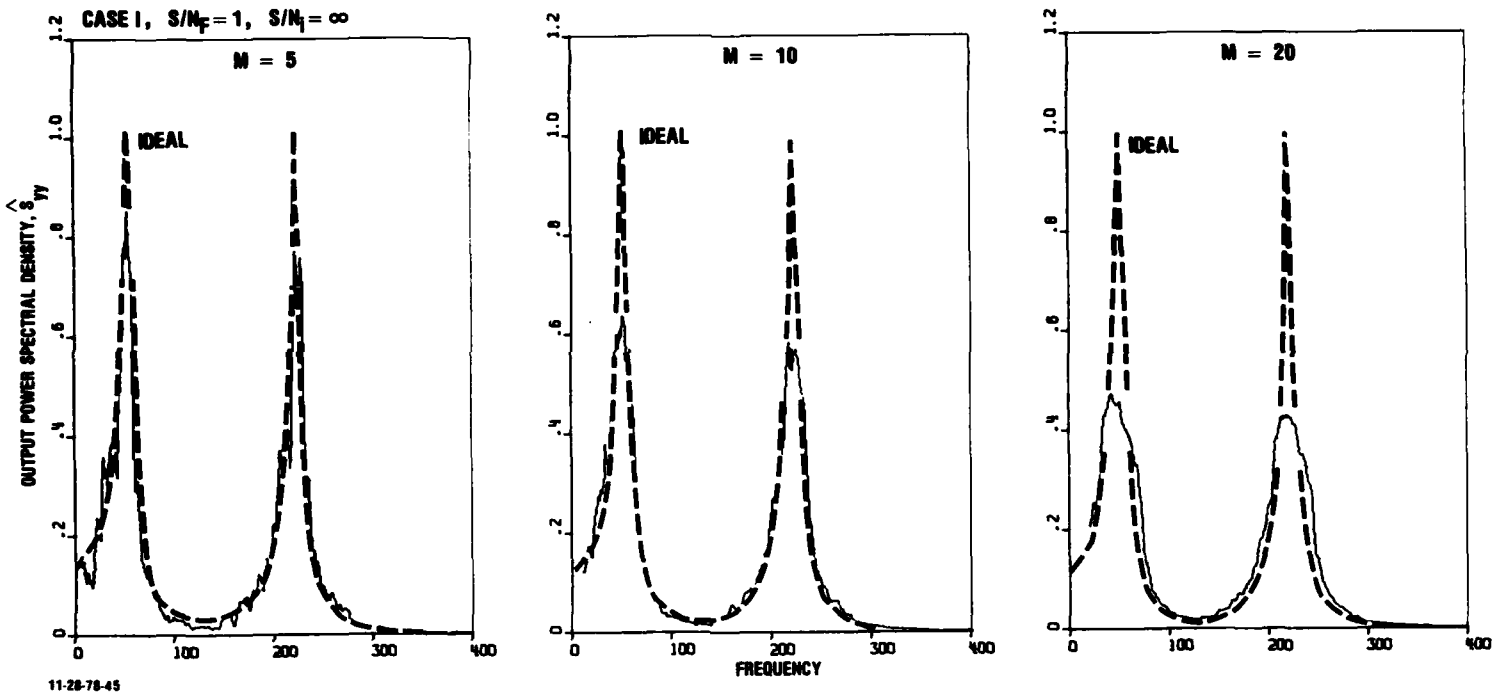

FIGURE 21. Comparison of ideal and estimator spectra for gradiometer output for low-frequency filters with $Lg_2/Lg_1 = 4.4$ for $S/N_i = \infty$.

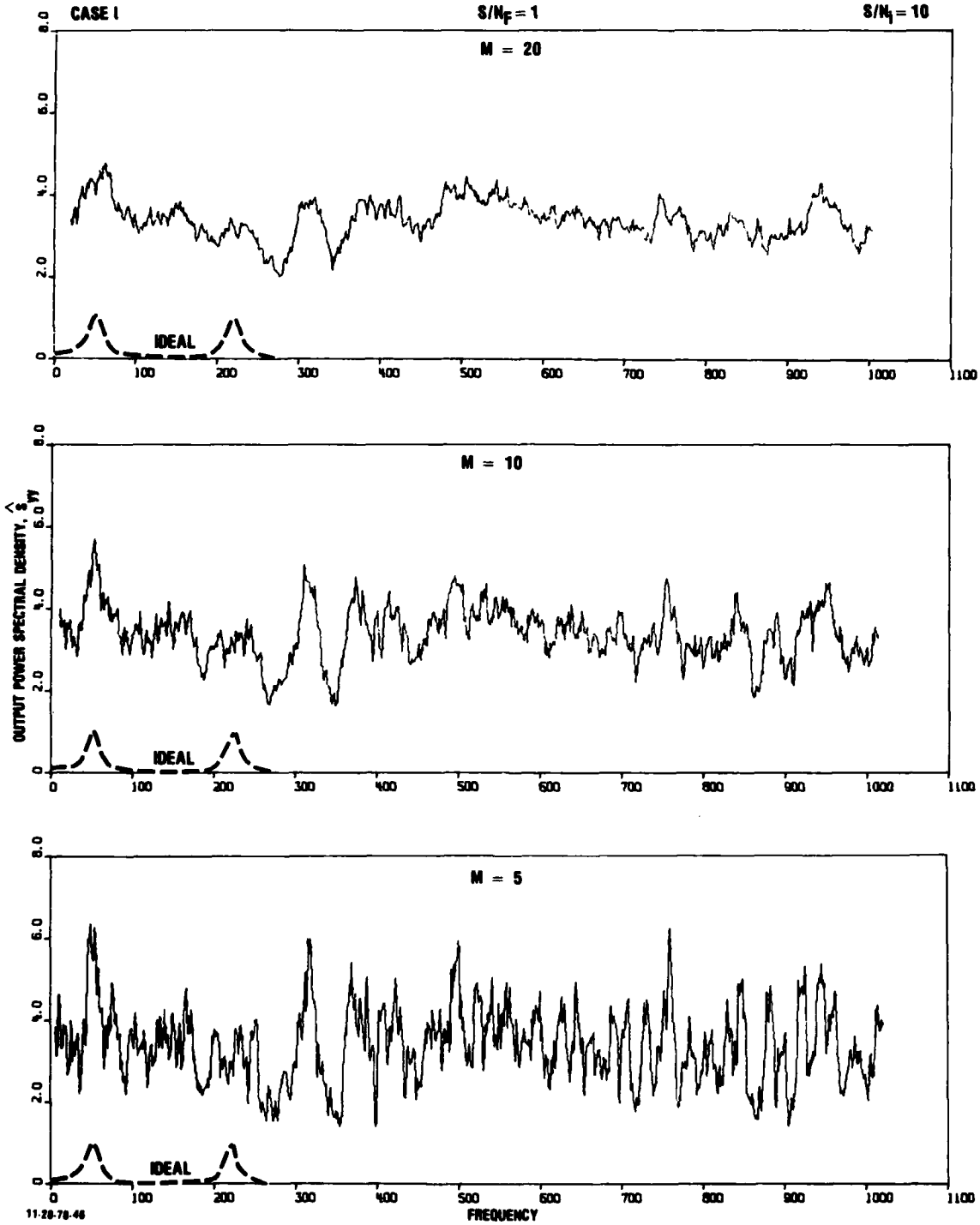

FIGURE 22. Comparison of ideal and estimator spectra for gradiometer output for low-frequency filters with $Lg_2/Lg_1 = 4.4$ for $S/N_i = 10$.

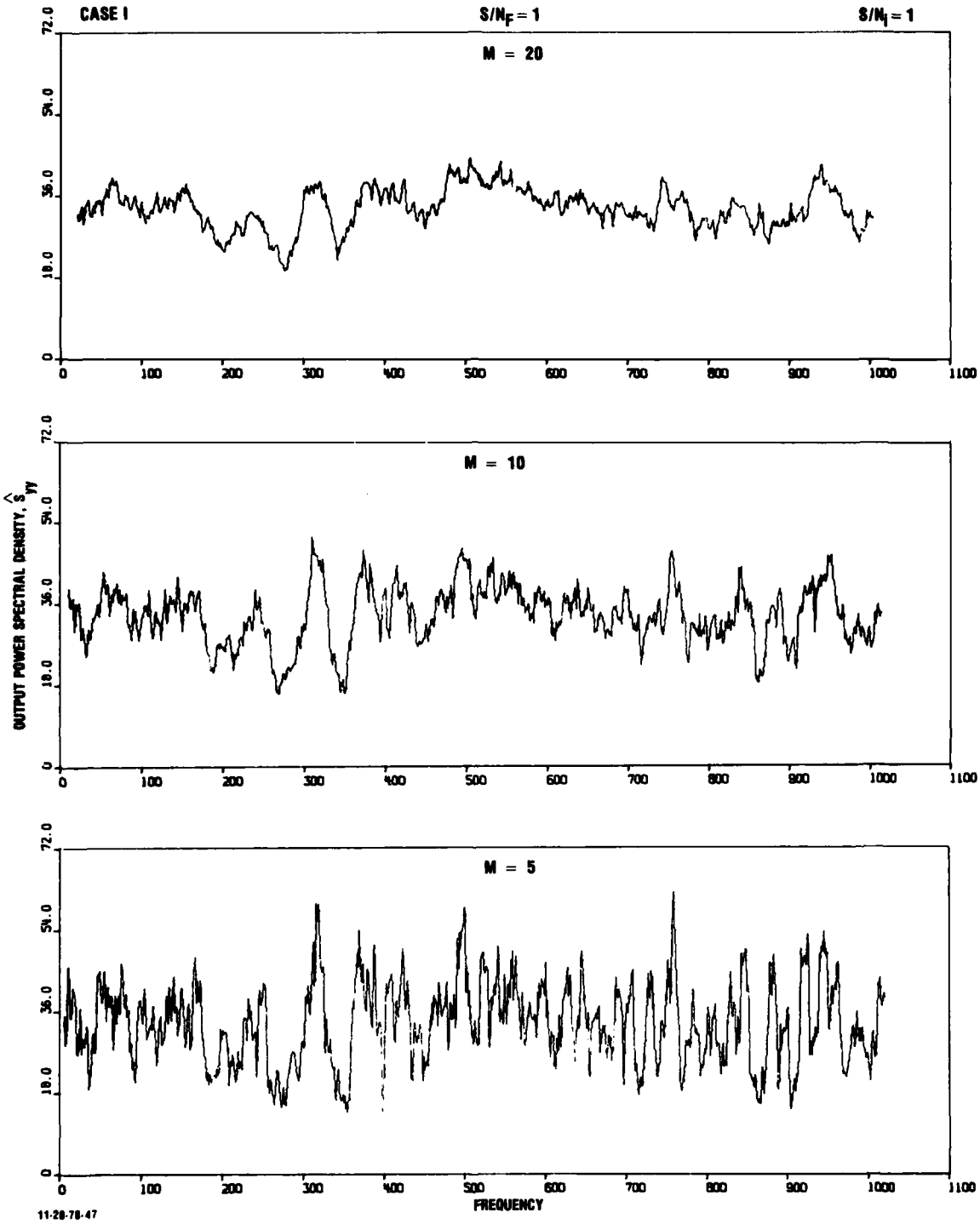

FIGURE 23. Estimator for gradiometer output spectra for low-frequency filters with $Lg_2/Lg_1 = 4.4$ for $S/N_i = 1$. Note that corresponding ideal spectra (Figs. 21, 22) would be very small in the much larger scales for $S/N_i = 1$.

Fig. 27 for the input coherence (Eq. 100), which has an ideal value of zero for uncorrelated inputs. These figures show the following:

- Figure 24 for the partial coherence, $\gamma^2_{1y.2}$, and $S/N_i = \infty$ indicates a sharp deviation from unity near the L_{g_1} frequency, a deviation that is aggravated with increased frequency averaging given by M/(B/2). Hence, the partial coherence would be a misleading indicator for low frequency signals, since it shows significant deviations from unity even for M/(B/2) ≈ 5/10 or 0.5. It should be noted that the numerical noise near L_{g_2} in the gain factor $|\hat{H}_1|$, as indicated in Fig. 9 is reflected in the partial coherence by (a) even sharper deviations from unity at L_{g_2} than at L_{g_1} and (b) deviations that are independent of M.

- Figure 25 for the partial coherence and $S/N_i = 10$ exhibits the expected impact of instrument noise, as indicated by its drastic deviations from unity across the frequency spectrum; a deviation that becomes worse with increased averaging given by M/(B/2). Although not shown in the figure, the partial coherence for relatively unaveraged (M=1) values exhibits a white noise structure between zero and unity across the frequency spectrum.

- Figure 26 for the partial coherence and $S/N_i = 1$ indicates results similar to those in the previous figure for $S/N_i = 10$. The results of Figs. 25 and 26 suggest that even very high signal-to-instrument noise ratios ($S/N_i > 10$) may cause significant deviations of the partial coherence from unity.

- Figure 27 for the input coherence γ^2_{12} for any signal-to-noise ratio shows that the conditions $\gamma^2_{12} \to 0$ for uncorrelated inputs requires frequency averaging given by M/(B/2) ≈ 2. Although not shown in the figure, the relatively unaveraged (M=1) values for γ^2_{12} show peak

values near unity, but with the white noise structures shown in Fig. 27. Although averaging with $M/(B/2) > 2$ might be desirable to reduce the input coherence for the uncorrelated stationary input series, such extreme averaging would deteriorate the biasing of the signal $\hat{S}_{\xi_1\xi_1}$ as indicated in Figs. 7 and 8.

4.1.5 Overall Results for Low-Frequency Gradiometer with $L_{g_2}/L_{g_1} > 1$

The overall results for the reconstruction of an imbedded *low*-frequency signal in a gradiometer channel characterized by $L_{g_2}/L_{g_1} = 4.4$ indicate the following

- For the ideal condition of no instrument noise, the algorithm introduces significant numerical noise in the estimates of the gradiometer transfer functions at the frequency L_{g_2} for the signal channel and at L_{g_1} for the gradiometer "noise" channel (Figs. 9, 14).
- For a signal-to-instrument noise ratio of 10, the required number of frequencies in the averaging of the gradiometer signal spectrum ($\hat{S}_{\xi_1\xi_1}$) and input coherence ($\gamma^2_{1,2}$) is between once and twice the bandwidth of the specified spectra, i.e., $1 < M/(B/2) < 2$ (Figs. 7, 27).
- For a signal-to-instrument noise ratio of 10, the estimates of the gradiometer transfer functions become undetectable due to both the algorithm numerical noise (Figs. 9, 14) as well as the white noise at frequencies higher than L_{g_2} (Figs. 11, 16).
- For a signal-to-instrument noise ratio of 10, the ideal spectrum of the gradiometer output $\hat{S}_{yy}$ is undetectable regardless of the magnitude of the $M/(B/2)$ parameter (Fig. 22).
- The partial coherence for the gradiometer signal channel is not a useful indicator of the fidelity of gradiometer

signal reconstruction because it has large deviations from unity even for the ideal conditions of no instrument noise and regardless of the magnitude of the M/(B/2) frequency averaging parameter (Fig. 24).

- For signal-to-instrument noise within the range of detectability (i.e., $S/N_1 = 1$), the ideal gradiometer signal spectrum, $S_{g_1 g_1}$, (Fig. 2) would be undetectable because of the presence of white noise comparable to the magnitude of the estimated signal spectrum $\hat{S}_{\xi_1 \xi_1}$ (Fig. 8).
- The white noise structure of the estimated gradiometer signal, $\hat{S}_{\xi_1 \xi_1}$, and estimator for the gradiometer output, $\hat{S}_{yy}$, is consistent with the corresponding appreciable white noise of the estimated gain factors $|\hat{H}_1|$ and $|\hat{H}_2|$ of the gradiometer transfer functions (Figs. 10, 15).

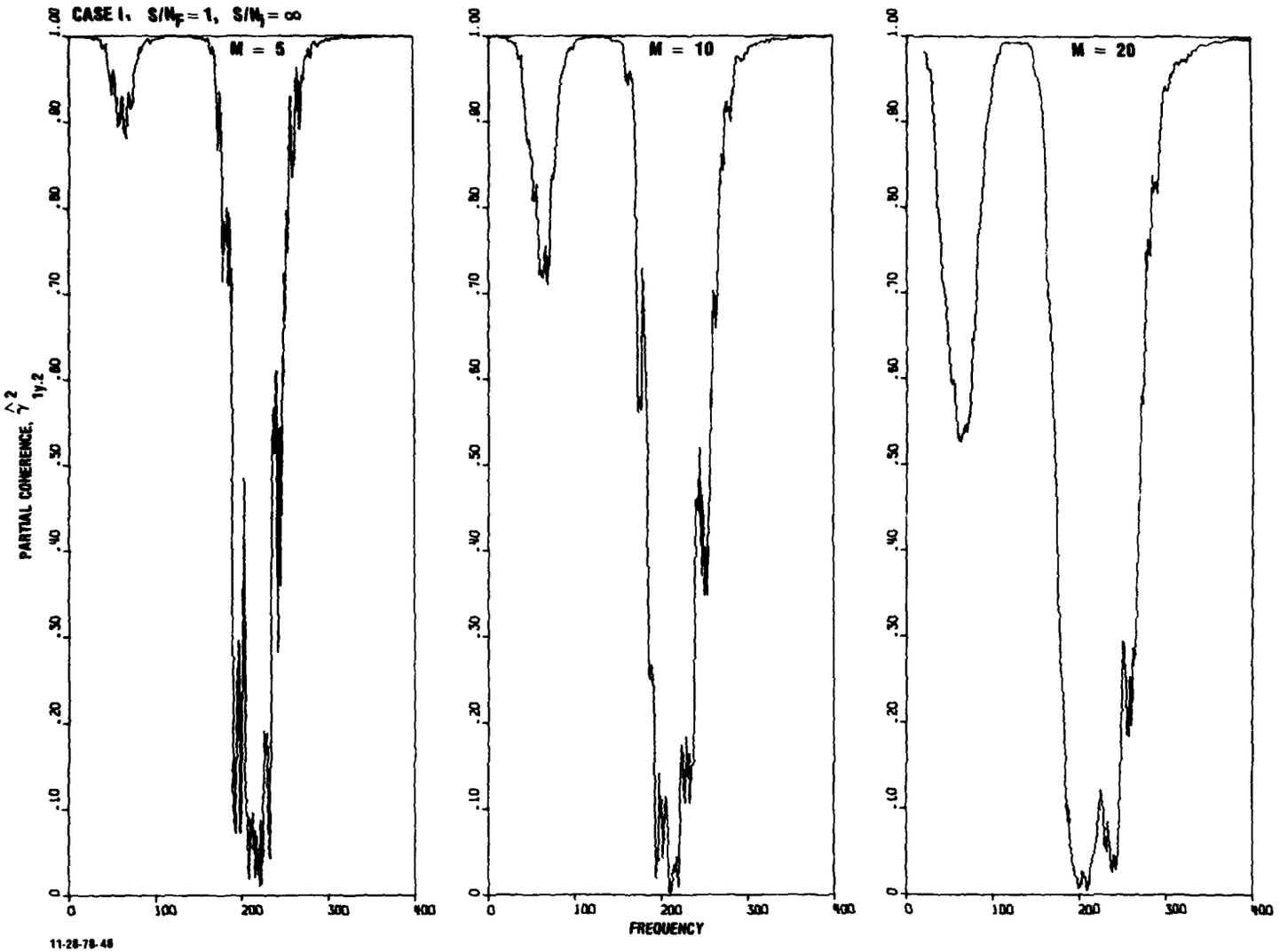

FIGURE 24. Estimated partial coherence for gradiometer signal channel for low-frequency filters with $Lg_2/Lg_1 = 4.4$ for $S/N_i = \infty$.

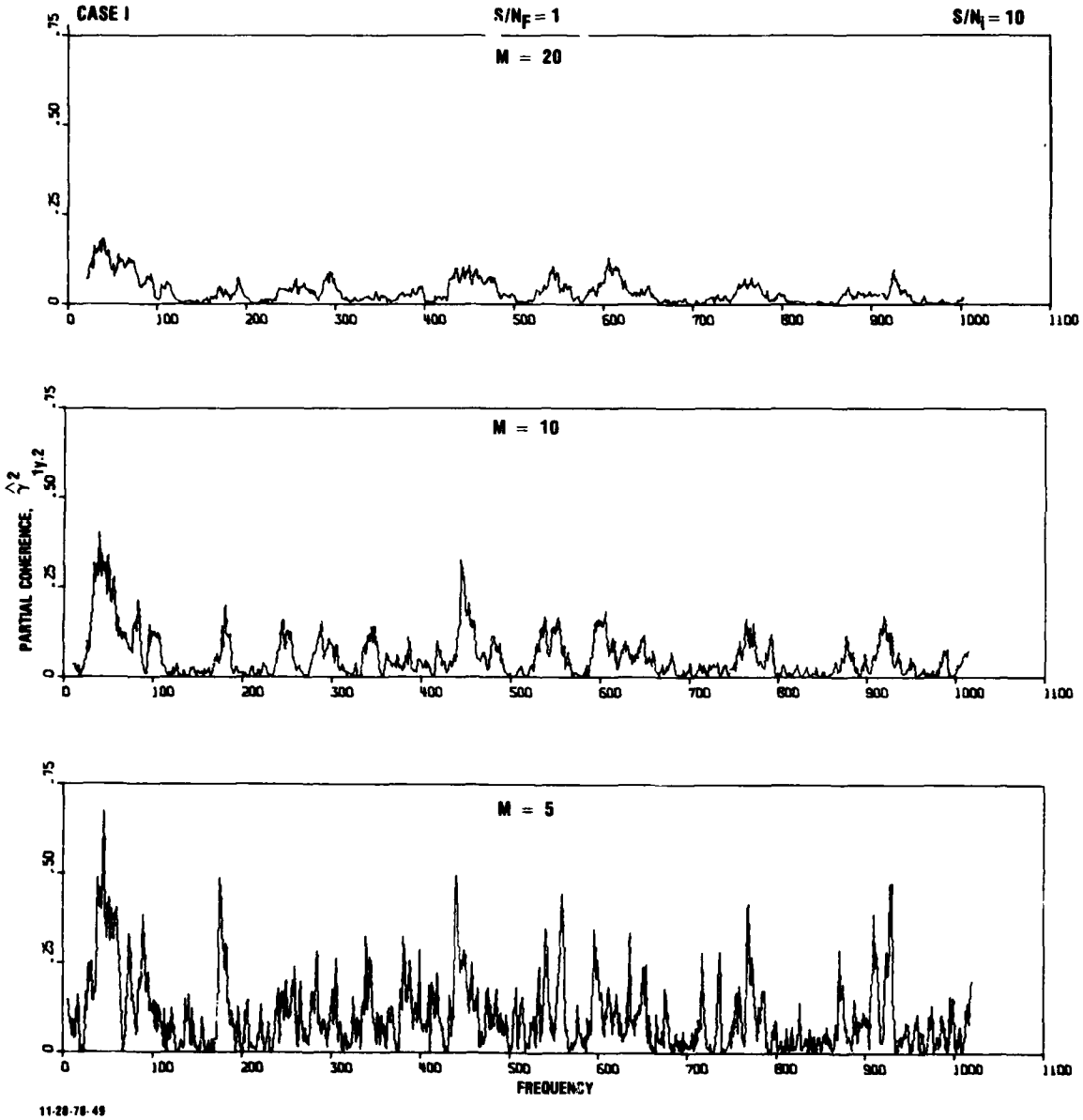

FIGURE 25. Estimated partial coherence for gradiometer signal channel for low-frequency filters with $Lg_2/Lg_1 = 4.4$ for $S/N_i = 10$.

AD-A079 329 INSTITUTE FOR DEFENSE ANALYSES ARLINGTON VA SCIENCE A--ETC F/G 9/2
PRELIMINARY EVALUATION OF AN ALGORITHM FOR ANALYSIS OF STATIONA--ETC(U)
JUL 79 H HIDALGO, W WASYLKIWSKYJ MDA903-79-C-0202
UNCLASSIFIED IDA-P-1388 IDA/HQ-79-21079 NL

2 OF 2
AD
A079329

END
DATE
FILMED
2-80
DDC

Shoot

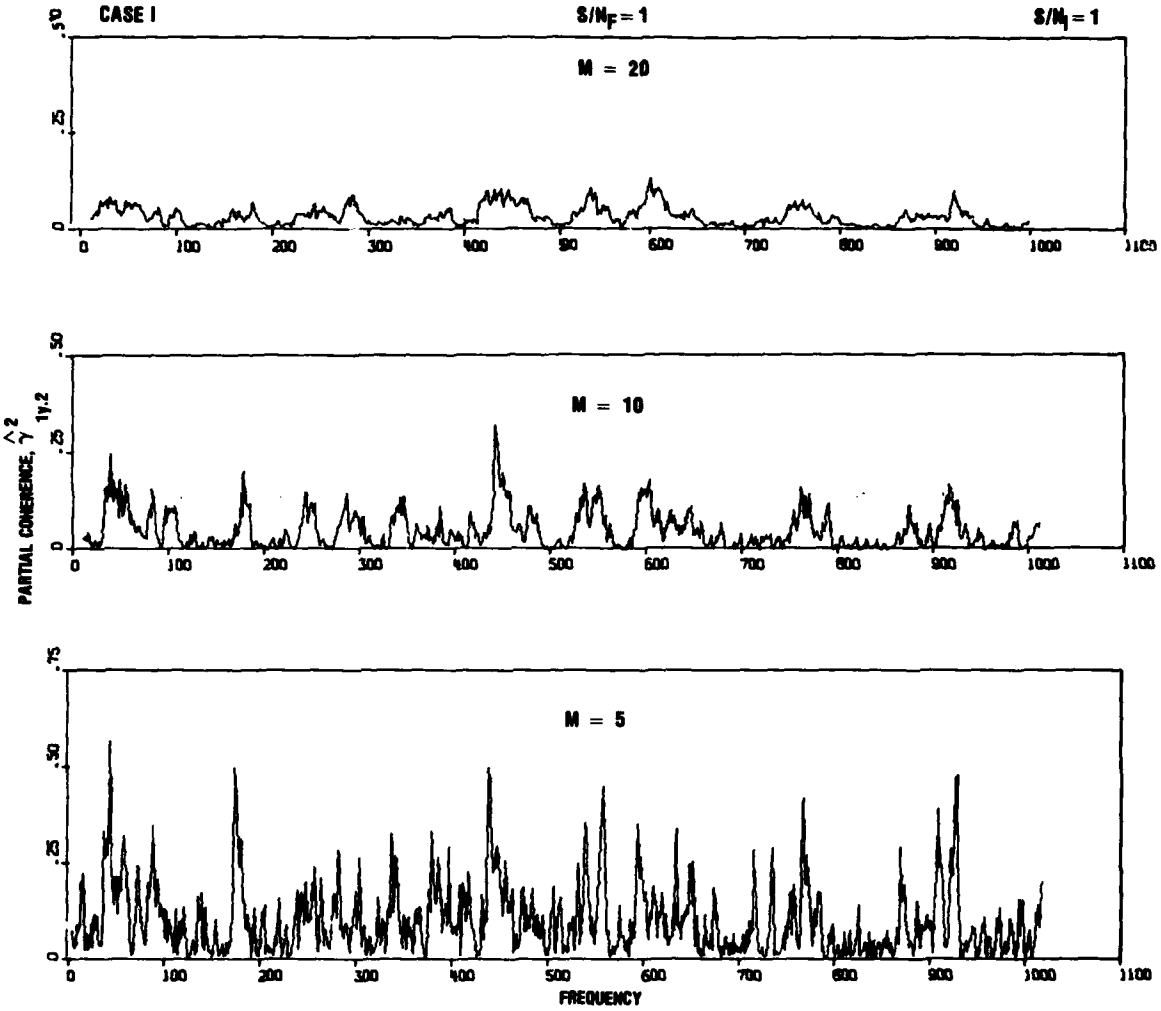

FIGURE 26. Estimated partial coherence for gradiometer signal channel for low-frequency filters with $Lg_2/Lg_1 = 4.4$ for $S/N_i = 1$.

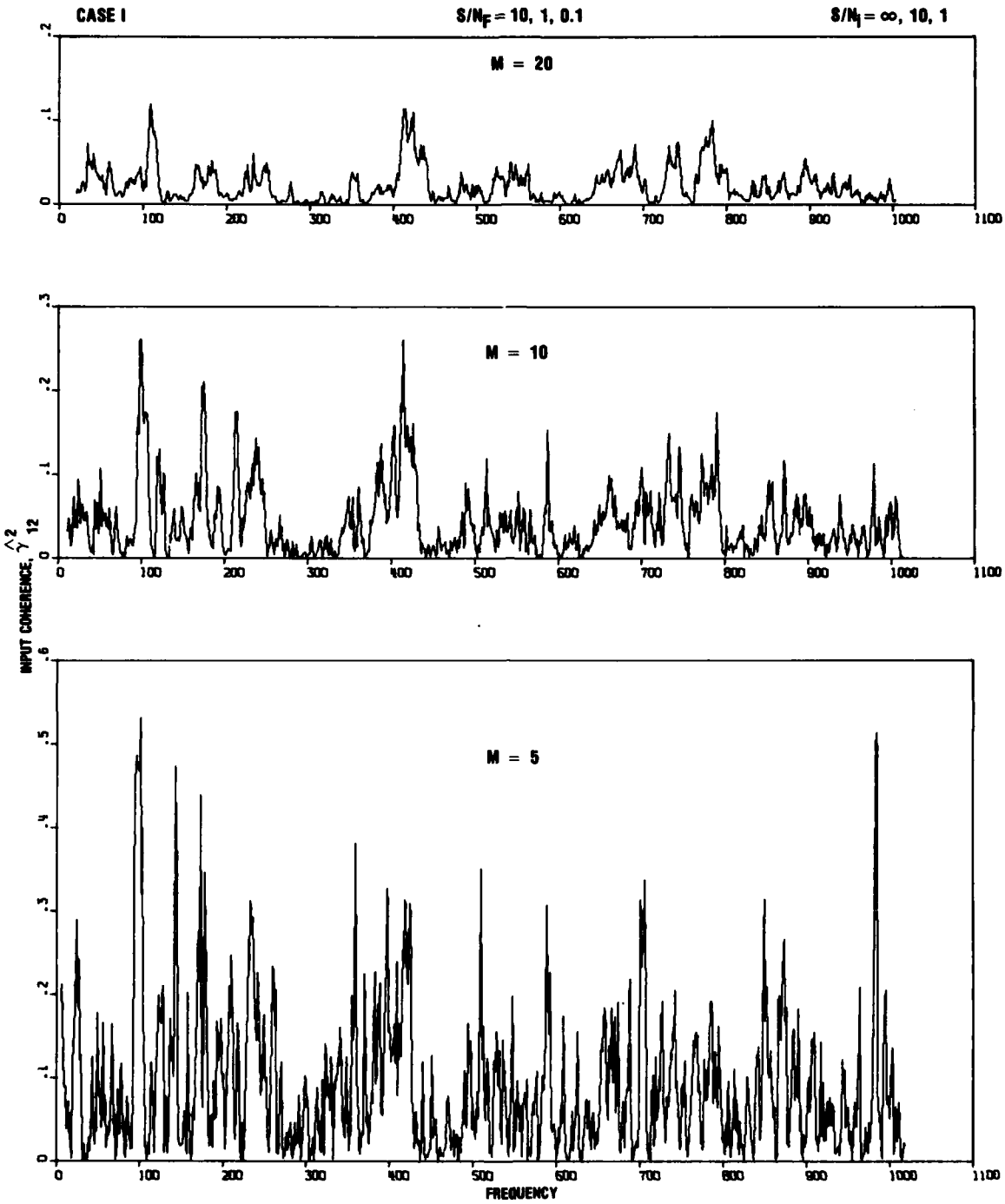

11-28-78-51

FIGURE 27. Estimated input coherence for two subsidiary current meter channels for low-frequency filters with Lg_2/Lg_1 = 4.4.

4.2 LOW-FREQUENCY GRADIOMETER WITH $L_{g_2}/L_{g_1} \simeq 1$

Figures 28-49 show in the subsequent subsections the results of the numerical simulations for Case II in Fig. 5, which are characterized by $L_{g_2} = 60$, $L_{g_1} = 50$, $L_{g_2}/L_{g_1} = 1.2$ and $B/2 = 20$.

4.2.1 Estimated Gradiometer Signal Spectrum

Figures 28-30 show comparisons of ideal and estimated spectra for the gradiometer signal channel as a function of signal-to-instrument noise ratio for $S/N_i = \infty$, 10, 1 respectively. These figures indicate the following

- Figure 28 compares ideal and estimated gradiometer signal spectra for the ideal conditions of $S/N_i = \infty$ and $M/(B/2)$ values that are as high as the bandwidth of the specified spectrum. These results are similar to the corresponding ones in Fig. 6 for the previous case with $L_{g_2}/L_{g_1} = 4.4$ and a bandwidth half the present value; i.e., the estimated spectrum is underestimated with about the same bias for $M/(B/2) = 0.5$ in both cases. Figure 28 shows then that an unbiased estimate of the gradiometer signal spectra required $M/(B/2) \simeq 0.25$ for this case.

- Figure 29 compares ideal and estimated gradiometer signal spectra for $S/N_i = 10$. As in the corresponding previous case (Fig. 7), the increased noise requires a higher $M/(B/2)$ parameter relative to that for $S/N_i = \infty$ so as to obtain an unbiased estimated signal spectrum. However, the results in Figs. 7 and 29 show that a lower L_{g_2}/L_{g_1} ratio tends to decrease the $M/(B/2)$ parameter for an unbiased estimator.

- Figure 30 compares ideal and estimated gradiometer signal spectra for $S/N_i = 1$. These results indicate no relative effect of the L_{g_2}/L_{g_1} ratio, i.e., Fig. 8 for $L_{g_2}/L_{g_1} = 4.4$ and Fig. 30 for $L_{g_2}/L_{g_1} = 1.2$ show the same results.

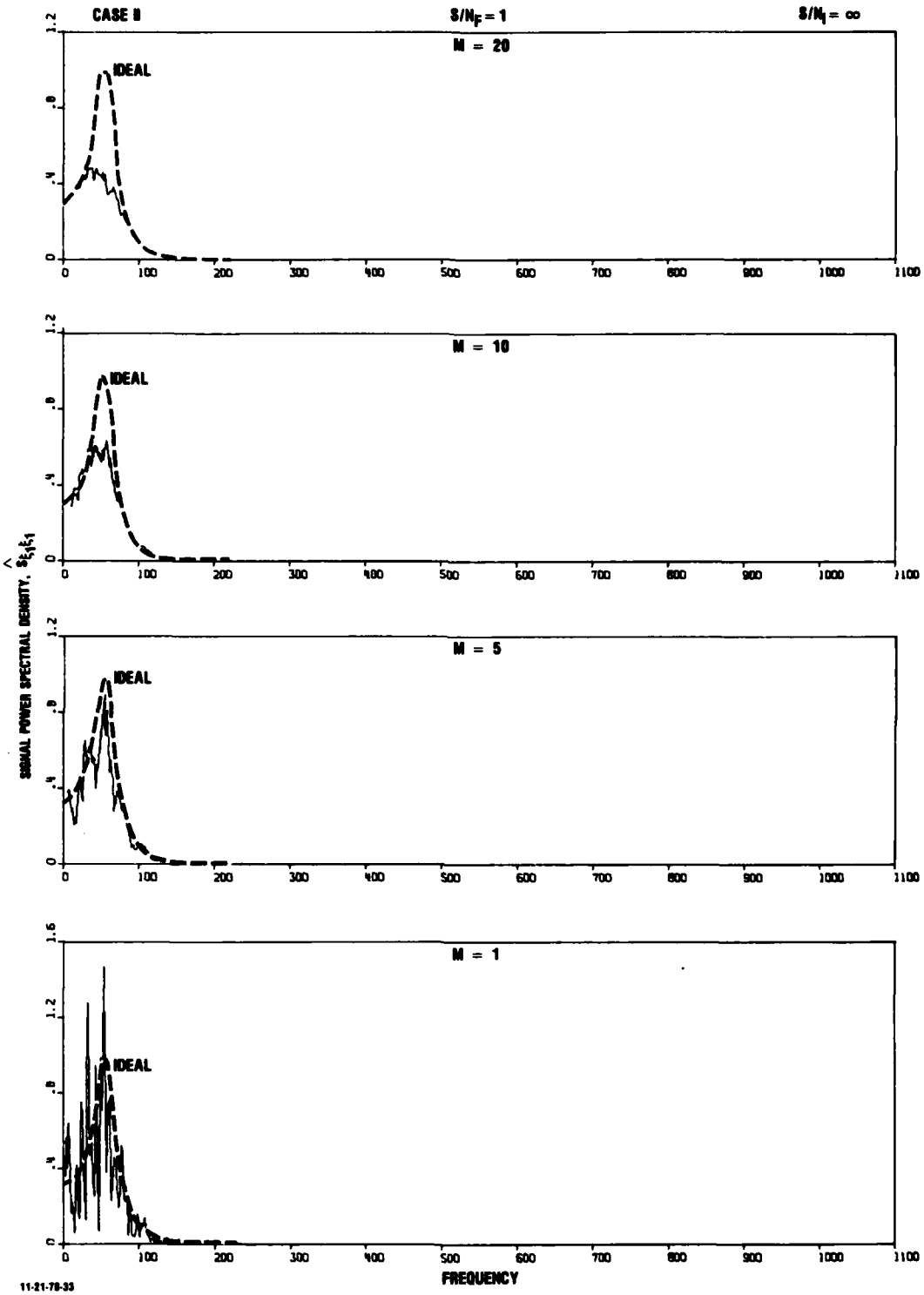

FIGURE 28. Comparison of ideal and reconstructed signal spectra for low-frequency filters with $Lg_2/Lg_1 = 1.2$ for $S/N_i = \infty$.

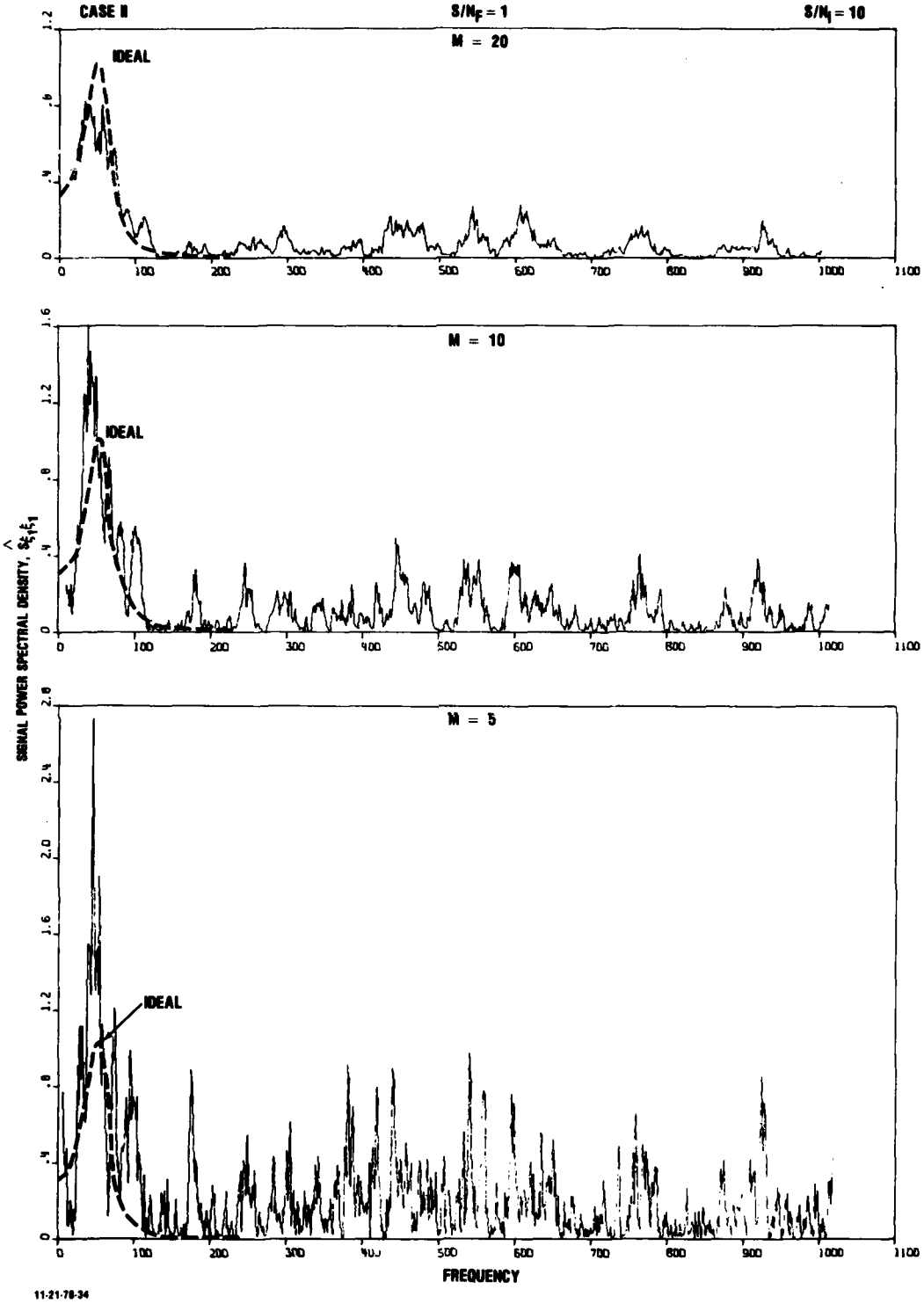

FIGURE 29. Comparison of ideal and reconstructed signal spectra for low-frequency filters with $Lg_2/Lg_1 = 1.2$ for $S/N_i = 10$.

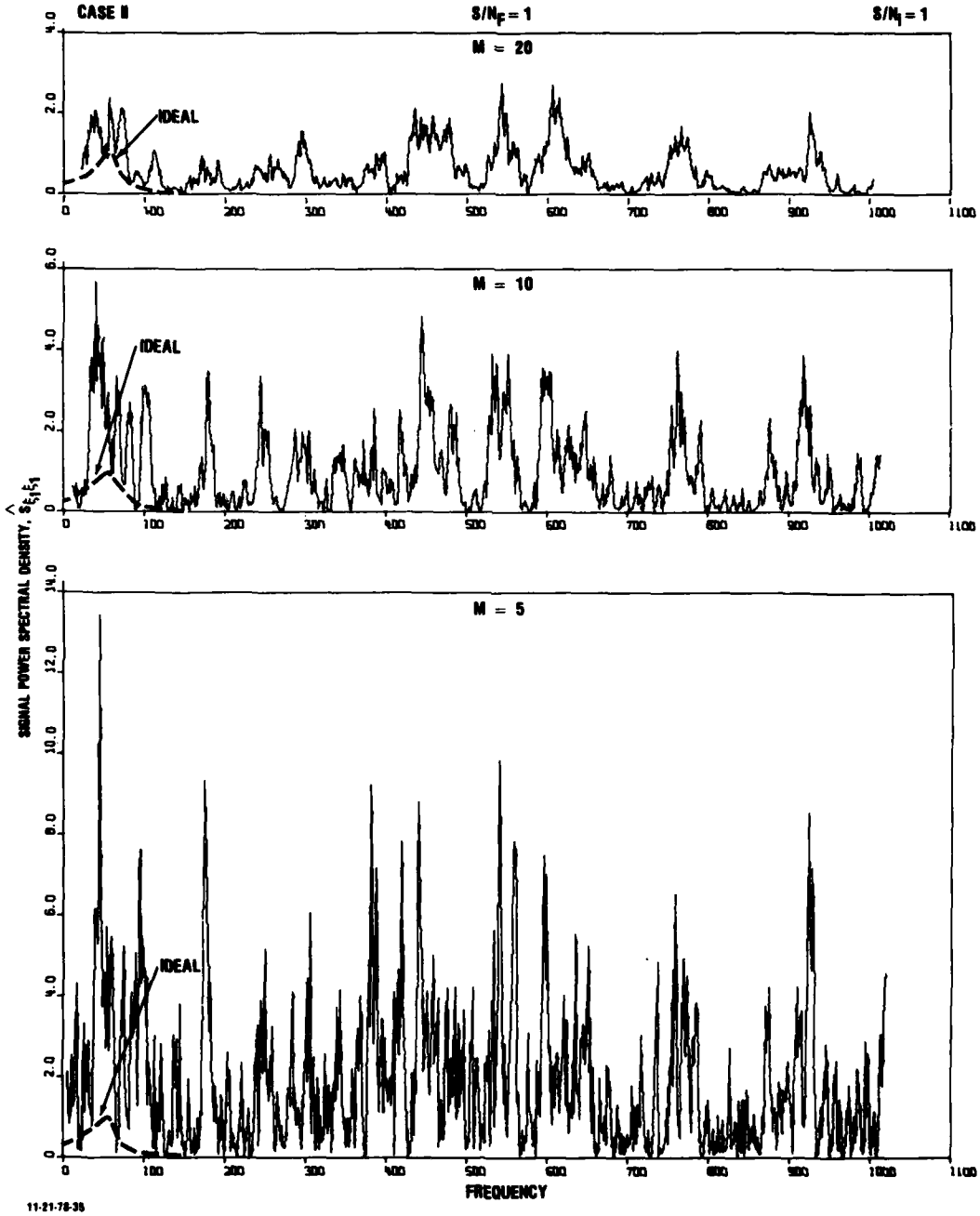

FIGURE 30. Comparison of ideal and reconstructed signal spectra for low-frequency filters with $Lg_2/Lg_1 = 1.2$ for $S/N_i = 1$.

4.2.2 Estimated Gain Factors

Figures 31-35 and 36-40 show the estimated gain factors for the gradiometer signal and "noise" channels, respectively, as a function of S/N_i and $M/(B/2)$. These figures indicate the following:

- Figure 31 compares ideal and estimated gain factors for the gradiometer signal channel for $S/N_i = \infty$. The outstanding result in this figure is the disappearance of the "numerical noise", which was present at L_{g_2} for the corresponding $L_{g_2}/L_{g_1} = 4.4$ case (Fig. 9). This result will become more evident from subsequent considerations of the respective partial coherences.

- Figure 32 shows estimated gain factors for the gradiometer signal channel for $S/N_i = 10$. By comparing the vertical scales of Figs. 32 and 10 of the previous case for the same S/N_i and $M/(B/2)$, it is apparent that the condition $L_{g_2}/L_{g_1} = 1.2$ in Fig. 32 has decreased by a factor of about 1/2 the white noise in the estimated gain factor for $L_{g_2}/L_{g_1} = 4.4$ in Fig. 10. These results explain the relatively lower amount of frequency averaging required to estimate $S_{g_1 g_1}$ for $S/N_i = 10$ and $L_{g_2}/L_{g_1} = 1.2$. Figure 33 compares ideal and estimated gain factors for the gradiometer signal channel for $S/N_i = 10$. As in the corresponding cas for $L_{g_2}/L_{g_1} = 4.4$ (Fig. 11) the white noise at higher frequencies in Fig. 33 would prevent detection of the gain factor for frequency averaging as high as $M/(B/2) = 1$.

- Figure 34 shows estimated gain factors for the gradiometer signal channel for $S/N_i = 1$. By comparing the vertical scales of Figs. 34 and 12 of the previous case for the same S/N_i and $M/(B/2)$, it is seen that the condition $L_{g_2}/L_{g_1} = 1.2$ in Fig. 34 has decreased by a factor of about 1/3 the noise in the estimated gain factors

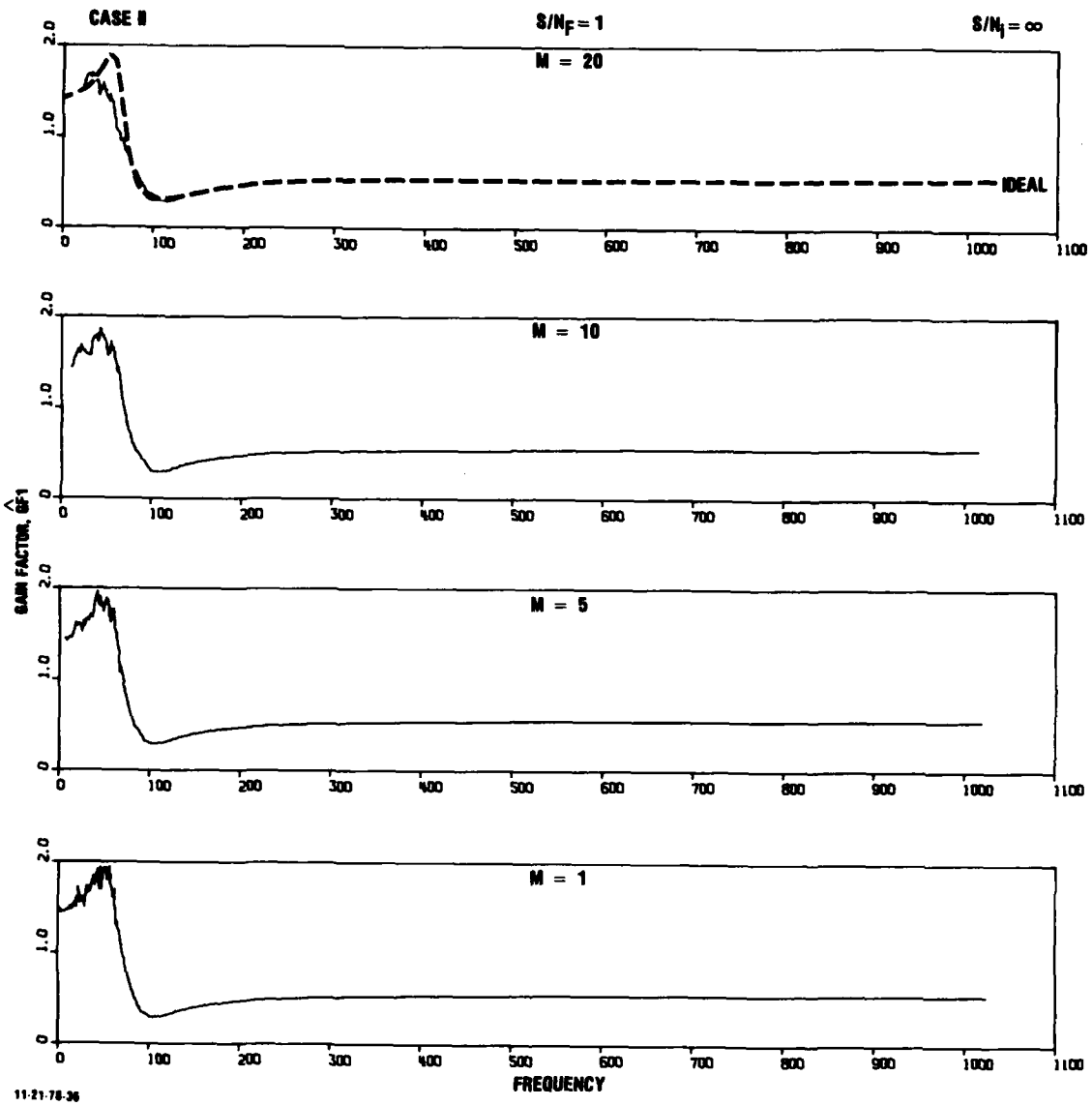

FIGURE 31. Comparison of ideal and estimated gain factors for gradiometer signal channel for low-frequency filters with $Lg_2/Lg_1 = 1.2$ for $S/N_1 = \infty$.

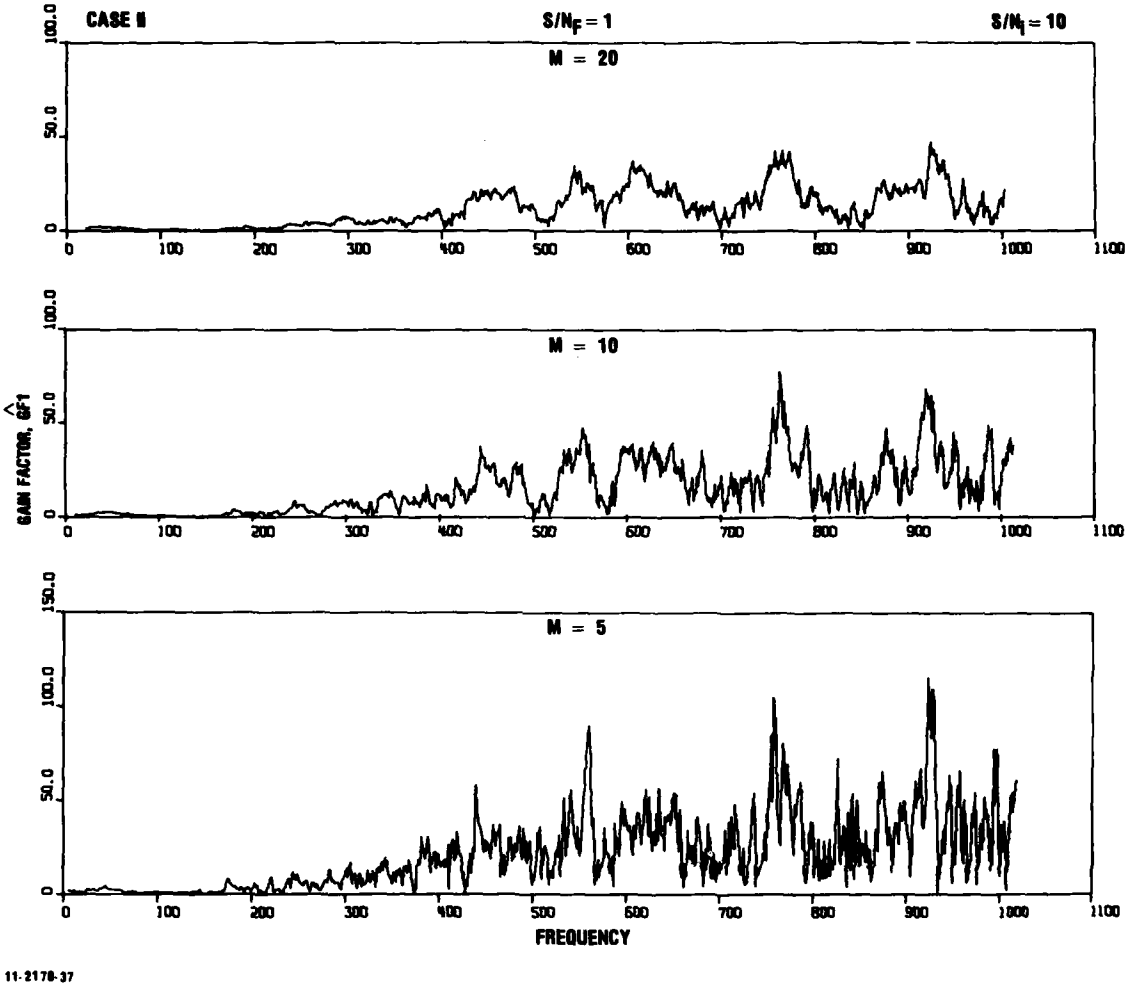

FIGURE 32. Estimated gain factor for gradiometer signal channel for low-frequency filters with $Lg_2/Lg_1 = 1.2$ for $S/N_i = 10$.

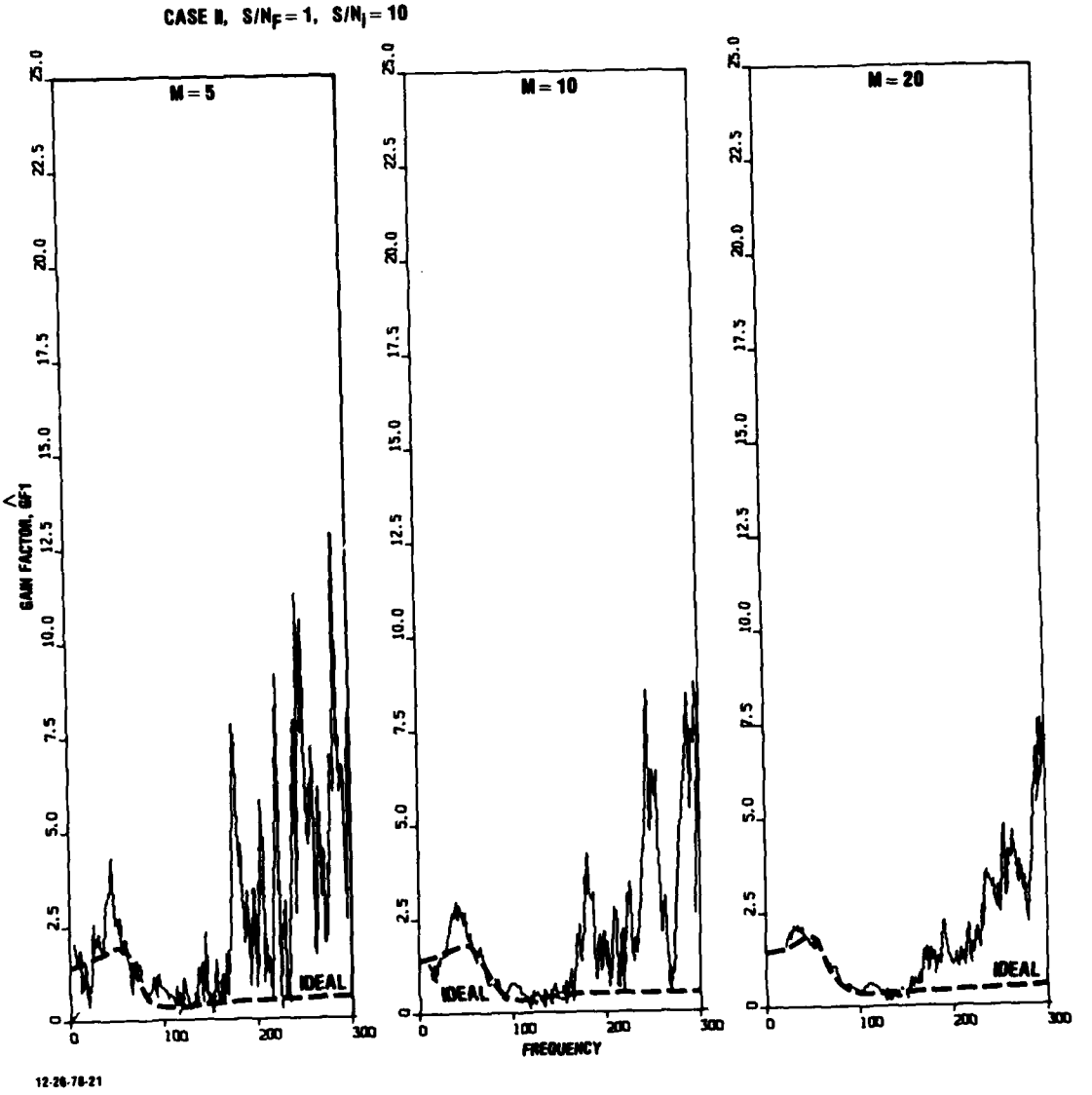

FIGURE 33. Comparison of ideal and estimated gain factors for gradiometer signal channel for low-frequency filters with Lg_2/Lg_1 = 1.2 for S/N_i = 10.

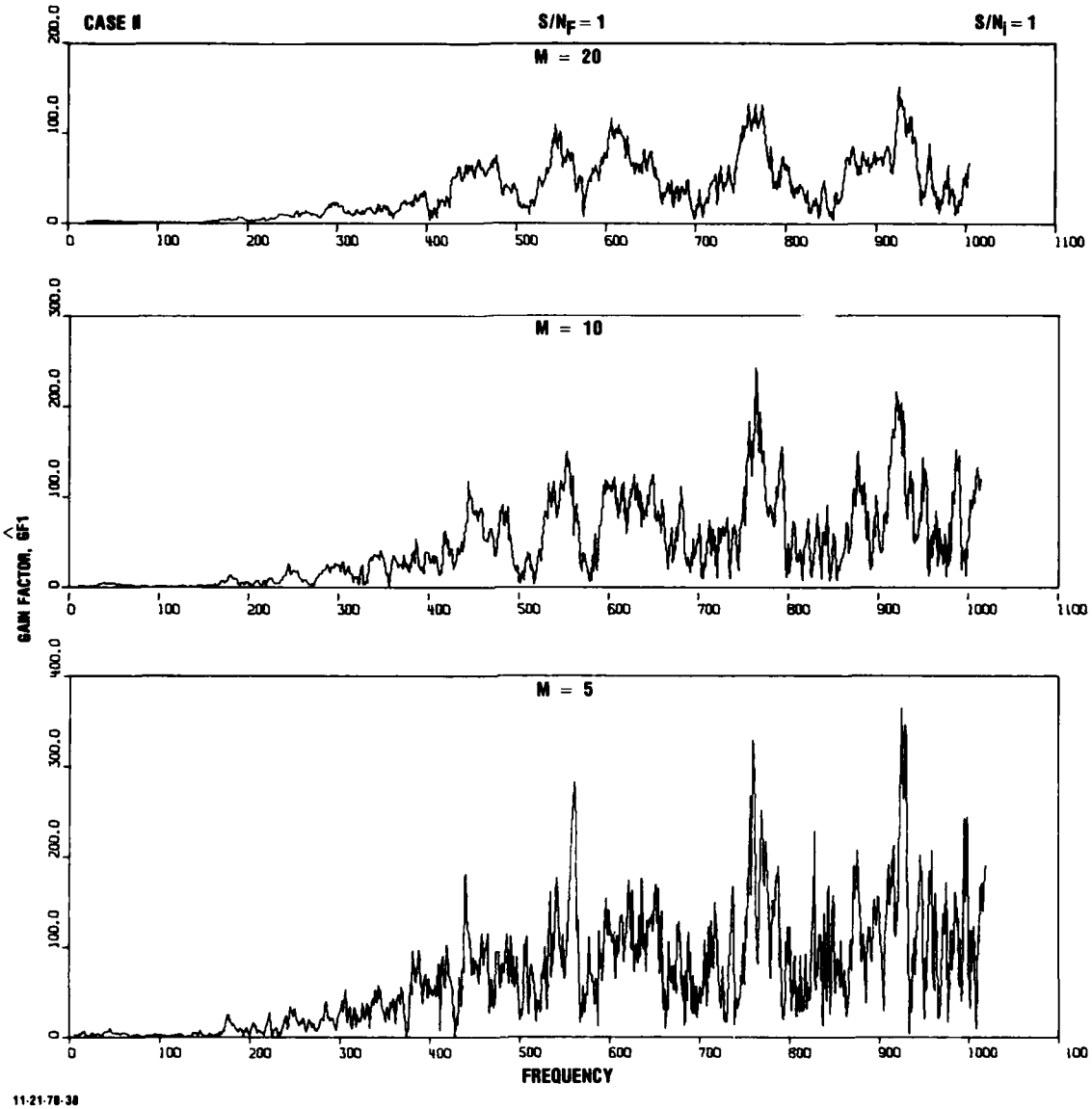

FIGURE 34. Estimated gain factor for gradiometer signal channel for low-frequency filters with $Lg_2/Lg_1 = 1.2$ for $S/N_i = 1$.

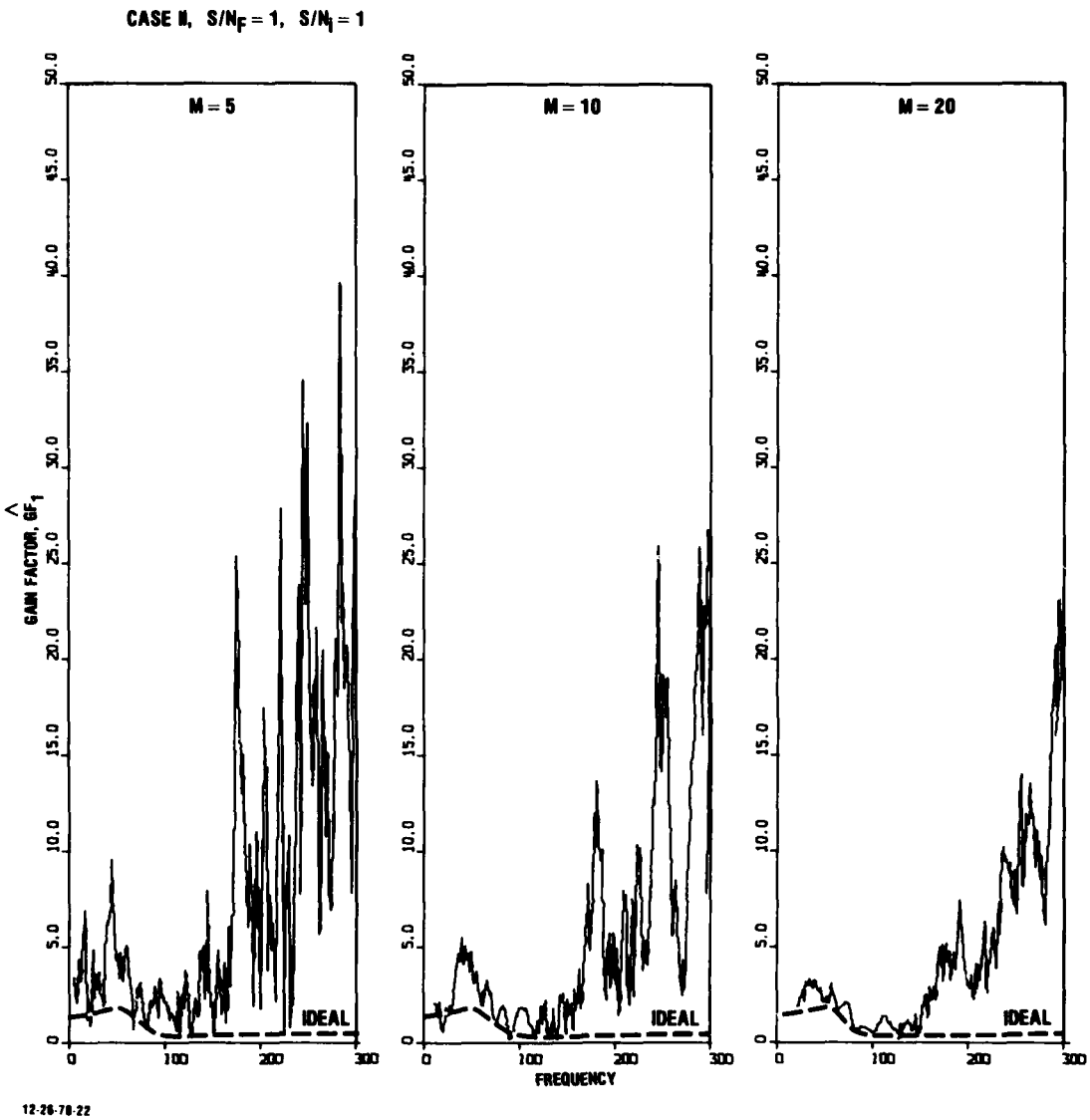

FIGURE 35. Comparison of ideal and estimated gain factors for gradiometer noise channel for low-frequency filters with Lg_2/Lg_1 = 1.2 for S/N_i = 1.

for $L_{g_2}/L_{g_1} = 4.4$. Figure 35 compares ideal and estimated $|\hat{H}_1|$ gain factors for $S/N_i = 1$ and $L_{g_2}/L_{g_1} = 1.2$. Figure 35 shows that the ideal $|\hat{H}_1|$ gain factor is not detectable due to the more than comparable white noise background.

- Figure 36 compares ideal and estimated gain factors for the gradiometer "noise" channel and $S/N_i = \infty$. Again, the outstanding results here is the absence of the numerical noise, which was present at L_{g_1}, for the case of $L_{g_2}/L_{g_1} \simeq 4.4$ (Fig. 14).

- Figure 37 shows ideal and estimated gain factors for the gradiometer "noise" channel and $S/N_i = 10$. These results for $L_{g_2}/L_{g_1} = 1.2$ are similar to the corresponding ones for $L_{g_2}/L_{g_1} = 4.4$ (Fig. 15), except that the amplitude of the white noise at high frequencies has increased by a factor of about two for $L_{g_2}/L_{g_1} = 1.2$ as compared with those for $L_{g_2}/L_{g_1} = 4.4$. Figure 38 compares ideal and estimated gain factors for the gradiometer "noise" channel. A comparison of Fig. 38 with the corresponding one for $L_{g_2}/L_{g_1} = 4.4$ (Fig. 16) shows the absence of numerical noise at L_{g_1}, i.e., this figure also implies a persistence of the numerical noise for $S/N_i = \infty$ and $L_{g_2}/L_{g_1} = 4.4$ (Fig. 16) for $S/N_i = 10$ and the same L_{g_2}/L_{g_1} ratio.

- Figure 39 shows estimated gain factors for the gradiometer "noise" channel and $S/N_i = 1$. A comparison of these and corresponding results for the previous case (Fig. 17) indicates similar trends, except that for the same $M/(B/2)$ value, the white noise at high frequency in Fig. 39 for $L_{g_2}/L_{g_1} = 1.2$ is about twice that in Fig. 17 for $L_{g_2}/L_{g_1} = 4.4$. Fig. 40 compares ideal and estimated gain factors for the gradiometer noise channel. As for $S/N_i = 10$ (Fig. 38), the gain factor would not be detectable, even

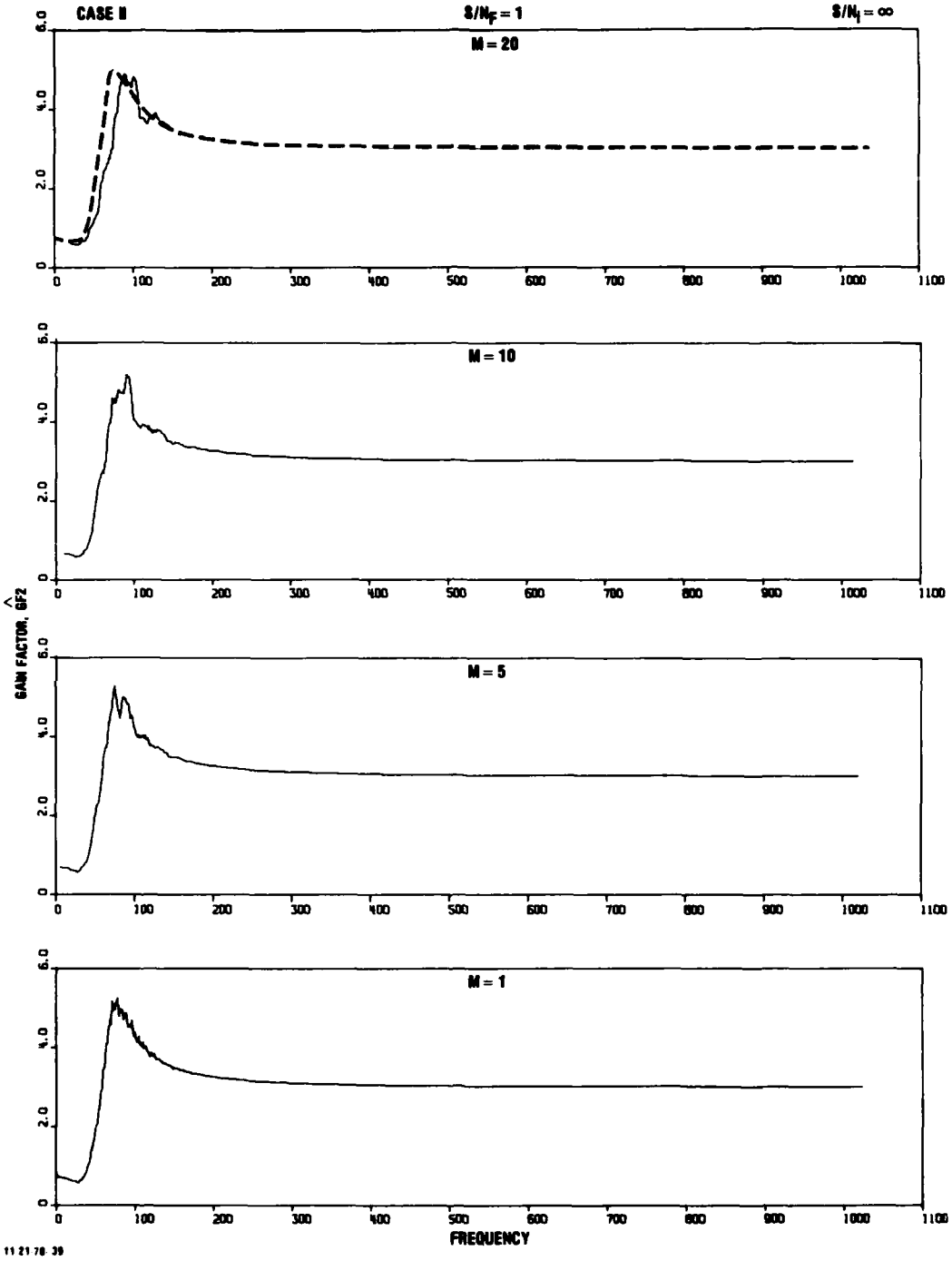

FIGURE 36. Comparison of ideal and estimated gain factors for gradiometer noise channel for low-frequency filters with $Lg_2/Lg_1 = 1.2$ for $S/N_I = \infty$.

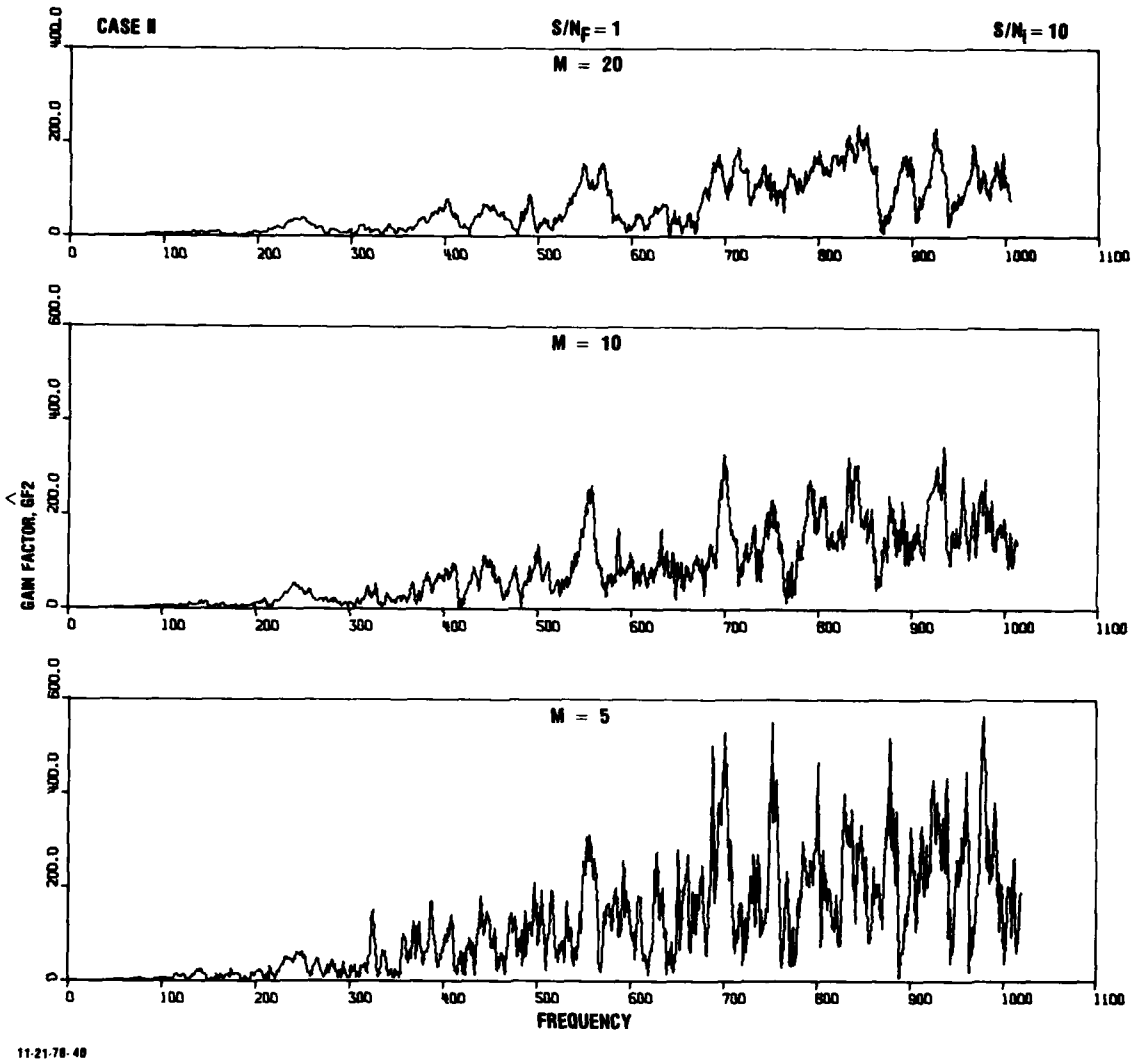

FIGURE 37. Estimated gain factor for gradiometer noise channel for low-frequency filters with $Lg_2/Lg_1 = 1.2$ for $S/N_i = 10$.

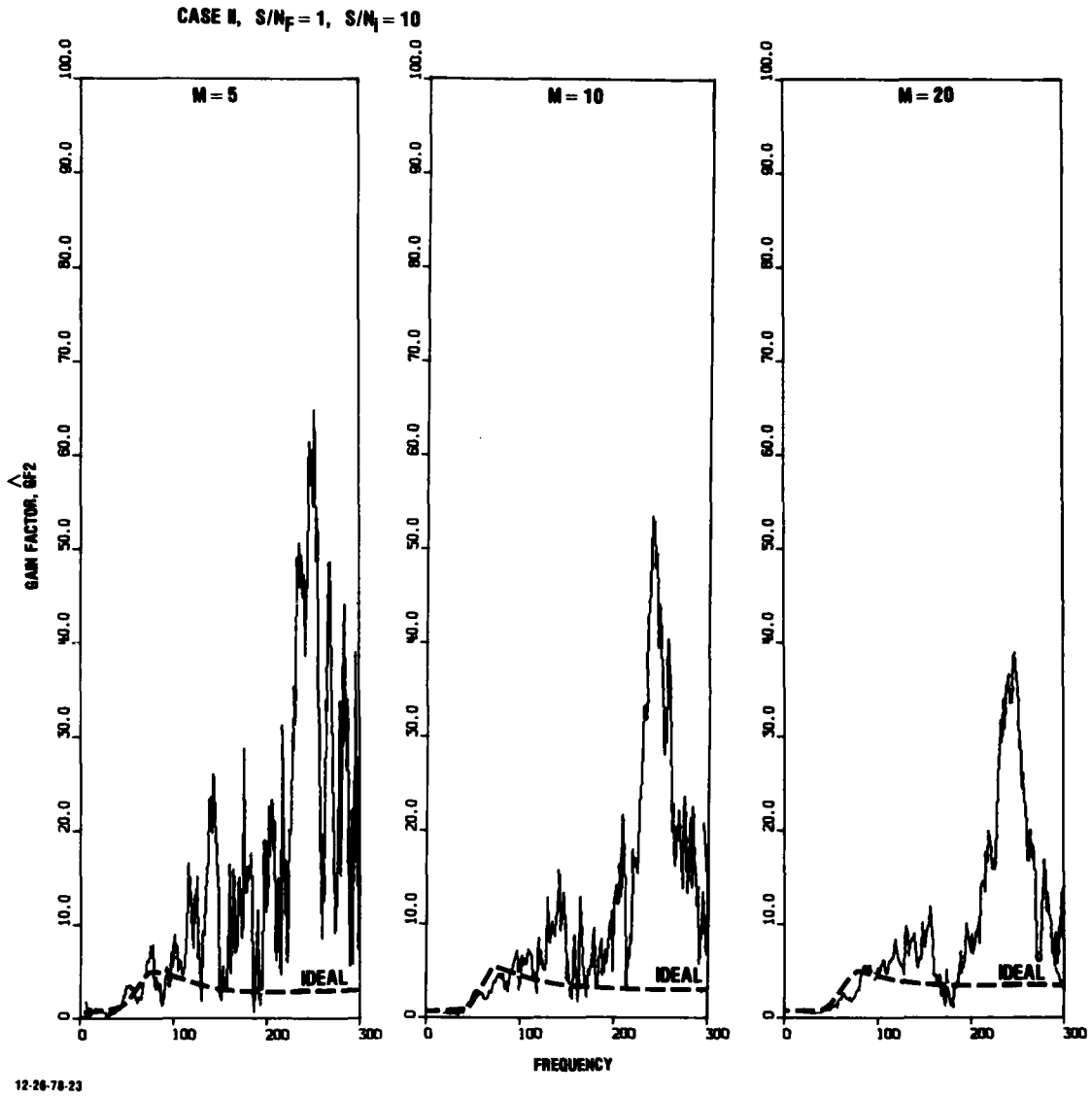

FIGURE 38. Comparison of ideal and estimated gain factors for gradiometer noise channel for low-frequency filters with $Lg_2/Lg_1 = 1.2$ for $S/N_i = 10$.

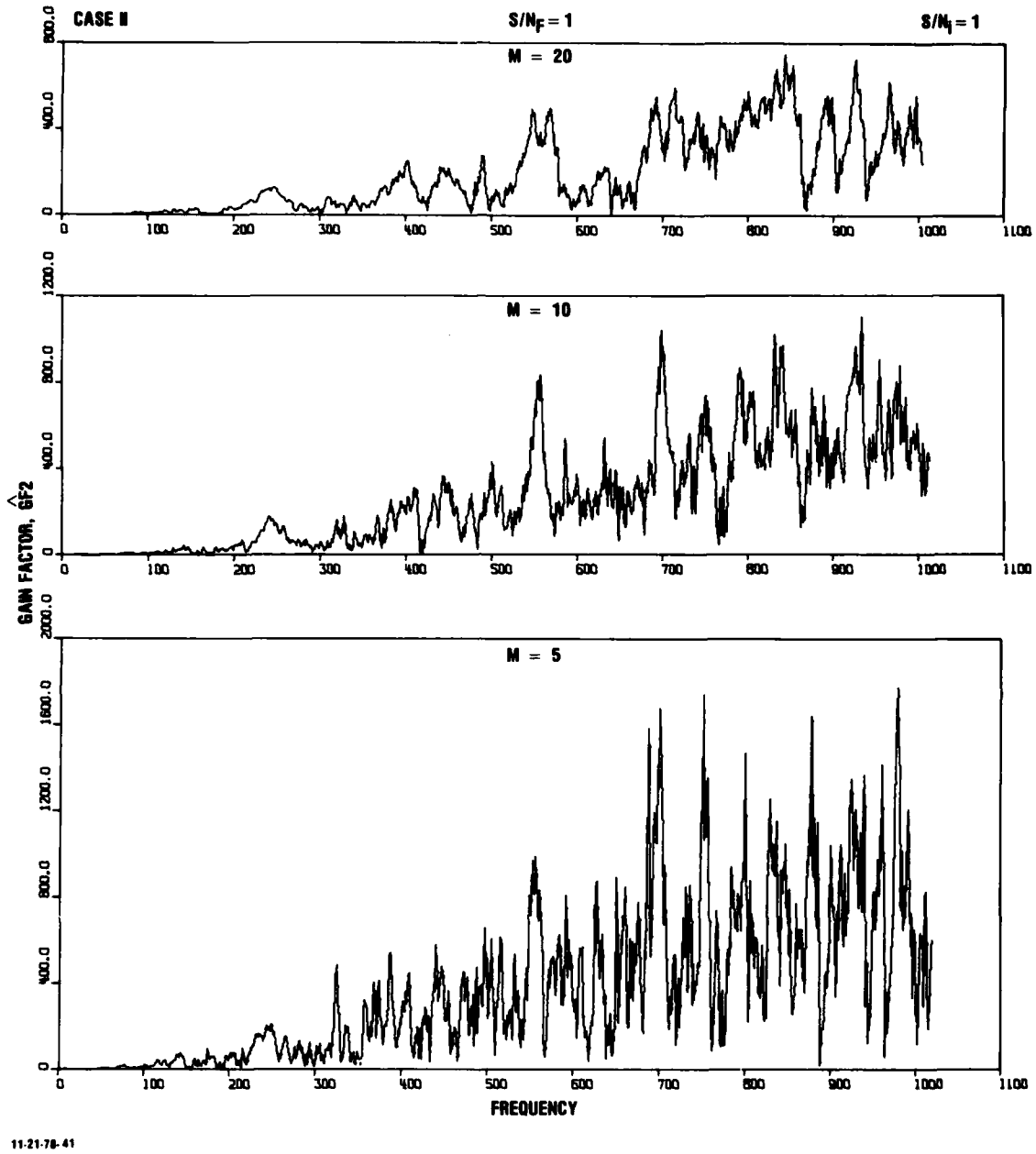

FIGURE 39. Estimated gain factors for gradiometer noise channel for low-frequency filters with $Lg_2/Lg_1 = 1.2$ for $S/N_i = 1$.

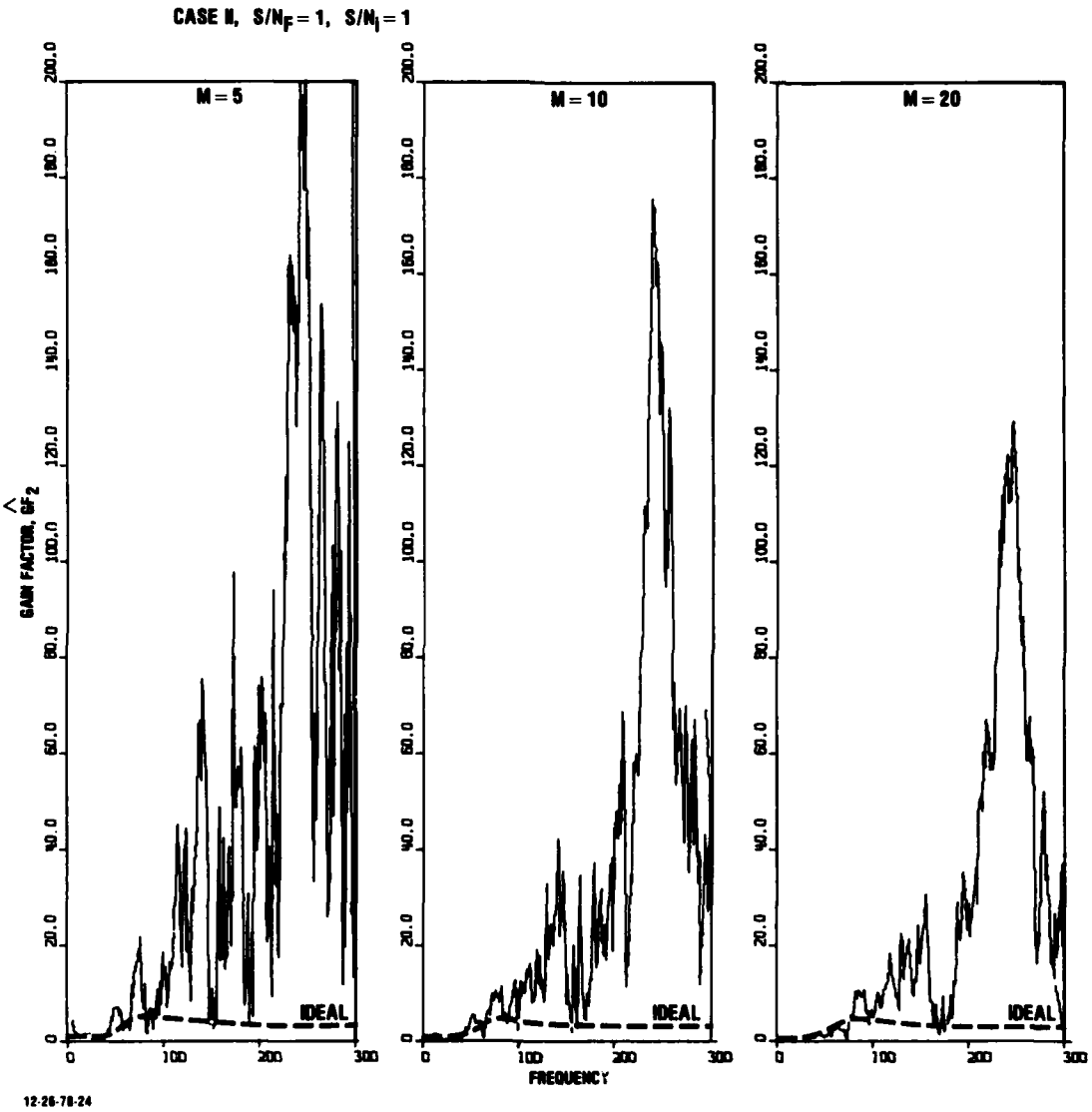

FIGURE 40. Comparison of ideal and estimated gain factors for gradiometer signal channel for low-frequency filters with Lg_2/Lg_1 = 1.2 for S/N_i = 1.

though the numerical noise at the low frequencies in the corresponding Fig. 18 for $Lg_2/Lg_1 = 4.4$ is now absent in Fig. 40 for $Lg_2/Lg_1 = 1.2$.

4.2.3 Estimator for Gradiometer Output Spectra

Figures 41-45 show comparisons of ideal and estimated spectra for the subsidiary channels and gradiometer outputs as a function of frequency averaging and also of signal-to-instrument noise ratio for the gradiometer output. A comparison of these figures with their counterparts for the previous case (Figs. 19-23) shows similar trends in regard to the effect of both frequency averaging on the bias of the estimators and white noise background for the detectability of the ideal spectrum of the gradiometer output at S/N_i other than infinity.

4.2.4 Estimated Partial Coherences

Figures 46-48 show the estimated partial coherences as a function of frequency averaging and S/N_i ratio. These results are similar to the corresponding ones for the previous case (Figs. 24-26), except that the larger constant drop from unity for any M for $S/N_i = \infty$ in Fig. 24 for $Lg_2/Lg_1 = 4.4$ is absent in the corresponding Fig. 46 for $Lg_2/Lg_1 = 1.2$ due to the absence of numerical noise in the gain factors for $Lg_2/Lg_1 = 1.2$, (i.e., Fig. 31 versus Fig. 9). The remaining drop from unity in Figs. 24 and 46 for $S/N_i = \infty$ also implies that the deterioration of the partial coherence at Lg_1 for $Lg_2/Lg_1 = 4.4$ is independent of the numerical noise in the corresponding transfer functions (Fig. 9). It is further noted that the remaining deterioration in the partial coherence remains significant for $M \cong 5$, i.e., the averaging required to obtain nearly unbiased estimates of the gradiometer signal spectra in this case (Fig. 6). Finally, Fig. 49 for the input coherence shows trends similar to those in Fig. 27 for $Lg_2/Lg_1 = 4.4$.

4.2.5 Overall Results for Low-Frequency Gradiometer with $L_{g_1}/L_{g_2} \approx 1.0$

The results for the reconstruction of an imbedded low-frequency signal in a gradiometer channel characterized by a ratio of $L_{g_2}/L_{g_1} = 1.2$ and $B/2 = 20$, indicate results similar to those for the previous case for $L_{g_2}/L_{g_1} = 4.4$ and $B/2 = 10$ with the following exceptions:

- For the ideal conditions of no instrument noise, the numerical noise introduced by the algorithm in the estimated gain factors for $L_{g_2}/L_{g_1} = 4.4$ disappears when $L_{g_2}/L_{g_1} = 1.2$. (Figs. 9 vs. 31 and 14 vs. 36).
- For a signal-to-instrument noise ratio of 10, the relative window, $M/(B/2)$, for the frequency averaging of the estimated gradiometer signal spectrum tends to decrease from $1 < M/(B/2) < 2$ for $L_{g_2}/L_{g_1} = 4.4$ (Fig. 7) to $0.5 < M/(B/2) < 1$ for $L_{g_2}/L_{g_1} = 1.2$ (Fig. 29).

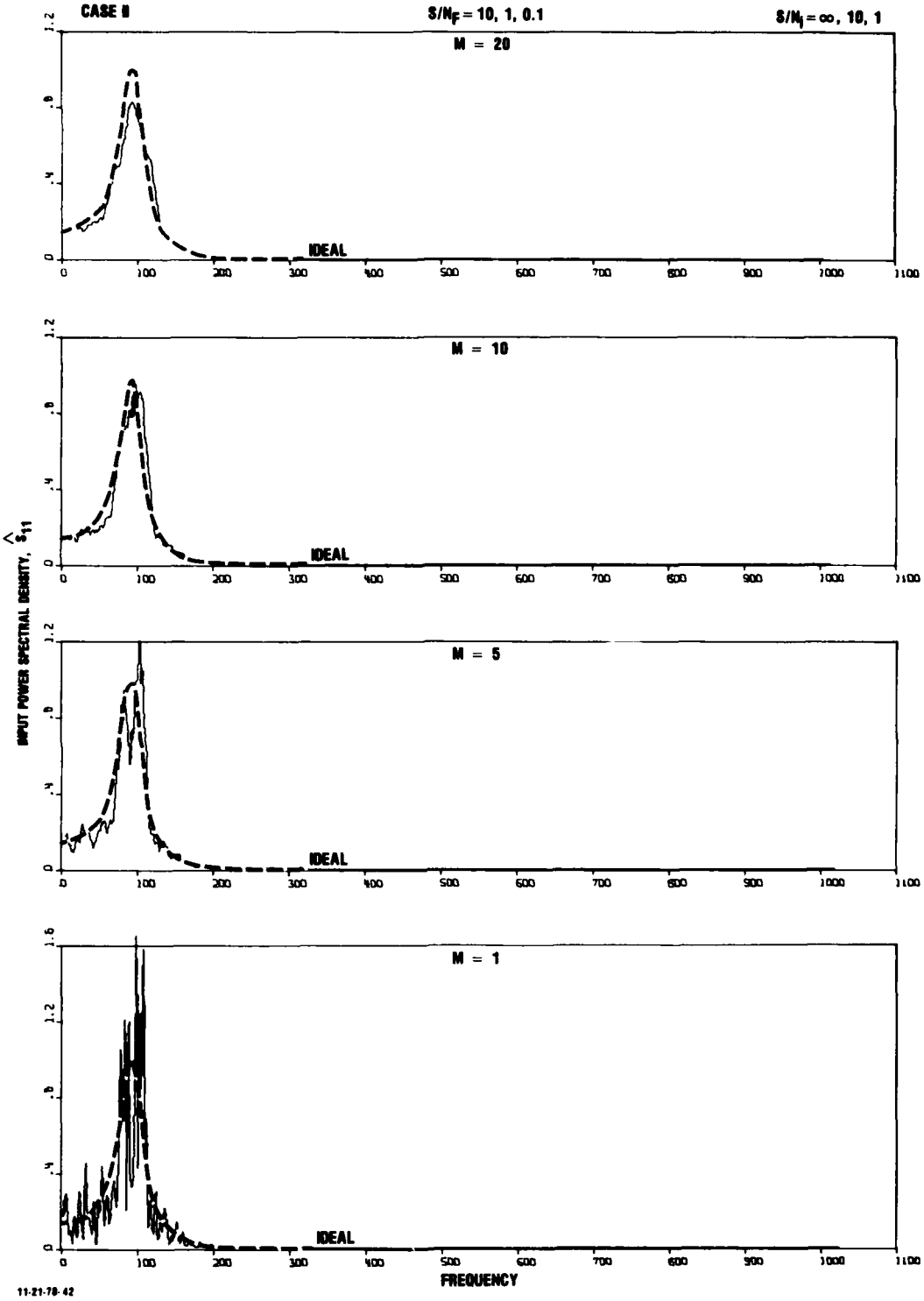

FIGURE 41. Comparison of ideal and estimator spectra for subsidiary "signal" channel for low-frequency filters with $Lg_2/Lg_1 = 1.2$.

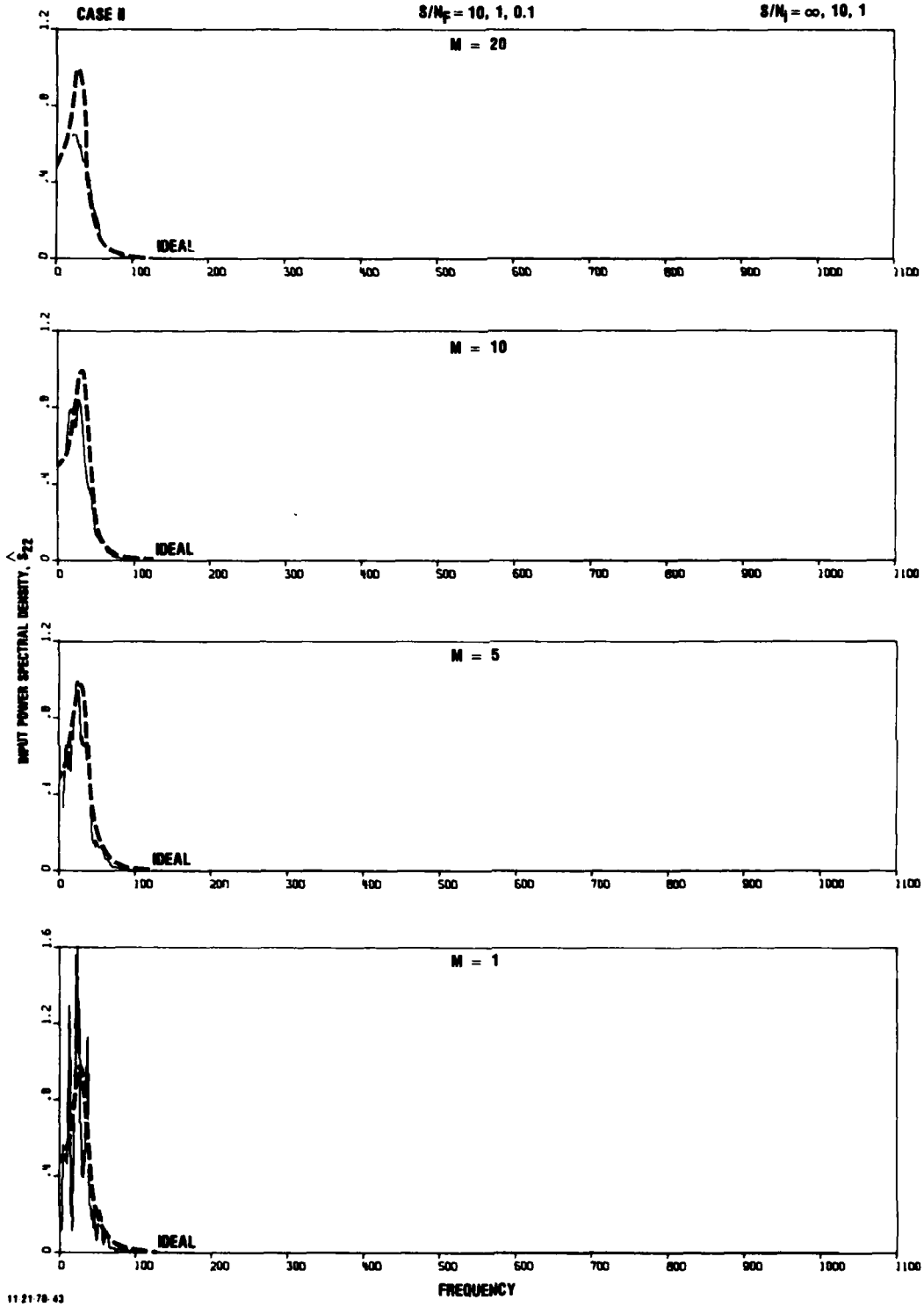

FIGURE 42. Comparison of ideal and estimator spectra for subsidiary "noise" channel for low-frequency filters with $Lg_2/Lg_1 = 1.2$.

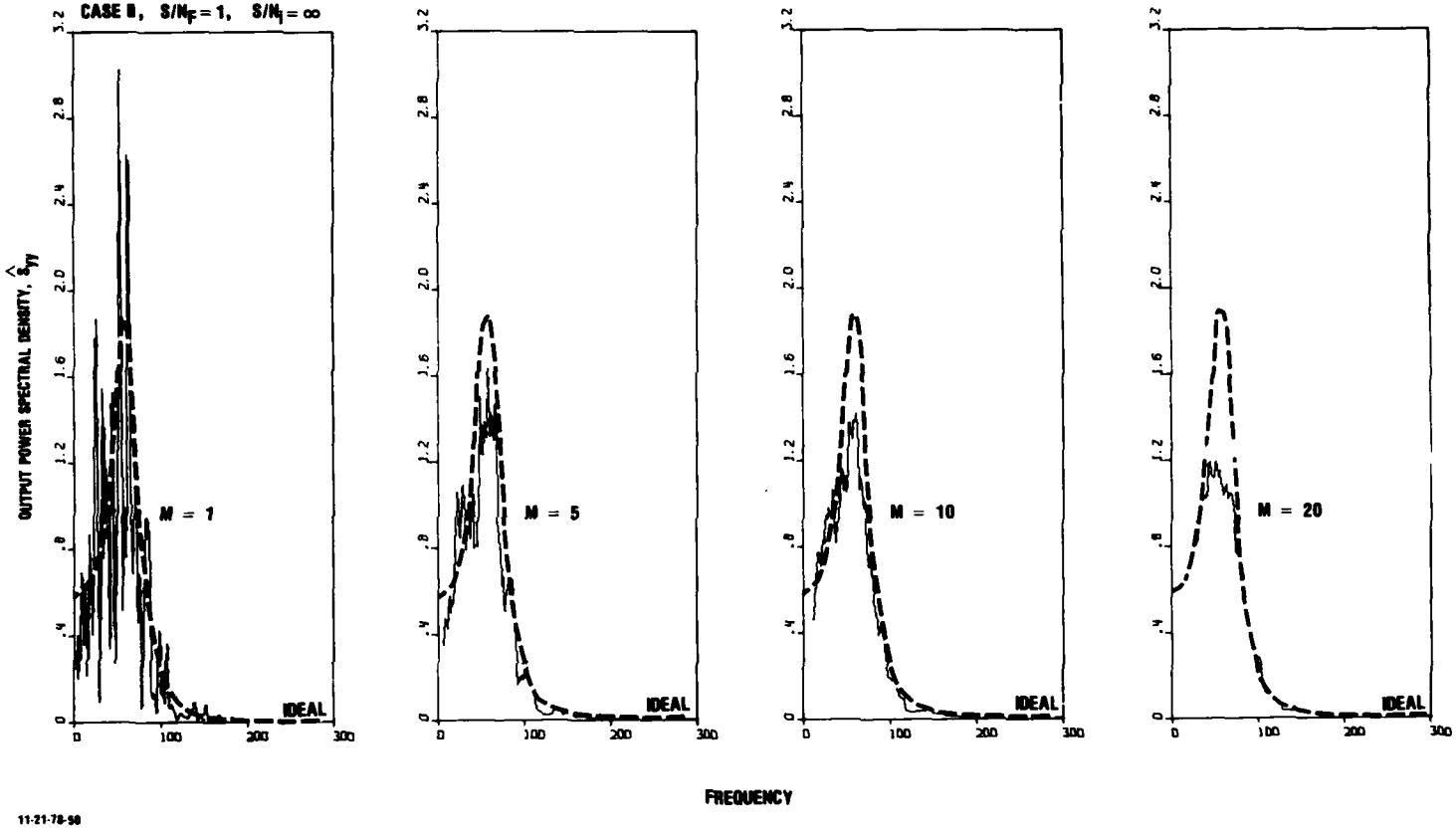

FIGURE 43. Comparison of ideal and estimator spectra for gradiometer output for low-frequency filters with $Lg_2/Lg_1 = 1.2$ for $S/N_i = \infty$.

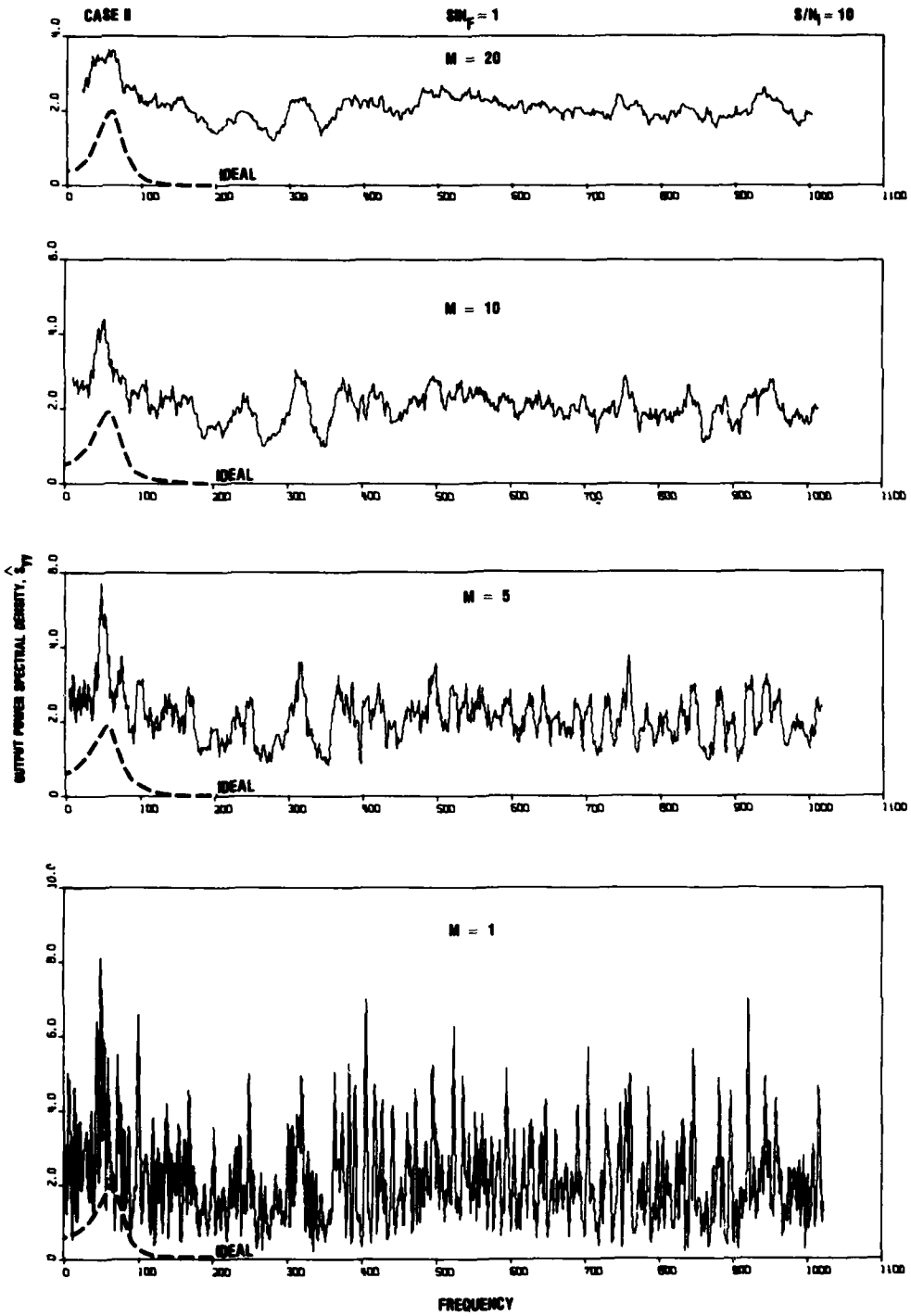

FIGURE 44. Comparison of ideal and estimator spectra for gradiometer output for low-frequency filters with $Lg_2/Lg_1 = 1.2$ for $S/N_1 = 10$.

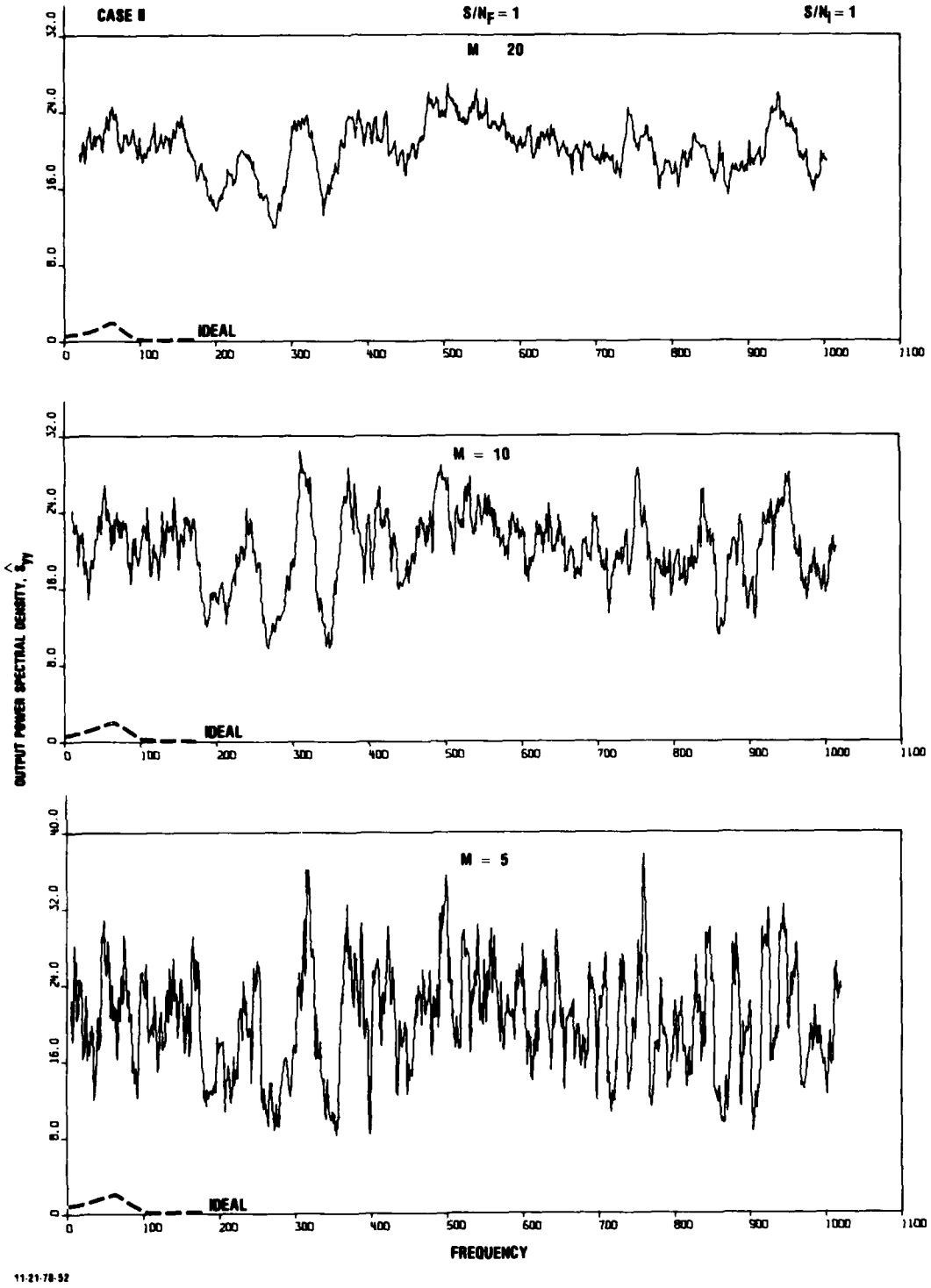

FIGURE 45. Comparison of ideal and estimator spectra for gradiometer output for low-frequency filters with $Lg_2/Lg_1 = 1.2$ for $S/N_i = 1$.

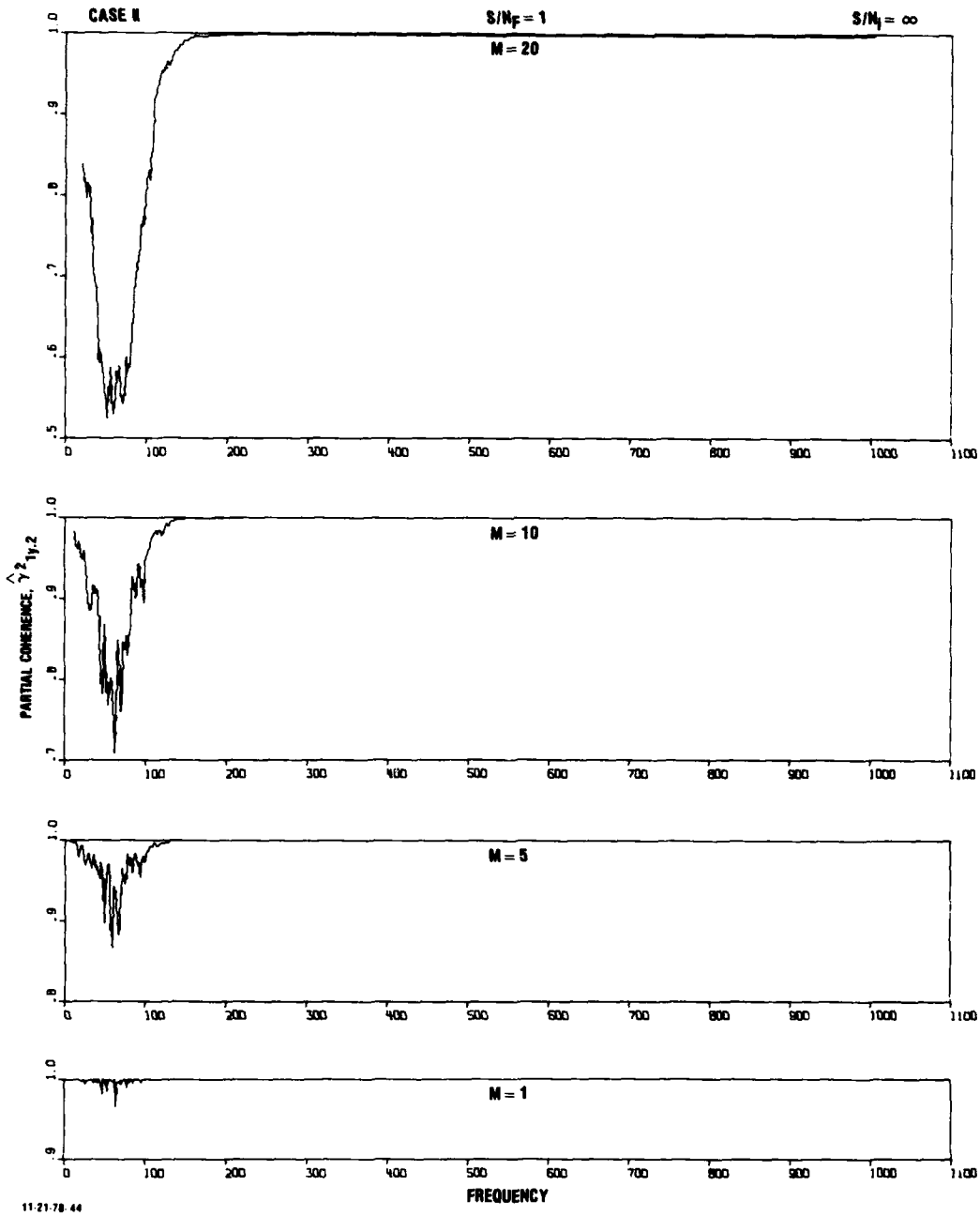

FIGURE 46. Estimated partial coherence for gradiometer signal channel for low-frequency filters with $Lg_2/Lg_1 = 1.2$ for $S/N_i = \infty$.

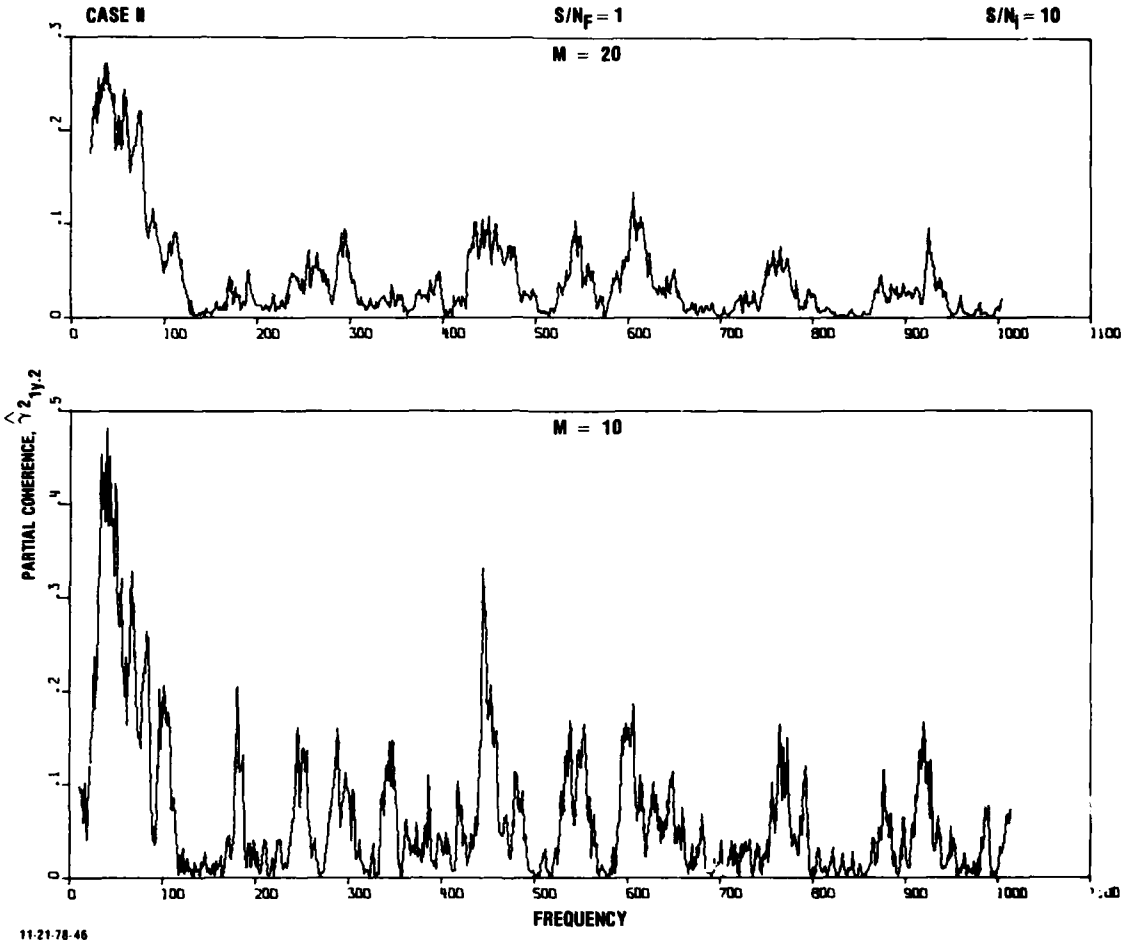

FIGURE 47. Estimated partial coherence for gradiometer signal channel for low-frequency filters with Lg_2/Lg_1 = 1.2 for S/N_i = 10.

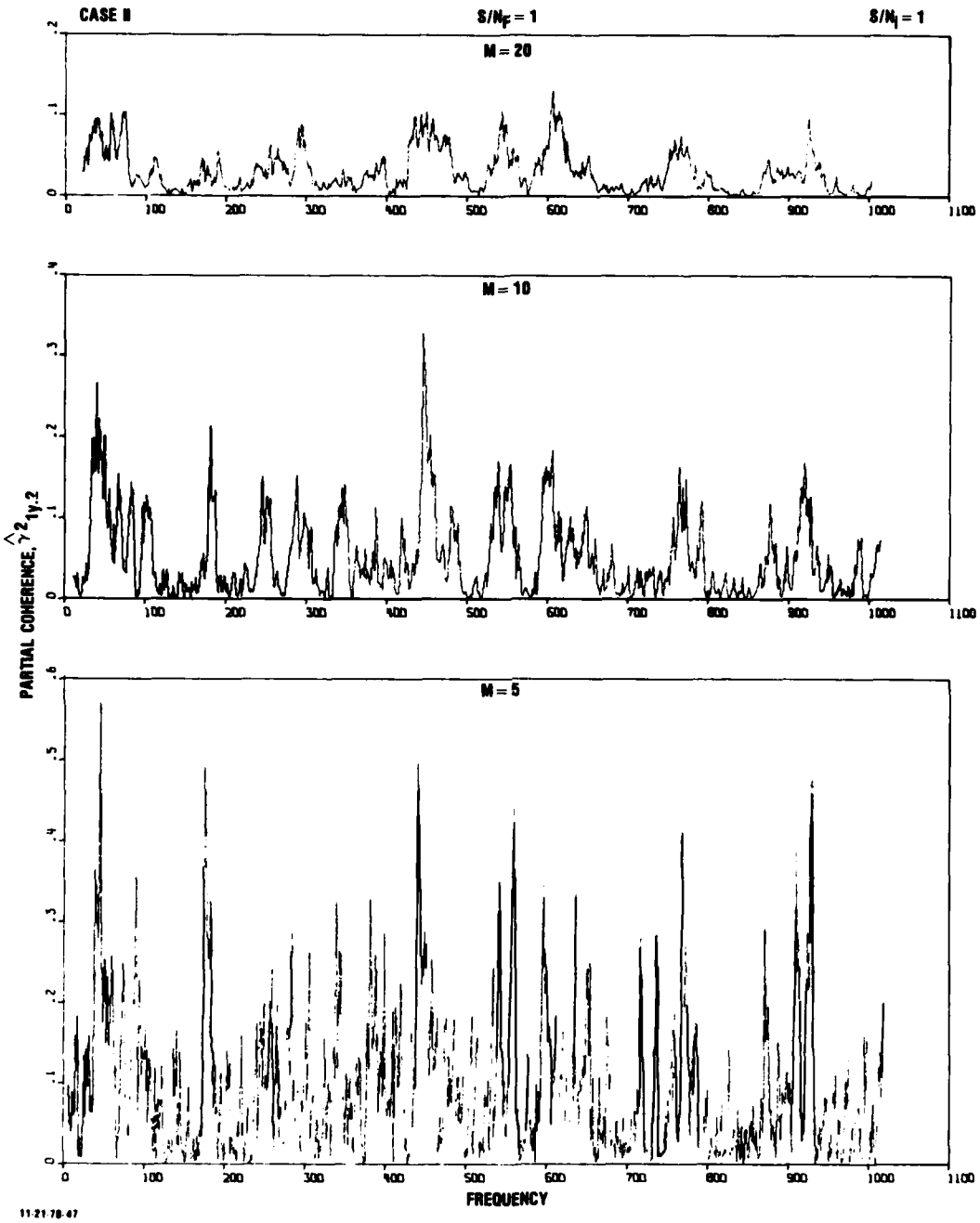

FIGURE 48. Estimated partial coherence for gradiometer signal channel for low-frequency filters with $Lg_2/Lg_1 = 1.2$ for $S/N_1 = 1$.

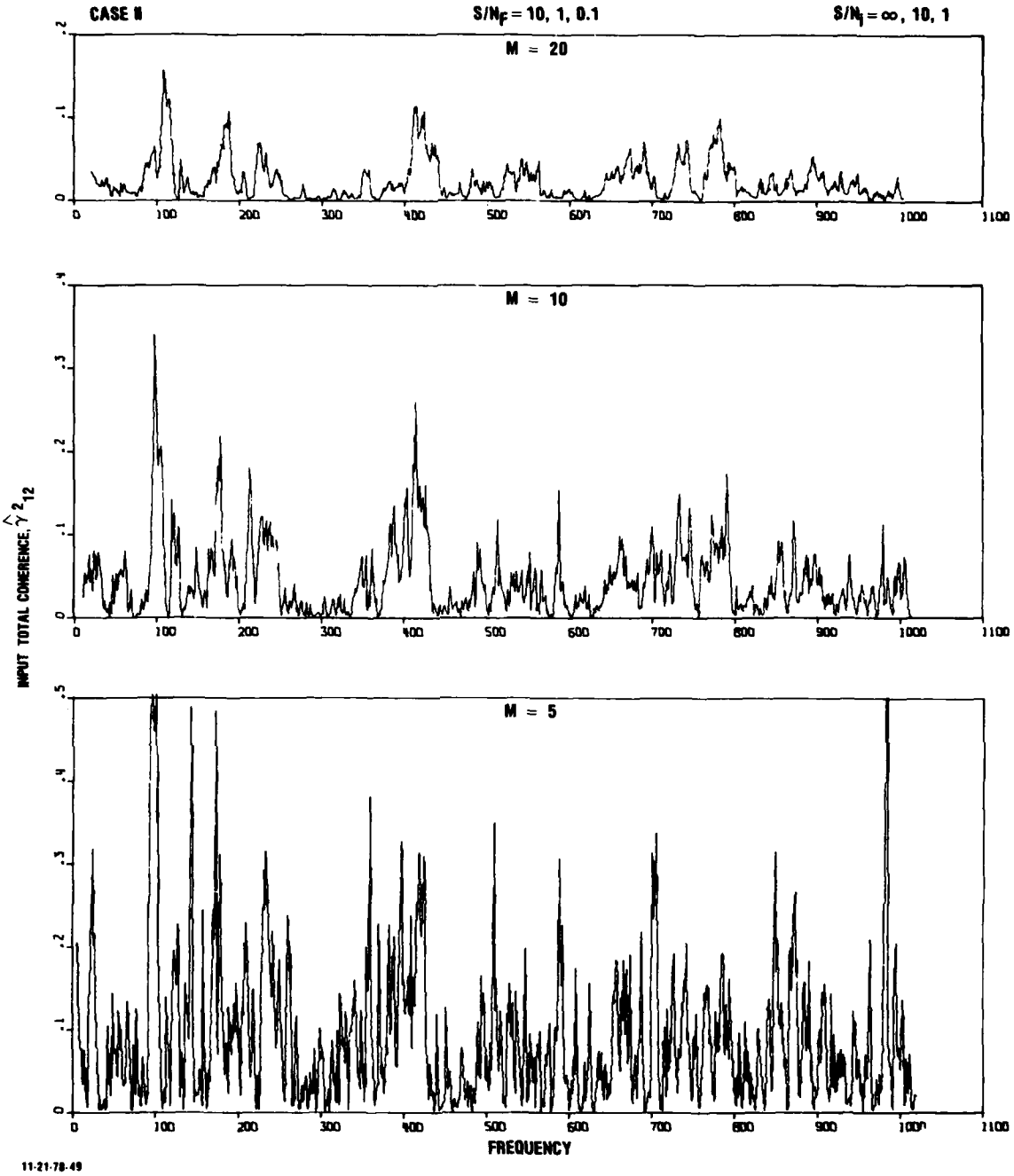

FIGURE 49. Estimated input coherence for two subsidiary current meter channels for low-frequency filters with $Lg_2/Lg_1 = 1.2$.

4.3 BROAD BANDWIDTH GRADIOMETER WITH $L_{g_2}/L_{g_1} = 1$

Figures 50-67 describe in the subsequent subsections the results for case III in Fig. 5, which is characterized by $L_{g_2} = 500$ $L_{g_2}/L_{g_1} = 1$ and $B/2 = 100$.

4.3.1 Estimated Gradiometer Signal Spectrum

Figures 50-52 compare ideal and estimated spectra for the gradiometer signal channel as a function of frequency averaging and signal-to-instrument noise ratio. For $S/N_i = \infty$, Fig. 50 indicates that the determination of an unbiased spectrum would require frequency averaging in the range $0.2 < M/(B/2) < 1$. A comparison of Figs. 50-52 with those for the previous case (Figs. 28-30) indicates a significant decrease in the white noise background for the broadband case for even $S/N_i = 1$. As a result, the ideal signal spectrum for $S/N_i = 1$ is reconstructed almost as well as for $S/N_i = \infty$ for $M = 100$ or $M/(B/2) = 1$.

4.3.2 Estimated Gain Factors

Figures 53-55 and 56-58 show the gain factors for the gradiometer signal and "noise" channels, respectively. As expected from the result in Fig. 52, for the reconstruction of the gradiometer signal spectrum for even $S/N_i = 1$, the white noise structures at high frequencies for the gain factors in the previous low frequency cases have now been reduced drastically even for $S/N_i = 1$. It appears then that the smoothing of the periodogram is a function of both the absolute value of M as well as the relative parameter $M/(B/2)$ since, as the bandwidth of the spectra broadens, the bias of the estimated spectrum is reduced significantly for a large value of M.

4.3.3 Estimators for Gradiometer Output Spectra

Figures 59-63 show the reconstructed spectra for the subsidiary and gradiometer channels outputs. Relative to the previous low-frequency case with $L_{g_2}/L_{g_1} = 1.2$ (Figs. 41-45), the

outstanding relative result for this case is the adequate reconstruction of the gradiometer output spectra for $S/N_1 = 10$ when $M/(B/2) = 1$ (Figs. 62 versus 44). However, the reconstruction of the ideal S_{yy} spectrum for $S/N_1 = 1$ fails to show a similar relative improvement for the broad bandwidth case (Figs. 63 versus 45).

4.3.4 Estimated Partial Coherences

Figures 64-66 show the partial coherences for the broad bandwidth spectra for signal-to-instrument noise ratio S/N_1 of ∞, 10 and 1. For the required averaging to detect an unbiased gradiometer signal spectra for $S/N_1 = \infty$, $0.2 < M/(B/2) < 1$, the results in Fig. 64 show no significant difference relative to the previous low-frequency case (Figs. 24, 46), i.e., the deviation of the partial coherence from unity for $S/N_1 = \infty$ remains essentially independent of the frequency characteristics of the output spectra for the subsidiary and gradiometer channels (Fig. 5). Figure 67 for the input coherence shows a significant improvement for broad bandwidths, i.e., $\hat{\gamma}_{12}^2 \to 0$ as $M/(B/2) \to 1$.

4.3.5 Overall Results for Broad Frequency Gradiometer with $L_{g_2}/L_{g_1} = 1$

The overall results for spectra with broad bandwidths indicate that the gradiometer signal spectrum and transfer functions can be reconstructed adequately for $M/(B/2) = 1$ even for signal-to-instrument noise ratios within the threshold of detectability ($S/N_1 = 1$). However, the spectrum of the gradiometer output can be reconstructed only for signal-to-instrument noise ratios $S/N_1 > 10$. The fundamental problem of the breakdown of the partial coherence as an index of the fidelity of reconstruction of the gradiometer signal spectrum remains independent of the frequency characteristics of such spectra.

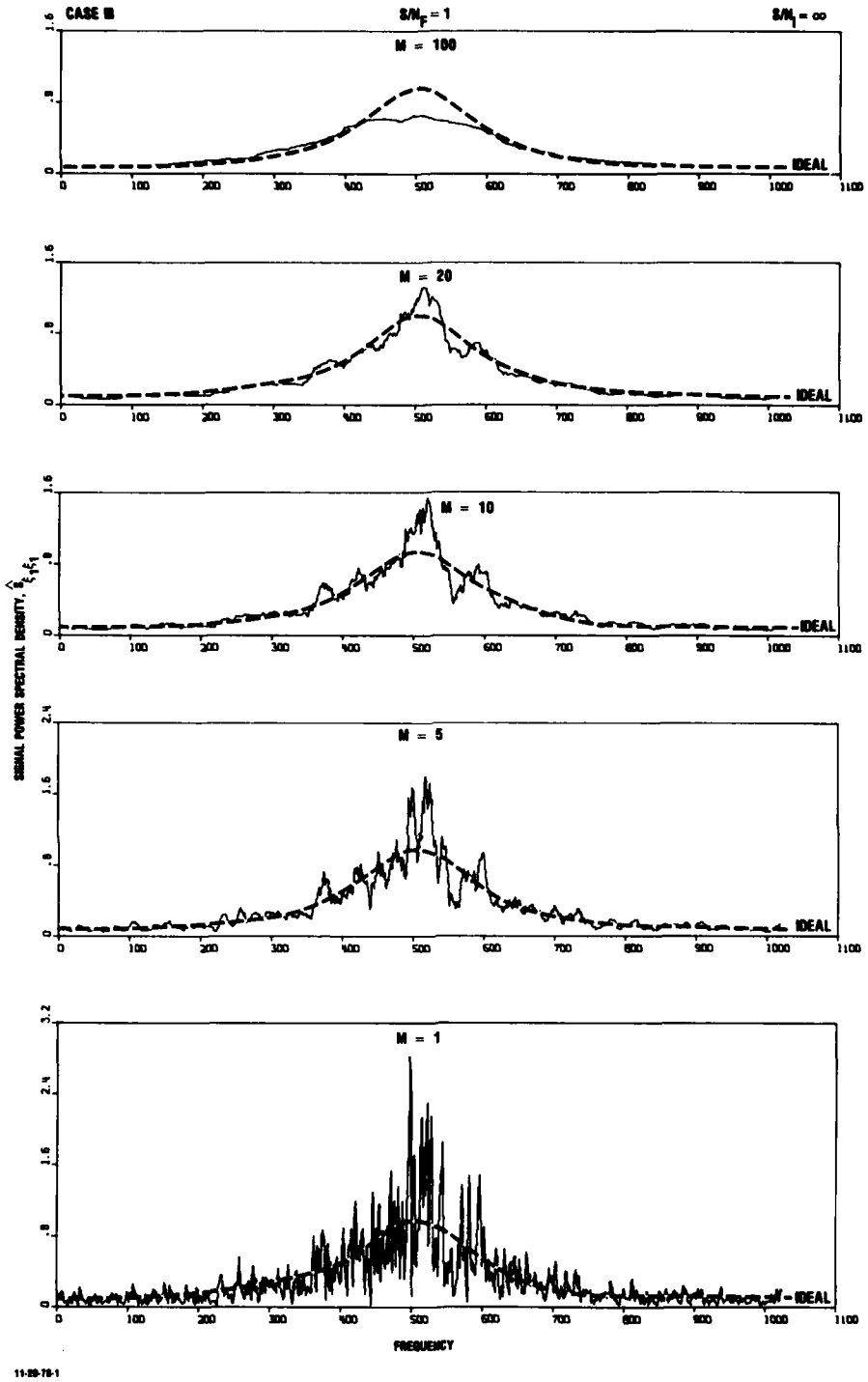

FIGURE 50. Comparison of ideal and reconstructed signal spectra for broad bandwidth filters with $Lg_2/Lg_1 = 1$ for $S/N_i = \infty$.

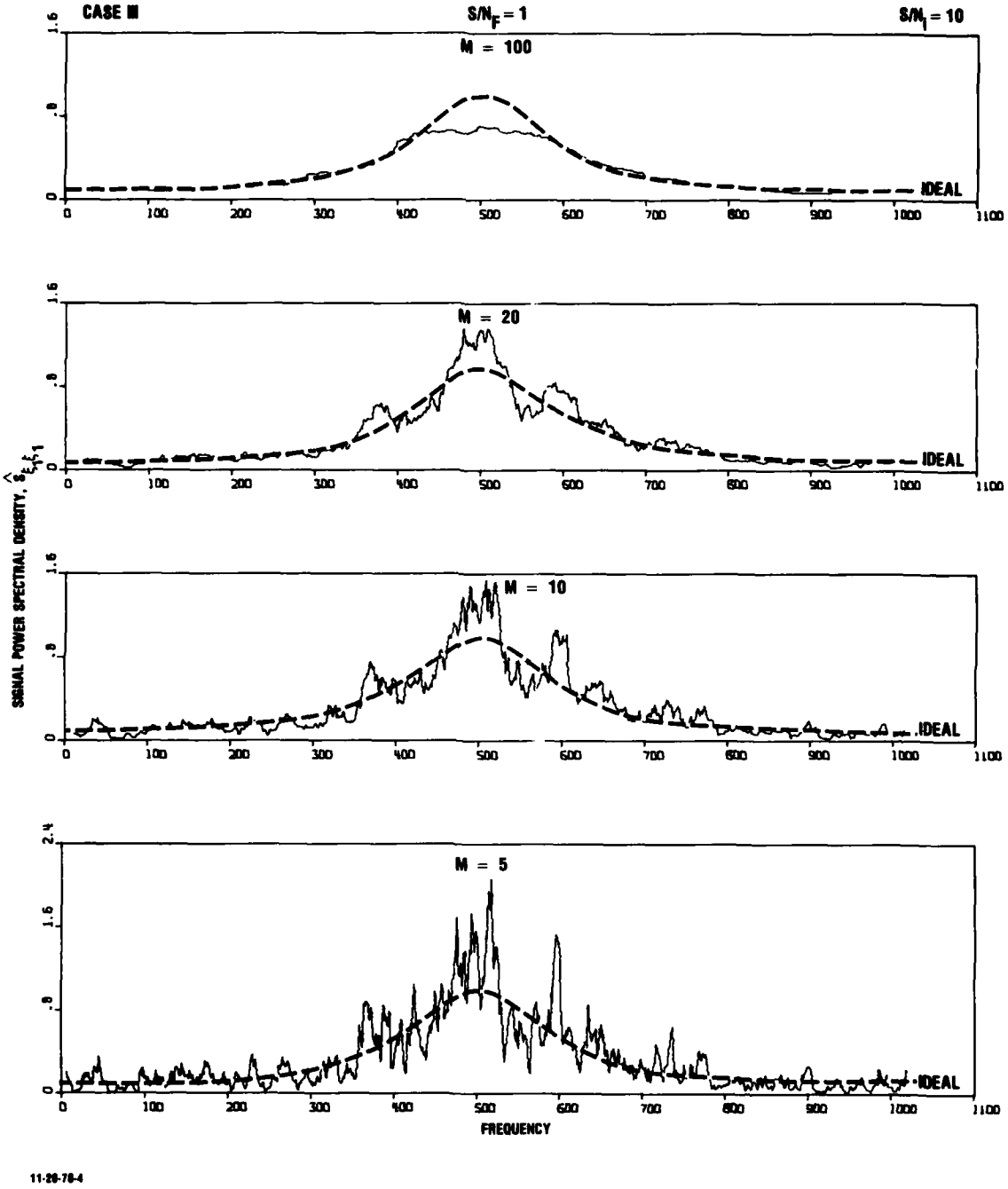

FIGURE 51. Comparison of ideal and reconstructed signal spectra for broad bandwidth filters with $Lg_2/Lg_1 = 1$ for $S/N_i = 10$.

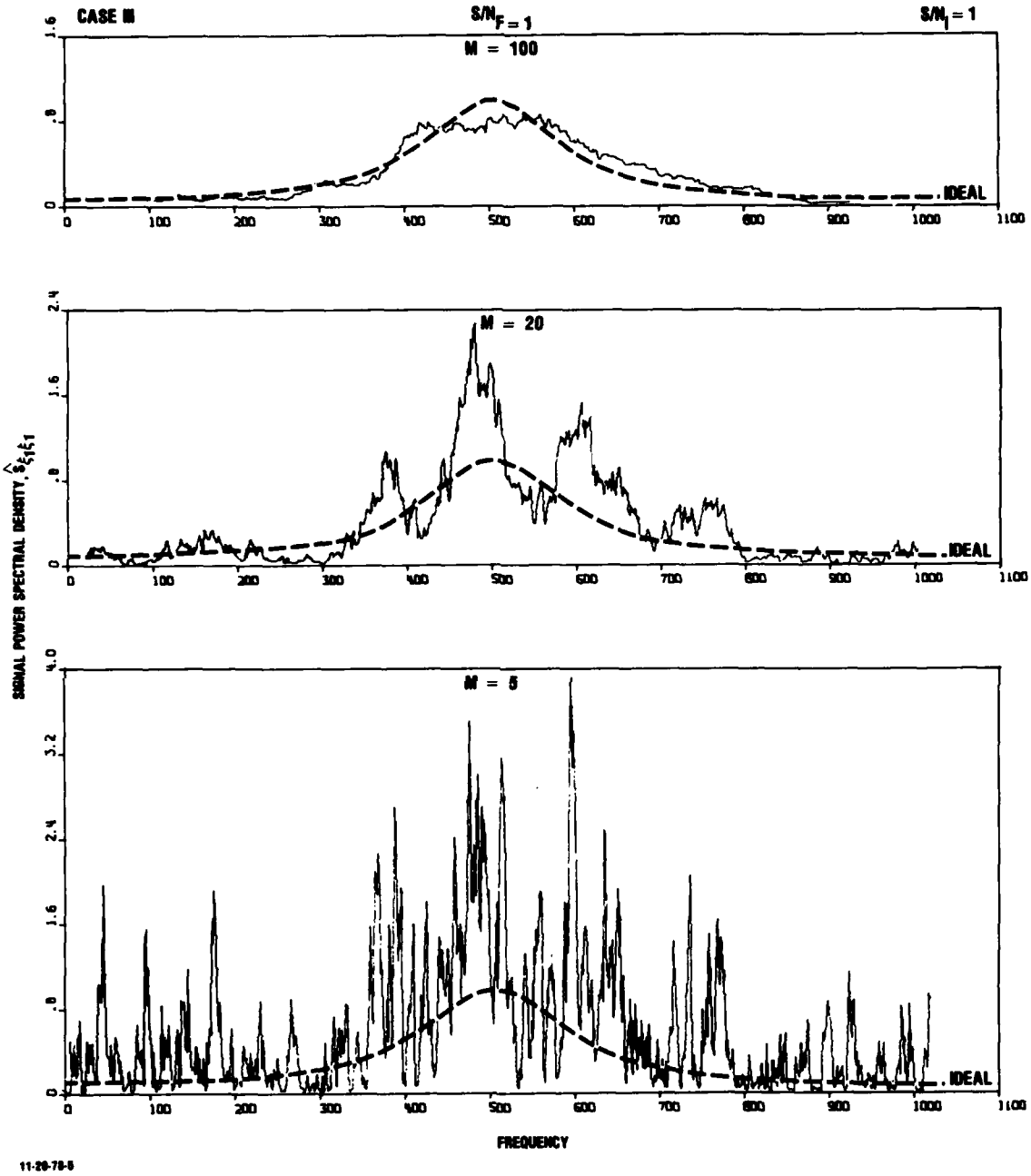

FIGURE 52. Comparison of ideal and reconstructed signal spectra for broad bandwidth filters with $Lg_2/Lg_1 = 1$ for $S/N_i = 1$.

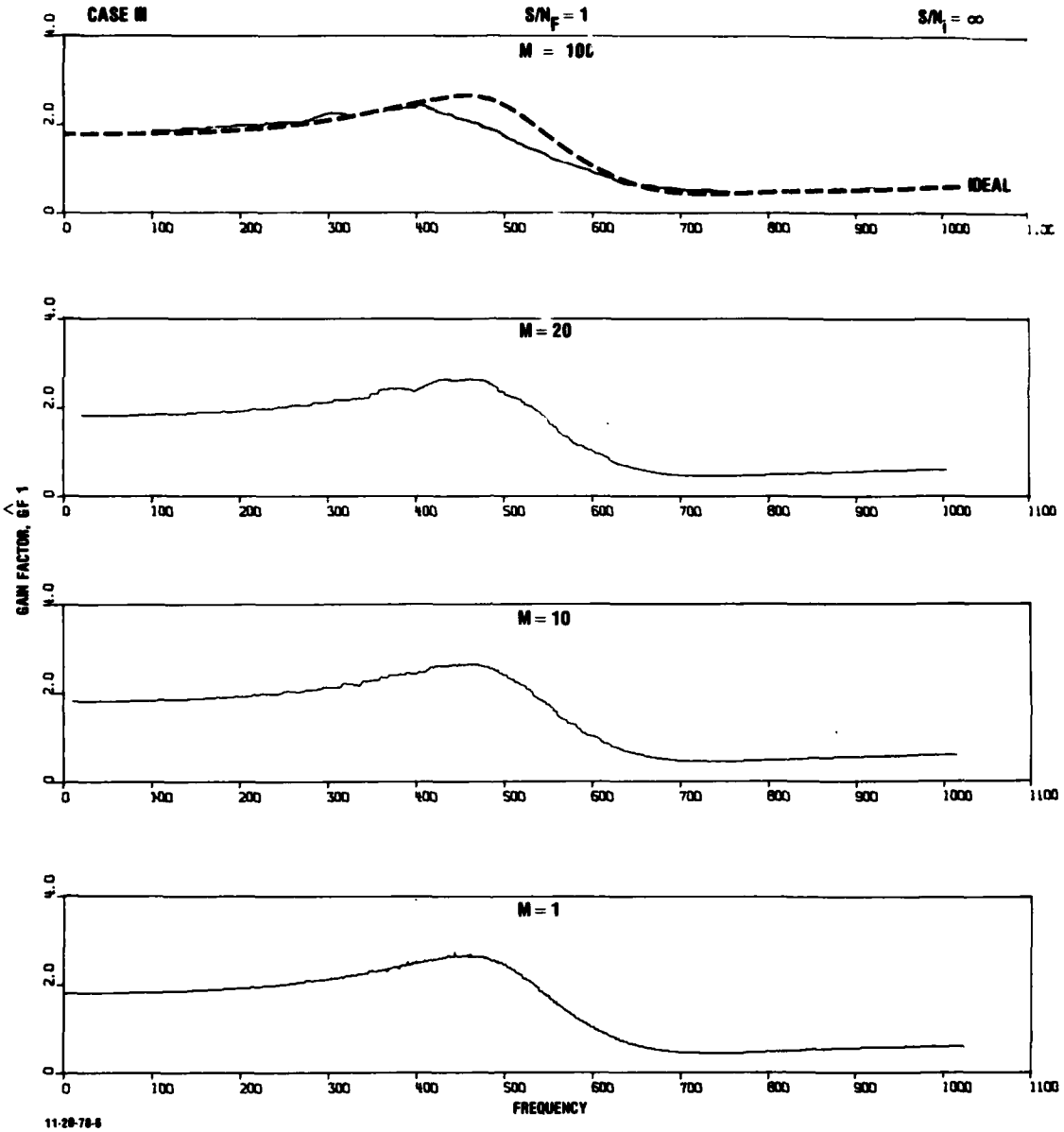

FIGURE 53. Comparison of ideal and estimated gain factors for gradiometer signal channel for broad bandwidth filters with $Lg_2/Lg_1 = 1$ for $S/N_i = \infty$.

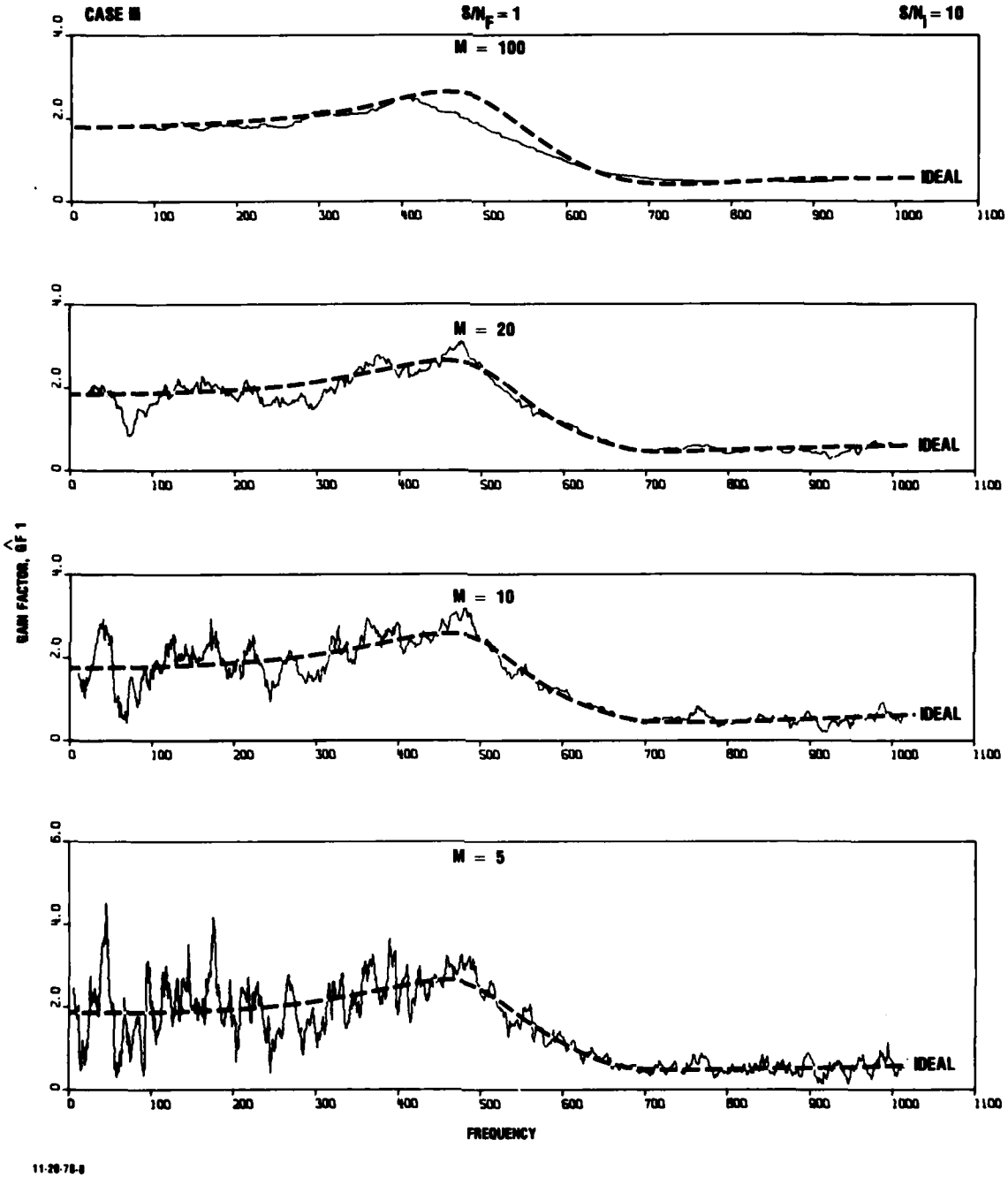

FIGURE 54. Comparison of ideal and estimated gain factors for gradiometer signal channel for broad bandwidth filters with $Lg_2/Lg_1 = 1$ for $S/N_i = 10$.

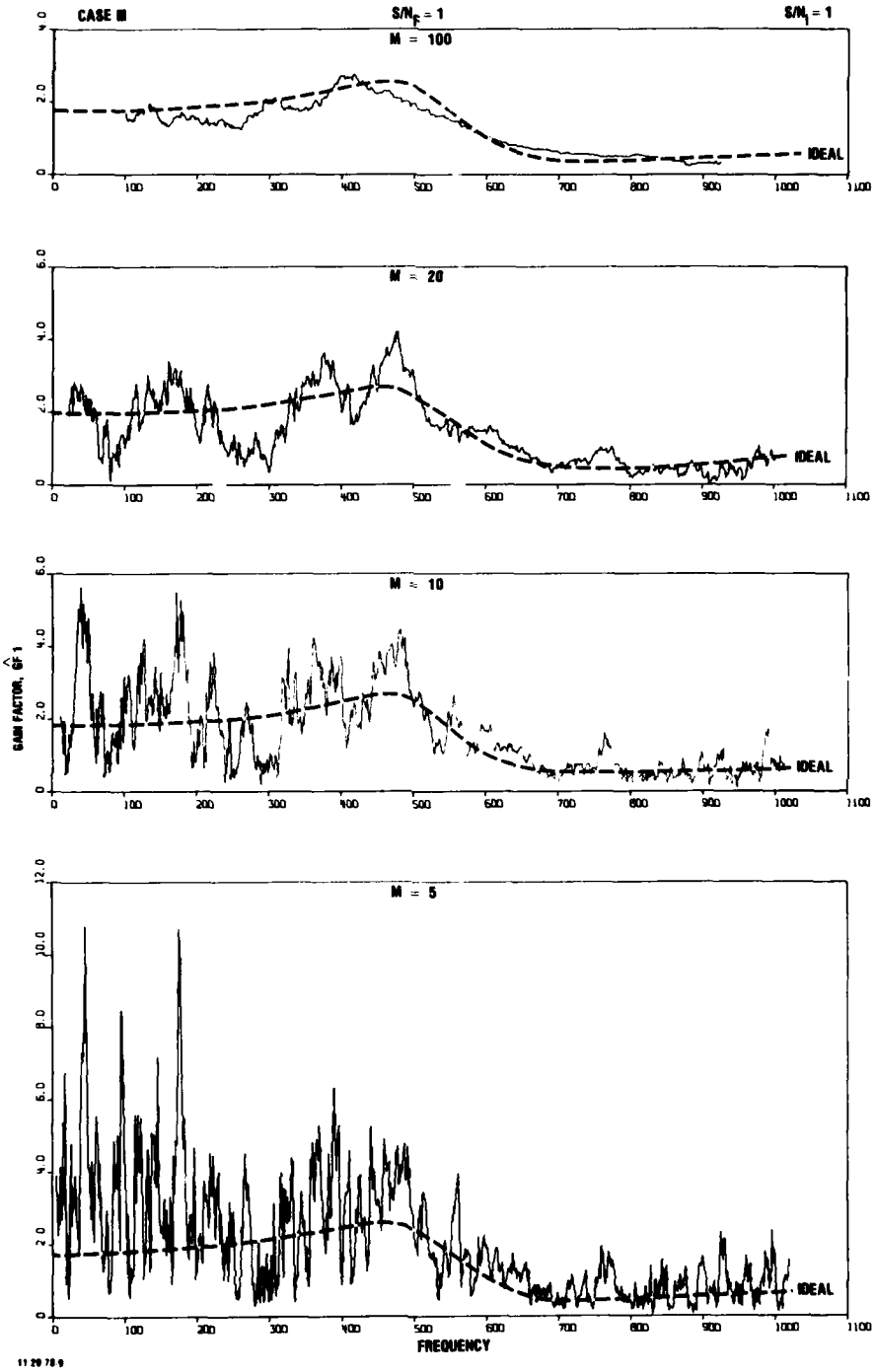

FIGURE 55. Comparison of ideal and estimated gain factors for gradiometer signal channel for broad bandwidth filters with $Lg_2/Lg_1 = 1$ for $S/N_i = 1$.

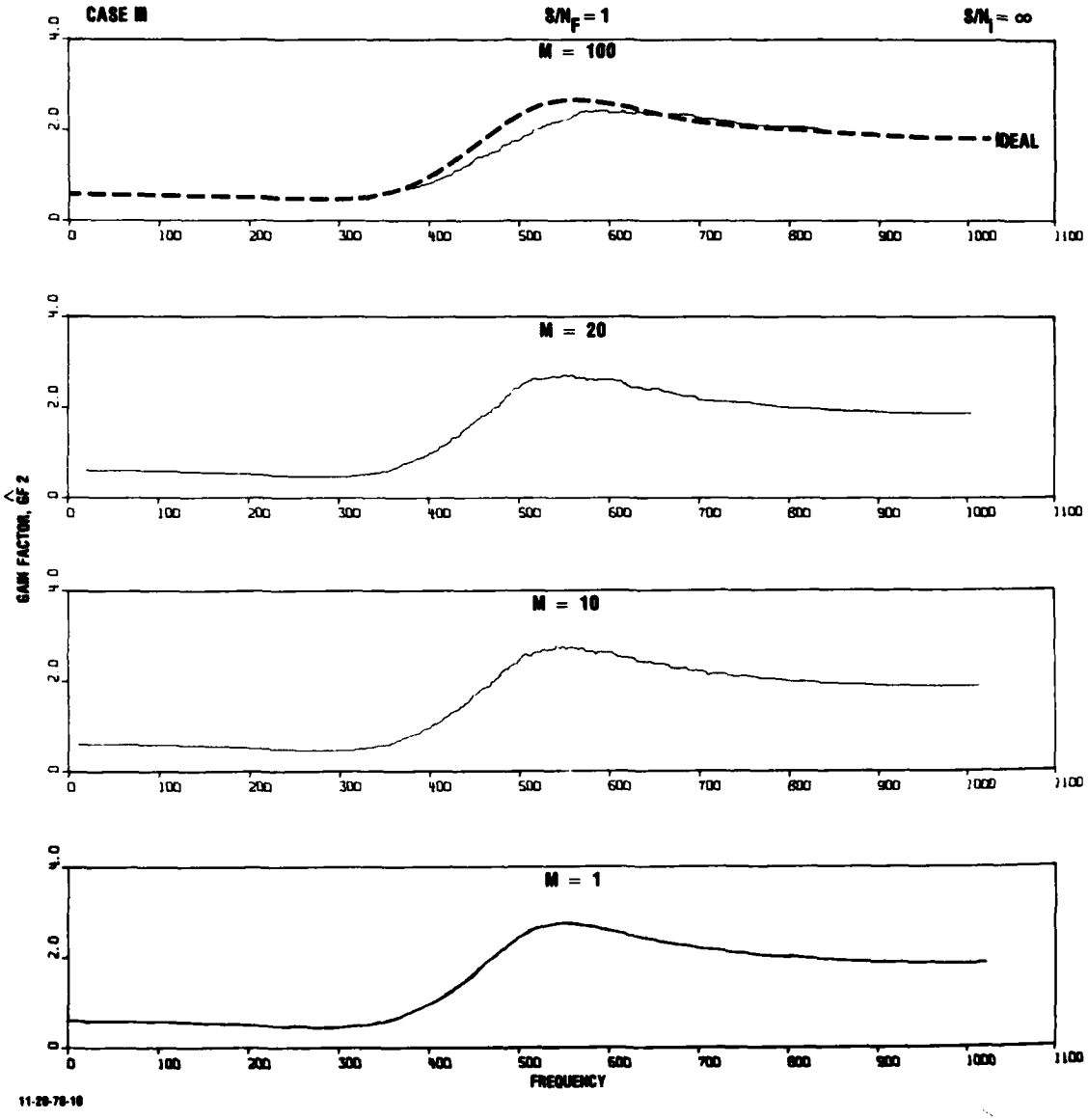

FIGURE 56. Comparison of ideal and estimated gain factors for gradiometer noise channel for broad bandwidth filters with $Lg_2/Lg_1 = 1$ for $S/N_i = \infty$.

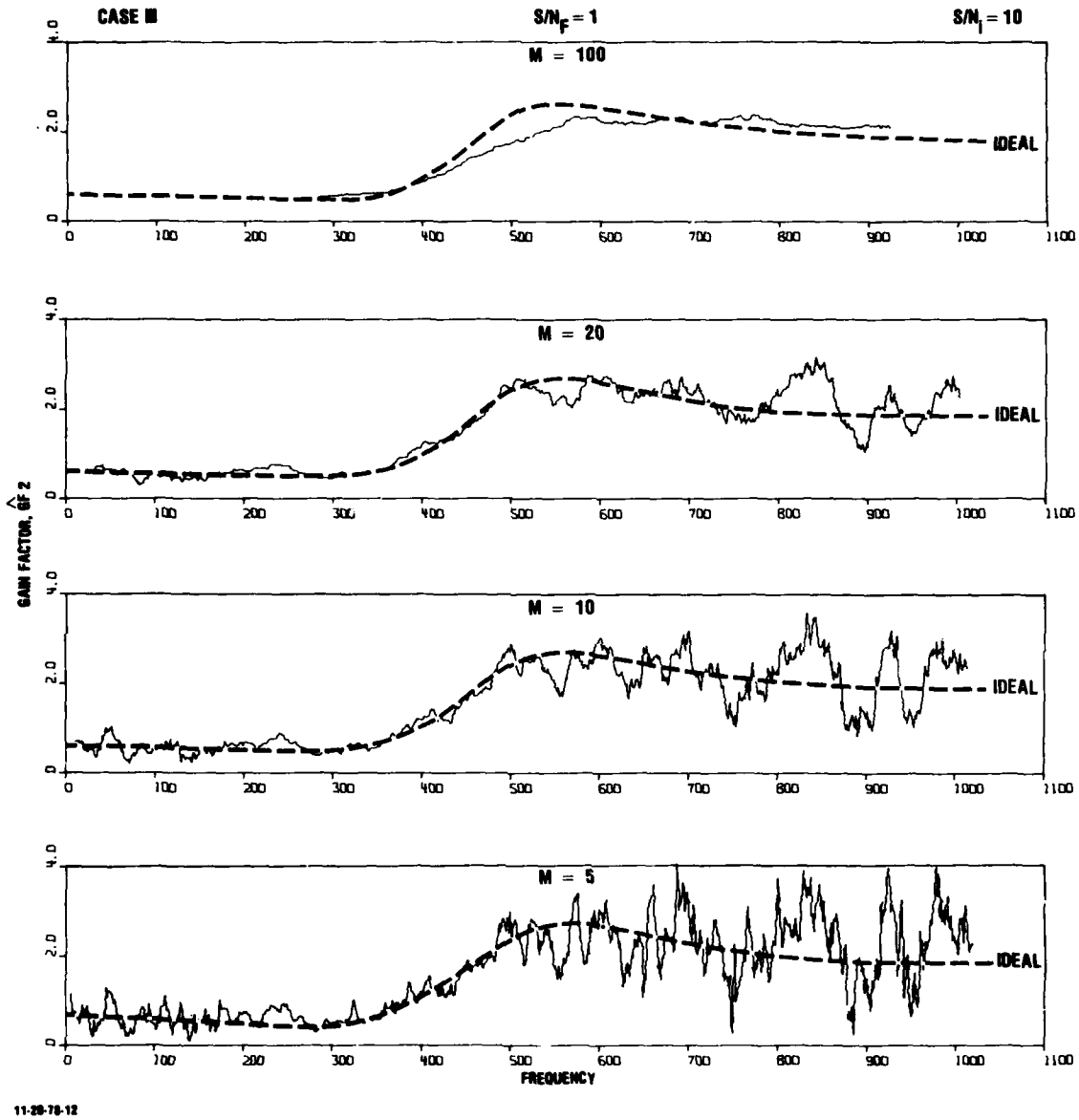

FIGURE 57. Comparison of ideal and estimated gain factors for gradiometer noise channel for broad bandwidth filters with $Lg_2/Lg_1 = 1$ for $S/N_i = 10$.

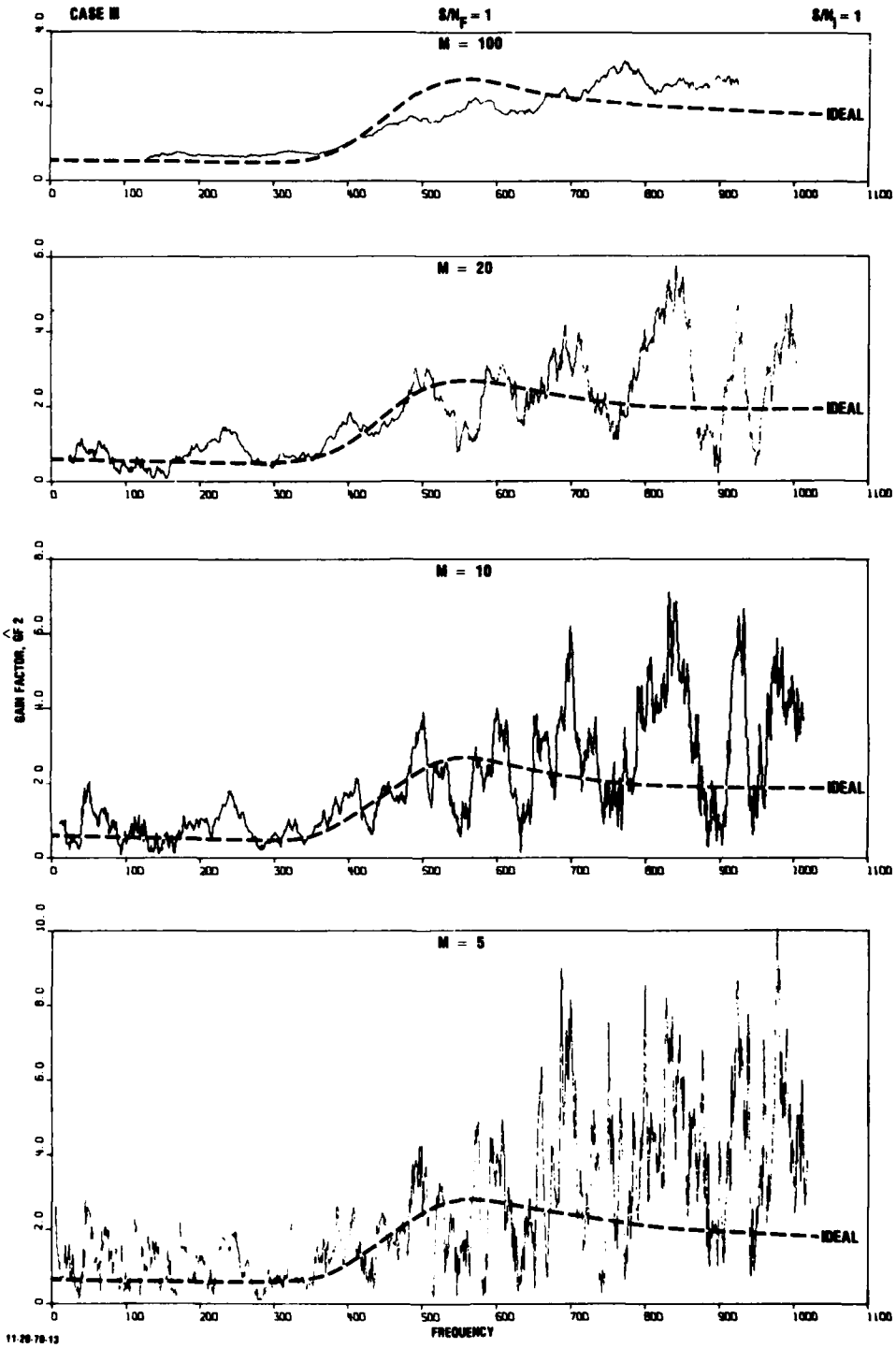

FIGURE 58. Comparison of ideal and estimated gain factors for gradiometer noise channel for broad bandwidth filters with $Lg_2/Lg_1 = 1$ for $S/N_i = 1$.

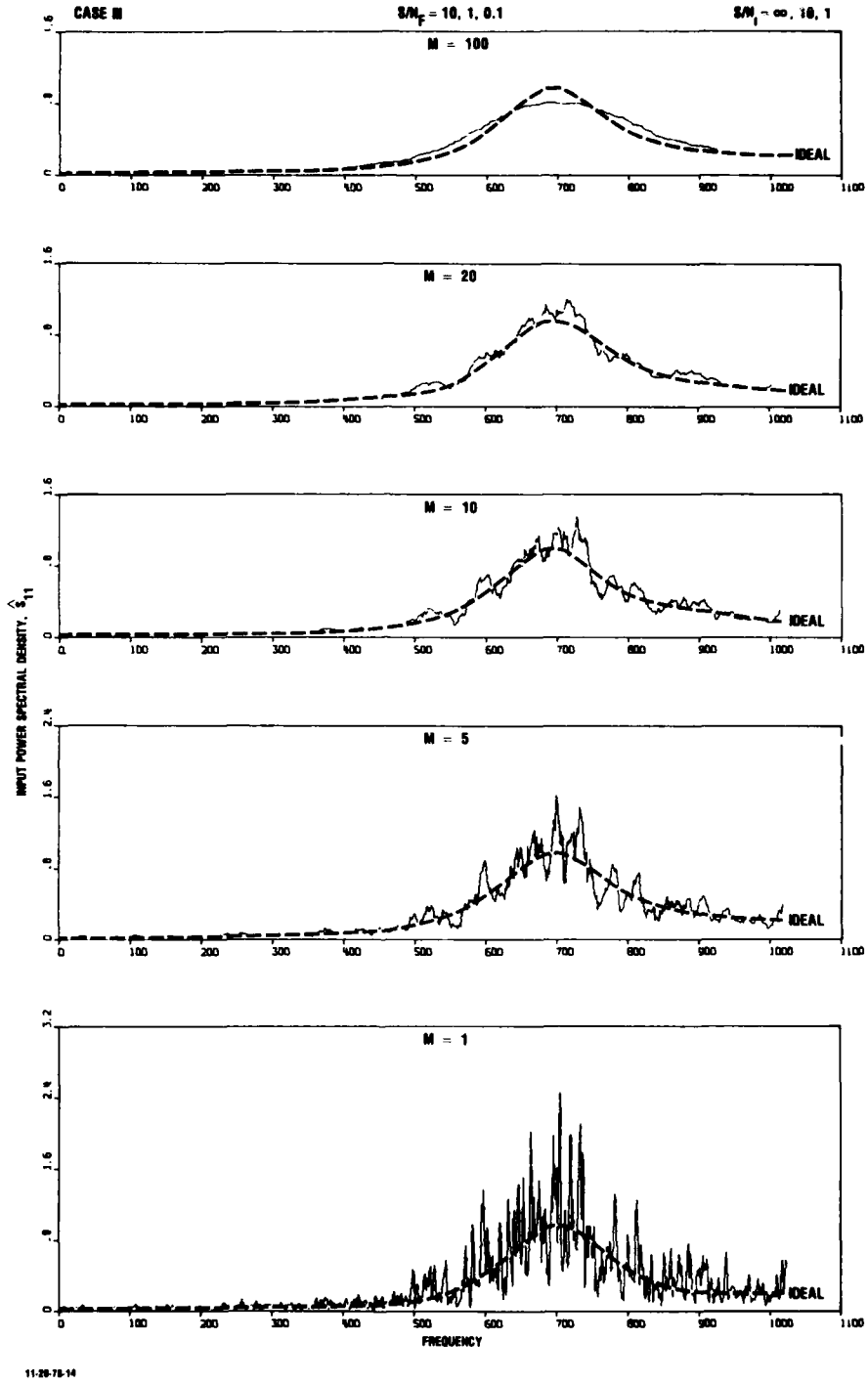

FIGURE 59. Comparison of ideal and estimator spectra for subsidiary "signal" channel for broad bandwidth filters with $Lg_2/Lg_1 = 1$.

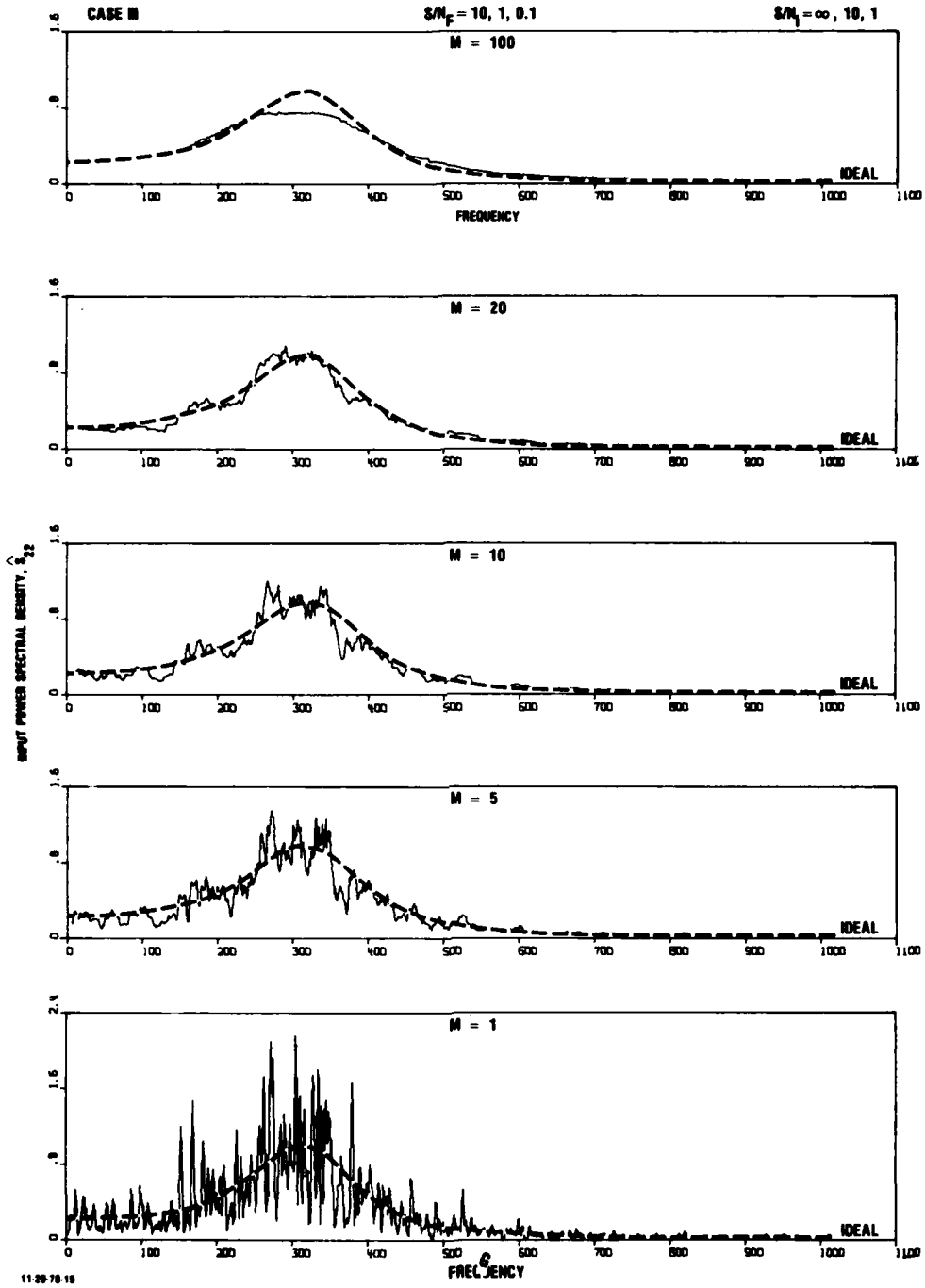

FIGURE 60. Comparison of ideal and estimator spectra for subsidiary "noise" channel for broad bandwidth filters with $Lg_2/Lg_1 = 1$.

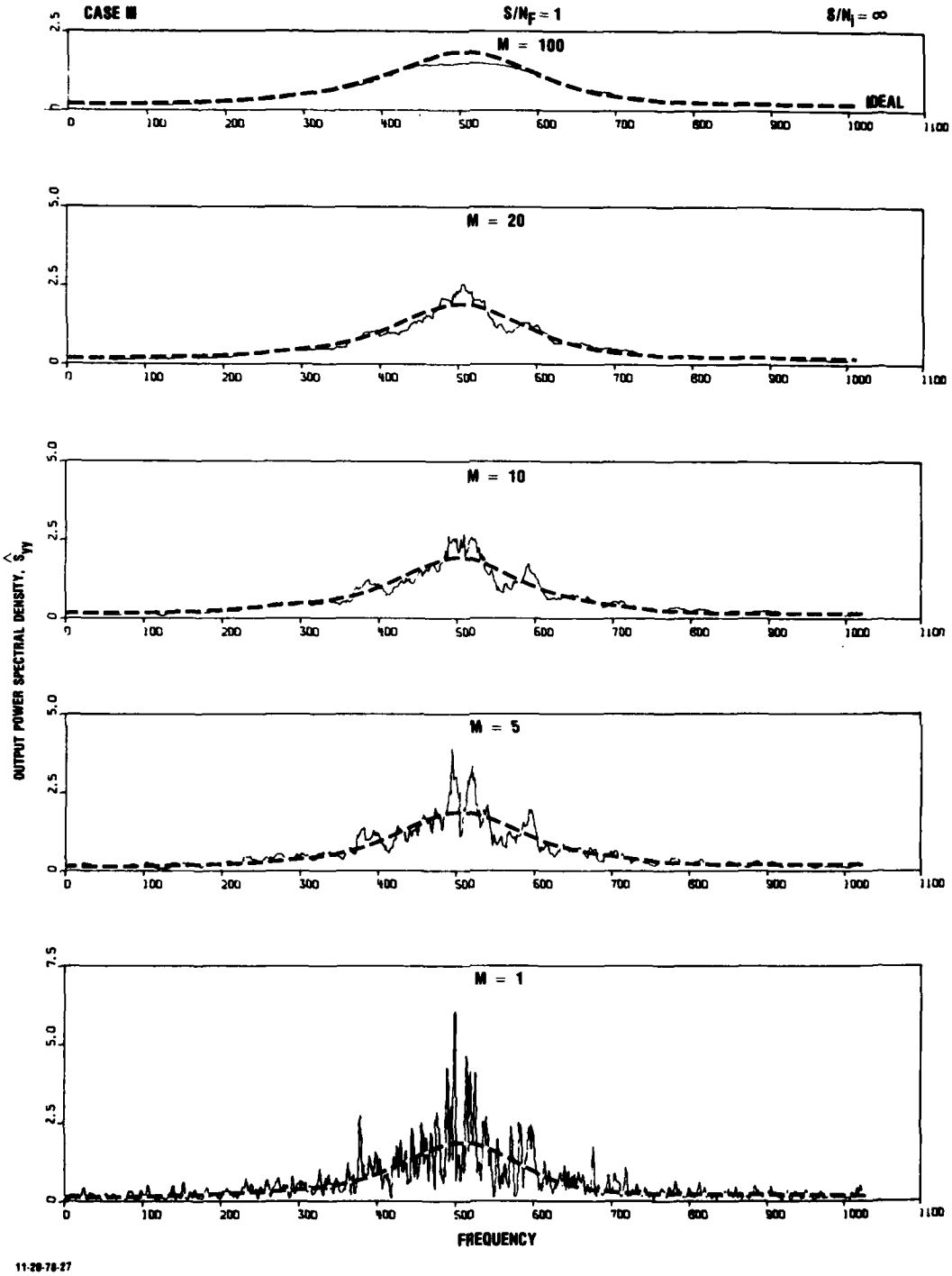

FIGURE 61. Comparison of ideal and estimator spectra for gradiometer output for broad bandwidth filters with $Lg_2/Lg_1 = 1$ for $S/N_i = \infty$.

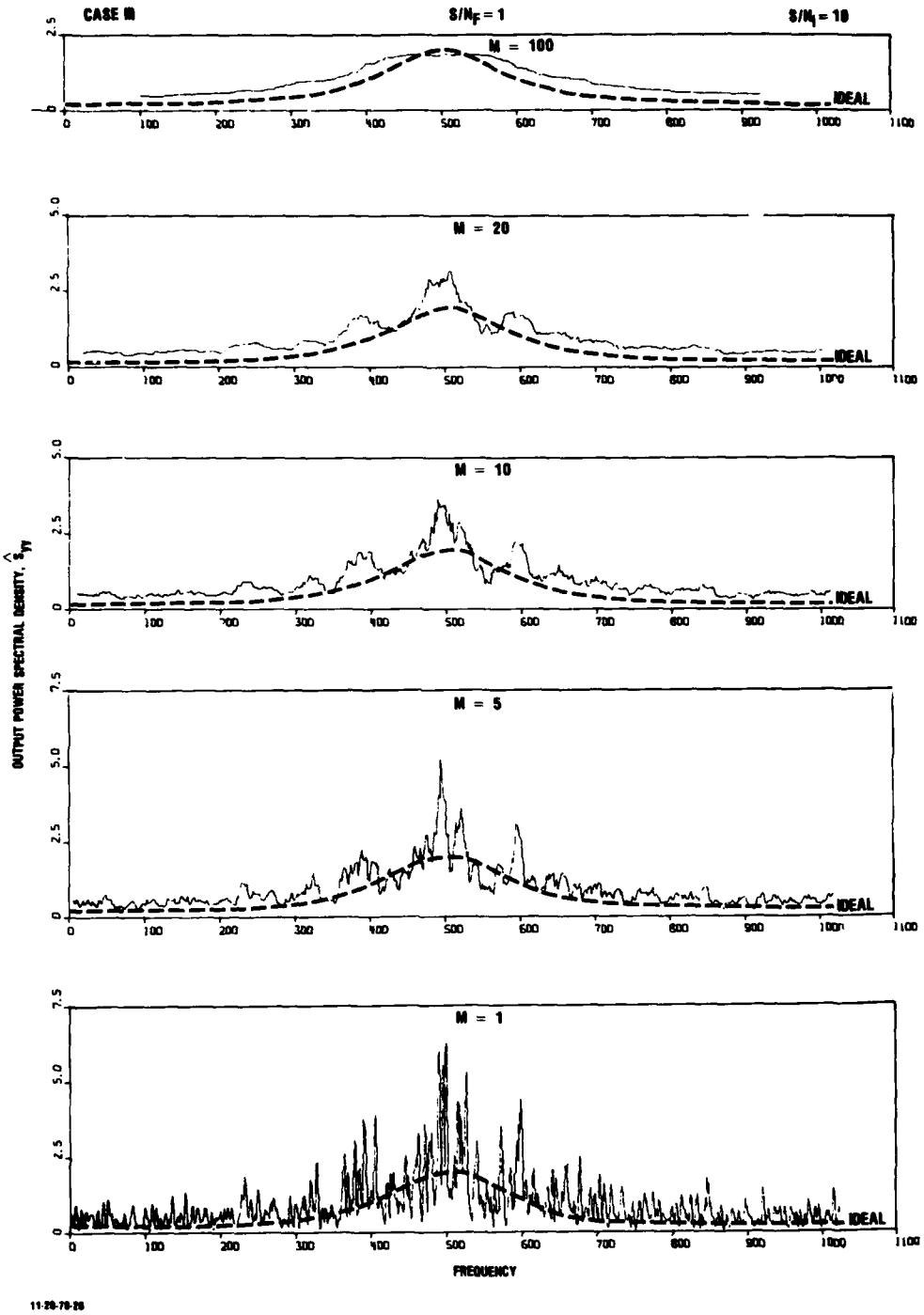

FIGURE 62. Comparison of ideal and estimator spectra for gradiometer output for broad bandwidth filters with $Lg_2/Lg_1 = 1$ for $S/N_i = 10$.

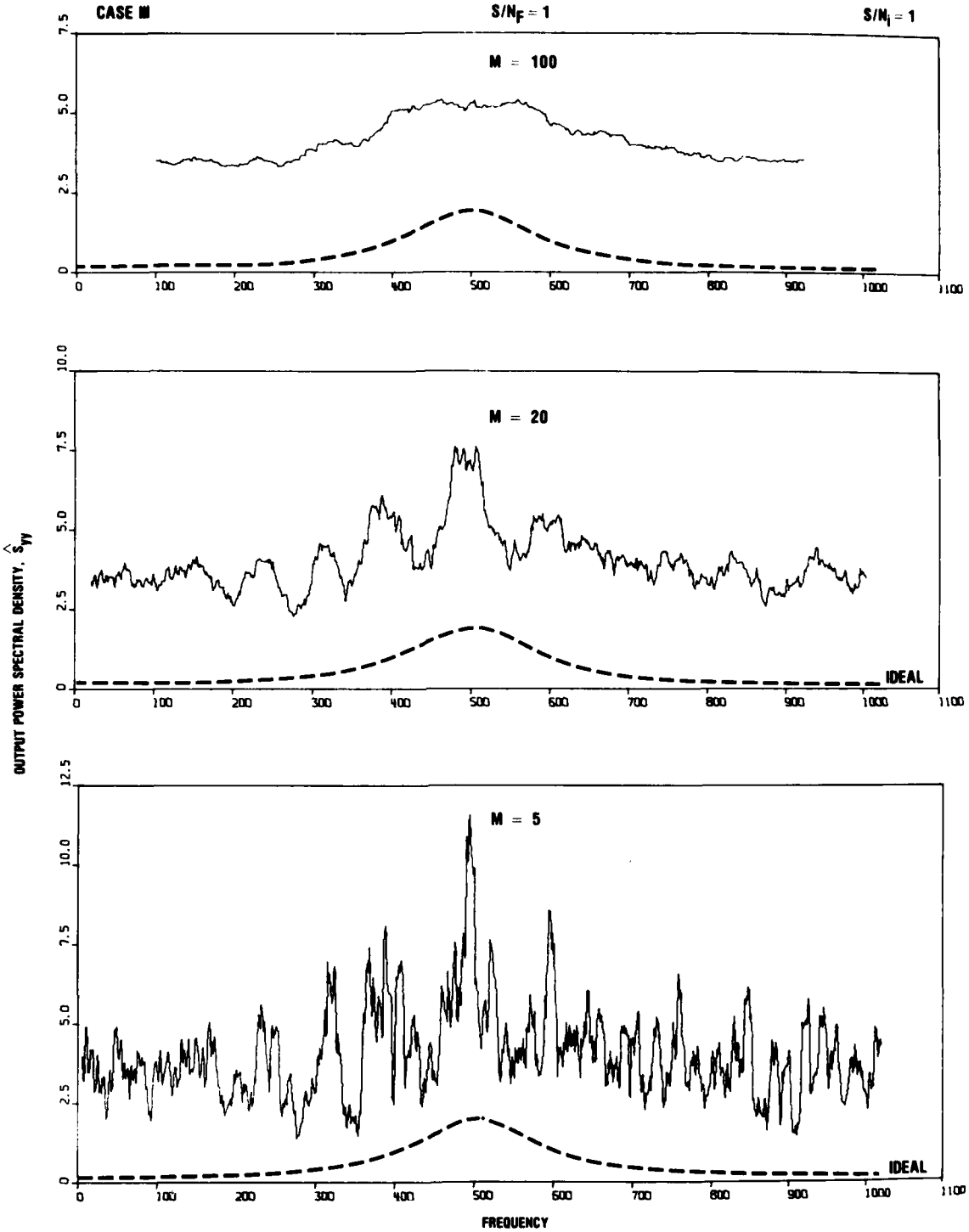

FIGURE 63. Comparison of ideal and estimator spectra for gradiometer output for broad bandwidth filters with $Lg_2/Lg_1 = 1$ for $S/N_i = 1$.

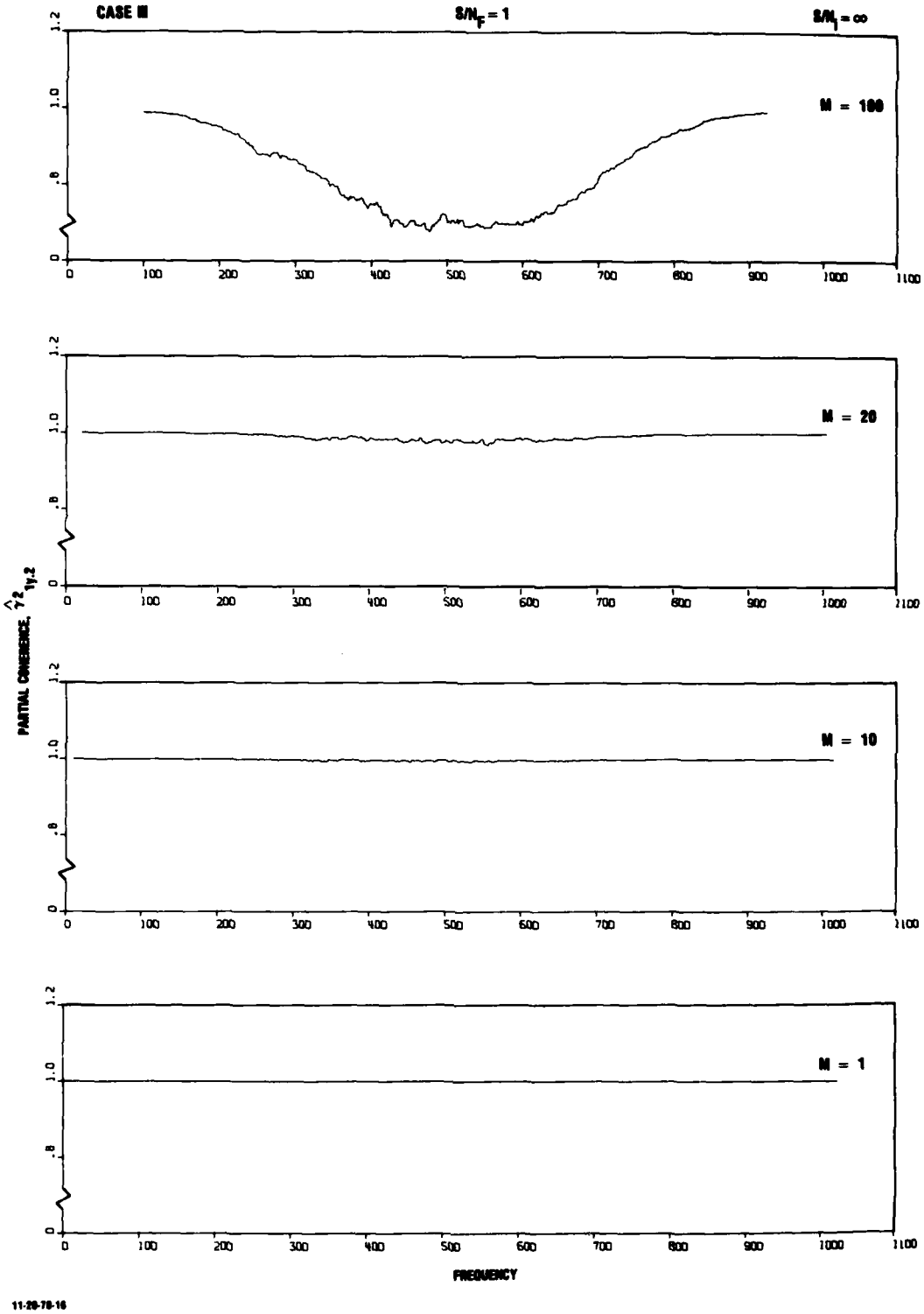

FIGURE 64. Estimated partial coherence for gradiometer signal channel for broad bandwidth filters for $Lg_2/Lg_1 = 1$ for $S/N_i = \infty$.

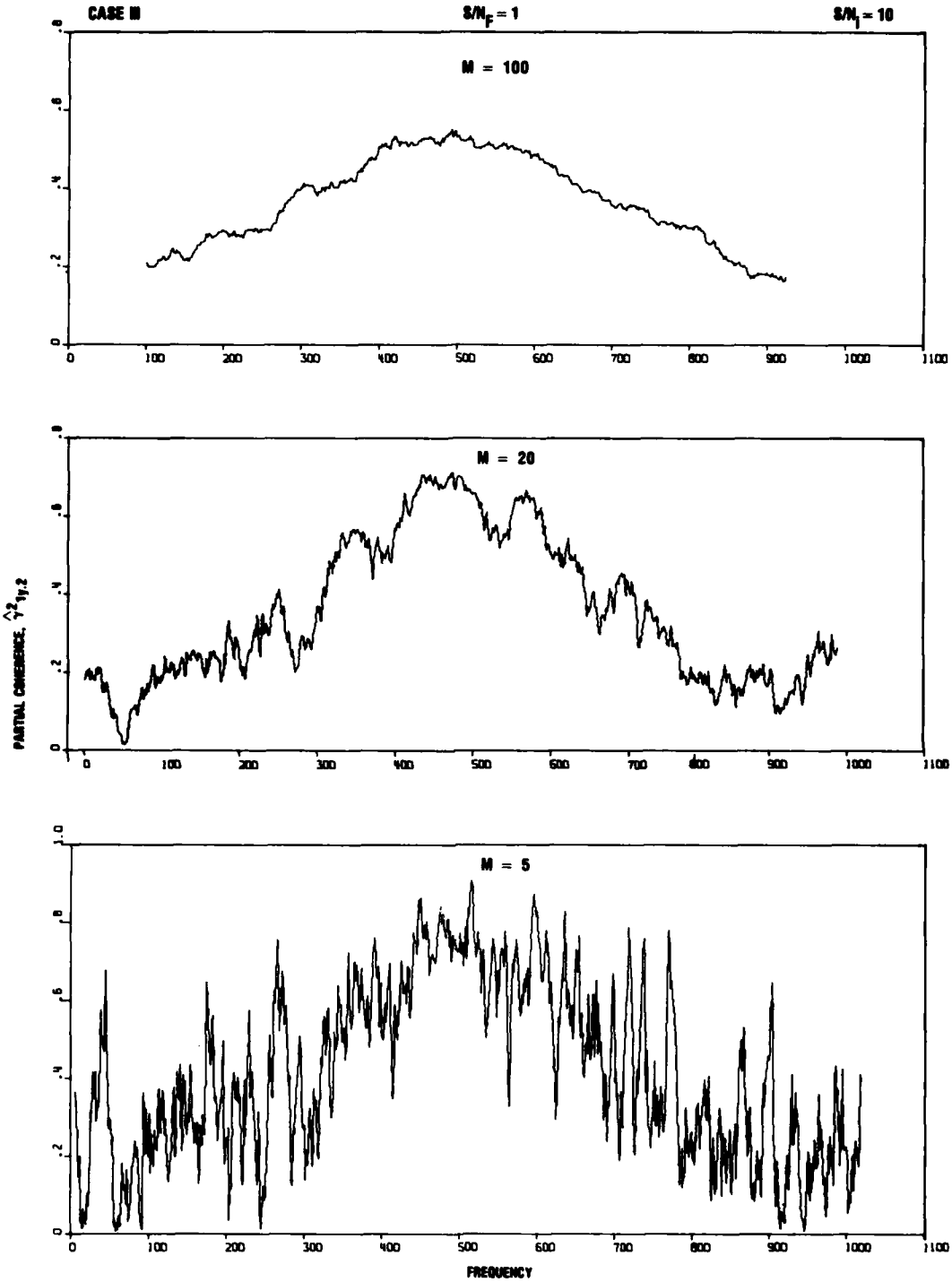

FIGURE 65. Estimated partial coherence for gradiometer signal channel for broad bandwidth filters for $Lg_2/Lg_1 = 1$ for $S/N_i = 10$.

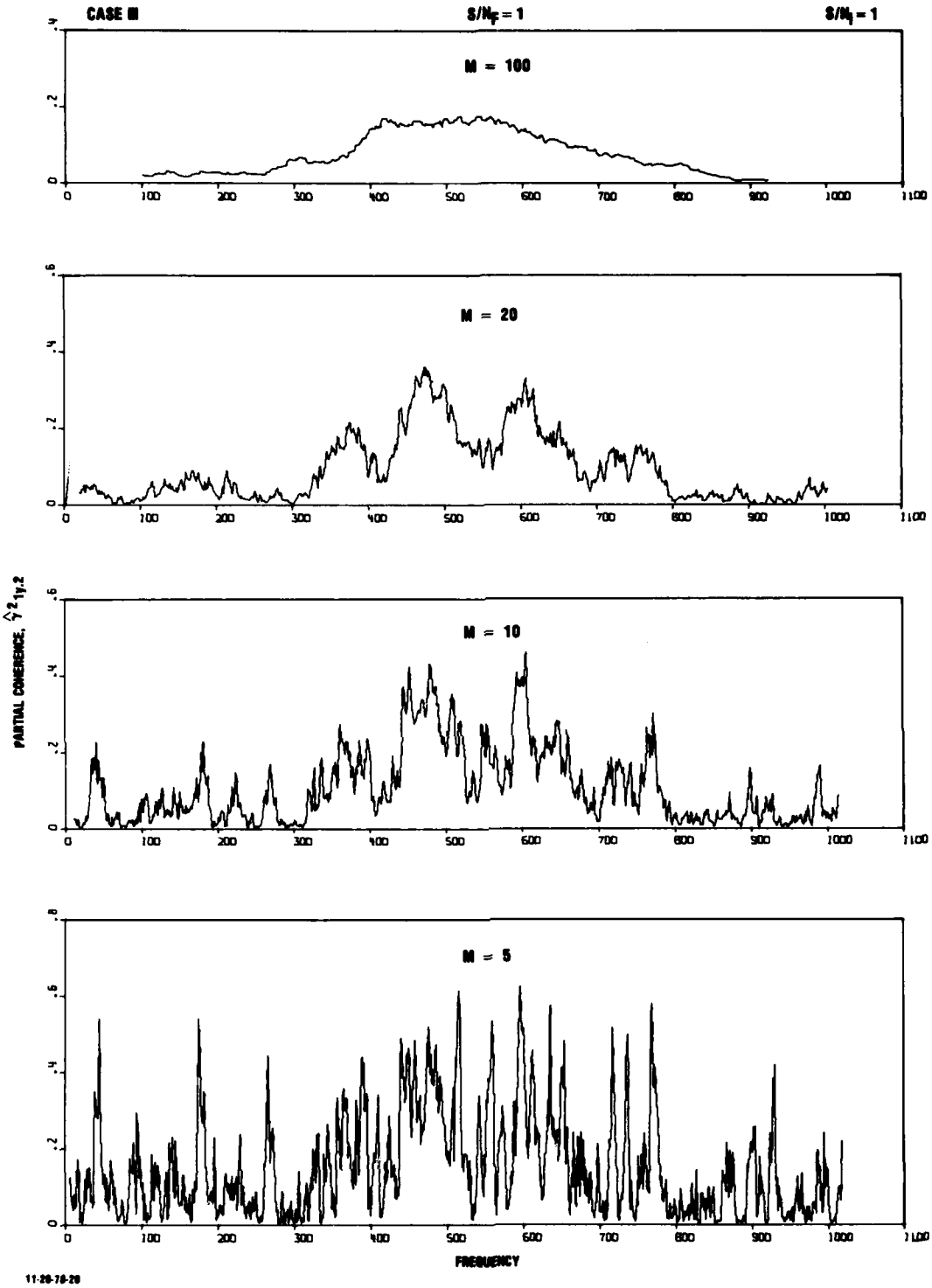

FIGURE 66. Estimated partial coherence for gradiometer signal channel for broad bandwidth filters for $Lg_2/Lg_1 = 1$ for $S/N_i = 1$.

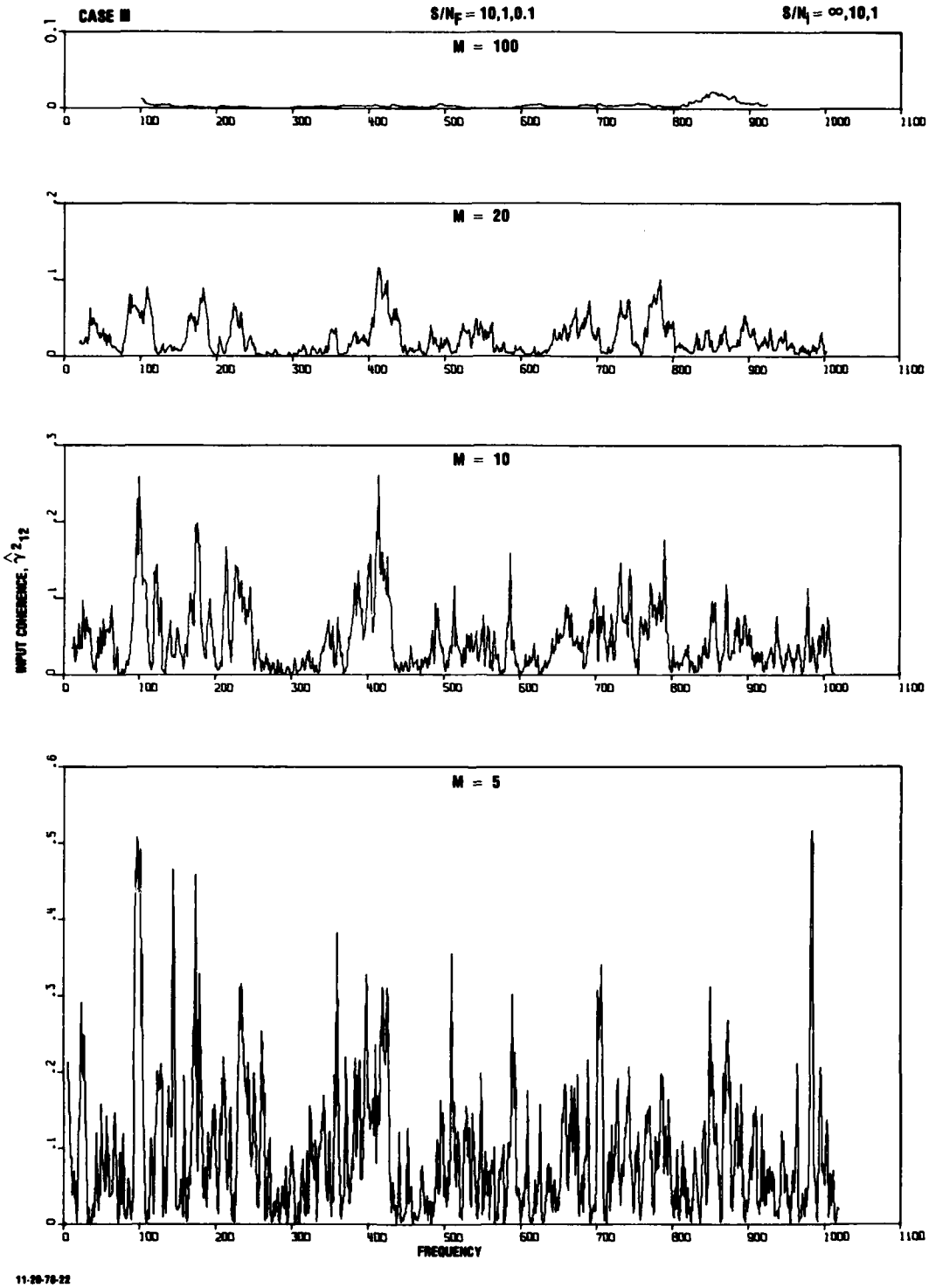

FIGURE 67. Estimated input coherence for two subsidiary channels for broad bandwidth filters with $L_{g_2}/L_{g_1} = 1$.

4.4 BROAD BANDWIDTH GRADIOMETER WITH $L_{g_2}/L_{g_1} \neq 1$

The normalized ideal spectrum for the gradiometer output, S_{yy}, for case III in Fig. 5, is identical to those for $S_{g_1g_1}$ and $S_{g_2g_2}$ because $L_{g_1} = L_{g_2}$ and the signal-to-gradiometer noise S/N_F is unity (Table 1). Since the results for this case with $S/N_i = 10$ for $S_{\xi_1\xi_1}$ (Fig. 51) and S_{yy} (Fig. 62) indicated that these spectra can potentially be reconstructed with $0.2 < M/(B/2) < 1$, it becomes of interest to investigate if the algorithm could do likewise for other shapes of the gradiometer spectra. In order to test this possibility, a similar case was considered by displacing L_{g_2} from 500 to 600 so as to change the shape of the S_{yy} spectra from that of its two components $S_{g_1g_1}$ and $S_{g_2g_2}$. This modified case is shown as case IVa, b, c in Fig. 5 and Table 1, which included two subcases so as to vary the bandwidth noise ratio, which were taken as $S/N_F = 10$ and 0.1 for the ideal condition of no instrument noise (Table 1). These two values of the S/N_F ratio would introduce relative opposite changes in the $S_{g_1g_1}$ and $S_{g_2g_2}$ spectra, and hence produce significant changes in the amplitude of S_{yy}. Figures 68-81 describe in the subsequent subsections the results for cases IVa, b, c in Fig. 5, which are characterized by $L_{g_2} = 600$, $L_{g_1} = 500$, $L_{g_2}/L_{g_1} = 1.2$ and $B/2 = 100$.

4.4.1 Gradiometer Signal-to-Noise of Unity

Because case IVa is very similar to the previous one with broad bandwidth and $L_{g_2}/L_{g_1} = 1$, the estimates for the gradiometer signal spectra and transfer functions are omitted. Figures 68-70 show the estimator $\hat{S}_{yy}$ for the case with a broad bandwidth and $L_{g_2}/L_{g_1} = 1.2$ as a function of frequency averaging and the three signal-to-instrument noise ratios. A comparison of the results for $S/N_i = 10$ (Fig. 69) with the corresponding one for the previous case (Fig. 62) shows a better match in the shapes of the ideal (S_{yy}) and estimator ($\hat{S}_{yy}$) spectra for $M/(B/2) = 1$, as a result of the less pronounced shape of S_{yy} caused by the shift of L_{g_2} away from L_{g_1}. Figures 71-73 show the estimated

partial coherences for the gradiometer signal channel as a function of signal-to-instrument noise ratio, results that are similar to those for the previous case (Figs. 64-66).

4.4.2 Effects of Gradiometer Signal-to-Noise Ratio

The effects of gradiometer signal-to-noise ratio are given by the two subcases with $S/N_F = 10$ and $S/N_F = 0.1$ for $S/N_i = \infty$. Figures 74-77 show results for $S/N_F = 10$ for the gradiometer signal spectrum, the gradiometer output spectrum, the gain factor for the gradiometer "noise" channel and the partial coherence of the gradiometer signal channel, respectively, whereas Figs. 78-81 do likewise for $S/N_F = 0.1$.

- A comparison of Figs. 74 and 75 for the gradiometer signal and output spectra for $L_{g_2}/L_{g_1} = 1.2$ and $S/N_F = 10$ with those for $L_{g_2}/L_{g_1} = 1$ and $S/N_F = 1$ (Figs. 50, 61) indicate (a) no significant difference in the relative bias of the gradiometer signal for $M/(B/2) = 1$, because the filter output $x_{g_1}(t)$ in Fig. 2 is unaffected by the gradiometer "noise" parameter $\sqrt{F}$, and (b) no significant improvement in the matching of ideal and estimator spectra for the gradiometer output.
- A comparison of Fig. 76 for the gain factor of the gradiometer channel for $S/N_F = 10$ with the corresponding one for the previous case with $S/N_F = 1$ (Fig. 56) shows only that the amplitude of the gain factor for $S/N_F = 10$ has decreased by a factor of about 1/4 from that for $S/N_F = 1$.
- A comparison of Fig. 77 for the estimated partial coherence for $S/N_F = 10$ with the corresponding one for the previous case with $L_{g_2}/L_{g_1} = 1$ and $S/N_F = 1$ (Fig. 64) shows no significant difference in the deviation of the partial coherence from unity for $S/N_i = \infty$.

- A comparison of the results for $S/N_F = 0.1$ (Figs. 78-81) with the corresponding ones for $S/N_F = 10$ (Figs. 74-77) indicate (a) no significant difference in the gradiometer signal, (b) a significant increase in the amplitude of the gradiometer spectra by almost an order of magnitude for $S/N_F = 0.1$ (Fig. 79) relative to that for $S/N_F = 10$ (Fig. 75), (c) a similar corresponding increase in the amplitude of the gain factor for the gradiometer noise channel for $S/N_F = 0.1$ (Fig. 80) relative to that for $S/N_F = 10$ (Fig. 76), and (d) a pronounced enhancement in the deviation from unity in the estimated partial coherence for $S/N_F = 0.1$ (Fig. 81) as compared with that for $S/N_F = 10$ (Fig. 77).

4.5 RECOVERY OF PARTIAL COHERENCE FROM S/N_i RATIO

For the ideal case of no instrument noise ($S/N_i = \infty$), the fidelity of the reconstruction of the gradiometer output, $\hat{y}(t)$, requires that the partial coherence be unity at any frequency (Eq. 114 or 46, 59-61). However, the previous results for $S/N_i = \infty$ and $M/(B/2) \approx 1$ (as required for detectability of the gradiometer signal spectra) indicate that the partial coherence deviates from unity independently of the frequency characteristics of the specified spectra (Figs. 24, 46, 64, 71) and for gradiometer signal-to-noise ratios as high as $S/N_F = 10$ (Fig. 77). Furthermore, the previous results for a signal-to-instrument noise ratio that is significantly above the threshold of signal detectability (i.e. $S/N_i = 10$) indicate a rather drastic collapse of the partial coherence away from unity (Figs. 25, 47, 65, 72). Hence, it becomes of interest to determine the magnitude of the highest signal-to-instrument noise ratio for a recovery of the partial coherence to the values given by the ideal case of $S/N_i = \infty$. Figures 82-87 show these results for the cases considered in Fig. 5. These figures indicate the following:

- Figures 82 and 83 for the narrow-band, low-frequency gradiometers considered in cases I and II (Table 1), respectively, show that signal-to-instrument noise ratios as high as $S/N_i = 10^4$ fail to recover the partial coherence toward unity.
- Figures 84 to 87 for the broad-band, high-frequency gradiometers considered in cases III and IV (Table 1), show that signal-to-instrument noise ratios in the range $10^2 < S/N_i < 10^3$ are required to recover the partial coherence toward unity.

The foregoing results are of great significance for practical applications, since such extremely high signal-to-instrument noise ratios would be required for the successful processing of time series data even in the case that it would become possible to extract the estimated spectra with minimum bias; i.e., when the partial coherence for $S/N_i = \infty$ would indeed become unity by removing the bias of the spectral densities in Eq. (68) for a multi-channel linear system as given by Eq. (15) instead of the more general form of Eq. (14).

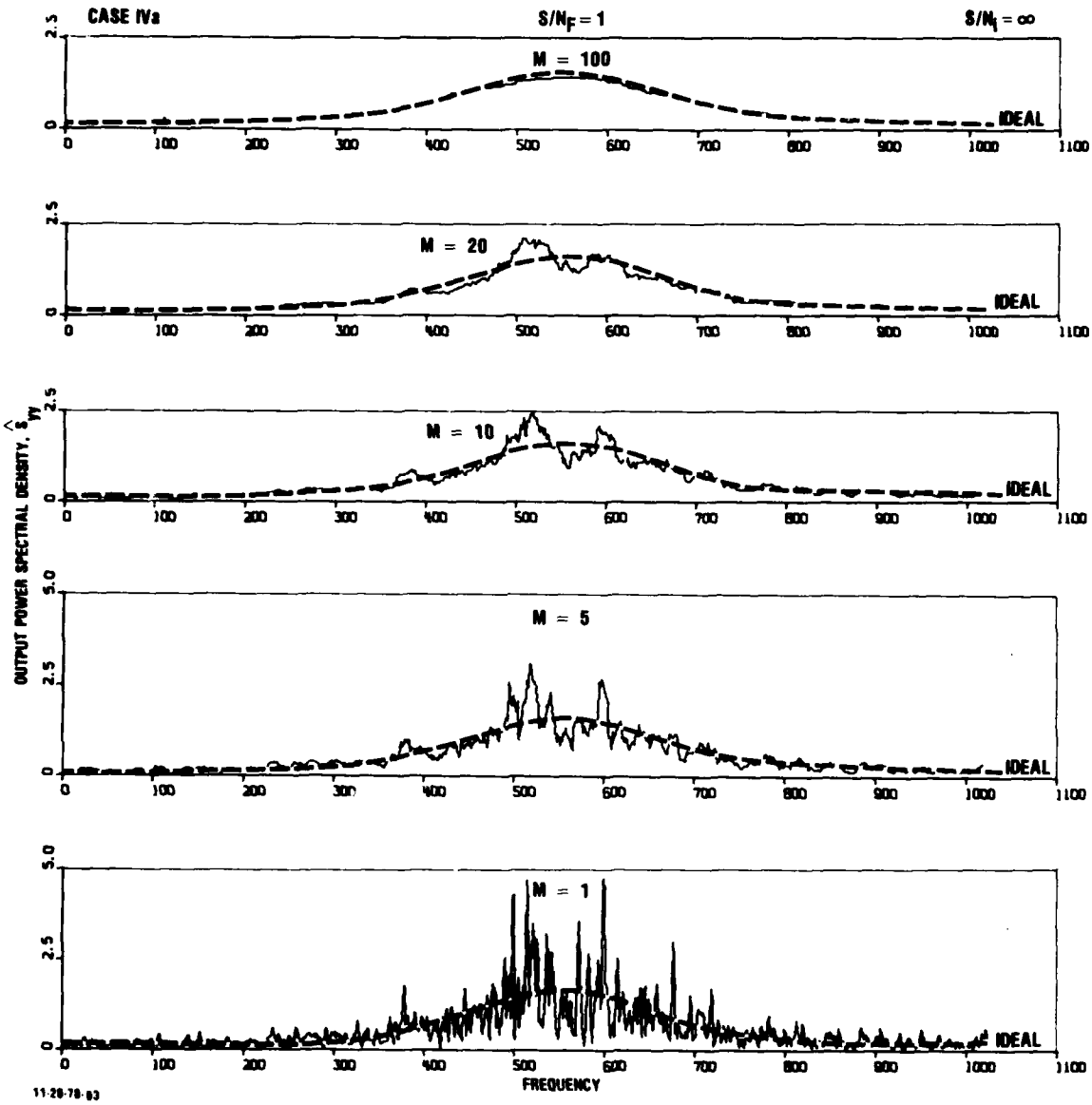

FIGURE 68. Comparison of ideal and estimator spectra for gradiometer output for broad bandwidth filters with $Lg_2/Lg_1 = 1.2$ for $S/N_i = \infty$.

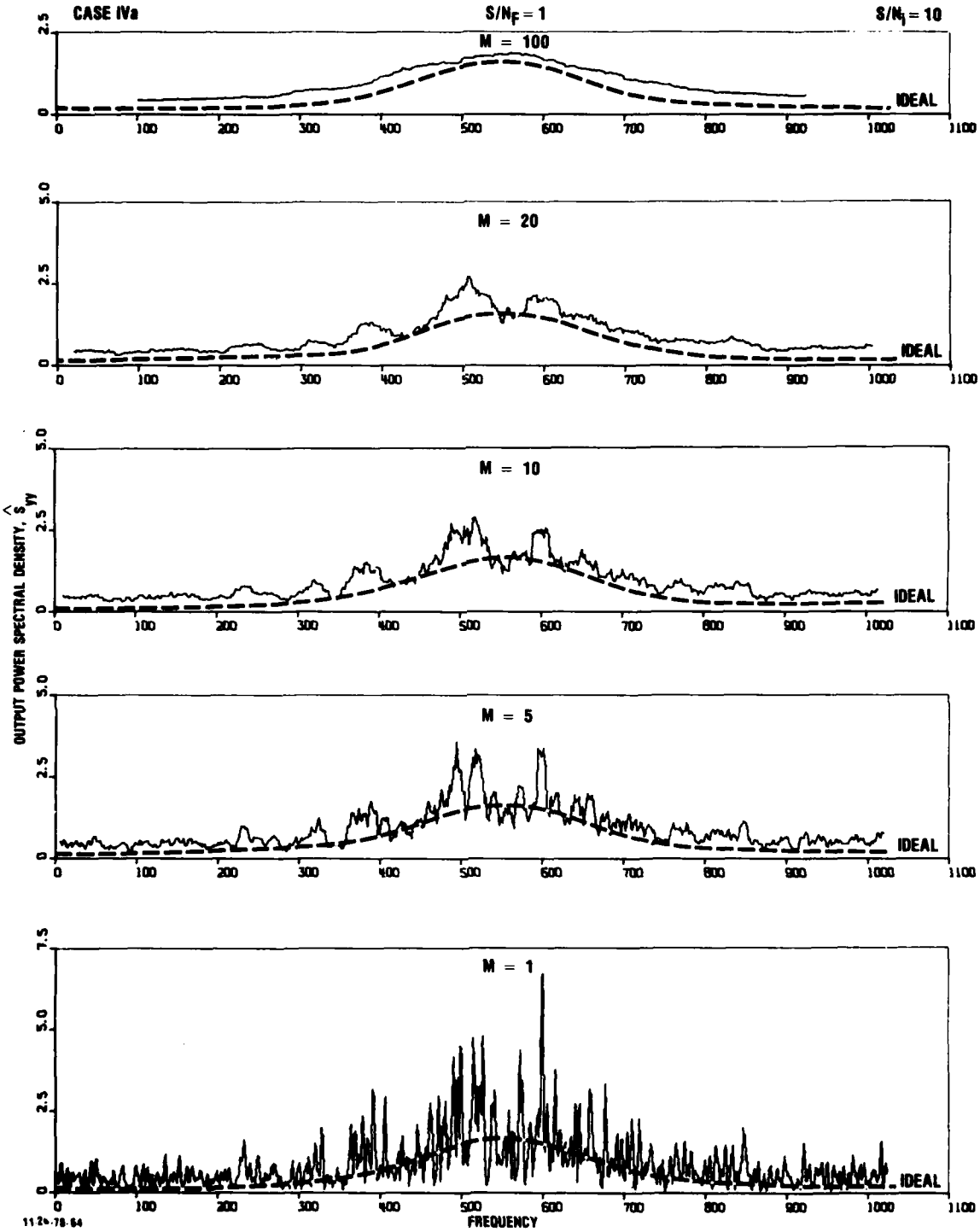

FIGURE 69. Comparison of ideal and estimator spectra for gradiometer output for broad bandwidth filters with $Lg_2/Lg_1 = 1.2$ for $S/N_i = 10$.

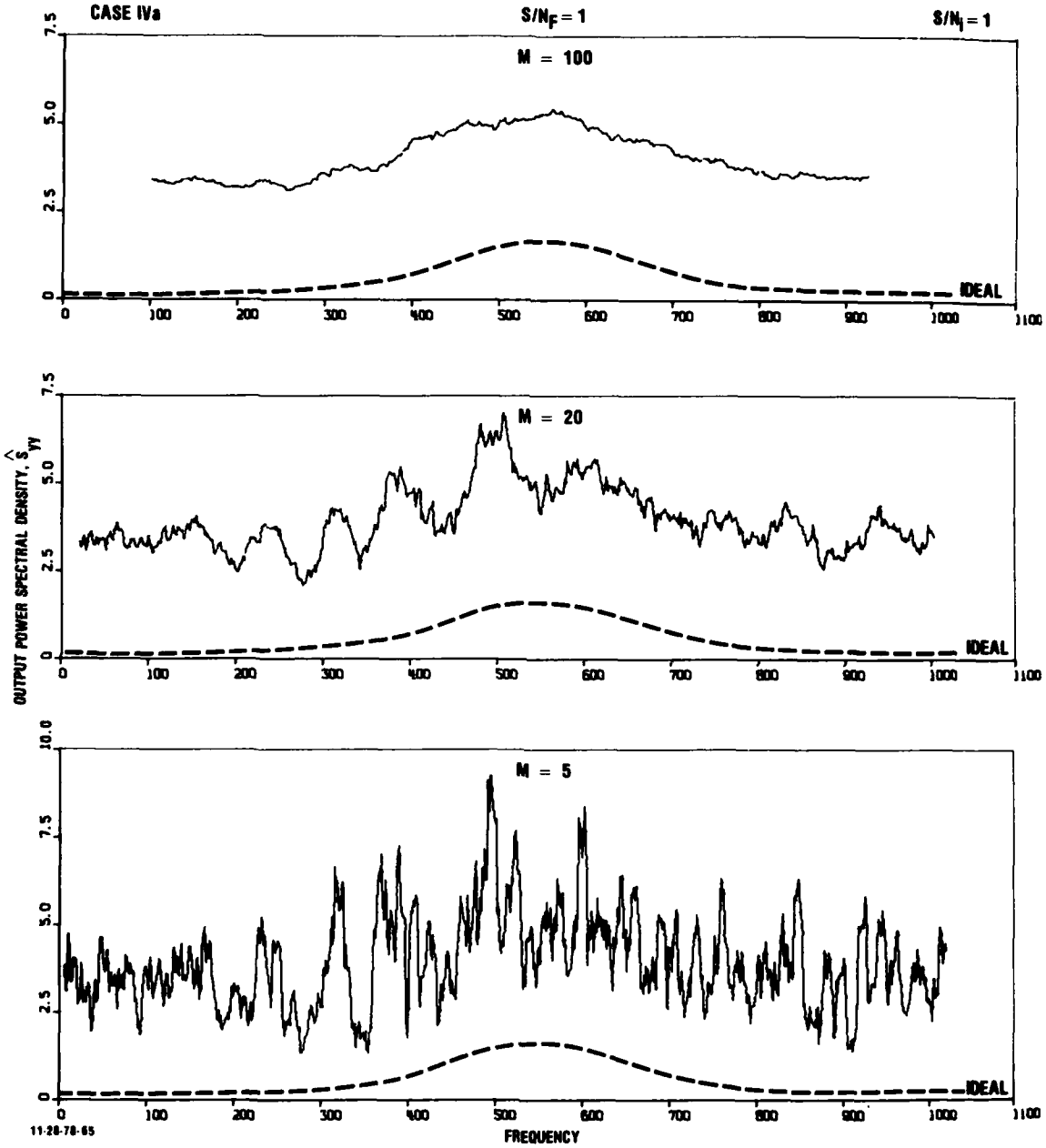

FIGURE 70. Comparison of ideal and estimator spectra for gradiometer output for broad bandwidth filters with Lg_2/Lg_1 = 1.2 for S/N_i = 1.

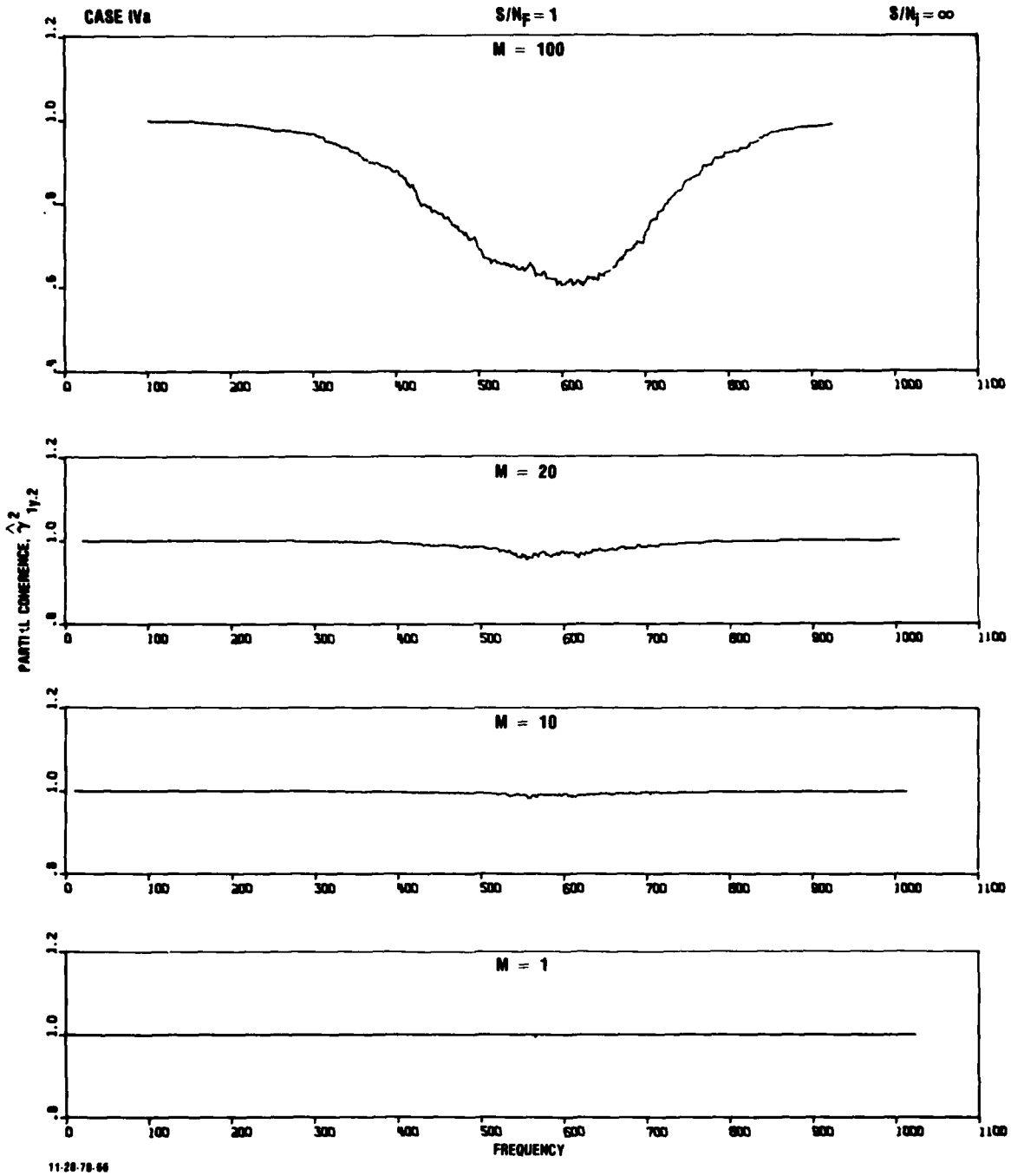

FIGURE 71. Estimated partial coherence for gradiometer signal channel for broad bandwidth filters for Lg_2/Lg_1 = 1.2 for S/N_i = ∞.

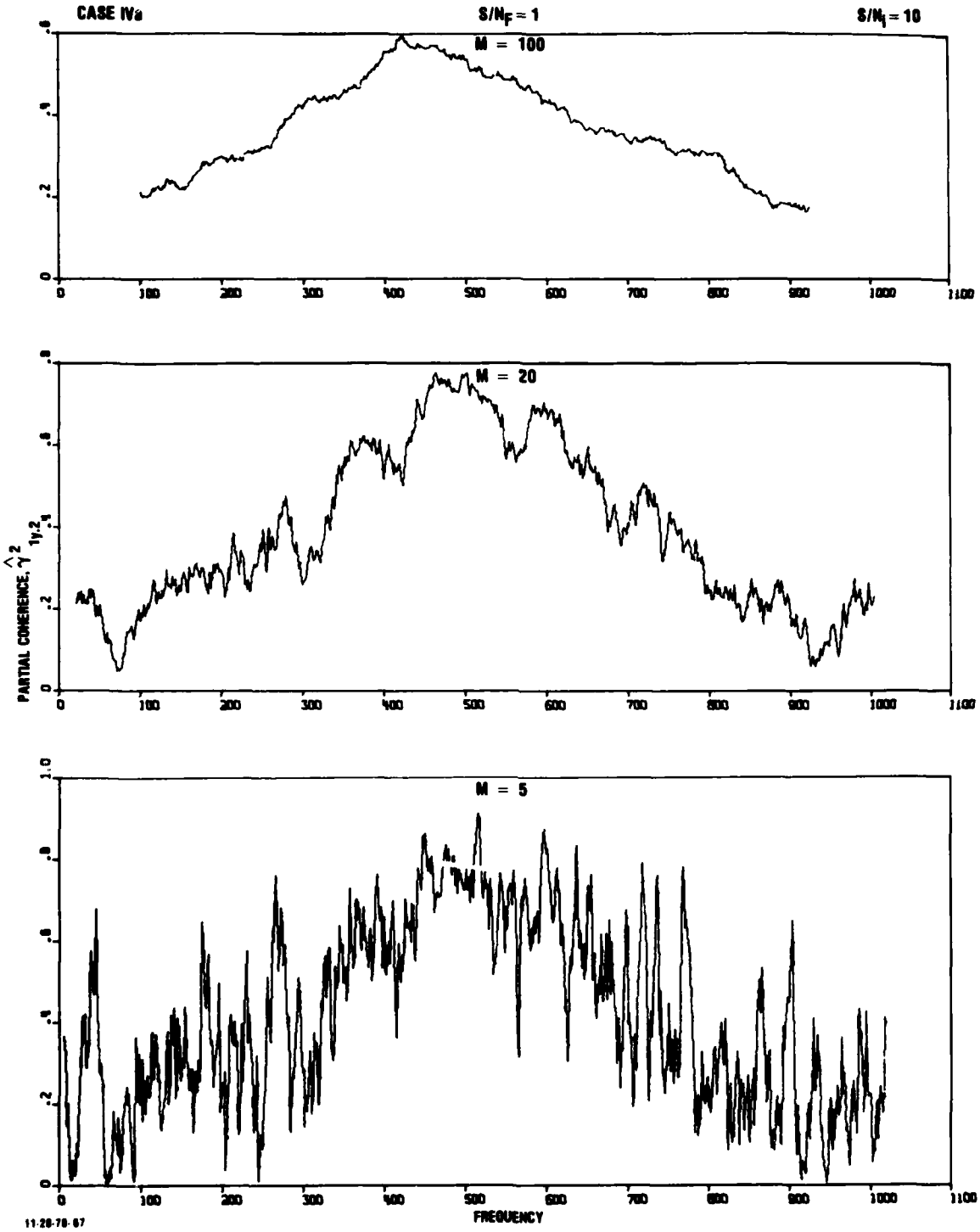

FIGURE 72. Estimated partial coherence for gradiometer signal channel for broad bandwidth filters for Lg_2/Lg_1 = 1.2 for S/N_i = 10.

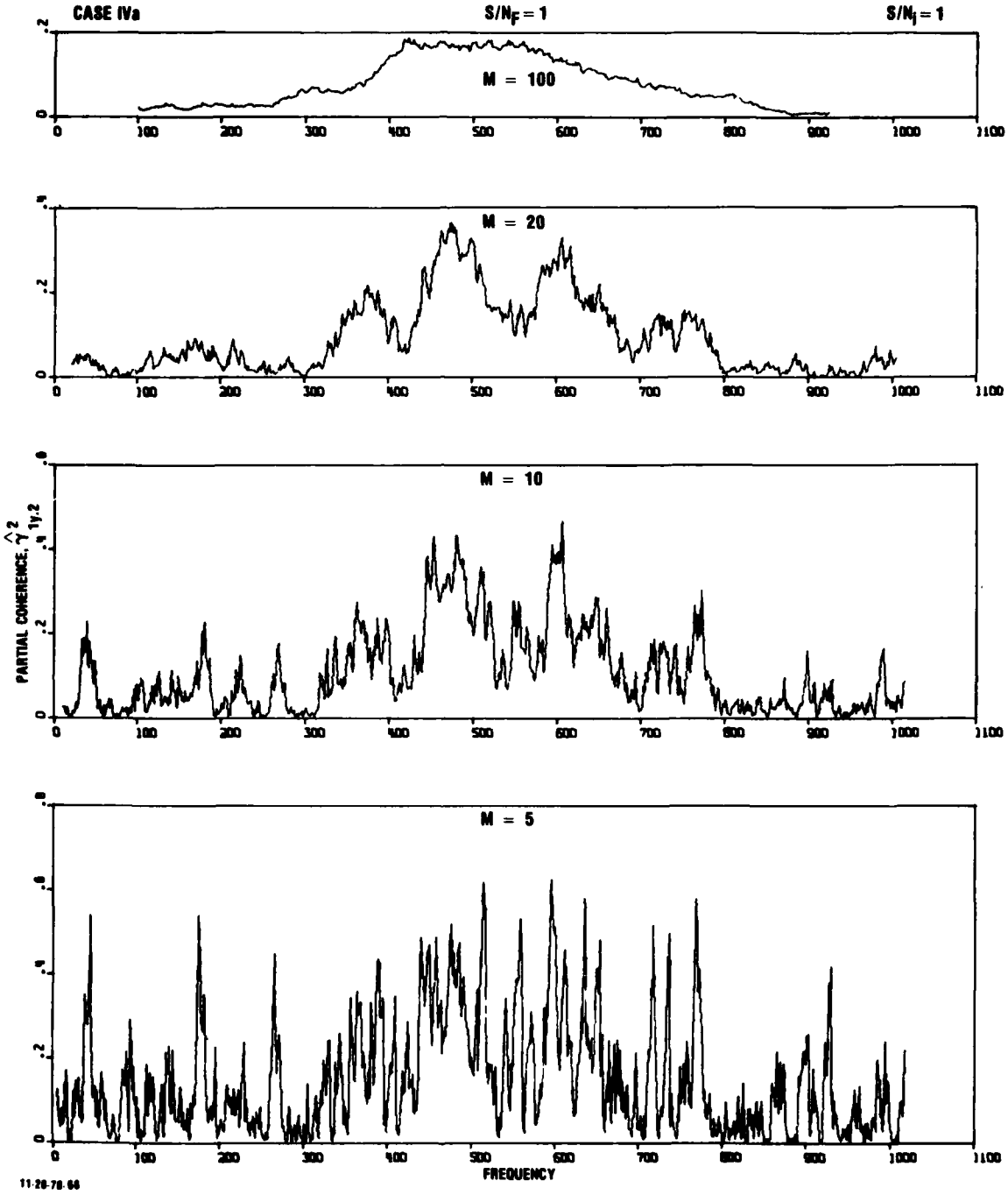

FIGURE 73. Estimated partial coherence for gradiometer signal channel for broad bandwidth filters for Lg_2/Lg_1 = 1.2 for S/N_1 = 1.

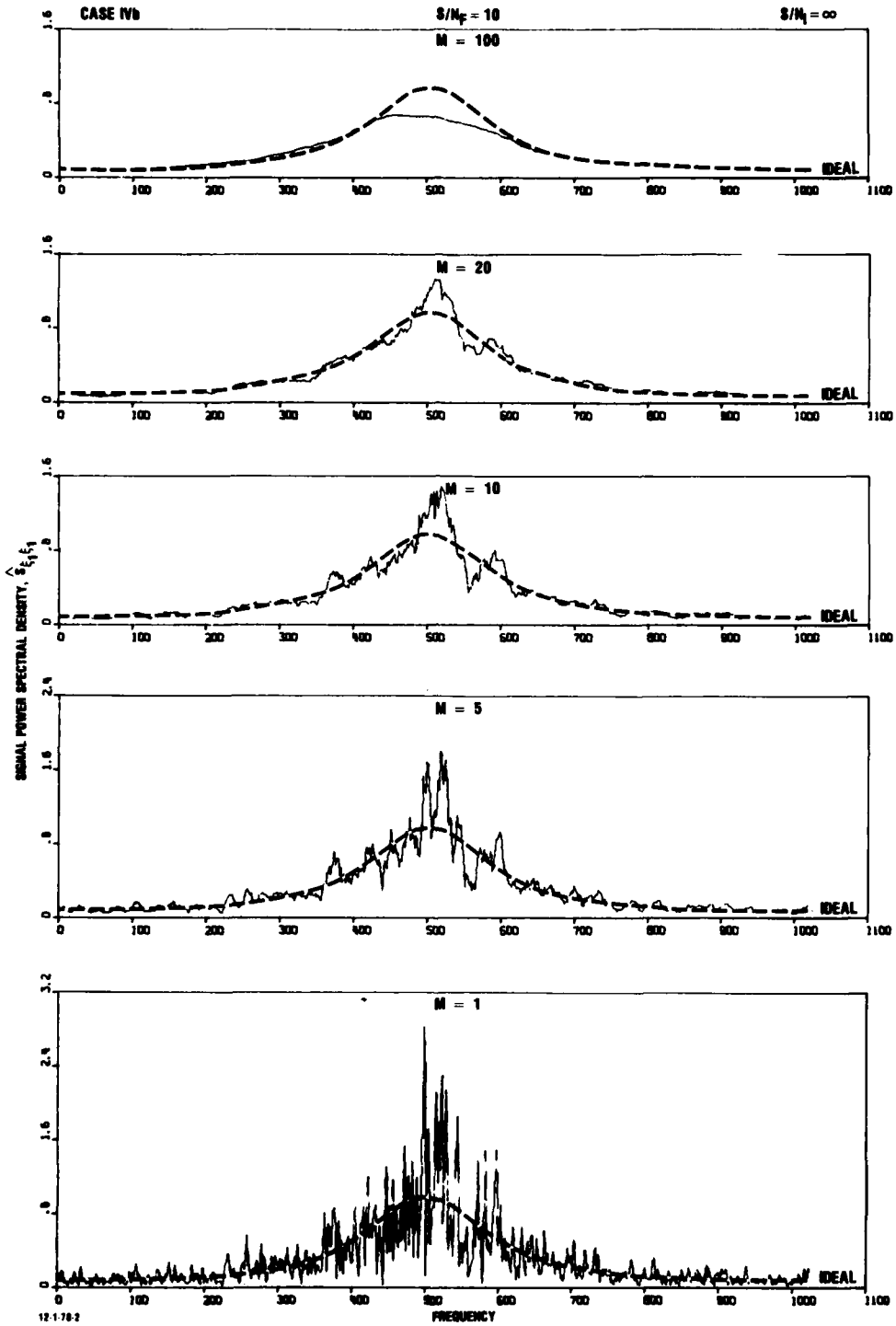

FIGURE 74. Comparison of ideal and reconstructed signal spectra for broad bandwidth filters with $Lg_2/Lg_1 = 1.2$ for $S/N_F = 10$.

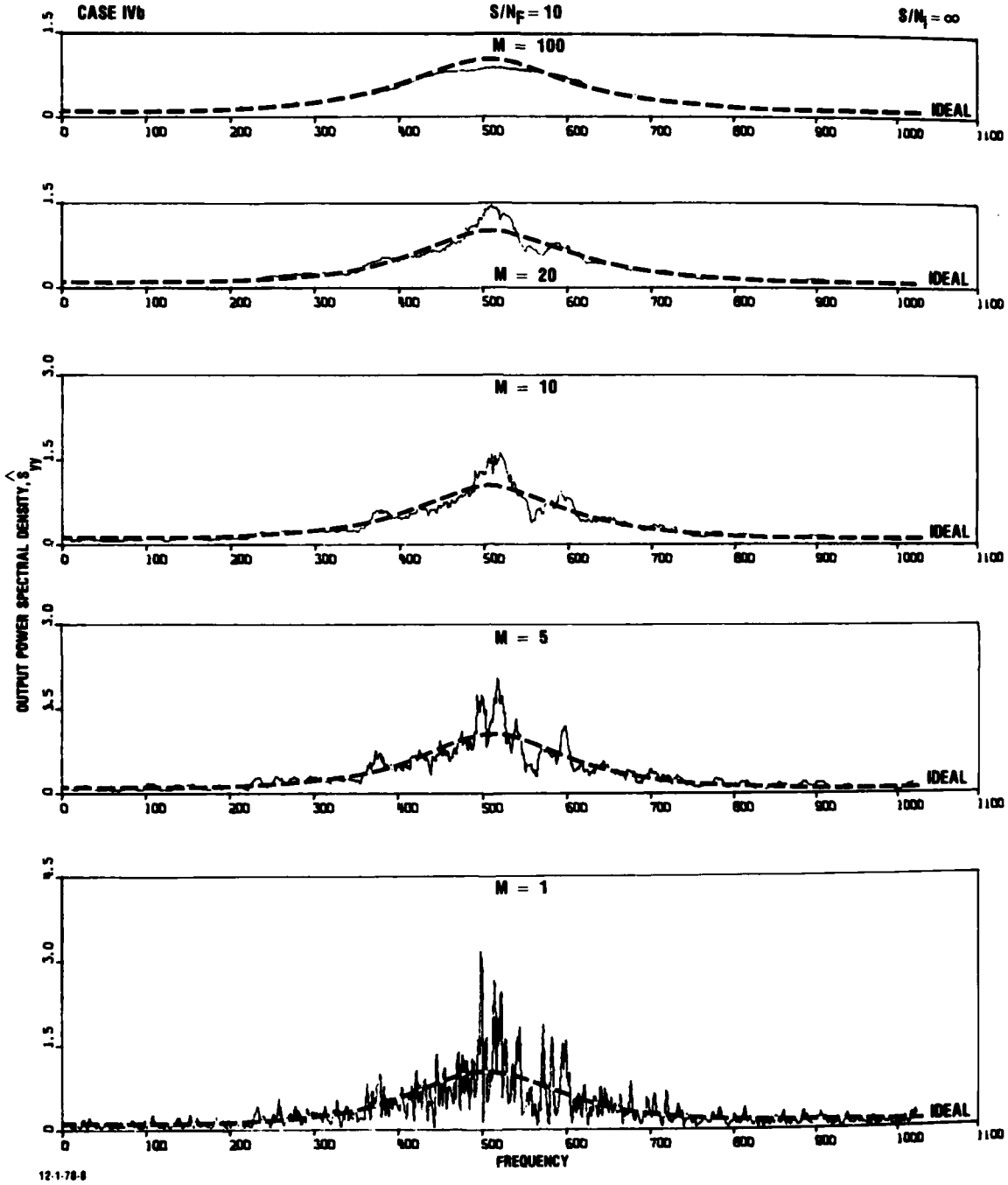

FIGURE 75. Comparison of ideal and estimator spectra for gradiometer output for broad bandwidth filters with $Lg_2/Lg_1 = 1.2$ for $S/N_F = 10$.

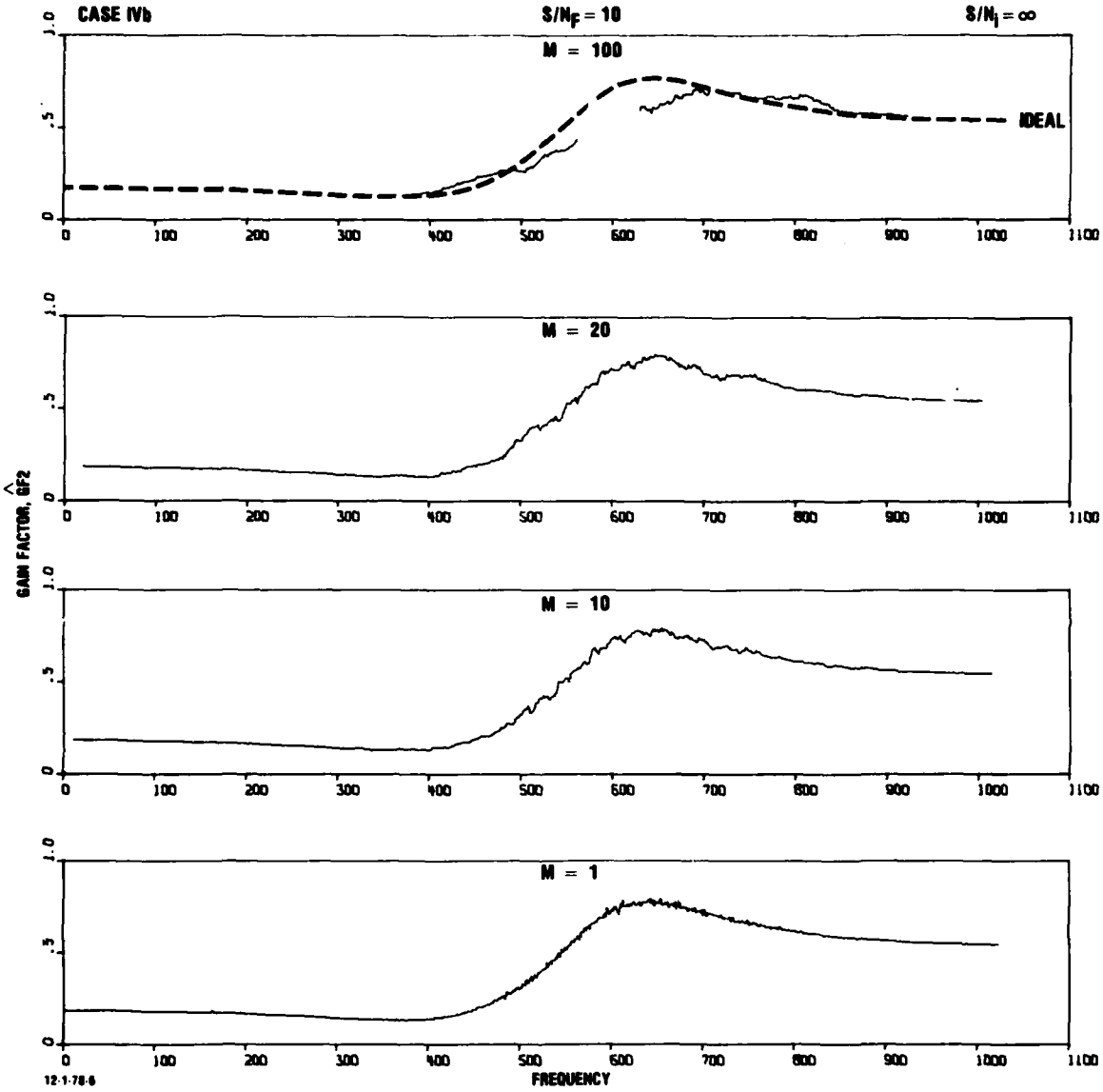

FIGURE 76. Comparison of ideal and estimated gain factor for gradiometer noise channel for broad bandwidth filters with Lg_2/Lg_1 = 1.2 for S/N_F = 10.

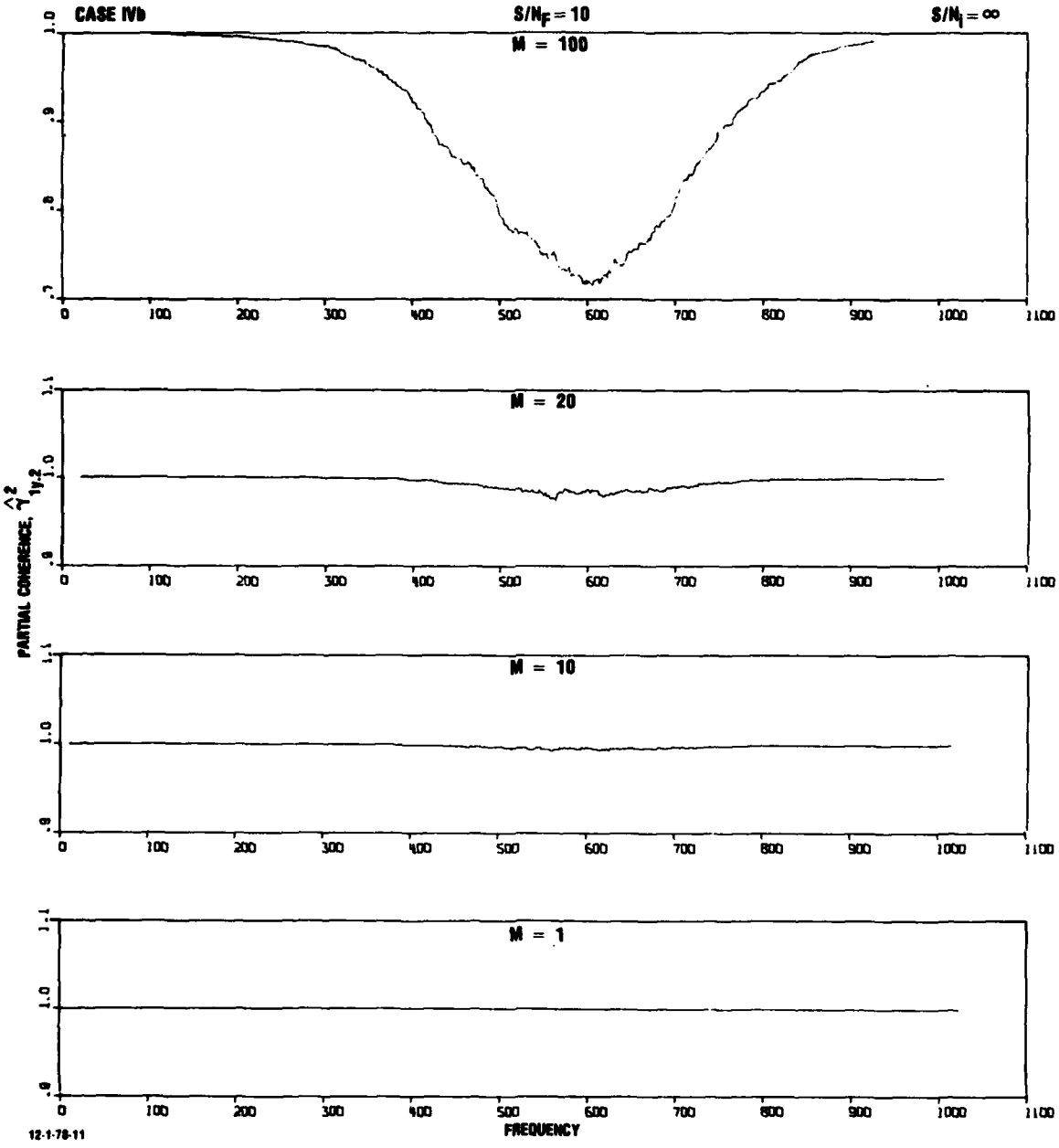

FIGURE 77. Estimated partial coherence for gradiometer signal channel for broad bandwidth filters with Lg_2/Lg_1 = 1.2 for S/N_F = 10.

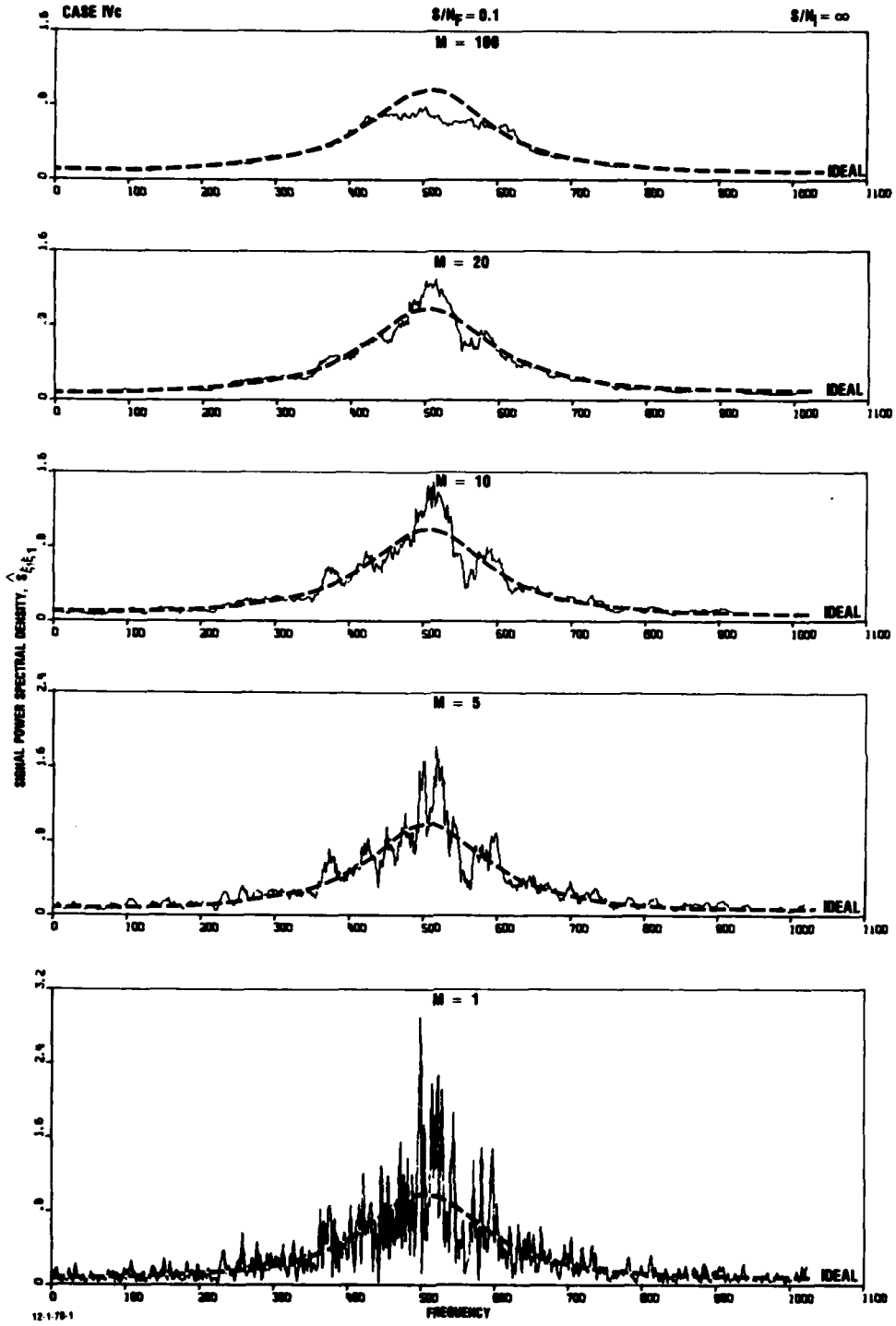

FIGURE 78. Comparison of ideal and reconstructed signal spectra for broad bandwidth filters with $Lg_2/Lg_1 = 1.2$ for $S/N_F = 0.1$.

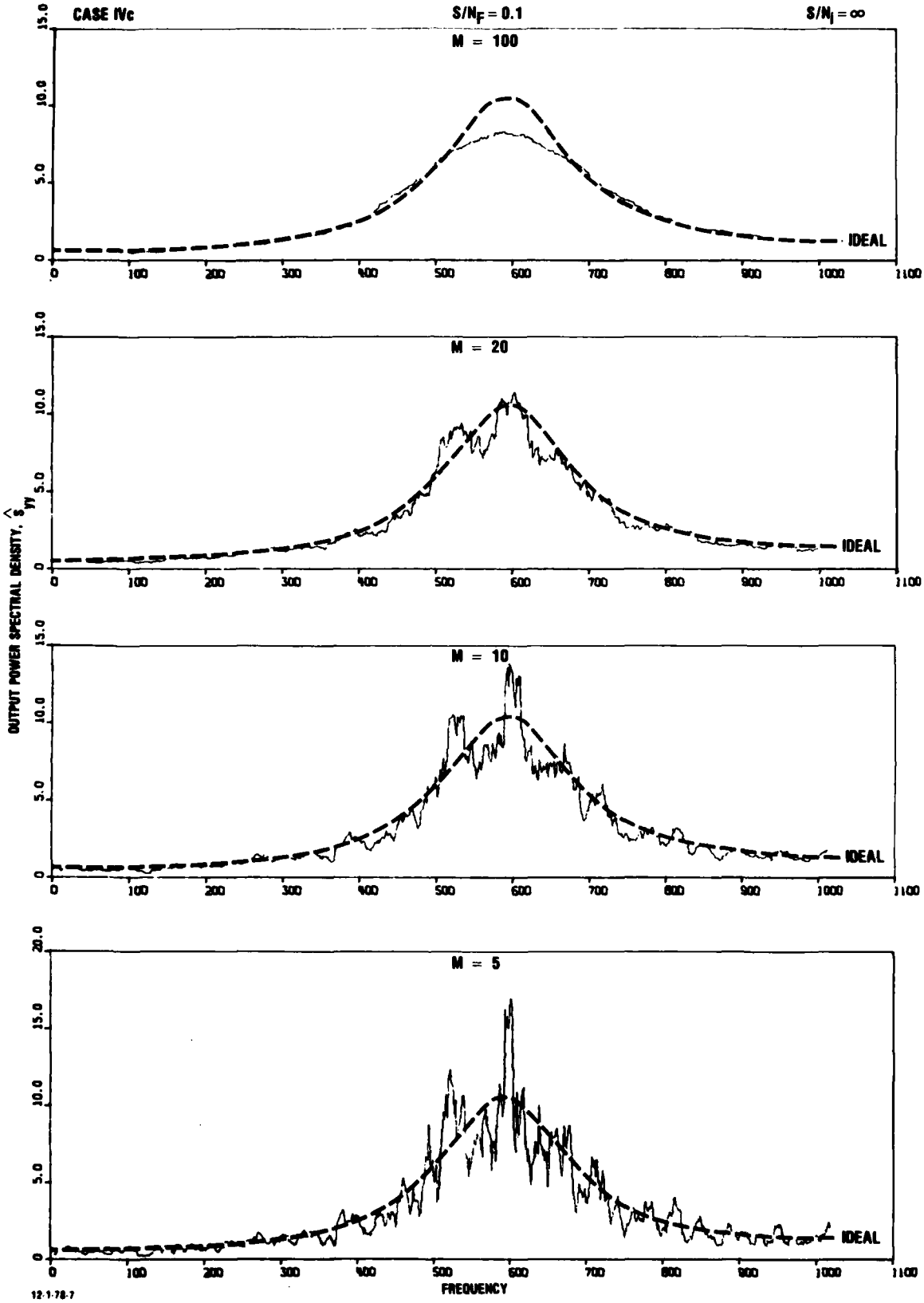

FIGURE 79. Comparison of ideal and estimator spectra for gradiometer output for broad bandwidth filters with Lg_2/Lg_1 = 1.2 for S/N_F = 0.1.

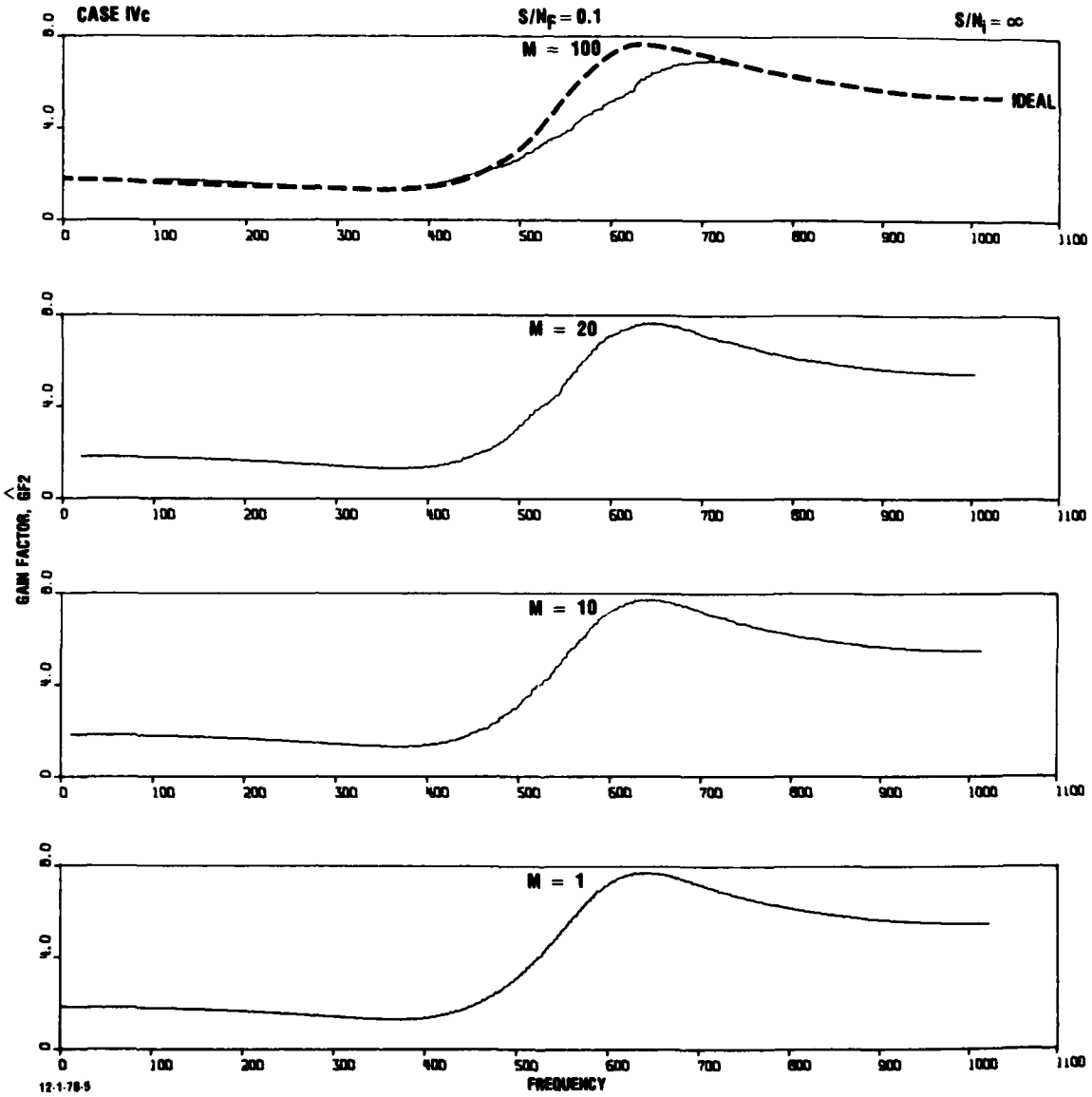

FIGURE 80. Comparison of ideal and estimated gain factor for gradiometer noise channel for broad bandwidth filters with Lg_2/Lg_1 = 1.2 for S/N_F = 0.1.

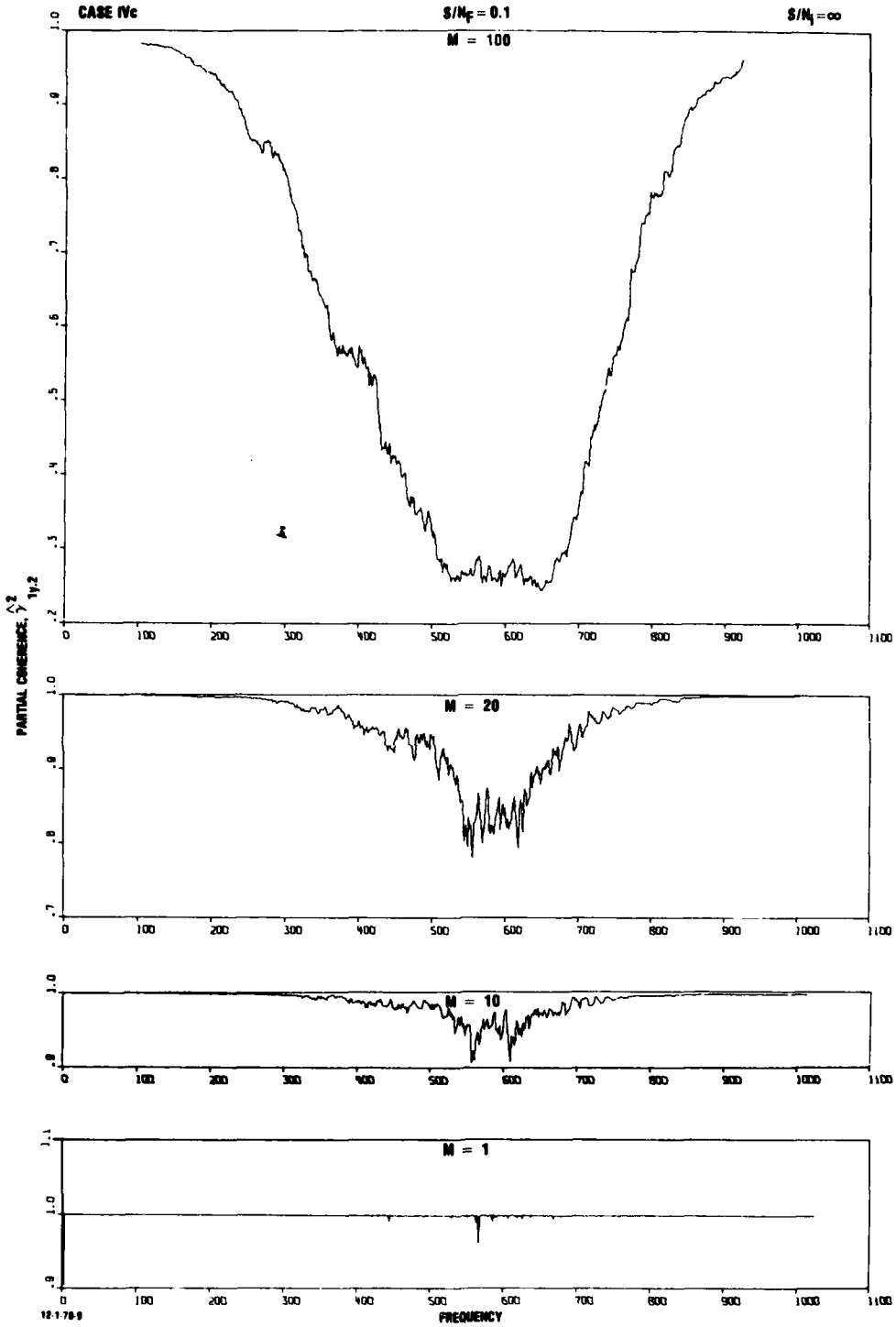

FIGURE 81. Estimated partial coherence for gradiometer signal channel for broad bandwidth filters with Lg_2/Lg_1 = 1.2 for S/N_F = 0.1.

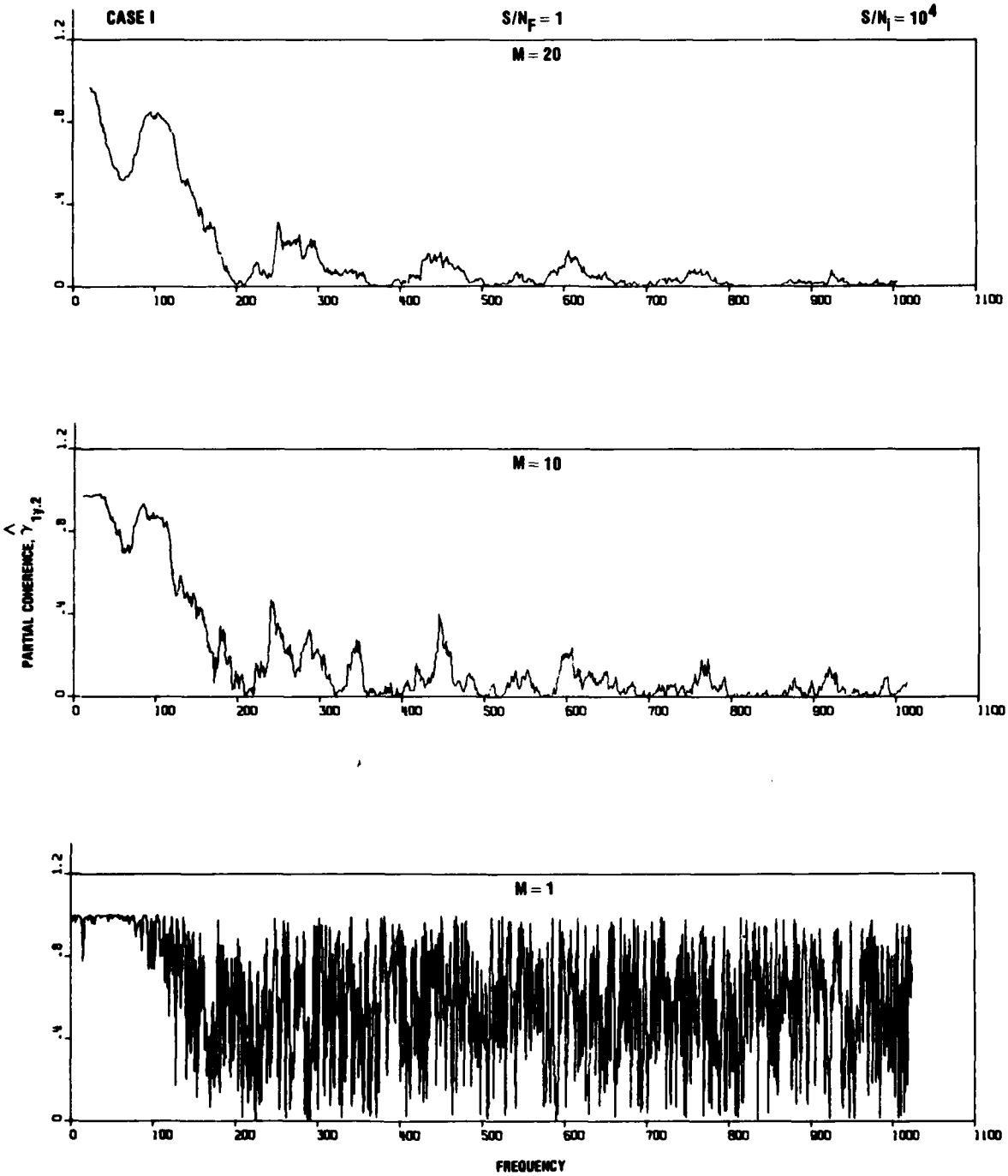

FIGURE 82. Estimated partial coherence for gradiometer signal channel for low-frequency filters with $Lg_2/Lg_1 = 4.4$ for $S/N_i = 10^4$.

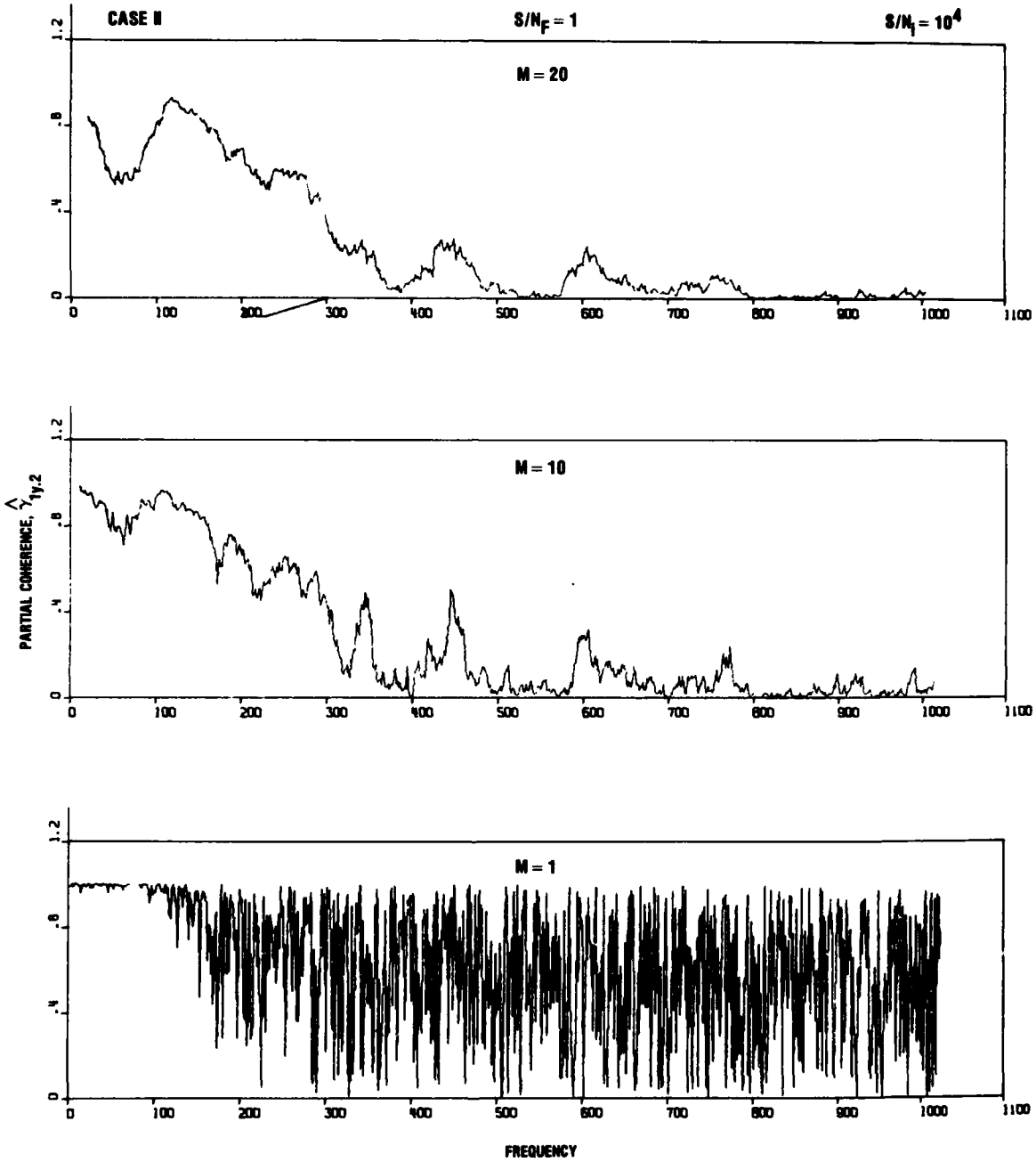

12-26-78-26

FIGURE 83. Estimated partial coherence for gradiometer signal channel for low-frequency filters with $Lg_2/Lg_1 = 1.2$ for $S/N_i = 10^4$.

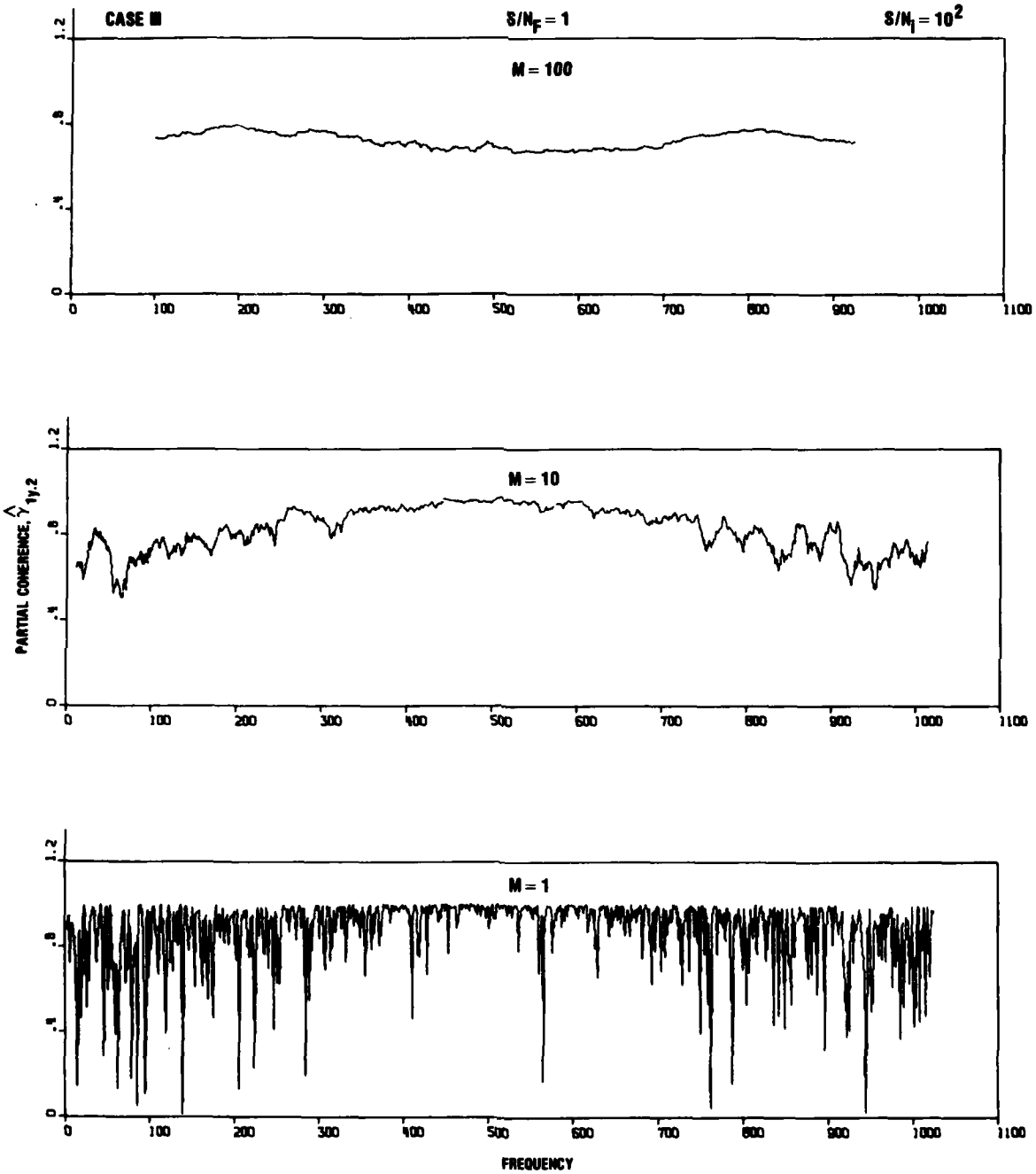

FIGURE 84. Estimated partial coherence for gradiometer signal channel for broad bandwidth filters with Lg_2/Lg_1 = 1 for $S/N_1 = 10^2$.

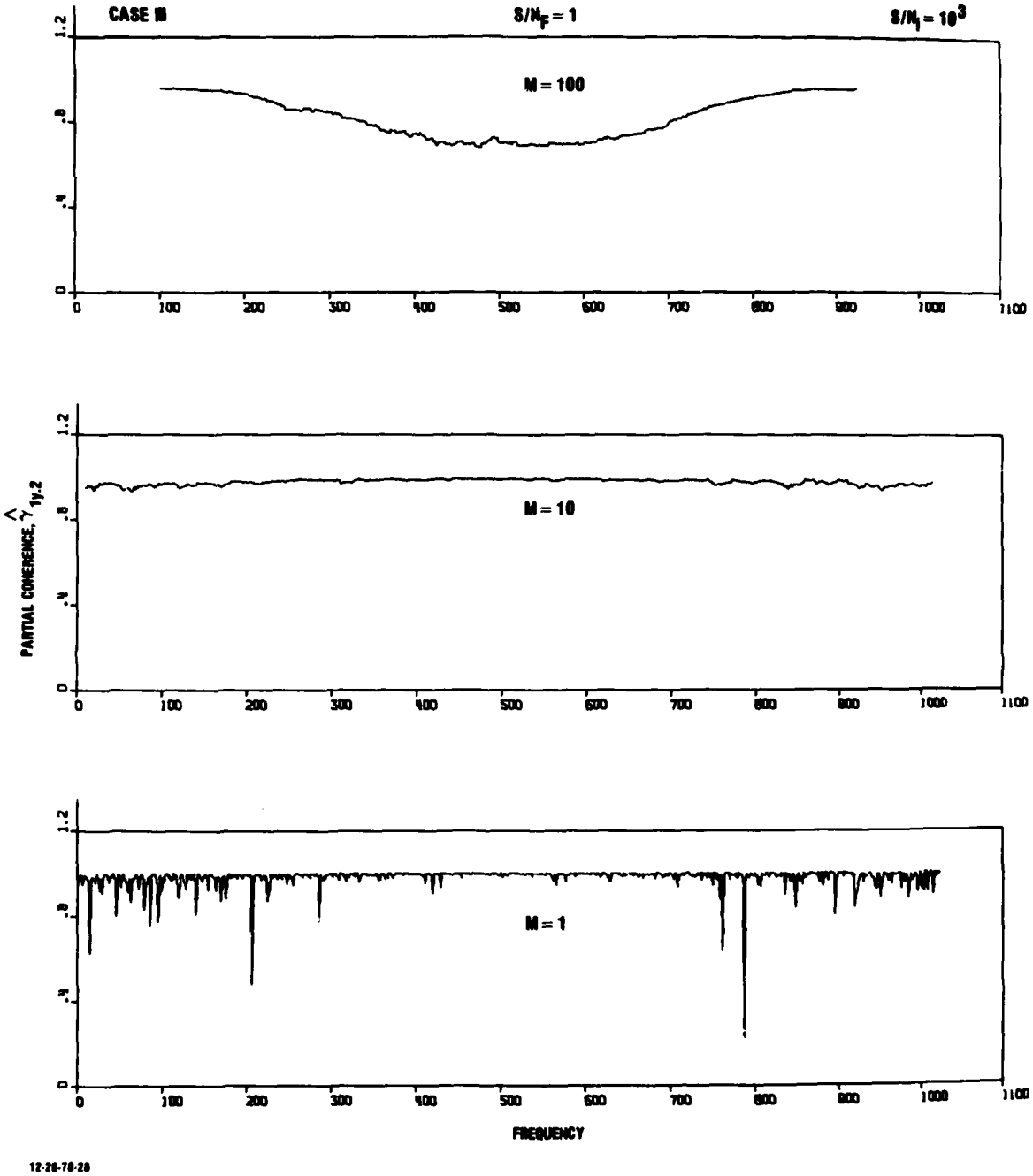

FIGURE 85. Estimated partial coherence for gradiometer signal channel for broad bandwidth filters with Lg_2/Lg_1 = 1 for $S/N_1 = 10^3$.

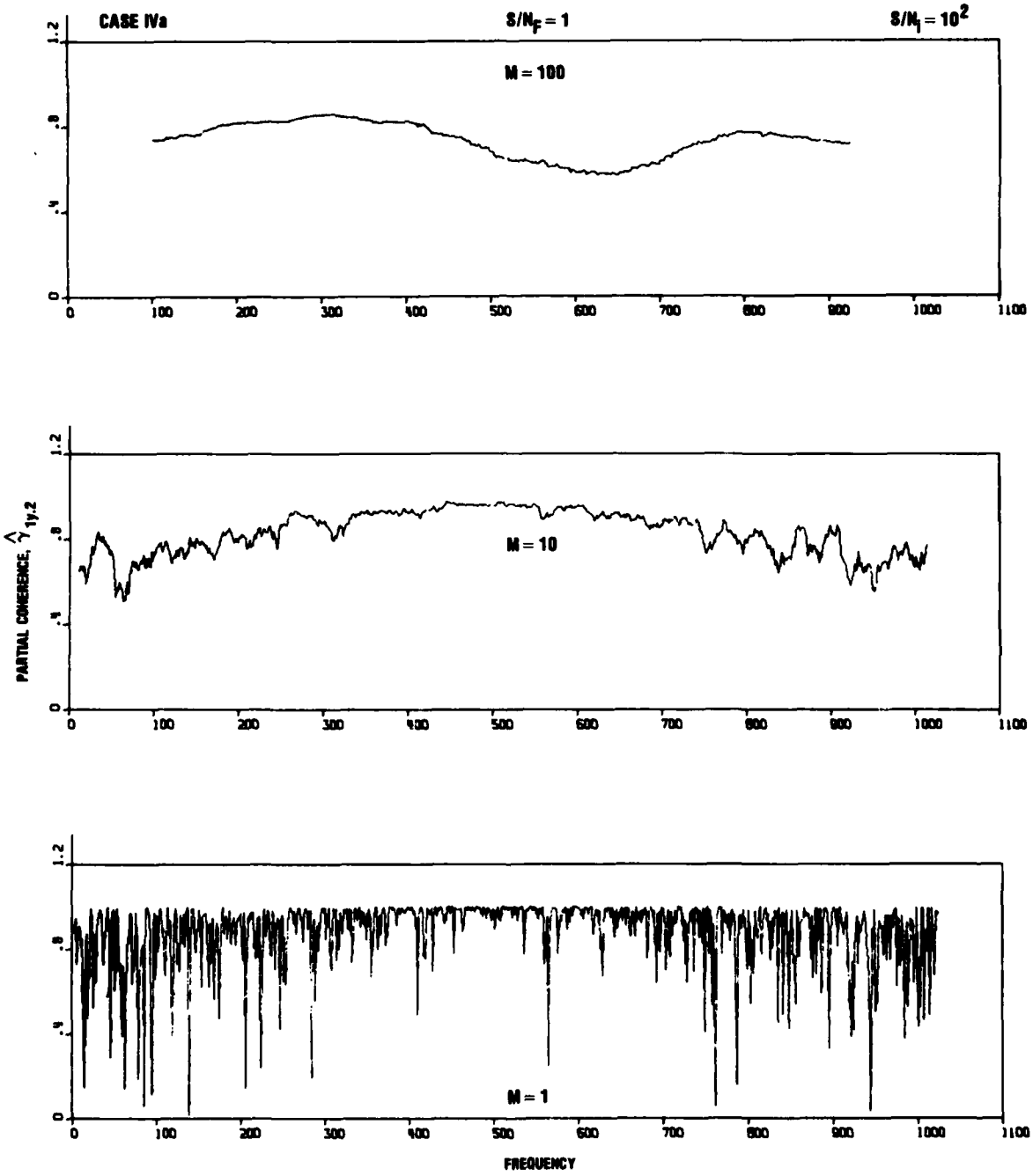

FIGURE 86. Estimated partial coherence for gradiometer signal channel for broad bandwidth filters with Lg_2/Lg_1 = 1.2 for $S/N_1 = 10^2$.

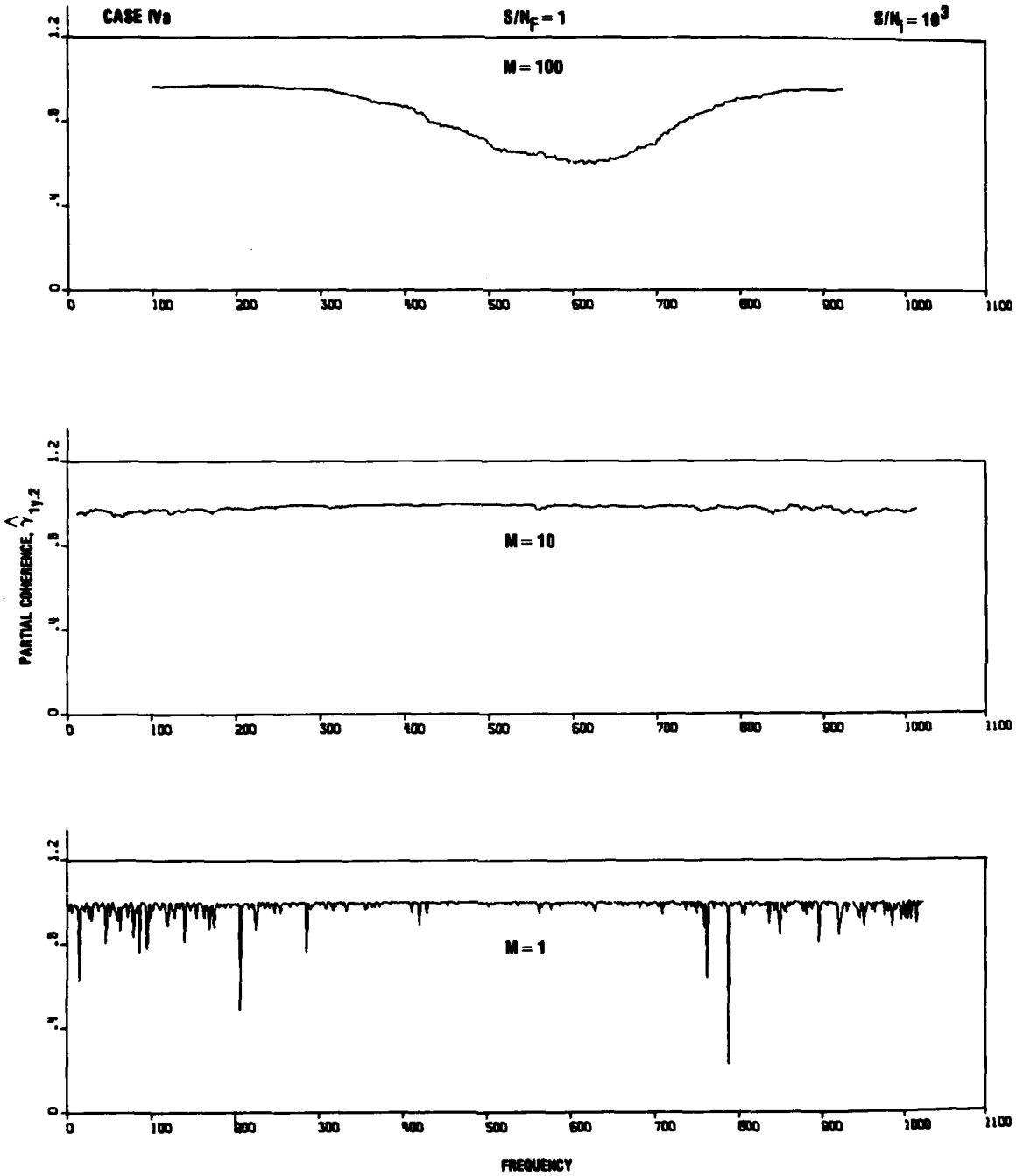

FIGURE 87. Estimated partial coherence for gradiometer signal channel for broad bandwidth filters with Lg_2/Lg_1 = 1.2 for $S/N_1 = 10^3$.

5. CONCLUDING REMARKS

A preliminary evaluation of how well a mean-squared estimation algorithm can decompose superposed time series in a main data channel has been made by (a) reviewing the basic assumptions for such a reconstruction algorithm, (b) doing the simplest and most revealing test of the algorithm as applied to a two-input gradiometer and two subsidiary channels, (c) using arbitrary but known spectra to simulate the gradiometer signal channel, so as to provide a reference to test the corresponding estimated spectra to be derived from the algorithm, and (d) performing parametric numerical simulations of the reconstruction process based on stationary random series inputs to simulated gradiometer and subsidiary channels. These parametric investigations allowed study of the effects on the reconstruction process of variables such as the frequency characteristics of the simulated gradiometer and subsidiary channels, the gradiometer and signal-to-instrument noise ratios, and the number of frequencies utilized in the averaging of periodograms so as to reduce their variance. Some of the most important points brought out in these investigations are as follows:

- There is no theoretical basis to support the specialized linear assumption utilized in the reconstruction algorithm, whereby functional linear relationship among the subsidiary channel outputs and superposed time series in the main channel are decoupled. Hence, the degree of confidence in the fidelity of reconstruction of the imbedded signal in the main data channel is no greater than the *a priori* knowledge concerning the validity of the above decoupling.

- The bias in the estimators for the spectral densities produced by the smoothing of their periodograms introduces deviations from unity in the partial coherences for ideal conditions of no instrument noise. This breakdown of the partial coherence as an indicator of the fidelity of signal reconstruction is independent of the frequency characteristics that were considered in the simulation of the gradiometer and current meter channels.
- The effect of instrument noise on the partial coherence is a function of the frequency characteristics of the simulated gradiometer and subsidiary data channels. For low center frequencies corresponding to peak amplitude of the gradiometer signal and noise spectra, Figs. 82 and 83 indicate that the partial coherence remains significantly different from unity for signal-to-instrument noise ratio as high as 10^4. However, for high center frequencies and broad bandwidths, Figs. 84 to 87 show that the partial coherences recover from the effect of instrument noise at signal-to-noise ratios in the range $10^2 < S/N_i < 10^3$.
- For low center frequencies corresponding to peak amplitudes of the gradiometer signal and "noise" spectra, the algorithm introduces significant numerical noise when the center frequency of the gradiometer noise spectra is significantly larger than that of the gradiometer signal spectra. However, this numerical noise disappears as the center frequency of the gradiometer noise spectra tends towards that of the gradiometer signal spectra.

It is important to emphasize that the specified spectra (Fig. 5) used to test the algorithm did not include the frequency dependence found in the Physical Dynamics experiments (Chapter 1), i.e., $S_{g_1 g_1} \sim f^{-2}$. Also, although the numerical

simulations were performed for a two-input gradiometer and two subsidiary channels, the computing code at IDA can handle the full nine channels of the Physical Dynamics experiments.

REFERENCES

1. W. Podney, Private Communication, Physical Dynamics, La Jolla, California 92038.

2. J.S. Bendat and A.G. Piersol, "*Random Data: Analysis and Measurement Procedures,*" Wiley-Interscience, New York, N.Y., 1971.

3. J.S. Bendat and A.G. Piersol, "*Measurement and Analysis of Random Data,*" John Wiley and Sons, Inc., New York, 1966.

4. F.R. Gantmacher, *The Theory of Matrices, Vol. 1,* Chelsea Publishing Co., New York, N.Y., 1959.